TECHNISCHE UNIVERSITÄT
MÜNCHEN

Lehrstuhl E23 für Technische Physik
Walther-Meißner-Institut für Tieftemperaturforschung
der Bayerischen Akademie der Wissenschaften

Electronic Properties of Electron-Doped Cuprate Superconductors Probed by High-Field Magnetotransport

Dissertation

Toni Helm

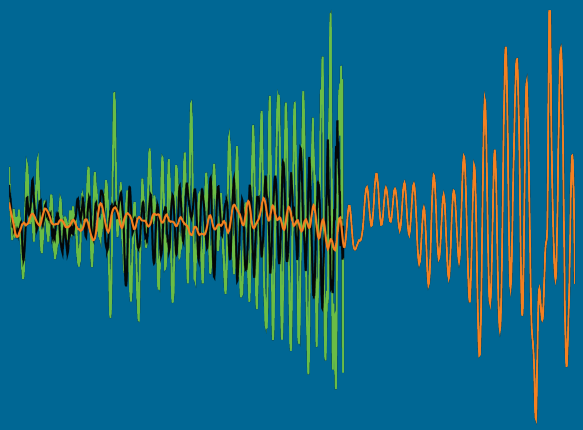

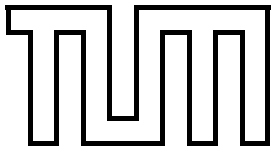

TECHNISCHE UNIVERSITÄT MÜNCHEN

Lehrstuhl E23 für Technische Physik

Walther-Meißner-Institut für Tieftemperaturforschung
der Bayerischen Akademie der Wissenschaften

Electronic Properties of Electron-Doped Cuprate Superconductors Probed by High-Field Magnetotransport

Toni Helm

Elektronische Eigenschaften von elektronendotierten Kupratsupraleitern untersucht mittels Hochfeld-Magnetotransports

Vollständiger Abdruck der von der Fakultät für Physik der Technischen Universität München zur Erlangung des akademischen Grades eines

Doktors der Naturwissenschaften

genehmigten Dissertation.

Vorsitzender:	Univ.-Prof. Dr. P. Vogl
Prüfer der Dissertation:	1. Univ.-Prof. Dr. R. Gross
	2. Univ.-Prof. Dr. C. Pfleiderer

Die Dissertation wurde am 02.09.2013 bei der Technischen Universität München eingereicht und durch die Fakultät für Physik am 18.09.2013 angenommen.

„Wenn man keinen Schritt nach vorn macht, bleibt man stehen."
eigene Überzeugung

"It is unwise to be too sure of one's own wisdom. It is healthy to be reminded that the strongest might weaken and the wisest might err."
Mahatma Gandhi

Kurze Zusammenfassung

In der vorliegenden Arbeit werden Ergebnisse zu Untersuchungen der elektronischen Eigenschaften des elektronendotierten Kupratsupraleiters $Nd_{2-x}Ce_xCuO_4$ (NCCO) im normalleitenden Zustand für einen breiten Dotierungsbereich, der fast das gesamte Phasendiagramm dieser Materialklasse abdeckt, vorgestellt. Magnetotransportmessungen in den weltweit höchsten, zerstörungsfrei erzeugten Magnetfeldern kamen als spektroskopisches Werkzeug zur Untersuchung der elektronischen Struktur von einkristallinem NCCO in Abhängigkeit von der Ladungsträgerkonzentration x zum Einsatz. Quanten- und semiklassische Oszillationen im Magnetowiderstand lieferten neue Erkenntnisse zu verschiedenen Eigenschaften der Fermi-Fläche und des Grundzustandes dieses Systems. Die Resultate der detaillierten Untersuchung des Einflusses der Temperatur, des magnetischen Feldes und der Magnetfeldorientierung auf den elektrischen Transport offenbaren einen engen Zusammenhang zwischen symmetriebrechenden Ordnungsphänomenen und der Supraleitung in NCCO.

Abstract

In the present work the normal-state properties of the electron-doped cuprate superconductor $Nd_{2-x}Ce_xCuO_4$ (NCCO) are investigated for a broad doping range, covering almost the whole phase diagram of this material. Magnetotransport measurements in the world's highest non-destructive magnetic fields were used as a spectroscopic tool for probing the electronic structure of single-crystalline NCCO as a function of the carrier concentration x. Quantum and semiclassical oscillations in the magnetoresistance provided new insights into various properties of the Fermi surface and the nature of the ground state in the system. The detailed investigations of the field- and temperature-dependent transport and its dependence on the field orientation have revealed a close correlation between symmetry-breaking ordering instabilities and the superconducting state.

Preface

Gegen Ende einer jeden Promotionszeit muss sich der angehende „Herr Doktor“ früher oder später Gedanken über die Zeit danach machen.

Was hat man bis zu diesem Zeitpunkt alles erreicht und was will man noch erreichen? Wie soll es weiter gehen?

Für die Entscheidungsfindung muss man auftauchen – auftauchen aus den Tiefen der Detailarbeit, aus der Spezialisierung, aus dem relativ eingeschränkten aber hochaufgelösten Mikrokosmos eines Doktoranden – um kurz Luft zu holen. Dann schaut man auf den Pfad zurück, welchen man eingeschlagen hat. Auf der Suche nach neuen Erkenntnissen hangelte man sich von einem Fragezeichen zum nächsten. Die Versuche sie zu lösen, führten ab und an in eine Sackgasse, aber auch des öfteren zu neuen noch viel spannenderen Fragestellungen. Die gewonnenen neuen Erkenntnisse sind Ergebnis intensiver, ausdauernder Arbeit am Detail, langer Diskussionen mit fachkundigen Kollegen, der Auseinandersetzung mit den Ergebnissen Anderer sowie ihrer Anwendung auf das eigene Problem. Außerhalb des eigenen kleinen Mikrokosmos traf man auf weitere Spezialisten anderer kleiner Teilgebiete. In Fachvorträgen wurden dann die Ergebnisse präsentiert und mittels wissenschaftlicher Belege verteidigt. Je weiter man sich von seinem eigenen Thema entfernte, desto weniger Überschneidungen zwischen der eigenen Arbeit und der Anderer fand man und umso mehr rückten Details in den Hintergrund.

Lässt man die Grenzen seines Fachbereiches hinter sich, sind es meist Familie, Freunde oder Bekannte welche gern einen Einblick in den Mikrokosmos haben möchten. Dann gilt es einen groben Umriss zu skizzieren und zu zeigen, welche Überschneidungen die eigene Forschungsarbeit mit dem Makrokosmos unserer

Gesellschaft hat beziehungsweise haben könnte. Die eigentlichen Fragen, mit denen man dann konfrontiert wird sind:

Welchen Sinn hat Grundlagenforschung? Und welchen positiven Nutzen hat der Einzelne im Alltag davon? Welchen Nutzen hat es, Unsummen an öffentlichen Geldern dafür aufzuwenden, kleine abstrakte, für das bloße Auge unsichtbare Teilchen (wie z. B. Elektronen) unter extremen Bedingungen zu quälen?

Jeder in der Wissenschaft Tätige sollte auf diese Fragen vorbereitet sein. Mittels konkreter Beispiele kann man versuchen seinen Gegenüber zu überzeugen. Beispielsweise wäre die digitale Welt von heute ohne Grundkenntnisse zu den elektronischen Eigenschaften von Halbleitern wie Silizium einfach undenkbar. Die etwas Älteren werden darauf hin abwinken und von der „guten alten Zeit“ ohne Computer und Mobiltelefon schwärmen. Doch nicht jeden wird das zufrieden stellen.

Das Hauptproblem der Grundlagenforschung ist wohl, dass der von Neugier getriebene Forscher meist im Dunkeln tappt. Er wird also nie zu einhundert Prozent wissen können, ob der eingeschlagene Weg einen konkreten praktischen Nutzen hervorbringen wird. Das Füllen von schwarzen Flecken auf Landkarten, das Lösen von einzelnen Ungereimtheiten, das Erkennen von gemachten Fehlern kann aber Neues initiieren. Grundlagenforschung ist also der Samen für zu lösende Probleme kommender Generationen und ist der Ursprung von so gut wie allen alltäglich genutzten Dingen unserer Gegenwart.

Unabhängig von persönlichen Umständen, welche die Entscheidungsfindung über die Zeit nach der Promotion beeinflussen, ist es wohl der Reiz des Ungewissen, welcher den Mikroorganismus „Forscher“ antreibt. Auch wenn die Arbeit des Einzelnen nicht den ganz großen Durchbruch erbringt, kann sie wegweisend für unser aller Zukunft sein bzw. einen kleinen Baustein für zukünftige Innovationen bilden.

Die vorliegende Arbeit beschäftigt sich mit einem sehr exotischem Material, einem sogenannten Kuprat-Hochtemperatursupraleiter. Der Effekt der Supraleitung, welcher unterhalb einer kritischen Sprungtemperatur T_c in bestimmten Materialien auftritt, wurde schon Anfang des 20-sten Jahrhunderts entdeckt. Es dauerte aber über 40 Jahre bis eine vollständige Beschreibung durch die BCS-Theorie gefunden werden konnte. Heute, knapp 100 Jahre später, ermöglicht die-

ses Grundverständnis den Bau von supraleitenden Magnetsystemen, ohne die bahnbrechende Experimente, wie beispielsweise die Beschleunigerexperimente am Large-Hadron-Collider (LHC) in Cern zur Ergründung des Ursprungs unseres Universums, undenkbar wären. Mit Magnet-Resonanz-Tomographie hat Supraleitung sogar Einzug in den medizinischen Alltag finden können.

Ende der 80-er Jahre wurde Supraleitung in keramischen Oxiden, den Kupraten, mit Sprungtemperaturen, welche alle bis dato gemachten theoretischen Vorhersagen in den Schatten stellten, entdeckt. Die Idee, möglicherweise Supraleitung bei Temperaturen nahe der Raumtemperatur realisieren zu können, entfachte weltweit große Anstrengungen, den Effekt der Hochtemperatursupraleitung zu verstehen. Doch bis zum jetzigen Zeitpunkt ist es noch nicht gelungen, eine umfassende Theorie zur Hochtemperatursupraleitung aufzustellen. Da es sich um hochkomplexe Materialien handelt, ist einer der limitierenden Faktoren, um experimentellen Zugang zur elektronischen Grundstruktur zu erhalten, die Probenqualität.

Im Folgenden werden Ergebnisse aus Experimenten an einkristallinen elektronendotierten Kupraten mit einer noch nie zuvor erreichten Probenreinheit vorgestellt. Der Zusammenhang zwischen Supraleitung und den elektronischen Eigenschaften dieser Materialklasse wurde bei extrem tiefen Temperaturen und unter dem Einfluss der weltweit höchsten, im Labor erzeugbaren zerstörungsfreien Magnetfelder untersucht. Dabei konnten Einblicke in den normalleitenden Zustand gewonnen werden, welche Hinweise auf das Zusammenspiel zwischen der supraleitenden Phase und symmetriebrechenden Odnungsphänomenen geben. Diese Arbeit liefert einen wichtigen Beitrag zur Erschließung des elektronischen Phasendiagrammes von elektronen-dotierten Kuprat-Supraleitern. Durch den Einsatz des aktuell technisch Machbaren konnten einige kontrovers diskutierte Fragen beantwortet sowie neue Ungereimtheiten offen gelegt werden. Es ist noch ein weiter Weg bis Wissenschaftler ein vollständiges Rezept für die Hochtemperatursupraleitung liefern werden. Ich bin sehr froh und überzeugt davon, dass ich mit meiner Promotion einen Teil zur Entschlüsselung eines der bedeutendsten und wohl auch mysteriösesten Phänomene im Bereich der Festkörperphysik beigetragen kann.

Contents

Part I

Introduction and Theory

1 Introduction

1.1 From the first superconductors till present

It took over 40 years since the discovery of superconductivity (SC) in 1911 by H. Kamerlingh Onnes [1], until a consistent and comprehensive theory was established. The BCS (Bardeen-Cooper-Schrieffer) theory [2, 3] stated that the superconducting phase can be described in terms of a collective ground state of condensed Cooper pairs (two electrons), bound together by the exchange of phonons (lattice vibrations). Based on this theory an upper limit for the critical transition temperature, T_c, was predicted below which the superconducting phase can be stable, to be not higher than 30–$40\,\mathrm{K}$. Although a vast number of new superconducting materials had been found over the years, with the highest observed $T_\mathrm{c} = 23\,\mathrm{K}$ for an A15 compound[1], the BCS limit stood unshaken, proving the theory right. It was in the mid 80s, a time when the hype of SC had already subsided, that all of a sudden G. Bednorz and A. Müller discovered SC in a doped ceramic copper-oxide compound (a so-called cuprate), namely $La_{2-x}Ba_xCuO_4$ with onset temperatures in the $30\,\mathrm{K}$ range [4]. The undoped La_2CuO_4 was well known for its insulating properties. Thus, the observation of SC by doping with barium came rather unexpected. Only half a year later SC with an incredibly high T_c of $\sim 92\,\mathrm{K}$ was observed in a similar cuprate compound from the same perovskite family[2], containing yttrium instead of lanthanum [5]. The existing theory was not capable to provide an explanation for SC at such high temperatures and for such unconventional superconductors.

It was a team of "a doer and a thinker, that hit upon a paradoxical approach to making superconductivity: fashioning them out of insulators. [...] They set off a

[1] A15 compounds are intermetallic compounds with the chemical formula A_3B, where A is a transition metal and B another metal or semiconductor.

[2] Copper-oxide superconductors are layered perovskites. The name perovskite comes from Russian mineralogist Count Lev Aleksevich von Perovski.

stampede to superconductivity", citing an article about an interview of the two scientists published in Fortune magazine in 1988 [6]. In the following years an unprecedented effort has been put into the investigation of high-temperature superconductivity (HTSC) in the cuprates. The number of different superconducting compounds has grown big. The world record with a $T_c = 138\,\mathrm{K}$ at ambient pressure is currently held by a mercury-based cuprate [7, 8]. In 2006 a new class of HTSC materials was discovered, the so-called iron pnictides [9]. The realization of SC above the BCS limit in a completely different but also very complex compound family relumed a new hype in the material science community. Persisting till present, it shifted cuprates a bit out of the spotlight. To date the origin of SC in cuprates has not been identified unambiguously. Besides SC, a huge diversity of physical phenomena, comprised by the cuprates family, has been excavated by uncountable experiments. The existing knowledge and experimental techniques developed during the "Copper age" of SC do help immensely to push scientific progress in this new material class fast forward. There are people who already declare the "Iron age" of SC since the huge number of compounds and comprised physical phenomena draw parallels to the cuprates. This new class, however, will not be discussed in the present work.

1.2 High-temperature superconductivity in cuprates

Cuprates are highly anisotropic layered compounds consisting of conducting planar CuO_2-layers sandwiched between insulating charge reservoir layers similar to the situation in modulation doped semiconductor heterostructures. SC emerges upon doping either holes or electrons into the CuO_2-layers. Importantly, SC in cuprates depends strongly on the charge carrier concentration x. Their undoped mother compounds are electrical Mott insulators[3], which show antiferromagnetic ordering of the Cu-spins. The Mott insulating state at $x = 0$ can be explained best by the Hubbard model, where a strong on-site Coulomb repulsion U is responsible for the splitting of the conduction band into a fully filled lower and an empty upper Hubbard band [11–13]. Therefore, at $x = 0$ the Fermi energy lies in between the bands and an energy gap exists, which causes the insulating

[3] From band theory such compounds are predicted to be of metallic character, but due to a strong local on-site correlation energy double occupation is suppressed, making them insulating [10].

state.

There are plenty of reviews and books that provide an overview on the different theoretical approaches and experimental results on SC in cuprates, see, e.g., [12–20]. As there is no clear consensus on the fundamental mechanism, responsible for the formation of Cooper pairs in this material class, a comprehensive discussion of the theory stays beyond the scope of this thesis.

One of the main issues in the field of HTSC is sample quality. It not only poses challenges to the experiments, but also to the interpretation of their results that provides a huge playground for theorists. Two main theories seem to have outlasted the past controversial and elusive discussions on the pairing mechanism: One is the resonating valence-bond theory first suggested by P. W. Anderson [21]. It is based on the given cuprate structure, where copper atoms are linked via oxygen atoms forming chemical valence bonds. These bonds enable the neighboring Cu-atoms to share an electron pair of opposite spins. The idea is that, although the spin pairs are localized due to the bonding and no current is supposed to be carried, doping of the material can loosen the pairs so that they can become mobile similar to a spin-liquid and condense into the coherent superconducting phase. Another theory [22] suggests spin fluctuations as a bonding glue between the pairing electrons in the superconducting phase. All cuprates have in common a stable long-range ordering, namely antiferromagnetism (AFM), present in their undoped insulating mother compounds. The idea here is that upon substitution of suitable atoms in the charge reservoir layers providing mobile charge carriers (electrons of holes) in the CuO_2-layers this antiferromagnetic lattice breaks up. Analog to phonons in BCS superconductivity, moving electrons can, in this case, affect the spins in their near environment, leading to a distortion of the antiferromagnetic lattice. This distortion could provide a binding mechanism for a second electron to be drawn into a Cooper pair. These are by far not the only theories but they have the biggest support in the scientific community.

Besides the large number of hole-doped (p-type) compounds, there are a few that can be doped with electrons (n-type) [23, 24]. The main representatives of the latter material class have the chemical structure $R_{2-x}M_xCuO_4$ with the lanthanide rare-earth atoms R: Pr, Nd, Sm or Eu and M is Ce or Th. Doping is achieved, for example, in $Nd_{2-x}Ce_xCuO_4$ by substituting Nd^{3+} partially with Ce^{4+}, providing additional electrons into the conducting CuO_2-layers. The correlations be-

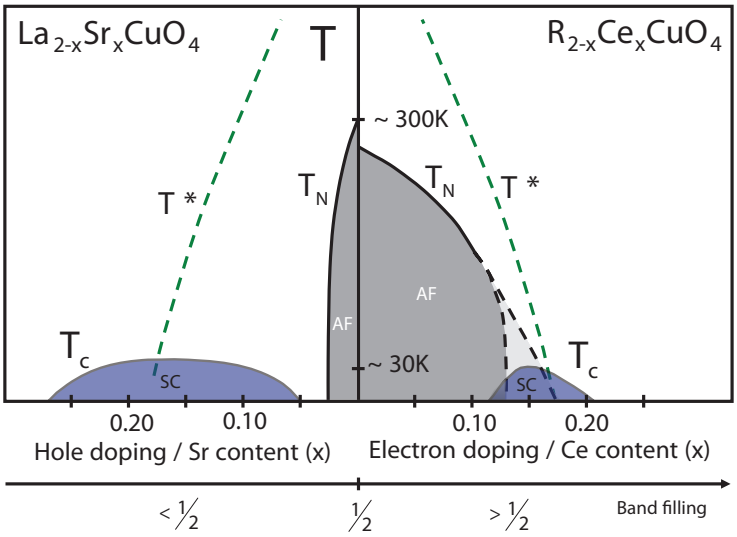

Figure 1.1: Schematic phase diagram of cuprate superconductors, according to various experimental results for $La_{2-x}Sr_xCuO_4$ and $Nd_{2-x}Ce_xCuO_4$, representing the p- and n-doped sides, respectively [25]. Around half band filling AFM emerges below the Néel temperature T_N. The doping at which SC has its maximum T_c is called optimal doping. T^* marks the temperature below which the anomalous region associated with pseudogap phenomena is found. For strong overdoping, i.e. at dopings outside the pseudogap and SC phases these compounds are believed to be conventional metals.

tween the superconducting transition temperature and doping is conflated in the generic phase diagram of cuprates, see Fig. 1.1. In the picture of the Hubbard model doping holes corresponds to a lowering of the Fermi level until it enters the lower Hubbard band and, respectively, electron doping would correspond to doping into the upper Hubbard band. One approach to the understanding of HTSC and its mechanism is to study the symmetries and differences between the hole- and electron-doped side in the cuprate phase diagram. For a comprehensive review about the main achievements in the field of n-doped cuprates see, e.g., [25].

Fig. 1.1 shows a schematic phase diagram for p- and n-doping for two crystallographically similar cuprate compounds. It should be mentioned that the critical temperatures on the hole doped side could be much higher ranging up to $138\,\mathrm{K}$, as mentioned above. An approximate symmetry between the n- and the p-doped

side is discernible. The main differences are found in the robustness of the antiferromagnetic and superconducting phases, which originates from the doping into different bands. The superconducting dome is much broader for the p-doped side as compared to electron-doping. AFM behaves rather different with respect to the charge carrier concentration x. For the p-doped compounds T_{N} vanishes quickly for already small doping (~ 0.03), whereas it persists at least up to the superconducting region on the electron-doped side. Whether it even coexists with SC (indicated by the light grey area surrounded by black dashed lines) is very controversially discussed and one of the current issues in the field of n-doped cuprates. Another very anomalous region of the phase diagram is indicated by the dashed green lines and labeled with T^*. These are approximately the temperatures below which various phenomena, observed experimentally, are associated with or comprised in the so-called pseudogap phase. Due to strong electronic correlations cuprates show anomalous normal-state properties. That is why they are often referred to as non-Fermi liquids. The nature of the ground state has not been understood yet. To gain further information on the mechanism of SC in cuprates it is important to know the properties of the normal-state carriers.

During the last 10 years new results came up, mainly fueled by an immense step forward in terms of sample quality and homogeneity and as well advances in experimental techniques, that initiated a re-examination of the existing fundamental picture. In particular high-field magnetotransport has proven very efficient in investigating the normal-state Fermi surface (FS) properties of cuprates. A breakthrough in the Fermiology of p-doped cuprates was made by the observation of semiclassical angle-dependent magnetoresistance oscillations (AMRO) [26, 27] and magnetic quantum oscillations (MQO) [28–33]. These high-field effects are known as a powerful tool for studying the FSs of conventional metals [34, 35] and have been extensively used for layered materials with correlated electrons, like organic metals [36].

This thesis will examine the high-field normal-state properties of the n-doped cuprate superconductor $Nd_{2-x}Ce_xCuO_4$. In particular, studies of MQO and semiclassical magnetotransport provide new information about the normal-state in the superconducting doping range and its evolution with doping. The findings provide strong arguments for a close relation of insulating ordering instabilities and superconductivity.

1.3 The electron-doped cuprate superconductor $Nd_{2-x}Ce_xCuO_4$

1.3.1 Crystal structure

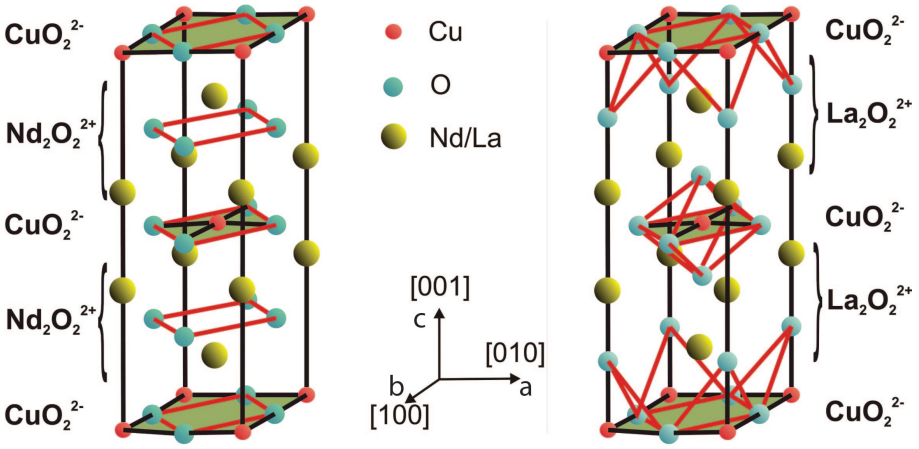

Figure 1.2: Body-centered tetragonal T′ (left) and T (right) structures of electron- and hole-doped 214 cuprates, respectively. For NCCO the corresponding lattice parameters, determined by X-ray diffraction, are $a = 3.95$ Å and $c = 12.07$ Å.

All n-doped cuprates are based on the body-centered (bc) tetragonal T′-Nd_2CuO_4 structure (with space group $I4 = mmm$), which is closely related to the T-La_2CuO_4 structure, typical of the p-doped counterpart. Both, T and T′ structures can be regarded as an intergrowth of infinite, flat CuO_2^{2-} layers containing Cu in square planar coordination alternating with $Re_2O_2^{2+}$ layers. The conducting properties are governed by the CuO_2 layers, which are shifted by $(\frac{a}{2}, \frac{a}{2})$ to each other (a being the unit cell constant in the layer plane), resulting in a unit cell of double size. The rare earth oxide layers act as a charge carrier reservoir and spacer for the CuO_2 layers. Thus, the single crystals are characterized by a strong in-plane to out-of-plane anisotropy in electronic transport.

In the T-La_2CuO_4 structure the $La_2CuO_2^{2+}$ layers have the rock salt structure, that is why La has a total oxygen coordination number of 9. Therefore, oxygen is located at the apical positions above and below Cu^{2+} ions in the CuO_2^{2-} layers. In

the center of the unit cell the tetragonally distorted octahedral Cu-O coordination sphere, typical for cuprates, is obtained, see Fig. 1.2. Generally, this structure, which most of the cuprates are based on, is called the perovskite structure. By contrast, in the T'-Nd_2CuO_4 structure the $Nd_2O_2^{2+}$ layers have a fluorite structure with an oxygen coordination number of 8 for the rare earth atom, leaving vacant the apex oxygen position directly below and above the Cu^{2+} ions, see Fig. 1.2.

1.3.2 Magnetic structure

An antiferromagnetic (AF) ordering for the Cu-spin sublattice was observed in the underdoped mother compound Nd_2CuO_4 (NCO) below a Néel-temperature of $T_N \approx 270\,\mathrm{K}$ [37]. Three interactions play a role in the magnetic structure of NCCO: Cu-Cu, Nd-Cu and Nd-Nd. The latter two become dominant at lower temperatures where the magnetic moment of the Nd-ions is found to increase significantly [38]. Due to the large magnetic moment of Nd-ions, $J = 9/2$, the competition between the different couplings leads to various magnetic structures depending on the temperature and field. In other n-doped cuprate compounds like, e.g., $Pr_{2-x}Ce_xCuO_4$, ordering related to the rare-earth ions is different or absent [39]. This strongly depends on the magnetic moment of the corresponding rare-earth ion.

The magnetic moments of the Cu-spins lie within the CuO-planes with a relatively strong intralayer coupling pointing along the Cu-O-Cu directions ([100], [010]) [40, 41]. For NCCO the intralayer exchange, $J_{\parallel} = 126\,\mathrm{meV}$ is much stronger than $J_{\perp} = 5 \cdot 10^{-3}\,\mathrm{meV}$, giving rise to a very anisotropic magnetic behavior [42, 43]. The Cu^{2+} spins order in a noncollinear structure, as it is sketched in Fig. 1.3 (a). The spin orientation is found to alternate between adjacent layers [38], as indicated by different colors for the Cu atoms in Fig. 1.3. For low doping, $x \leq 0.03$, a spin-flop transition from the noncollinear into the collinear Cu-spin structure above a critical magnetic field of approximately $4 - 5\,\mathrm{T}$ was observed in magnetization and neutron scattering experiments [39, 44].

In the insulating mother compound Nd_2CuO_4 the Nd-moments were found to couple to the Cu-sublattice [44, 45] and as the temperature was decreased, several transitions associated with different Nd-Cu moment configurations were observed [38]. At $T \leq 1\,\mathrm{K}$, the same ordering of the Nd-sublattice as for the Cu-spins was found. More recently a complex magnetic structure was proposed by

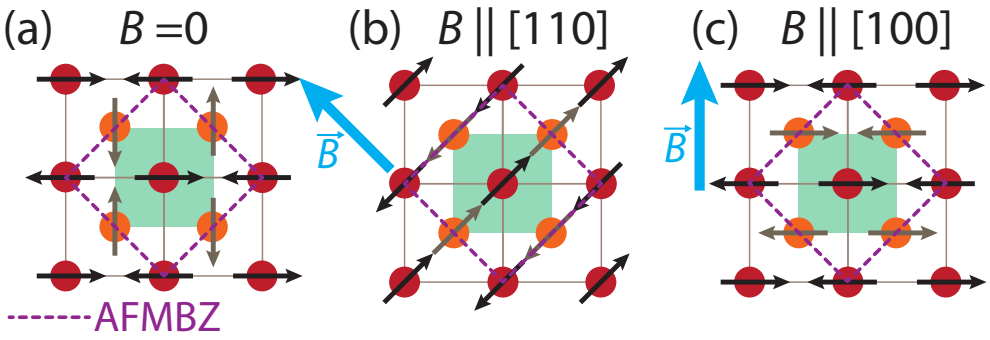

Figure 1.3: Magnetic structure of Nd_2CuO_4: (a) in the noncollinear antiferromagnetic phase at zero field and (b), (c) in the collinear phase above the spin-flop transition with a field aligned parallel to the Cu-Cu and Cu-O-Cu direction, respectively, according to Lavrov et al. [39]. Only Cu-atoms of two adjacent layers (red and orange circles) are shown. The dashed purple line indicates the antiferromagnetic unit cell, which is two times larger than the non-magnetic unit cell (green square).

Richard et al. [46], with different ordering configurations depending on the magnetic field strength, that could explain their results on ultrasound in NCCO. Field-orientation-dependent transport measurements in strongly underdoped NCCO revealed a strong coupling of the Nd-sublattice structure to the conducting channel [47].

1.3.3 The 2D Fermi surface

First principles calculations [48] have shown that the electronic band structure for a layered anisotropic cuprate conductor, such as NCCO, can be described in terms of the tight-binding approximation with the hopping energies $t_{ij}(\mathbf{R})$, representing the effect of overlapping of atomic orbitals between the origin and another site $\mathbf{R}$. The corresponding electronic structure is derived from the eigenvalues of the Hamiltonian matrix

$$H_{ij} = -\sum_{\mathbf{R}} t_{ij}(\mathbf{R}) \cos(\mathbf{k}\cdot\mathbf{R}), \tag{1.1}$$

summing up over all lattice vectors [49]. The two-dimensional in-plane band dispersion of NCCO $\epsilon(\mathbf{k})$ is represented by the one obtained from band structure

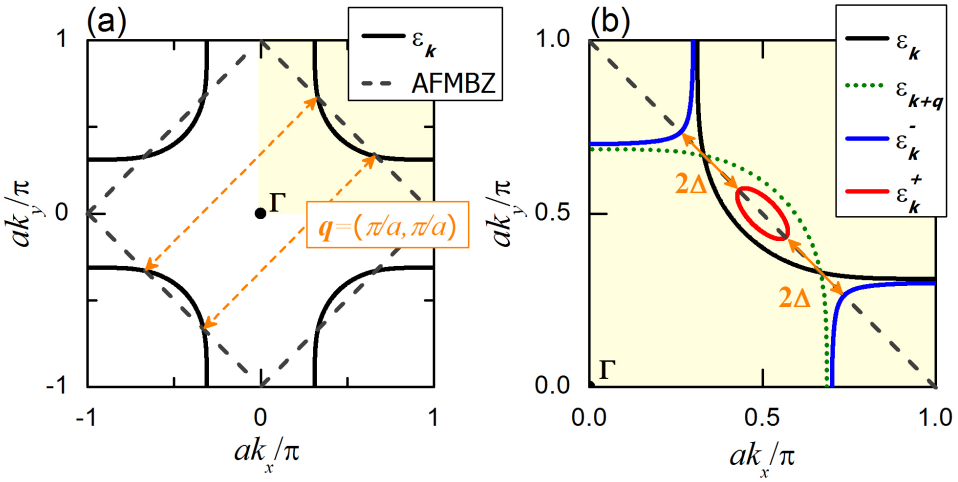

Figure 1.4: (a) Hole-like FS centered around $(\frac{\pi}{a}, \frac{\pi}{a})$, according to band theory [48] and Eq. (1.2). The dashed, grey line highlights the antiferromagnetic Brillouin zone (AFMBZ). (b) Suggested reconstructed FS in the first quadrant of the BZ, according to Eq. (1.3), consisting of hole- (red) and electron-like (blue) parts, in the presence of a $(\frac{\pi}{a}, \frac{\pi}{a})$ -ordering represented by the energy gap Δ.

calculations for $YBa_2Cu_3O_{7-\delta}$ by Andersen et al. [48]:

$$\epsilon(k_x, k_y) = -2t(c_x + c_y) + 4t'c_xc_y - 4t''(c_x^2 + c_y^2 - 1) + \alpha, \tag{1.2}$$

where $c_i = \cos(k_i a)$, a is the in-plane lattice constant and α represents the effect of doping. t, t', t'' are the nearest-, 2nd- and 3rd- nearest-neighbor in-plane-hopping energies, generally assumed to be doping independent. The resulting hole-like FS of NCCO is centered around the corner of the BZ and has a distorted circular shape with a stronger convexity along the diagonals of the BZ, see Fig. 1.4 (a).

As will be discussed in Sect. 1.4, the FS of cuprates is believed to undergo a reconstruction in a certain controversially discussed doping range. Due to the antiferromagnetism (AFM), existing in all underdoped cuprates, so-called "hot spots" become important in the BZ. These are the crossing points of the antiferromagnetic Brillouin zone (AFMBZ) boundary and the FS. AFM arises due to the underlying spin-density-wave background from a certain AFM ordering of the copper spins in the conducting layers, as was shown in the previous section. The corresponding superlattice has a two-times larger magnetic unit cell (see Fig. 1.3). Thus, the resulting AFMBZ in k-space is reduced as compared to the original BZ

by a factor of 2 and rotated by $45°$ (indicated by the dashed lines in Fig. 1.4 (a) and (b)). It can be shown via degenerate perturbation theory that in the presence of static long-range-AFM charge carriers close to the AFMBZ boundary will be Bragg-reflected by $\mathbf{q} = (\frac{\pi}{a}, \frac{\pi}{a})$ [50–52]. Hence, the FS is folded by this vector, i.e. the FS is reconstructed into hole- and electron-like parts separated by an energy gap Δ, opening up at the edge of the new AFMBZ. This is described by the new dispersion relation:

$$\epsilon_k^{\pm} = \frac{1}{2}\left[\epsilon_k + \epsilon_{k+q} \pm \sqrt{(\epsilon_k - \epsilon_{k+q})^2 + 4\Delta^2}\right], \tag{1.3}$$

where $\pm$ denotes the new electron- and hole-like FS parts separated by 2Δ due to a $(\frac{\pi}{a}, \frac{\pi}{a})$-scattering potential, see Fig. 1.4 (b).

1.4 Relevant experimental results

At present, for both sides of the phase diagram, p- and n-type, the main target of experimental activities has been to investigate the evolution of the electronic state from an AFM Mott insulator to a high-temperature superconductor. A central issue for superconductivity in cuprates is the nature of the normal state and whether it can be described in terms of conventional Fermi liquid theory.

For investigating well defined quasiparticles, low temperatures are prerequisite to suppress thermal distortions. In this respect, the n-doped cuprates have, by contrast to their p-doped counterparts, much lower critical magnetic fields. Therefore, the normal state at low temperatures can be easily accessed. There have been uncountable experiments investigating the normal state properties of cuprates.

For example, for n-doped $Pr_{2-x}Ce_xCuO_4$ (PCCO) with almost optimal doping, $x = 0.15$, measurements of the thermal conductivity [53] performed in a magnetic field of $B = 13\,\mathrm{T}$ revealed a clear violation of the Wiedemann-Franz law, which is one of the main fingerprints of Fermi liquids. By contrast, nuclear magnetic resonance experiments [54] on the n-doped cuprate $Pr_{1-x}LaCe_xCuO_4$ with $x = 0.11$[4] observed a rather conventional behavior of the spin-relaxation rate be-

[4] In $Pr_{1-x}LaCe_xCuO_4$ half of the Pr atoms are replaced by La, that helps stabilizing crystallization. SC appears at $x = 0.09$ and weakens upon increasing x. Thus, $x = 0.11$ corresponds to slight overdoping.

tween $55 - 0.2\,\mathrm{K}$. For p-doped cuprates a violation of the Wiedemann-Franz law was reported in underdoped $Bi_{2+x}Sr_{2-x}CuO_{6-\delta}$ [55], whereas it was found to be obeyed in overdoped samples [56, 57].

An anomalous phenomenon, common for both sides, is the pseudogap. This phenomenon can be understood as the appearance of an anisotropic suppression of electronic states near the Fermi energy level, originating from a not yet clearly understood ordering process. Such a gap has been mainly detected by surface-sensitive experiments, such as angle-resolved photoemission spectroscopy (ARPES) [16, 25, 50]. Indications of it have been observed mainly in the vicinity to SC between the underdoped antiferromagnetic and the more conventional overdoped metallic regions for various compounds even outside the cuprate family [58–62]. It is still unclear whether the pseudogap and its relation to SC can be understood as a precursor with preformed pairs or if it is completely irrelevant. In the pseudogap region an unconventional behavior of various physical properties such as photoemission spectra, optical conductivity and Hall effect, electrical and thermal transport coefficients, etc. indicated a strong deviation from the conventional Landau Fermi liquid behavior [13, 16, 63–65]. Thus, for cuprates the general opinion was that the conventional fermionic quasiparticle picture is not obeyed and the theory needed to find other more exotic constructions to describe the observed phenomena.

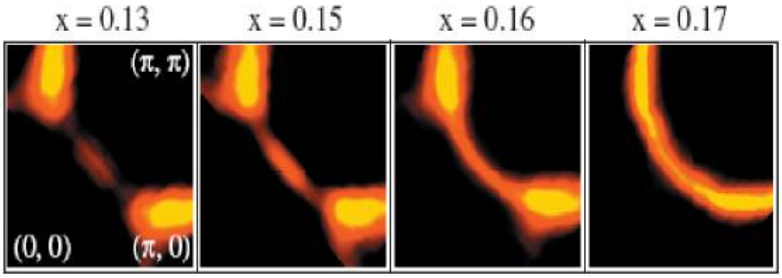

Figure 1.5: ARPES intensity integrated over $\pm 20\,\mathrm{meV}$ with respect to the Fermi energy at $30\,\mathrm{K}$ as a function of k_x, k_y for several doping levels of NCCO by Matsui et al. [66]. A pseudogap, that is a suppression of the spectral weight near the FS, is observed for $x \geq 0.15$. Only below optimal doping a real gap is resolvable. Figure reproduced from [66].

Only in the strongly overdoped, metallic region of the phase diagram a more conventional behavior is predicted. Indeed, ARPES experiments performed on

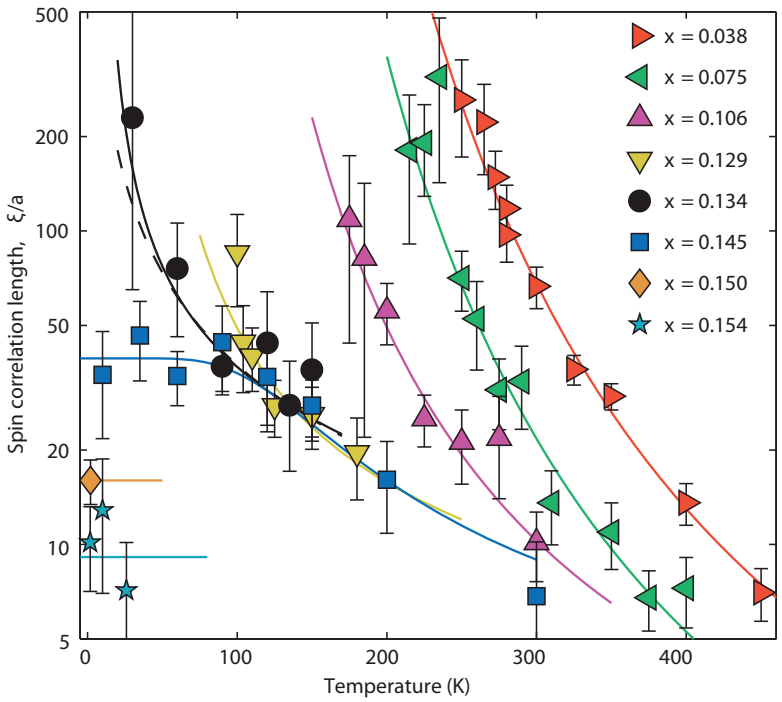

Figure 1.6: Temperature dependence of the spin correlation length ξ of NCCO in units of the in-plane lattice constant a for various cerium concentrations obtained from inelastic neutron scattering experiments. Figure reproduced from [75].

n-doped cuprate compounds [66–71] confirm a large closed FS near optimal doping. In addition, for $x \geq 0.15$ indications for pseudogap feature were found, that is a suppression of the intensity at the Fermi level similar to what was observed in p-doped cuprates. An example of ARPES results on NCCO is presented in Fig. 1.5. Apparently, the suppression of the quasiparticles is found strongest at the so-called "hot-spot" regions [50, 66]. These are the regions where the large FS is crossing the AFM Brillouin zone (AFMBZ) boundary. Various theoretical predictions suggested a coupling of the charge carriers to a superlattice potential with the characteristic ordering vector $(\frac{\pi}{a}, \frac{\pi}{a})$ [72–74], leading to a FS reconstruction as described by Eq. (1.3).

The close proximity of SC to the antiferromagnetic phase naturally suggests AFM being the responsible ordering. However, the exact doping at which AFM vanishes is controversially discussed. There where neutron scattering experiments that showed evidences for commensurate AFM, coexisting with SC even

in strongly overdoped NCCO [37, 76–78], whereas more recent inelastic neutron scattering (INS) experiments [75] provided arguments against the coexistence. Fig. 1.6 shows spin-correlation data from the latter INS experiments performed in zero magnetic field. The divergence of the spin correlation length ξ at low T, associated with long-range ordering, is observed to vanish as the doping exceeds $x = 0.134$. For $x = 0.145$, see Fig. 1.6, ξ saturates for low T at about $45a$, which would correspond to a rather short range ordering. In addition, the spin stiffness was found to vanish already at $x = 0.134$ and thus, it is argued that no long-range AFM does coexist with SC. These findings were in favor of theoretical predictions of a close relation between the pseudogap phenomena and antiferromagnetic fluctuations in the superconducting doping range [79, 80]. But also a hidden $d_{x^2-y^2}$ density-wave ordering was suggested as a possible origin of the pseudogap [81].

Several experiments in high magnetic fields on p-doped compounds have provided evidence for the existence of a well established Fermi surface (FS) in the normal state at different doping levels, and thus revealed that cuprates may behave more conventionally than thought. The topology and shape of the FS reflects the main electronic properties of a conductor in the normal state and, thus, provide important information on the charge carriers that are responsible for the superconducting state below T_c. On the strongly overdoped side of the phase diagram of p-doped cuprate superconductors, both the semiclassical angle-dependent magnetoresistance oscillations (AMRO) [26, 27, 82, 83] and quantum oscillations of the resistance [28] have been found for the compound $Tl_2Ba_2CuO_{6+\delta}$. These experiments provided evidence for a large cylindrical Fermi surface, as expected from band-structure calculations [48, 84], Hall effect measurements [85] and ARPES [16]. Remarkably, it was possible to describe all these experimental results within the standard Fermi liquid model. By contrast, for underdoped $YBa_2CuO_{6.5}$ [28, 32, 33] and YBa_2CuO_8 [29, 30], slow SdH and de Haas-van Alphen (dHvA) oscillations were observed, indicating a reconstruction of the Fermi surface. These observations reveal substantial disagreements with ARPES results and are controversially interpreted at present (see e.g. [18, 86–92]). The exact FS topology is under discussion but it is clearly reconstructed. ARPES is known to be a surface sensitive technique and thus effects like self doping on the surface [93] can result in very different observations as

compared to bulk sensitive techniques like electrical transport.

For n-doped cuprates only few experiments in high magnetic fields had been performed till the beginning of the present work. For example, a reconstructed FS, i.e. a FS consisting of hole- and electron-like parts, would explain recent results from Hall effect measurements in n-doped thin films [94–96], where at low temperatures both positive and negative contributions have been observed. Lin & Millis [73], for example, were able to qualitatively describe the results on Hall effect in NCCO by applying a two-band model. However, they noted difficulties when attempting to reach a quantitative agreement. In addition, Hall effect data obtained in high magnetic fields for thin films of n-doped $Pr_{2-x}Ce_xCuO_4$ have suggested a quantum critical phase transition at $x = 0.165$ underneath the superconducting dome associated with a FS transformation [96, 97]. More recent quantitative analyses by Lambacher et al. [98] of results from Hall effect in single-crystalline NCCO samples, similar to those used in the present work, indicated the presence of two bands even in the strongly overdoped regime.

So far, the electron-doped cuprate compounds have been lacking quality. For example, this is a critical issue for neutron scattering experiments, requiring large specimens. In particular, the apical oxygen is believed to introduce disorder into the CuO_2-layers, leading to a suppression of SC and enhancing AFM [99]. This is an issue especially for thin films, where it is reported that the annealing process has a strong impact on transport coefficients such as the Hall coefficient [100]. Recently, there was a huge progress in the improvement of the growth and preparation of high-quality single crystals of NCCO [98, 99]. The first results of semi-classical AMRO and quantum oscillations in the resistance [101, 102] revealed a well established FS for various doping levels in the superconducting overdoped regime, $x \geq 0.15$, of NCCO, see Sect. 2.3.

NCCO offers the unique opportunity to study the n-type side of the electronic phase diagram over the full doping range starting near the Mott insulating phase until the upper edge of the superconducting region. The quality of the samples investigated here has proven very high through the discovery of MQO.

One advantage of the n-doped over the p-doped compounds, with respect to magnetotransport measurements, is their much lower upper critical field B_{c2}. Consequently, superconducting effects are expected to be less influential than in p-doped cuprates with their high T_c and B_{c2} values [103]. For the prelimi-

nary characterization of the NCCO samples the available magnetic fields up to $15\mathrm{T}$ perpendicular to layers are already high enough to access the normal state for all available doping levels at $T = 1.4\mathrm{K}$, as the highest value of $B_{c2,\perp}$ derived from resistivity measurements [104] is stated to be below $10\mathrm{T}$ for optimally doped NCCO.

Furthermore, its primitive unit cell contains only a single conducting layer and no chains as compared to many p-doped cuprate compounds, such as YBCO, for example. Therefore, bilayer-splitting effects or contributions from chains to the conduction bands are absent and the band structure is expected to be rather simple [48].

Another advantage is that the carrier concentration can be directly derived from the Ce content, which is precisely controllable during the synthesis. Finally, this compound offers the possibility to cover the whole SC range by only a small change in doping. This is particularly important for understanding how the electronic properties develop with doping within one system.

2 Relevant theoretical aspects

An overview on the fundamentals of the theory of metals can, for example, be found in the book of A. A. Abrikosov [105]. Furthermore, a comprehensive examination of experiments and theory related to magnetic quantum oscillations in metals is given in the book of D. Shoenberg [35]. A nice review on recent developments in the field of magnetotransport in layered conductors was published by M. V. Kartsovnik [36]. In the following, certain aspects relevant for understanding the analyses in this thesis are presented according to the literature mentioned above.

2.1 Semiclassical electrons in magnetic fields

In the semiclassical model ($\omega_c\tau \leq 1$), an electron moving in a magnetic field $\mathbf{B}$ is subject to the Lorentz force $\mathbf{F}_L$. The rate of change in the momentum of the electron $\hbar\dot{\mathbf{k}}$ is equal to the Lorentz force

$$\hbar\dot{\mathbf{k}} = \mathbf{F}_\mathrm{L} = -e\left(\mathbf{v}\times\mathbf{B}\right), \tag{2.1}$$

where $-e$ is the electron charge and $\mathbf{v}$ the electron velocity. The velocity of an electron is related to energy ϵ_k over

$$\mathbf{v}(\mathbf{k}) = \frac{1}{\hbar}\nabla_\mathbf{k}\epsilon_\mathbf{k}, \tag{2.2}$$

where $\hbar$ is the reduced Planck constant. One immediately can see from Eq. (2.1) that only the component of the electron wave vector normal to the magnetic field is changing with time. The Lorentz force does not change the electron energy, since it is always perpendicular to the electron velocity. Consequently, the motion of electrons in k-space is described by an orbit of constant energy perpendicular to the magnetic field.[1] In real space $\mathbf{v}$ has a component parallel as well as

[1] Only *closed orbits* are discussed here, but it must be mentioned that orbits also can be open.

perpendicular to the field, thus the electron moves along a helical trajectory. The angular frequency with which the electron traces the orbit is called cyclotron frequency ω_c. Integrating the elapsed time for one complete orbit perpendicular to the field orientation yields the time period of circulation, $T = 2\pi/\omega_c$ and, hence, the cyclotron frequency

$$\omega_c = \frac{2\pi eB}{\hbar^2} / \left(\frac{\partial S}{\partial \epsilon_k}\right)_{k_{||}}, \tag{2.3}$$

where S is the area enclosed by the cyclotron orbit. The component $k_{\|}$ parallel to $\mathbf{B}$ is constant and

$$m_c = \frac{\hbar^2}{2\pi} \left(\frac{\partial S}{\partial \epsilon_k}\right)_{k_{||}} \tag{2.4}$$

is called the cyclotron mass. For a gas of free electrons of mass m_e it follows

$$\epsilon_k = \frac{\hbar^2 k^2}{2m_e}, \tag{2.5}$$

where the constant energy surfaces are spheres with radius k. Because of the nature of the Fermi distribution only the energies close to the Fermi level are important and, thus, for a certain Fermi vector k_F this gives the Fermi energy $\epsilon(k_F)$, the so-called *Fermi surface*. Here the cyclotron frequency is simply

$$\omega_c = \frac{eB}{m_e}. \tag{2.6}$$

2.2 Semiclassical magnetoresistance of conventional metals

At low magnetic fields the electron momentum $\mathbf{k}$ does not change significantly during the scattering time τ, thus, its trajectory is only slightly curved. The characteristic radius of curvature, called Larmor radius, $r_L = \hbar k_F/(eB)$, is much larger than the mean free path l. In this case, it can be shown [105] for the relative change in resistivity:

$$\frac{\rho(B) - \rho(0)}{\rho(0)} \equiv \frac{\Delta\rho(B)}{\rho(0)} \propto \left(\frac{l}{r_L}\right)^2 \propto B^2 \tag{2.7}$$

At fields, at which the Larmor radius becomes smaller than the mean free path ($r_L \leq l$), the momentum of each individual electron will considerably change

within the time τ. Therefore, the velocity $\mathbf{v_k} = \frac{\partial\epsilon(\mathbf{k})}{\partial\mathbf{k}}$ will vary depending on the momentum. To calculate the conductivity one has to solve the Boltzmann kinetic equation in the presence of electric and magnetic fields. Using the semiclassical τ approximation, one obtains for the conductivity tensor:

$$\sigma_{\alpha\beta} = -\frac{2e^2\tau}{(2\pi)^3}\int \frac{df_0}{d\epsilon} v_\alpha(\mathbf{k})\bar{v}_\beta(\mathbf{k})d\mathbf{k}, \tag{2.8}$$

where α, β are the x,y,z-components and f_0 is the equilibrium Fermi distribution function. $\bar{v}_\beta(\mathbf{k})$ is basically the velocity averaged over the scattering time:

$$\bar{v}_\beta(\mathbf{k}) = \frac{1}{\tau}\int_{-\infty}^{0} v_\beta(\mathbf{k}, t)e^{t/\tau}dt \tag{2.9}$$

Consequently, the conductivity is determined by the averaged velocity, which strongly depends on magnetic field. In the high field limit, $\omega_c\tau >> 1$ (or $r_L/l << 1$), the electron completes many turns around the closed Fermi surface and therefore the time-averaged velocity tends to zero. Therefore, the conductivity components should decrease as $\mathbf{B} = (0, 0, B)$ increases and the conductivity tensor is expressed as [105]

$$\sigma_{\alpha\beta} = \begin{pmatrix} \frac{a_{xx}}{B^2} & \frac{a_{xy}}{B} & \frac{a_{xz}}{B} \\ \frac{-a_{xy}}{B} & \frac{a_{yy}}{B^2} & \frac{a_{zy}}{B} \\ \frac{-a_{xz}}{B} & \frac{-a_{yz}}{B} & a_{zz} \end{pmatrix}, \tag{2.10}$$

with the material specific, field-independent coefficients $a_{\alpha\beta} > 0$. The algebraic inversion of this tensor yields the resistivity tensor, $\rho_{\alpha\beta} = \sigma^{-1}_{\alpha\beta}$, which in the lowest order in $1/B$ has the form:

$$\rho_{\alpha\beta} = \begin{pmatrix} b_{xx} & b_{xy}B & b_{xz} \\ -b_{xy}B & b_{yy} & b_{zy} \\ -b_{xz} & -b_{yz} & b_{zz} \end{pmatrix}, \tag{2.11}$$

where the diagonal components $\rho_{\alpha\alpha}$ are constant. Thus, the magnetoresistance is expected to saturate at high fields in the case that electrons traverse closed cyclotron orbits. Open FSs will lead to deviations from this behavior, but are not considered in the following.

Hall effect

In high magnetic fields, i.e. $\omega_c\tau >> 1$ the Hall-conductivity component σ_{xy} is determined by Eq. (2.8). It can be shown that with $v_x = -\frac{\hbar}{eB}\frac{\mathrm{d}k_y}{\mathrm{d}t_1}$, obtained from Eq. (2.1) [105]

$$\sigma_{xy} = -\frac{2e}{(2\pi)^3 B}\int \mathrm{d}k_z \int_0^T k_x \frac{\mathrm{d}k_y}{\mathrm{d}t_1} dt_1, \tag{2.12}$$

where t_1 was chosen so that the initial $k_y(t_1 = 0) = 0$. Thus, the second integral corresponds to

$$\oint k_x \, \mathrm{d}k_y = \left[S_\mathrm{e}(k_z) - S_\mathrm{h}(k_z)\right], \tag{2.13}$$

with the cyclotron areas $S_\mathrm{e}(k_z)$ and $S_\mathrm{h}(k_z)$ of the electron- and hole-like parts of the FS, respectively. Hence, the Hall conductivity is a sum of the contributions from the charge carriers on the electron- and hole-like FSs:

$$\sigma_{xy} = \frac{e}{B}(n_\mathrm{e} - n_\mathrm{h}), \tag{2.14}$$

yielding the Hall coefficient

$$R_\mathrm{H} = \frac{\rho_{xy}}{B} = \frac{1}{\sigma_{xy}B} = \frac{1}{(n_\mathrm{e} - n_\mathrm{h})e}. \tag{2.15}$$

In the experiment usually the difference between the signal for positive and negative magnetic field directions is determined:

$$R_\mathrm{H} = \frac{\rho_{xy}(B) - \rho_{yx}(-B)}{2B} \tag{2.16}$$

to cancel spurious contributions of $\rho_{xx}(B)$.

Determining R_H can be very helpful in identifying the sign of the contributing charge carriers and it is very sensitive to changes in the topology and shape of the FS.

2.3 Magnetic quantum oscillations

The periodic oscillations of various physical quantities, such as magnetization, resistivity etc., depending on the magnetic field, have proven a powerful tool for investigating the Fermiology for a great number of diverse conductors [35, 36, 106].

2.3.1 The origin of magnetic quantum oscillations

De Haas-van Alphen (dHvA) oscillations, i.e. oscillations of the magnetization in response to a magnetic field change, first, have been suggested by L. D. Landau in 1930 as a side note in his paper on diamagnetism in metals [107]. Although he stated that this effect was by far too challenging for experiments to be observable, in the same year de Haas and van Alphen observed it in single-crystalline bismuth at around $14.2\,\mathrm{K}$, the evaporation temperature of hydrogen [108]. The detailed theory, giving the frequency, amplitude and phase of the oscillations in the magnetization, was developed by I. M. Lifshitz and A. M. Kosevich in 1954-55 [109].

The origin of de Haas-van Alphen oscillations is the quantization of the electron motion, which restricts the permitted states. The quantization of a periodic motion is described by the Bohr-Sommerfeld expression:

$$\oint \mathbf{p} \cdot d\mathbf{q} = (n + \gamma)\, 2\pi\hbar \; ; \; n = 0, 1, 2... \; , \tag{2.17}$$

where $\mathbf{p}$ and $\mathbf{q}$ are the canonical conjugated momentum and position variables. γ is the phase variable which is exactly $1/2$ for a parabolic band (case of free electrons) but in general, depending on energy and field, it is slightly different. For an electron in a magnetic field

$$\mathbf{p} = \hbar\mathbf{k} - e\mathbf{A} \; ; \; \mathbf{q} = \mathbf{r}_{\perp}, \tag{2.18}$$

where $\mathbf{A}$ is the vector potential of $\mathbf{B}$ and $\mathbf{r}_{\perp}$ the vector in the plane of the electron orbit.

The **Onsager** relation, which was derived independently by I. M. Lifshitz at about the same time but published two years later, provides an expression for the area of an electron trajectory in a magnetic field:

$$S_{\perp,n}\left(\epsilon_k, k_{\parallel}\right) = (n + \gamma)\, 2\pi eB/\hbar, \tag{2.19}$$

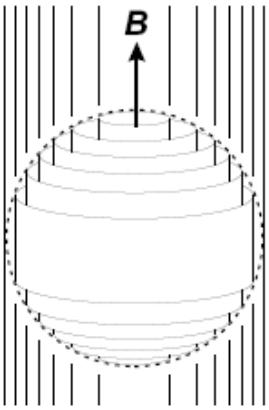

Figure 2.1: Co-axial Landau tubes parallel to the applied magnetic field in the case of free electrons. The Fermi level is marked by the dotted circumference.

where the area $S_\perp$ depends on the energy dispersion of the considered orbit and the value $k_\parallel$ parallel to the magnetic field B, marking the point at which the cross section is regarded.

If $k_\parallel$ is varied for a fixed field the orbits of constant energy will form a cylinder parallel to B, the so-called Landau tube. Then the Onsager relation can be understood in the way that it restricts the allowed states in k-space to lie on the Landau cylinders. Applied to the free electron gas, described by the parabolic dispersion Eq. (2.5) the Onsager relation yields:

$$\epsilon_{n,k_\parallel,\sigma} = \hbar\omega_c\,(n + 1/2) + \frac{\hbar^2 k_\parallel^2}{2m_e} + \sigma\mu_\mathrm{B}B \tag{2.20}$$

The last term comes from the electron spin with $\sigma = \pm 1/2$ with the Bohr magneton $\mu_\mathrm{B} = e\hbar/2m_e$. This is the simple case of co-axial circular cylinders for free electrons (shown in Fig. 2.1), which, in general, are not parallel to the field or even cylindrical.

In zero field, the number of electronic states per unit volume of k-space is $\frac{2V}{(2\pi)^3}$. According to the Onsager relation, Eq. (2.19), the area between adjacent Landau levels is given as

$$\Delta S = \frac{2\pi eB}{\hbar}. \tag{2.21}$$

Hence, the number N of states on a length of a Landau tube between $k_\parallel$ and

$k_\parallel + dk_\parallel$ is:

$$\Delta S dk_\parallel \frac{V}{4\pi^3} \tag{2.22}$$

By switching on the field the allowed states are restricted to the Landau tubes.

For experimentalists it is of interest at what rate, with increasing magnetic field, subsequent Landau levels leave the Fermi surface. From the Onsager relation Eq. (2.19) follows:

$$(1/B_{n+1} - 1/B_n) = \frac{2\pi e}{\hbar}\frac{1}{S_{extr}}, \tag{2.23}$$

where S_{extr} is the extremal cross-section of the Fermi surface perpendicular to the field. As the field increases the diameter of the Landau levels grows continuously until it exceeds the Fermi level. Thus, quantities, depending on the density of states near the Fermi energy, show oscillations periodic in $1/B$, with the frequency

$$F = \frac{1}{\Delta(\frac{1}{B})} = \frac{\hbar}{2\pi e} S_{\text{extr}}. \tag{2.24}$$

2.3.2 De Haas-van Alphen oscillations

This effect is described in terms of the magnetic field dependence of the Gibbs thermodynamic potential Ω [35], which is directly related to the electronic density of states. The derivative of Ω with respect to field for a constant temperature is the magnetization

$$\mathbf{M} = -\left(\nabla_{\mathbf{B}}\Omega\right)_{\xi,T,p}, \tag{2.25}$$

where the chemical potential ξ, the temperature T and the pressure are kept constant and $\mathbf{B} = \mathbf{H}/\mu_0$. As the magnetic field is changed, oscillations of the density of states near the Fermi level give rise to oscillations in Ω and consequently in the magnetization of the system. For a system of conduction electrons, obeying the Fermi-Dirac statistics, the thermodynamical potential Ω is given by the sum over all possible states ϵ

$$\Omega = -k_{\mathrm{B}}T \sum_{\epsilon} \ln\left(1 + \exp\left(\frac{\xi - \epsilon}{k_{\mathrm{B}}T}\right)\right), \tag{2.26}$$

where k_{B} is the Boltzmann constant. After including the degeneracy Eq. (2.22) and energy eigenvalues E_n of the n-th Landau levels this becomes

$$\Omega = -k_{\mathrm{B}}T \int_{-\infty}^{\infty} dk_\parallel \left(\frac{eBV}{2\pi^2\hbar}\right) \sum_n \ln\left(1 + \exp\left(\frac{\xi - E_n}{k_{\mathrm{B}}T}\right)\right) \tag{2.27}$$

where the integral is taken over all the orbits defined by $k_{||}$. The solution of the integral above is done by using the Poisson summation formulas or the Euler-MacLaurin formulas [35]. As a result, the oscillatory component of Ω can be expressed as a sum of p harmonics periodic in $1/B$:

$$\tilde{\Omega} = \left(\frac{e^5}{8\pi^7\hbar S''}\right)^{1/2} \frac{VB^{5/2}}{m_c} \sum_{p=1}^{\infty} \frac{1}{p^{5/2}} \cos\left[2\pi p\left(F/B - 1/2\right) \pm \pi/4\right], \tag{2.28}$$

where only slices in the vicinity of extremal areas add up constructively and

$$S'' = \left|\frac{\partial^2 S_{extr}}{\partial k_{||}^2}\right|_{extr}. \tag{2.29}$$

The component of **M** parallel to **B** is $M_{||} = -\left(\frac{\partial\Omega(\epsilon_F)}{\partial B}\right)_{T,p}$. Thus,

$$\tilde{M}_{||} = -\left(\frac{e^5 B}{2\pi^5\hbar S''}\right)^{\frac{1}{2}} \frac{VF}{m_c} \sum_{p=1}^{\infty} \frac{1}{p^{3/2}} \sin\left[2\pi p\left(\frac{F}{B} - \frac{1}{2}\right) \pm \frac{\pi}{4}\right]. \tag{2.30}$$

The component of **M** perpendicular to **B** is

$$M_{\perp} = -\frac{1}{F}\frac{\partial F}{\partial \theta} M_{||}. \tag{2.31}$$

For layered metals with a weakly corrugated cylindrical FS, assuming the warping to be smaller than the Landau level spacing, a big part of the charge carriers contributes in phase to the MQO. This leads to a strong enhancement of the oscillation amplitude and in the extremly quasi-2D case to violations of the standard theory [36].

2.4 Lifshitz-Kosevich formula

For experiments it becomes necessary to regard effects of finite temperature, finite relaxation time τ due to scattering, and effects of electron spin. All these effects give contributions in a form of reduction factors R_T, R_D, R_S (which have to be included in Eq.(2.30)), leading to the *Lifshitz-Kosevich (LK) formula* for an electronic system with one extremal orbit [35, 109]:

$$\tilde{M}_{||} = -\left(\frac{e^5 B}{2\pi^5\hbar A''}\right)^{\frac{1}{2}} \frac{VF}{m_c} \sum_{p=1}^{\infty} R_D R_T R_S \frac{1}{p^{3/2}} \sin\left[2\pi p\left(\frac{F}{B} - \frac{1}{2}\right) \pm \frac{\pi}{4}\right] \tag{2.32}$$

2.4.1 Shubnikov-de Haas oscillations

The Shubnikov-de Haas (SdH) effect, i.e. magnetic quantum oscillations in the conductivity, basically originates from deviations of the τ approximation, taking into account different scattering processes, and is, therefore, more complex and more difficult to derive, see [110]. Its theory goes beyond the scope of this brief introduction.

The SdH effect can be satisfactorily described by starting with Pippard's idea [111] that the scattering probability and, consequently, the resistivity are directly proportional to the density of states near the Fermi energy level $D(\epsilon_{\mathrm{F}})$. This is because of the proportionality between the $D(\epsilon_{\mathrm{F}})$ and the spin susceptibility, which is defined as $\chi = \mu_0(\frac{\partial M}{\partial B})$. Therefore, it can be shown, see [35] that the field derivative of the oscillatory magnetization is directly connected with oscillations in the density of states:

$$\left(\frac{m_{\mathrm{c}}B}{S_{\mathrm{extr.}}}\right)^2 \frac{\partial \tilde{M}}{\partial B} \propto \tilde{D}(\epsilon_{\mathrm{F}}) \tag{2.33}$$

Thus the oscillatory part of the conductivity is given by:

$$\frac{\tilde{\sigma}}{\sigma_0} = \sum_{p=1}^{\infty} \frac{1}{p^{1/2}} a_p \cos\left[2\pi\left(\frac{F}{B} - \frac{1}{2}\right) \pm \frac{\pi}{4}\right], \tag{2.34}$$

where

$$a_p = \frac{m_{\mathrm{c}}\sqrt{B}}{\sqrt{S''_{\mathrm{extr}}}} R_{\mathrm{T}} R_{\mathrm{D}} R_{\mathrm{S}}$$

and σ_0 is the background conductivity. Due to the direct relation to the dHvA effect, the same considerations for the reduction factors are valid in the case of SdH quantum oscillations.

2.4.2 Reduction factors

The effect of finite temperature

Due to the fact that absolute zero is never reached the Fermi distribution is smeared:

$$f(\epsilon) = \frac{1}{1 + \exp\left(\frac{\epsilon - \xi}{k_{\mathrm{B}}T}\right)} \tag{2.35}$$

An electronic system at a finite temperature T can be treated as a superposition of hypothetical metals at $T = 0$ with different Fermi energies distributed in the

range of $\Delta\epsilon \sim k_\mathrm{B}T$ around ϵ_F. Each of them contributes with a slightly different frequency which leads to a phase smearing and hence to a damping of the oscillation amplitude by [109]

$$R_\mathrm{T}(p) = \frac{2\pi^2 p k_\mathrm{B}T/\left(\hbar\omega_\mathrm{c}\right)}{\sinh\left[2\pi^2 p k_\mathrm{B}T/\left(\hbar\omega_\mathrm{c}\right)\right]} = \frac{Kp\mu T/B}{\sinh\left(Kp\mu T/B\right)}, \tag{2.36}$$

where p is the harmonic index and

$$\mu = \frac{m_\mathrm{c}}{m_e} \tag{2.37}$$

is the effective cyclotron mass in dimensions of the free electron mass and $K = 2\pi^2 k_\mathrm{B} m_e/(\hbar e) \approx 14.69\,\mathrm{T/K}$. Experimentally, one can extract the effective cyclotron mass directly from the temperature dependence of the oscillation amplitude. Deviations of m_c from the band mass, i.e. the mass obtained from band structure calculations which disregard electron-electron and electron-phonon interactions, can provide information about the influence of many-body interactions in the system [35].

The effect of finite relaxation time

From Heisenberg's uncertainty principle, $\Delta\epsilon \approx \frac{\hbar}{\tau} < \hbar\omega_\mathrm{c}$ it is known that a finite relaxation time τ leads to a broadening of quantized Landau levels. In analogy to the temperature damping, this broadening leads to an additional reduction of the oscillation amplitude and is expressed through the so-called *Dingle reduction factor* first introduced by Dingle in 1952 [112]:

$$R_\mathrm{D} = \exp\left(-\frac{\pi p}{\omega_\mathrm{c}\tau}\right) = \exp\left(-Kp\mu T_\mathrm{D}/B\right), \tag{2.38}$$

where

$$T_\mathrm{D} = \frac{\hbar}{2\pi k_\mathrm{B}\tau} \tag{2.39}$$

is the Dingle temperature representing the transport scattering and thus the mean free path in the specific compound. Provided that the value for the effective cyclotron mass μ was obtained from the temperature dependence one can extract T_D from fitting the B-dependence of the oscillation amplitude to Eq. (2.32 or 2.34) with Eq. (2.38).[2]

[2] τ derived from the Dingle factor is usually considerably lower than the normal transport relaxation time τ_tr [36]. Because the amplitude of MQO is highly sensitive to long-range scattering

The effect of electron spin

It was explained above that the Fermi edge smearing can be considered as a splitting in different levels which causes an extra damping R_{T}. In magnetic field, the Zeeman splitting lifts the spin degeneracy of energy levels. Thus, each Landau level splits in two $E_k \pm \frac{1}{2}\Delta E$ with a difference in energy of $\Delta E = g\mu_{\mathrm{B}}B$, where $\mu_{\mathrm{B}} = \frac{e\hbar}{2m_e}$ is the Bohr magneton and g the $Landé$ factor (for free electrons $g = 2.0023$). The resulting reduction of the oscillation amplitude is expressed through [113]

$$R_S = \cos\left(\frac{\pi}{2}pg\mu\right), \tag{2.40}$$

where both, g and μ are renormalized by electron-electron and electron-phonon interaction. Provided a known μ from the analysis of the temperature dependence Eq. (2.36) one can evaluate the g-factor. It can strongly deviate from the value g_{ESR}, measured by electron-spin-resonance, which is insensitive to many-body interactions. In the 2D-case, as the polar field orientation θ is changed from perpendicular towards parallel to the conducting layers in the x, y-plane, the area of the cyclotron orbits increases proportional to $1/\cos\theta$, leading to a decrease of the cyclotron frequency, $\omega_{\mathrm{c}} \propto \cos\theta$, see Eqs. (2.3), (2.4), and, accordingly, an increase of the effective cyclotron mass

$$\mu = \mu_0/\cos\theta, \tag{2.41}$$

with $\mu_0 = \mu(\theta = 0°)$. Therefore, R_{S} vanishes periodically when $pg\mu_0/\cos\theta$ is an odd integer, which is called the "*spin-zero*" effect. One can easily see that this zero is accompanied by a sign-change for R_{S} which leads to a phase inversion, i.e. a π-shift in the oscillation phase as the angle θ increases, passing through the spin-zero. Therefore, by varying θ, one can gain information about the spin-orbit coupling and many-body-interactions that lead to a renormalization of the product $g\mu$ [35].

2.4.3 Magnetic breakdown

The topology of the Fermi surface is determined by the band structure properties of the material. As long as the cyclotron energy $\hbar\omega_{\mathrm{c}}$ is much smaller than the rel-

defects, such as dislocations, and macroscopic spatial inhomogeneities [35], which do not affect the normal classical transport.

evant band energy around the Fermi energy ϵ_F, the electrons traverse along well established paths, like the above mentioned orbits. For high enough fields, electrons can tunnel, with a certain probability, from one band to another, if Δ_g, the gap between them, is sufficiently small. This effect is called *magnetic breakdown* [114] and the probability P of electrons to tunnel between the bands increases exponentially with increasing magnetic field:

$$P = \exp\left(-B_{MB}/B\right), \tag{2.42}$$

where B_{MB} is the breakdown field which can be estimated as

$$B_{MB} \approx \frac{m_c \Delta_g^2}{e\hbar\epsilon_F}. \tag{2.43}$$

In other words, magnetic breakdown can be expected for conditions, where

$$\hbar\omega_c \gtrsim \Delta_g^2/\epsilon_F. \tag{2.44}$$

The criterion for magnetic breakdown (MB) to occur given by Blount [115] is that the energy spacing between two Landau levels should be equal to or larger than the square of the energy gap divided by the Fermi energy. As a consequence, MB gives rise to an additional damping of MQO with the corresponding reduction factor

$$R_{\mathrm{MB}} = (ip)^{n_1} q^{n_2}, \tag{2.45}$$

with $p = \sqrt{P} = \exp\left(-B_{\mathrm{MB}}/2B\right)$, where P is the probability for electrons to tunnel through the gap at n_1 points, and $q = \sqrt{Q} = [1 - \exp\left(-B_{\mathrm{MB}}/B\right)]^{1/2}$, where Q is the probability for Bragg reflection at n_2 points along the cyclotron orbit.

2.5 Semiclassical Angle-dependent MagnetoResistance Oscillations (AMRO)

Due to several works in the field of layered organic superconductors during the 90s, the effect of angle-dependent magnetoresistance oscillations (AMRO) was established as a powerful method for exploring the Fermi surface (FS) geometry by using inter-layer magnetotransport, for a review see [36]. In this section a layered metal with a cylindrical Fermi surface is considered. It was noted above that the conductivity and, hence, the resistivity in metals with a cylindrical Fermi surface

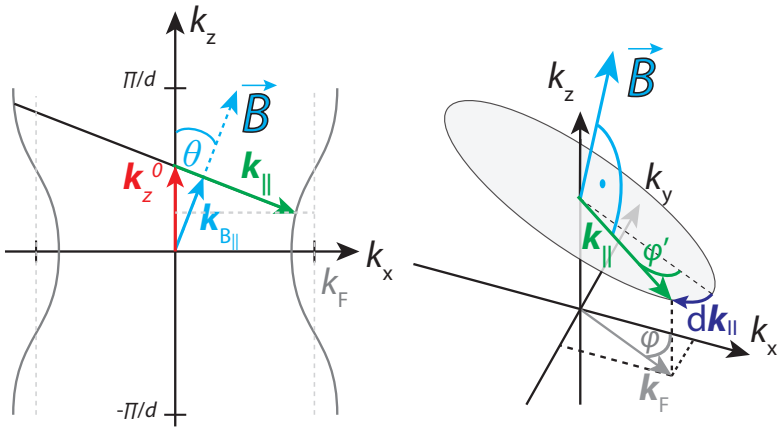

Figure 2.2: Corrugated cylindrical Fermi surface, θ is the polar angle with respect to the direction of the magnetic field, for a certain θ the cross-sections (grey) perpendicular to **B** have the same area independent of k_z, see [116]

depends on the averaged electron velocity, see Eq. (2.8). From this, one would expect clear changes in the behavior of the interlayer resistivity by turning the magnetic field from the direction perpendicular to the conducting layers to parallel. Beside an obvious change from a regime with closed FS cross-sections to open orbits, which the electrons traverse, a new effect has been observed for several layered compounds [36]. At certain polar angles θ the resistivity is strongly enhanced, showing AMRO.

The first calculation for the polar angle positions, at which an AMRO maximum should appear for a cylindrical Fermi surface, was done by Yamaji [116]. He considered a simplified energy dispersion for a slightly corrugated cylindrical Fermi surface:

$$\epsilon(k) = \frac{\hbar^2}{2m}(k_x^2 + k_y^2) - 2t_\perp \cos(k_z d), \tag{2.46}$$

where $t_\perp << \epsilon_F$ is the interlayer hopping energy and d the interlayer spacing constant. The tilted cyclotron orbit with the position along the k_z-direction, labeled by k_z^0, lies in the plane perpendicular to the magnetic field **B** defined by

$$k_x \sin\theta + k_z \cos\theta = k_{B_\parallel} = k_z^0 \cos\theta. \tag{2.47}$$

Yamaji noted that the orbit's area S_{orb} can be calculated by the following integral:

$$\begin{aligned} S_{\mathrm{orb}} \cos\theta &\approx \int_0^{\pi} \mathrm{d}\varphi \left[k_{\mathrm{F}}^2 + 4mt_{\perp} \cdot \cos\left(k_z^0 d - k_{\mathrm{F}} d \tan\theta \cos\varphi\right)\right] \\ &= \pi k_{\mathrm{F}}^2 + 4\pi m t_{\perp} \cos(k_z^0 d) \cdot J_0(k_{\mathrm{F}} d \tan\theta), \end{aligned} \tag{2.48}$$

where $k_{\mathrm{F}} \tan\theta \cos\varphi$ is the projection of $k_{||}$ on the k_x-direction within the $k_x k_y$-plane, see Fig. 2.2. For certain polar angles that is exactly when the Bessel function $J_0 = 0$, $S_{\mathrm{orb}} \cos\theta$ becomes independent of the position k_z^0. Therefore, in the ideal case, all the cyclotron orbits enclose the same area when

$$|\tan\theta| = \frac{\pi}{k_F d}(n - 1/4) \; ; \; n = 1, 2... \tag{2.49}$$

Eq. (2.49) is called "Yamaji's condition". AMRO are a semiclassical geometrical effect, that is why they can even be observed at conditions, where quantum oscillations are suppressed completely.

Later on, Yagi et al. [117] simulated AMRO, with the characteristic angles of Eq. (2.49) by means of numerical integration of Eq. (2.8) and using the energy dispersion from Eq. (2.46). The physical nature of AMRO is understood as in the following. One can see from Eqs. (2.8) and (2.9) that the conductivity σ_{zz} depends on the velocity in k_z-direction averaged over one period of the motion of an electron along the cyclotron orbit perpendicular to the field. With Eqs. (2.2) and (2.4) for an electron traversing such an orbit, the averaged velocity in the strong field limit, $\omega_{\mathrm{c}}\tau >> 1$ is[118]:

$$\overline{v_z} = \frac{1}{\hbar}\overline{\partial\epsilon(k)/\partial k_z} = -\frac{\partial S_{\mathrm{orb}}(k_z)/\partial k_z^0}{\hbar \partial S_{\mathrm{orb}}/\partial \epsilon_{k_z}} = -\frac{\hbar \partial S_{\mathrm{orb}}(k_z)/\partial k_z^0}{2\pi m_{\mathrm{c}}} \tag{2.50}$$

Consequently, when the orbit area becomes independent of the position k_z^0 along the k_z-direction, the averaged velocity amounts to zero and, consequently, the conductivity shows a minimum. In real systems, the basal plane has typically a lower symmetry than circular and, additionally, the vector $\mathbf{h} = (u_x, u_y, h_z)$ of the interlayer hopping has an in-plane component $\mathbf{u}$. Thus, Yamaji's condition Eq. (2.49) for maximums in the resistivity then has to be modified to [118]

$$|\tan\theta| = [\pi(n - 1/4) \pm (\mathbf{k}_{\perp}^{max} \cdot \mathbf{u})]/k_{\parallel}^{max} d, \tag{2.51}$$

where positive and negative polar angles θ are included with plus and minus, respectively. The vector $\mathbf{k}_{\parallel}^{max}$ lies within the plane perpendicular to $\mathbf{B}$ and $k_{\parallel}^{max}$

is defined as its projection in the direction of the field with maximum value. By applying this condition to field rotations in different planes (set by the azimuthal angle φ) perpendicular to the layers, one can derive the shape of the Fermi surface, in a non-circular case. This procedure is also called caliper measurement [119] because of its method of shape determination.

2.6 The 3D FS of NCCO

In Sect. 2.2 it was shown that the interlayer conductivity Eq. (2.8) directly depends on the integral over the interlayer component of the Fermi velocity, which is given by Eq. (2.2). Therefore, a complex FS warping, as it is expected for NCCO (see the discussion below), should have certain implications for the field and angle dependence of magnetotransport in NCCO. This issue will be discussed in this thesis in terms of interlayer MR, SdH oscillations, and AMRO observed in NCCO at various doping levels.

According to the tight-binding approximation the energy dispersion can be expressed as

$$\epsilon(\mathbf{k}) = \sum_n -2t_n(k_x, k_y)\cos(nk_z d), \tag{2.52}$$

where $d = c/2 = 6.04$ Å is the primitive unit cell parameter. The shape of the FS in the xy-plane is determined by $n = 0$ term. For a layered, anisotropic compound as NCCO the energy dispersion $\epsilon(\mathbf{k})$ is a three-dimensional cylinder with weak interlayer corrugation represented by the interlayer-hopping energy $t_\perp$. Due to its strongly anisotropic transport properties, i.e. a large ratio between the inter- and the intralayer resistivities $\rho_c/\rho_{ab} \approx 10^3$, the interlayer transport is characterized by a weak hopping energy of approximately $t_\perp \approx \epsilon_F/60$. Since $t_\perp << \epsilon_F$, only hopping between adjacent layers, i.e. $n \leq 1$ will be considered and hence Eq. (2.52) can be simplified to:

$$\epsilon(\mathbf{k}) = t_0(k_x, k_y) - 2t_\perp(k_x, k_y)\cos(k_z d), \tag{2.53}$$

with $t_0(k_x, k_y) \hat{=}$ Eq. 1.2, the intralayer dispersion relation of NCCO.

One can get an idea of how this modulation perpendicular to the conducting layers should look like by examining the symmetries determined by the crystal structure, thus by investigating the symmetry constraints of the 3D-BZ, shown

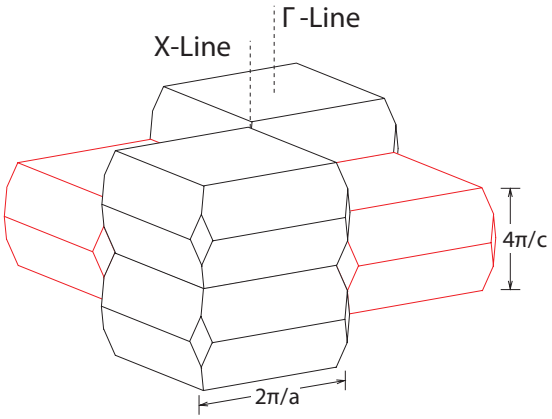

Figure 2.3: Extended sketch of the Brillouin zone in 3D k-space for a bct crystal symmetry [49], characteristic of $Nd_{2-x}Ce_xCuO_4$.

in Fig. 2.3. NCCO has a body-centered tetragonal (bct crystal structure, see Sect. 1.3.1.

The 3D-BZ is similar to that of, for example, Sr_2RuCuO_4 and $Tl_2Ba_2CuO_{6+\delta}$ (Tl-2201) with slightly different lattice constants [26, 49]. Bergemann et al. [49] introduced a harmonic expansion of the local Fermi wave vector $k_F(\varphi, \kappa_z)$ in cylindrical coordinates:

$$k_F(\varphi, \kappa_z) = \sum_{m,n\geq 0} k_{mn}^{\left\{\substack{c\\s}\right\}\left\{\substack{c\\s}\right\}} \left\{\substack{\cos\\\sin}\right\} n\kappa_z \times \left\{\substack{\cos\\\sin}\right\} m\varphi, \tag{2.54}$$

where $\kappa_z = k_z d$ runs from $-\pi$ to π along the k_z-direction of the BZ, and φ denotes the azimuthal orientation within the k_x, k_y-plane. Here, the parameter k_{m0} represents the k_z-independent, in-plane FS, while the interlayer dispersion, i.e. the φ-dependent warping normal to the conducting layers, is reflected in k_{mn} with $n > 0$.

Certain symmetry constraints of the 3D-BZ have to be taken into account. For example, the $\sin n\kappa_z$ terms can be omitted since they do not comply with the $k_z \rightarrow -k_z$ inversion symmetry. Fig. 2.4 gives an illustrative overview on the further possible symmetry operations that restrict the number of non-zero k_{mn}:
(a) The twofold rotational symmetry $\varphi \rightarrow \varphi + \pi$ allows only even integer values of m;
(b) The mirror reflection $\varphi \rightarrow \pi/2 - \varphi$, with respect to the mirror plane indicated by dashes in Fig. 2.4, allows only $\cos(m\varphi)$-terms with $m \bmod 4 = 0$ and $\sin(m\varphi)$-

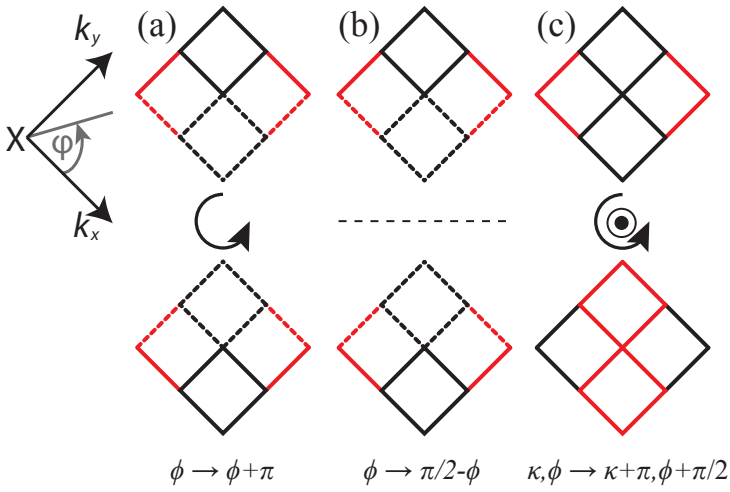

Figure 2.4: Top view on the extended BZ scheme and relevant symmetry operations for the bct crystal of NCCO in the ab-plane: (a) twofold rotational symmetry (b) mirror reflection (c) screw axis symmetry. Note: The color code is the same as in Fig. 2.3.

terms with $m \bmod 4 = 2$;
(c) The screw axis symmetry $\kappa_z, \varphi \rightarrow \kappa_z + \pi, \varphi + \pi/2$ allows $\cos(m\varphi)$-terms for even integer values of n and $\sin(m\varphi)$-terms for odd n.

Finally the parametrization reduces to:

$$k_{\mathrm{F}}(\varphi, \kappa_z) = \sum_{\substack{m,n\geq 0 \\ m \bmod 4=0 \\ n \text{ even}}} k_{mn} \cos(n\kappa_z) \cos(m\varphi) + \sum_{\substack{m,n\geq 0 \\ m \bmod 4=2 \\ n \text{ odd}}} k_{mn} \cos(n\kappa_z) \sin(m\varphi). \tag{2.55}$$

Regarding only interlayer-hopping to the nearest layer, i.e. $n \leq 1$, the first terms that fulfill all the symmetry requirements are k_{00}, k_{40}, k_{21}, k_{61}, k_{101}, etc. The terms with k_{00} and k_{40} represent the k_z-independent in-plane shape of the 2D FS. k_{21}, k_{61} and k_{101} are the warping parameters that proved sufficient for numerical simulations of the AMRO effect, originating from a large FS, observed in Tl-2201 [26].

The harmonic expansion with k_{mn} decreasing at larger m, n is generally not justified. On the other hand, one can use a similar form for the energy dispersion. Its justification immediately follows from the validity of the tight-binding

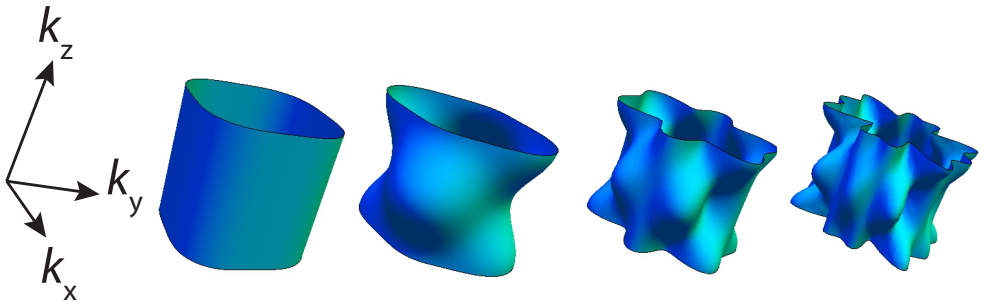

Figure 2.5: FS cylinders according to Eq. (2.57). From left to right: all $a_m = 0$; $a_2 = 1$; $a_2, a_6 = 1$; and $a_2, a_6, a_{10} = 1$. Note: For a better illustration the strength of the warping is exaggerated.

approximation [36, 120]. Then one simply uses Eq. (2.52), with the interlayer-hopping energy $t_\perp$ as it is expected to be for NCCO according to the symmetry considerations:

$$t_\perp(\varphi) = t_\perp \cdot \left[a_2 \sin(2\varphi) + a_6 \sin(6\varphi) + a_{10} \sin(10\varphi)\right], \tag{2.56}$$

with the constants a_m, specific for NCCO. Hence, the 3D energy dispersion for NCCO in cylindrical coordinates is:

$$\epsilon(\kappa_z, k_{||}\varphi) = \epsilon_{||}(k_{||}, \varphi) - 2t_\perp \cdot \cos\kappa_z \cdot \left[a_2 \sin(2\varphi) + a_6 \sin(6\varphi) + a_{10} \sin(10\varphi)\right], \tag{2.57}$$

where $\epsilon_{||}(k_{||}, \varphi)$ is the in-plane-dispersion from Eq. (1.2).

The corresponding 3D FS-cylinders are presented in Fig. 2.5, where the a_m terms are switched on successively.

Part II

Sample Characterization and Measurement Techniques in High Magnetic Fields

3 Single-crystal characterization and sample preparation

In this Part an overview is given on the preparation and preliminary characterization of the single-crystalline samples that were used in the studies carried out in this thesis. Thereafter, details on the different applied measurement techniques and setups that were applied for investigating the high-field properties of these samples will be presented.

3.1 Crystal preparation

The single-crystal growth, though the key to the high quality of the single crystals investigated, has not been the main part of this thesis. All the crystals have been provided by M. Lambacher and A. Erb. Within the doctoral thesis of M. Lambacher [98], the technique for growing bulk single-crystals of NCCO has been brought to a new level in quality that built the foundation for the high-resolution studies on transport effects in the world's highest nondestructive magnetic fields, presented in this thesis.

Crystal growth

All the samples, investigated in the present work, were grown by the Traveling-Solvent-Floating-Zone (TSFZ) technique, see [98, 121]: polycrystalline material, compressed in the shape of a rod and placed vertically in a parabolic-mirror furnace, is molten locally by absorption of heat radiation. This melting zone is thereafter drawn upwards through the rod, while fresh material, continuously, gets molten at the upper edge of this floating zone and the crystal crystallizes below. The transport of the melt is led by diffusion and gravity.

One of the main advantages of this method is that the crystals are grown crucible free. All commonly used container materials like refractory ceramics or noble metals are known to react with the aggressive melts and solutions of copper oxide superconductors [122]. This causes impurities, i.e. spurious atoms of the container materials, in the single crystals that lead to strong changes of their electronic properties [123]. Another disadvantage of crucible growth for cuprates is that it often leads to an inhomogeneous doping with cerium for these solid solution systems: the distribution coefficient differs from unity which leads to an intrinsic doping gradient in the crystals [123, 124]. With the TSFZ technique, the purity of the crystals is only affected by the purity of the starting materials and the contamination problems due to crucible corrosion are avoided. In addition, by using suitable growth conditions (oxygen partial pressure, flux composition, temperature, growth velocity) one can overcome the problem of an inhomogeneous Ce doping and large crystals of several centimeters in length can be grown under exactly the same conditions. Fig. 3.1 (left) shows an as-grown crystal rod, where the copper oxide layers were oriented parallel to the long axis of the rod

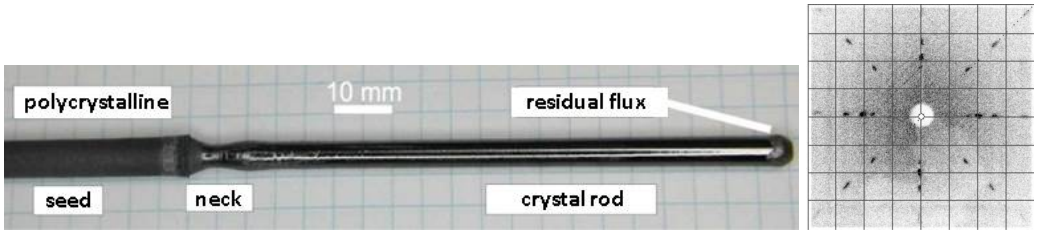

Figure 3.1: Left: a $6\mathrm{mm}$ thick polycrystalline feed rod with a neck, indicating the starting point of the growth process, the grown crystal rod with its shiny surface and the eutectically solidified residual flux on the top [98]. Right: Detected Laue back scattering shows the orientation of the c-axis, i.e. [001], grown out sidewards

and the c-axis grows out sidewards. Therefore the dimension of the samples in c-direction is limited by the thickness of the rod.

Grain separation, crystal orientation and cutting

Within the thickness of the as-grown crystal rod usually more than one single-crystal grain are present. These are macroscopic regions of different growth direction, which have to be separated manually. This was done by the use of a wire saw in combination with a diamond paste. Grain boundaries can be detected by a polarization microscope and need to be separated. This was done by simply cutting pieces out of the rods in a way that they consisted only of a single grain. With the help of a digital Laue back-scattering camera system, the orientation of the c-axis (see Fig. 3.1, right) and a-axis were determined to an accuracy of better than $0.5°$. By gradually grinding of the a, b-surfaces a uniform thickness in c-direction is realized. In the last step four cuts perpendicular to each other, parallel to the a, c- or b, c-plane, respectively, are set. Thus, the sample geometry can be set according to the experimental requirements. For the interlayer-transport, a large sample signal is desired to provide a reasonable signal-to-noise ratio. Thicknesses of $0.1 - 2.0\,\mathrm{mm}$ in the c-direction were obtained, depending on the grain size and doping level. As the doping is increased towards the solubility limit, $x = 0.175$, the grain size decreases significantly and only short lengths ($\leq 0.3\,\mathrm{mm}$) in c-direction are possible.

Heat treatment

Since the crystals grown by the TSFZ technique do not show SC in their as-grown state [1], all crystals, which were used in the experiments reported in this thesis, were annealed under the same conditions to reduce the apical oxygen content. These crystals received a standard reduction treatment in an argon gas flow at 900–$950^{\circ}\mathrm{C}$, close to the decomposition temperature [98], for $20\mathrm{h}$ followed by moderate cooling (50–$100\mathrm{K/h}$) to room temperature to achieve sharp superconducting transitions in the zero field temperature curves.

3.2 Sample geometries, fixations and contacting (overview)

Contacts with low ohmic resistances are crucial to get sufficiently low-noise signals. For the electrical contacts the two-component silver paste EpoTek H20E was used. Since attaching these wires manually to the crystals requires some space, for the interlayer-transport measurements two different geometries were used, depending on the available crystal thickness. In the case when only a short thickness in c-direction of $c \sim 0.1$–$0.3\,\mathrm{mm}$ was obtained, the cross-sectional area parallel to the CuO_2-layers was cut to approximately $(l_a \times l_b) = (0.5 \times 0.7)\,\mathrm{mm}^2$, see Fig 3.2 (a). When a larger length along c was available, the cross-sectional area was cut to approximately $(0.2 \times 0.3)\mathrm{mm}^2$, see Fig 3.2 (b).

Under an optical microscope annealed platinum wires of 10–$20\mu\mathrm{m}$ diameter were attached to the sample surface manually by using silver paste. The contact resistances achieved by simply drying under ambient conditions are in the range of several hundred ohms up to kiloohms. Therefore, the contacted crystals, including the wires, were cured by a heat treatment at $500^{\circ}\mathrm{C}$ for at least $1\mathrm{h}$ in air, which lead to contact resistances of $\sim 5\,\Omega$. It has to be noted that this short heat treatment does not affect notably the oxygen content of the samples, since the oxygen mobility at this temperatures is very small in n-doped cuprates, see Refs. [125, 126].

[1] As-grown, optimally doped $Nd_{1.85}Ce0_{0.15}CuO_4$ crystals are already superconducting with a broad transition and $T_c < 10\mathrm{K}$, when grown in an atmosphere of low oxygen partial pressure. [98]

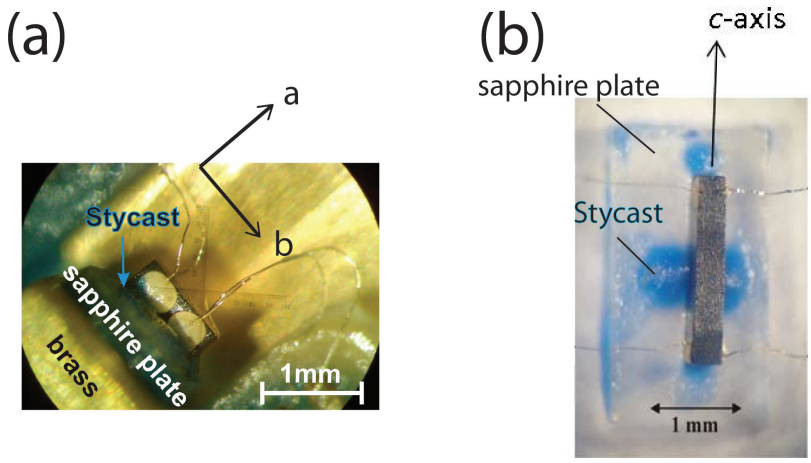

Figure 3.2: Contacted and mounted NCCO crystals for interlayer transport measurements under the optical microscope, two different geometries due to a short (a) and a large (b) size along the c-axis. 10–$20\,\mu\mathrm{m}$ thick platinum wires were attached with silver paste. The crystals are firmly fixed by Stycast (blue) to a sapphire substrate.

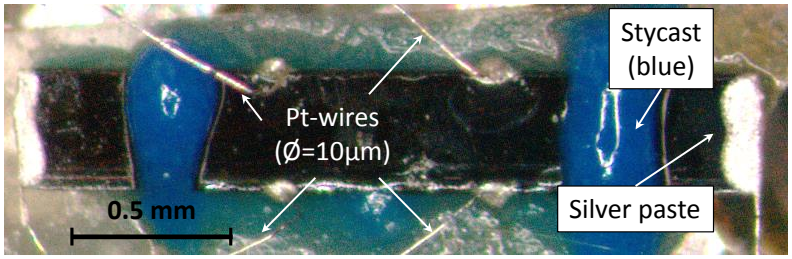

Figure 3.3: Contacted and mounted NCCO crystals under the optical microscope prepared for in-plane transport measurements. $10\,\mu\mathrm{m}$ thick Pt-wires were attached with silver paste. The crystal is firmly fixed by Stycast (blue) to a sapphire substrate.

It turned out that the samples felt a strong torque mainly induced by the neodymium moments in a magnetic field. Therefore, Stycast 2850 FT, prepared with Catalyst 24 LV, was used as glue to fix the samples on a sapphire plate. Sapphire is chosen because of its perfect electrical insulating and good thermal conducting properties. Stycast 2850 FT is characterized by a high thermal conductivity, small thermal expansion and a low viscous consistency, before it hardens.

For the in-plane transport measurements samples were prepared with as thin as possible thicknesses of $35 - 100\,\mu\mathrm{m}$ along the c-direction. To achieve this thicknesses the crystals were carefully thinned by grinding them mechanically. Due to the mechanical stress the crystals broke easily, making it impossible to reduce the thickness below $35\,\mu\mathrm{m}$ without destroying them. Fig. 3.3 shows a typical in-plane-contacted sample with dimensions $(l_a \times l_b \times l_c) = (0.4 \times 2.5 \times 0.05)\mathrm{mm}^3$. To avoid stress, induced by the fixation onto the sapphire, upon cooling to liquid ^{4}He temperatures, the samples were imbedded in pillows made from blue Stycast 2850FT that kept the bar slightly above the sapphire surface. To guaranty a homogeneous current distribution, the silver contacts were attached so that the full sides of the crystal bar were fully covered.

3.3 Preliminary characterization of the NCCO samples

The nominal doping is given by the initial proportions of the Ce and Nd, when composing the polycrystalline rods for the crystal growth process. This is also checked afterwards by energy-dispersive X-ray spectroscopy. Finally, only samples, showing a narrow superconducting transition and a transition temperature that corresponds to the nominal doping x (according to earlier studies [98, 99]), were chosen for the further high-field investigations.

3.3.1 Superconducting critical temperature T_c

As was mentioned above, one of the important steps in preparing the samples for magnetotransport studies is the annealing process right after the growth. The ideal temperature conditions for extracting the apical oxygen had been determined before [98, 99]. The superconducting transition was used as a criterion for checking the quality of the doping distribution in the crystals and the effect of the heat treatment.

Since NCCO is a perfect diamagnet in the superconducting state the transition can be detected via the magnetic susceptibility. In Fig. 3.4 the temperature dependence of the a.c. susceptibility for several doping levels x is presented. The measurements were performed using a Quantum Design SQUID magnetometer system (MPMS XL-7). The a.c. susceptibility is defined as $\chi = \frac{\partial M}{\partial H} = \chi' + i\chi''$, where the real part χ' describes the shielding of magnetic field ($\chi' = -1$ in the superconducting phase) and the imaginary part χ'' is the dissipative contribution in the Shubnikov phase. Upon decreasing T NCCO becomes superconducting at T_c and in the Meissner phase the external field is expelled, giving rise to a magnetic susceptibility of -1.

Fig. 3.5 presents the temperature dependence of the zero-field resistivity divided by its room temperature value $\rho_c(300\,\mathrm{K})$ below $50\,\mathrm{K}$ for crystals with different doping levels. In (a) the data for current applied perpendicular to the conducting CuO_2-layers, i.e. along the c-axis, and in (b) those for current applied in-plane, i.e. along the a-axis, are shown.

In Fig. 3.6 (a) and (b) the temperature at the midpoint of the superconduct-

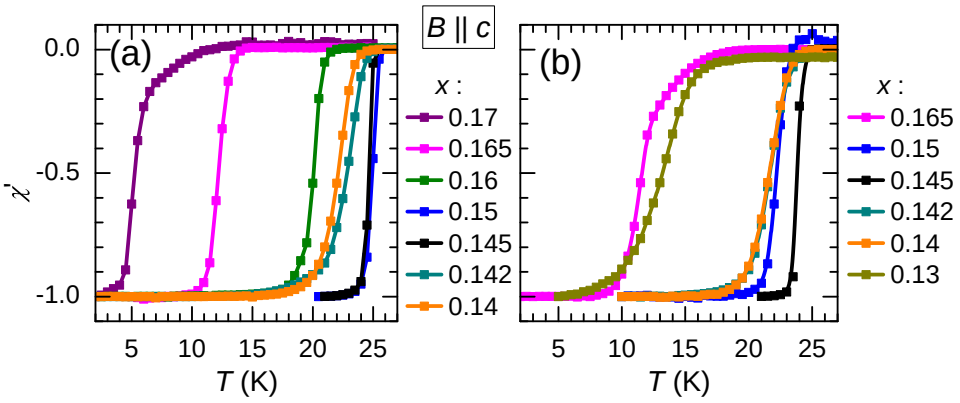

Figure 3.4: Temperature dependence of the a.c. susceptibility $\chi'(T)$ for different x. An a.c. field of 5 Oe was applied perpendicular to the conducting CuO_2-layers (i.e. $B||c$-axis): (a) Samples with a long length along the c-axis but small ab-cross sectional area used for interlayer magnetoresistance measurements, see Fig. 3.2 and (b) Samples with a small thickness along the c-axis but a large length along a prepared for intralayer transport measurements, see Fig. 3.3.

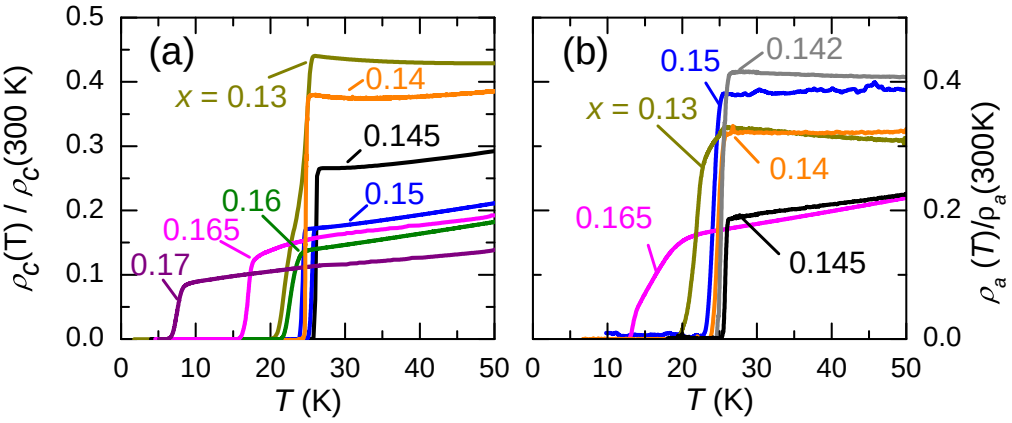

Figure 3.5: Temperature dependence of the (a) interlayer resistivity $\rho_c/\rho_c(300\,\mathrm{K})$ and (b) in-plane resistivity $\rho_a(T)/\rho_a(300\,\mathrm{K})$ normalized to their room temperature values for different x in zero magnetic field.

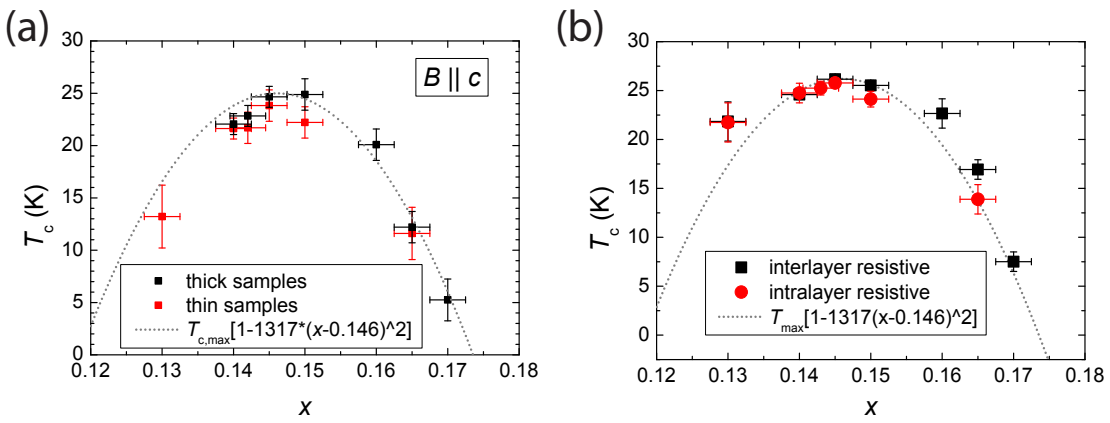

Figure 3.6: Critical superconducting temperature T_c obtained from the temperature dependence of (a) the a.c. susceptibility data in Fig. 3.4 and (b) the inter- and intralayer resistivity data in Fig. 3.5 for different x. T_c is taken from the midpoint of the superconducting transition. The error bars correspond to the temperatures at which the signal is, respectively, 10 and 90 % of its normal-state value right above the transition. The grey curve is an empirically determined fit obtained from a.c. susceptibility data for similar samples [98].

ing transition is plotted versus the cerium concentration x for the resistivity and susceptibility data, respectively, presented in Figs. 3.6 and 3.7. The grey curve is an empirically determined fit obtained from a.c. susceptibility data for similar samples [98].

3.3.2 Field dependence of the resistivity at different temperatures

In pulsed magnetic fields the temperature during the pulse deviates from the zero-field value due to a field-induced overheating. In addition, commonly used T sensors feel a MR that also depends on the T. Thus, a reliable temperature control is an issue for experiments in pulsed fields.

In NCCO SC is suppressed completely by fields of $\geq 10\,\mathrm{T}$ for all available doping levels. Since the sharp transition into the normal state depends on temperature this can be used as a tool for determining the exact T in the beginning and at the end of a pulse. In Fig. 3.7 it is demonstrated for an $x = 0.15$ sample how

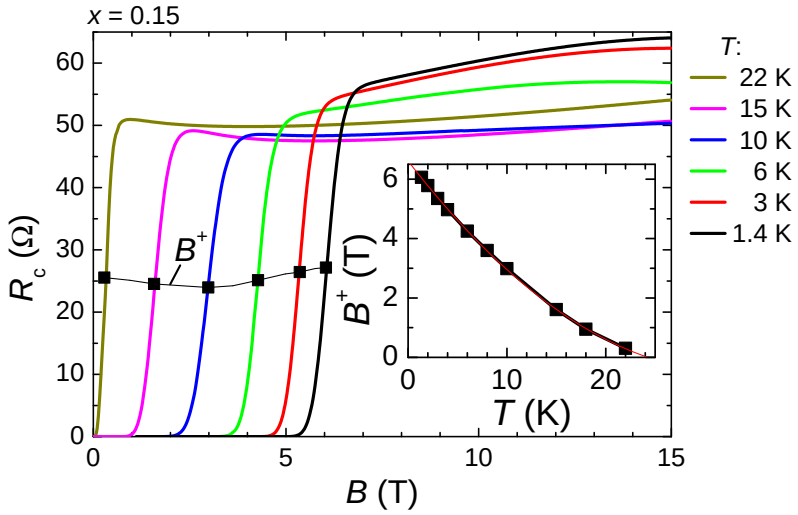

Figure 3.7: Interlayer magnetoresistance versus the applied magnetic field $B = \mu_0 H_{\mathrm{ext}}$ for a slightly overdoped, $x = 0.15$, NCCO sample recorded in steady fields up to $15\,\mathrm{T}$ applied along the c-axis. Inset: Critical field at the midpoint of the superconducting transition, plotted versus the temperature.

the temperature dependence of the critical magnetic field is determined in steady fields up to $15\,\mathrm{T}$. The extracted temperature dependence of the critical field B^+ is then used as a T-calibration in the pulsed field experiments.

4 Experimental setups and techniques

4.1 Magnet systems

The experimental results presented in this work were obtained at several different high-field magnet facilities.

Steady-field experiments in fields of up to $17\,\mathrm{T}$ were performed in a liquid ^{4}He cooled superconducting magnet system available at the Walther-Meißner Institut (WMI). The system is operated with a maximum current of $115.6\,\mathrm{A}$.

Even higher steady fields of up to $35\,\mathrm{T}$ were provided by the Laboratoire National des Champs Magnétique Intense in Grenoble, France (LNCMI-G), which is a member of the European Magnet Field Laboratory (EMFL). These fields are reached by a massive resistive magnet system, a combination of Bitter and Polyhelix magnets cooled with water. The magnet is operated with a maximum current of $\sim 14\mathrm{kA}$ and the produced heat dissipation is caught by the water cooling, which amounts to a consumption of $\sim 24\,\mathrm{MW}$.

The highest steady magnetic fields of up to $45\,\mathrm{T}$, available at present, were provided by the National High Magnetic Field Laboratory in Tallahassee, USA (NHMFL). This Hybrid magnet is a combination of a resistive, water cooled magnet, providing $33.5\,\mathrm{T}$, surrounded by a large liquid ^{4}He cooled superconducting magnet, providing $11.5\,\mathrm{T}$. The ^{4}He liquification and the operating current of $\sim 57\mathrm{kA}$ through the resistive magnet amount to a consumption of $\sim 33\,\mathrm{MW}$.

Non-destructive pulsed-field experiments were performed at the HLD in

Dresden-Rossendorf, Germany (HLD) and at the LNCMI-T in Toulouse, France, both members of the EMFL, providing magnetic fields of up to $87\,\mathrm{T}$ and $70\,\mathrm{T}$, respectively. The fields are generated by liquid nitrogen cooled, resistive magnets that are especially built for standing the strong pressure induced by the high currents of up to $100\,\mathrm{kA}$ during a short time period ($\sim$ 0.1–0.2ms), see Fig. 4.1. The power sources are high-energy capacitor banks providing energies of up to $50\,\mathrm{MJ}$ and $14\,\mathrm{MJ}$ in Dresden and Toulouse, respectively. The high thermal power of up to $5\,\mathrm{GW}$ to the coil follows from the extreme energy input, $Q = \int_0^{t_\mathrm{pulse}} R(T(t))I(t)^2\,dt$, with the discharge current $I(t)$ and the coil resistance R during one pulse of the duration t_pulse. The exposed energy must be absorbed completely by the coil system, which warms to almost room temperature right after the pulse. Thus, after each pulse there is a cooling time of about 1–5 hours.

Even higher fields of up to $100\,\mathrm{T}$ are reached in a two-coil pulsed-magnet system where a larger coil is pulsed first, providing a maximum field of about 40–$50\,\mathrm{T}$ followed by a second pulse from the inner, smaller coil, see the red curve in Fig. 4.1.

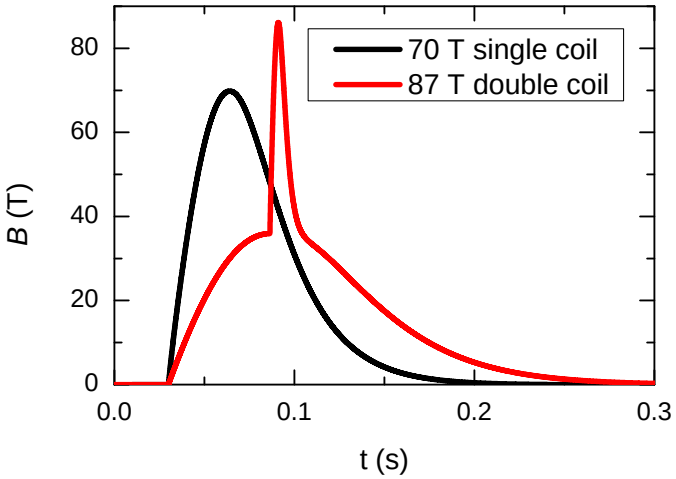

Figure 4.1: Magnetic field versus time profiles of two pulses for two different magnets at the HLD.

4.2 Resistance measurements: a.c. 4-probe technique

For the measurements of the interlayer resistance the standard a.c. 4-probe method is used. Four contacts are attached to the sample, two on each side as shown in Fig. 4.2 (a) and (b). One pair of opposite contacts is used to apply the current and the other to measure the induced voltage. This method makes it possible to measure the pure interlayer resistance without the contributions of the contact resistances. Due to the layered crystal structure, NCCO shows a large anisotropy in the conductivity for currents within or perpendicular to the conducting CuO_2-layers. The anisotropy ratio is [98]

$$\frac{\rho_c}{\rho_{ab}} \approx 10^3,$$

with the interlayer resistivity $\rho_c = U/I \cdot (l_a l_b)/l_c$. For a sample of the size $(l_a \times l_b \times l_c) = (0.5 \times 1.0 \times 0.1)\,\mathrm{mm}^3$ this would correspond to an isotropic system with a similar a, b-cross-sectional area of $(0.5 \times 1.0)\mathrm{mm}^2$ but a thickness of $l_c \approx 3\mathrm{mm}$. Therefore, the current can be regarded as uniformly distributed over the whole bulk even for the thinner samples (see Sect. 3.2) used for the interlayer-transport experiments presented in this thesis.

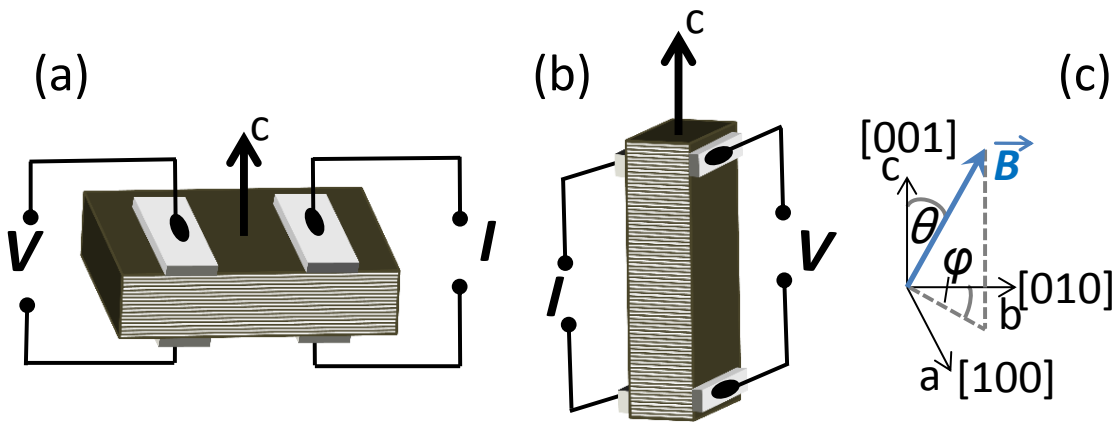

Figure 4.2: (a) and (b) Illustration of the interlayer transport configurations, i.e. current applied perpendicular to the CuO_2-layers, for two different sample geometries characterized by a short or large length in the c-direction, respectively. (c) Definition of the angles θ and φ with respect to the crystal axes.

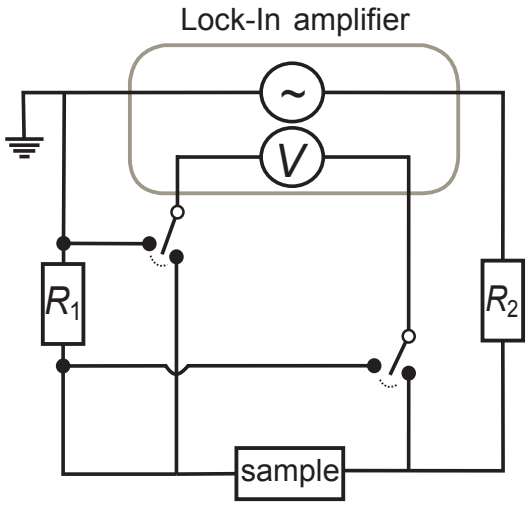

Figure 4.3: Block-diagram of the measuring setup with a variable reference resistor $R_1 = 10,\ 100\Omega$ and a load resistor $R_2 = 1\text{k}\Omega$ to $100\text{k}\Omega$. The sample voltage is measured by using a lock-in amplifier.

Measurements in steady fields

For the current supply a high-ohmic (1–$100\,\text{k}\Omega$) resistor R_2 was set in series to the internal a.c. voltage generator of the lock-in amplifier. Hence, the a.c. current was set by adjusting the output voltage from the lock-in amplifier[1]. The reference resistor R_1 of $10\,\Omega$ or $100\,\Omega$ was connected in series to the sample. Thus, the a.c. current can be precisely adjusted and one can check if there is any out-of-phase component, showing capacitive contributions. To provide equal conditions and low overheating, during the measurements in Garching, Grenoble and Tallahassee the applied current was always set to relatively low currents of 0.1–$0.5\,\text{mA}$ with a frequency of $f \approx 300\,\text{Hz}$ or 11–$18\,\text{Hz}$ in case of very small signals. Because of the large, compared to the sample resistances, value of R_2, the change to zero resistance in the superconducting state affects the current by less than 1% and, therefore, guaranties a stable current during the whole experiments.

[1]Lock-in amplifiers used: Stanford Research Systems, models 830 and 850; EG& G Princeton Applied Research, models 5302 and 5210

Measurements in pulsed fields

Due to the non-negligible overheating effect in pulsed field experiments usual low-temperature measurements were done in liquid ^{4}He. The experience shows that having the samples completely immersed in liquid resulted in the best thermal coupling, i.e. the observable overheating was weakest. Sample holders and the parts of the probe near the samples had to be made of non-metallic materials to avoid additional eddy currents.

A similar a.c. 4-probe resistive setup, as described above, was used with the difference that during the short time-window of $t_{pulse} \approx 0.2\mathrm{s}$ for one pulse, see Fig. 4.1, the raw a.c. voltage signal from the sample was recorded by a high-speed digital oscilloscope with a sampling rate of $1\mu\mathrm{s}$. The signal was than processed by laboratory self-developed programs using the same technique like the lock-in synchrodetector. The main advantage is that one can play with the raw data, trying to optimize the signal after the pulse, whereas with the lock-in one has to make many pulses, playing "trial and error", in order to optimize the signal. It should be noted here that the cooling of the coil after a pulse to highest field takes, depending on the model, several hours, and thus "trial and error" would be very time-consuming. Higher a.c. currents of 0.5–$10\,\mathrm{A}$ and a frequency of 60–$90\,\mathrm{kHz}$ were applied. This increased the local heating of the sample slightly. The temperature of the sample was than evaluated by comparing the critical field, at which superconductivity was suppressed with former steady-field measurements at known temperatures.

After the first pulsed-field experiments with a relative high noise [101] the signal-to-noise ratio was successfully improved by approximately two orders of magnitude. Several factors led to this significant improvement:

- new samples with an optimized sample geometry, i.e. a large length along the crystallographic c-axis, resulted in very large sample resistances;
- low-ohmic contacts of less than $5\,\Omega$, that decreased further on at low temperatures, were achieved by using the two-component silver paste EpoTek H20E instead of Dupont 4929 silver paste;
- the shielding of the measurement probes and their grounding configurations were improved essentially;

- immobilizing all the essential wires till as close as possible to the sample eliminated moving induction loops perpendicular to the applied magnetic fields.

Intralayer transport measurements in pulsed and steady fields

Fig. 4.4 (a) shows an example of a sample mounted for measurements of the intralayer resistivity and the Hall resistance. Thereby the same a.c. lock-in techniques were used to measure the two channels, V_{xx} and V_{xy}, simultaneously. The wires were aligned so that induction loops perpendicular to the magnetic field were minimized. Fig. 4.4 (b) shows an example of a mounted pulsed-field sample holder, made from plastic, with two in-plane samples fitting to a sample space of less than $5\,\mathrm{mm}$ in diameter.

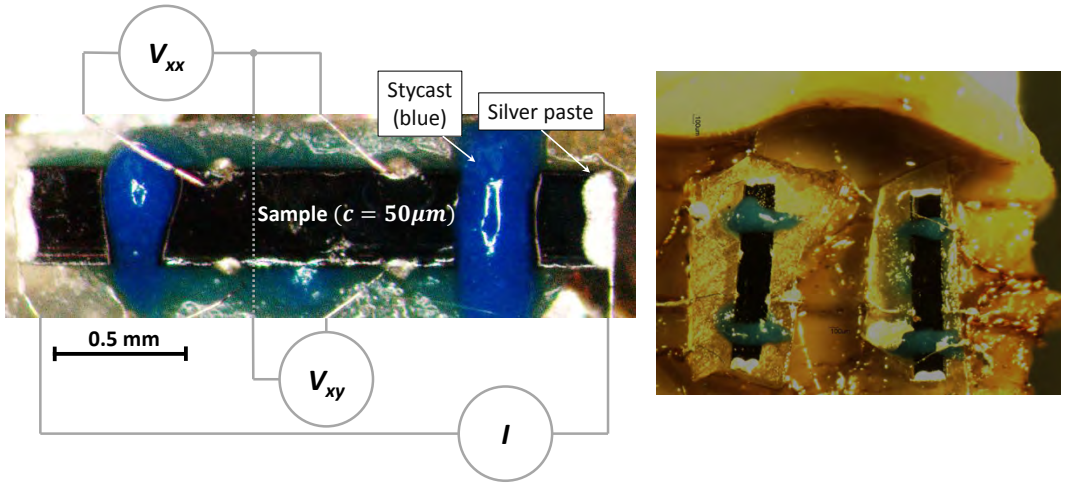

Figure 4.4: Sample configuration for in-plane measurements in pulsed fields: (a) principal sketch of how the longitudinal and transverse voltages are measured on a typical in-plane contacted NCCO sample. (b) Photograph of a plastic holder mounted with two in-plane contacted samples.

4.3 Rotating sample stages

Each magnet system had different requirements to the sample holders and measurement inserts. In the following some basic principles of the rotating sample stages used in steady and pulsed fields are presented. Field rotations in a plane parallel to the crystallographic c-axis are described by the polar angle θ, where $\theta = 0°$ corresponds to $B||[001]$. The azimuthal orientation, i.e. parallel to the CuO_2-layers, will be described by φ, with $\varphi = 0°$ and $45°$ corresponding to $B||[100]$ and $B||[110]$, respectively (as sketched in Fig. 4.2 (c).

Two-axis rotator designed for the 17 T superconducting and 28 T resistive magnet systems

This insert fits to the superconducting magnet available at the WMI and the 28 T resistive magnet system at the LNCMI-G. It was constructed in the framework of the Ph.D. thesis of D. Andres [127]. In Fig. 4.5 the principle of rotation is illustrated. The rotation is provided by two worm gear units. The θ-rotation is driven by a long rod coupled to a piezo-electric motor on top of the whole insert outside the cryostat. The azimuthal φ-orientation can be controlled by the screwdriver

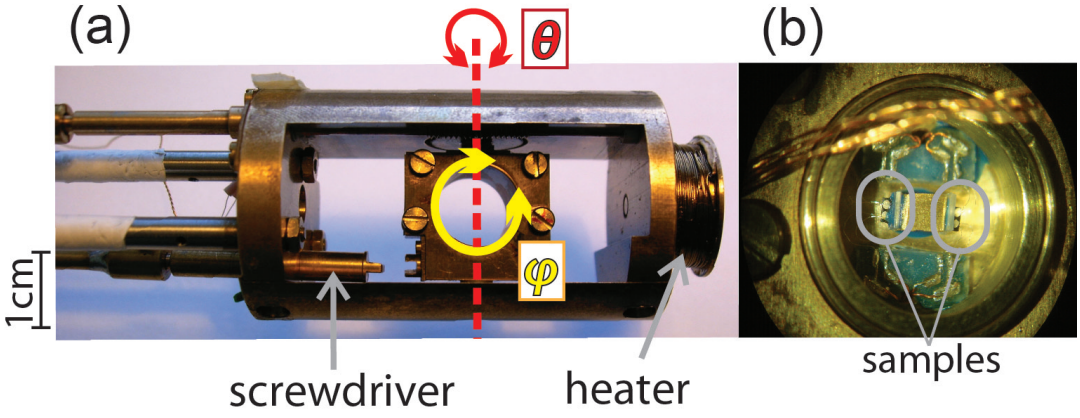

Figure 4.5: (a) Photo of the two-axis rotator with introduced rotation angles: φ is controlled by the screwdriver, which can be decoupled from the rotator platform, and θ is controlled by a driving axis coupled via a worm gear in the upper wall. (b) Sample holder with two samples mounted with the CuO_2-layers parallel to the rotator platform.

only when the rotation platform is in its initial position parallel to the screwdriver, as it shown in Fig. 4.5 (a). The screwdriver can be manually controlled from outside. Thus, during an experiment the φ-position has to be set manually by sliding the screwdriver in and out. After decoupling the screwdriver manually from the platform, a continuous θ-rotation can be performed fully automatically. Both angles can be set to an accuracy of $\leq 0.05°$. The sweeping rate of the sample rotation can be continuously changed in a range of $0.003 - 10°/\mathrm{s}$ via a mechanical gear placed outside between the motor and the driving rod. Two samples can be placed, as depicted in Fig. 4.5 (b), usually with their crystallographic c-axis oriented perpendicular to the rotation platform. Thus, any angular orientation with respect to the magnetic field can be set with this setup.

Two-axis rotator designed for $35\,\mathrm{T}$ resistive and $45\,\mathrm{T}$ hybrid magnet systems

In Fig. 4.6 a drawing of the rotating sample stage designed for 2-axis rotations in fields of up to $45\,\mathrm{T}$ is shown. The main challenge here was the narrow inner diameter of $\leq 18\,\mathrm{mm}$ of the variable temperature insert, limited by the inner bore of the magnet, in which this rotator had to fit. For such small dimensions two integrated worm gears for the translation of the two rotations, as it is realized in the insert discussed above, were no option. Therefore, a design combining a pulling-string driven rotation together with a central screwdriver was chosen, see Fig. 4.6.

The main rotating body contains the sample holder, providing space for two samples in the 4-probe configuration. The inner part of this container is turnable in the φ-plane, since it is only fixed by a flat plate-like spring pressed via the cap (see the green ring under the brown fixable ring cap in Fig. 4.6). The azimuthal φ-orientation can, thus, be set when the rotating body is aligned with its long side parallel to the screwdriver. By sliding in and out the screwdriver one can access the slit (marked by the black arrows) in the sample holder and set any φ. After the screwdriver is decoupled from the rotating body the θ-rotation can be performed over $\sim 120°$ in both directions, controlled via a string fixed to the wheel at the side. As a string, a commercially available fishermen steel string has proved sufficient. The insert is designed so that the tension of the string

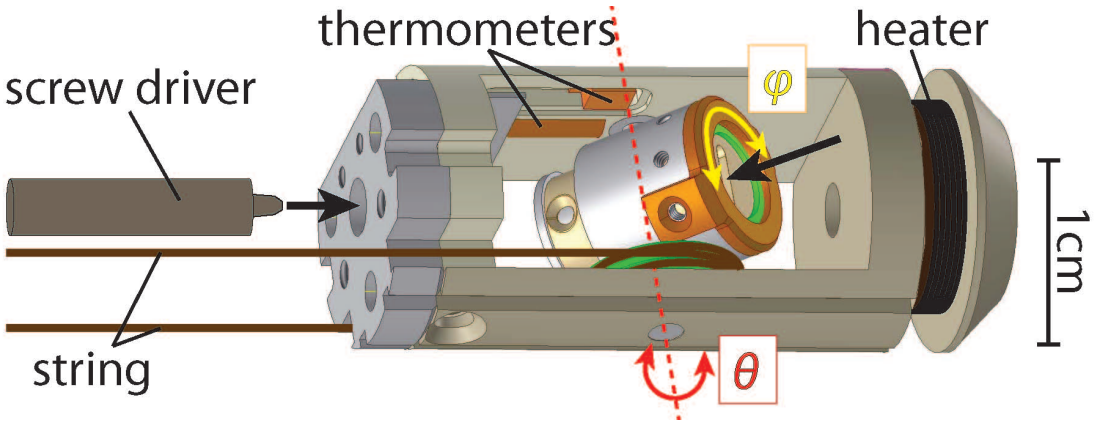

Figure 4.6: 3D drawing of the 2-axis rotator installed to a $45\,\mathrm{T}$ low-temperature insert. Samples are mounted to a turnable holder kept by a container which is fixed to the θ-rotation axis. The θ-rotation is controlled via a string and the angle φ can be set via the screw driver, see text.

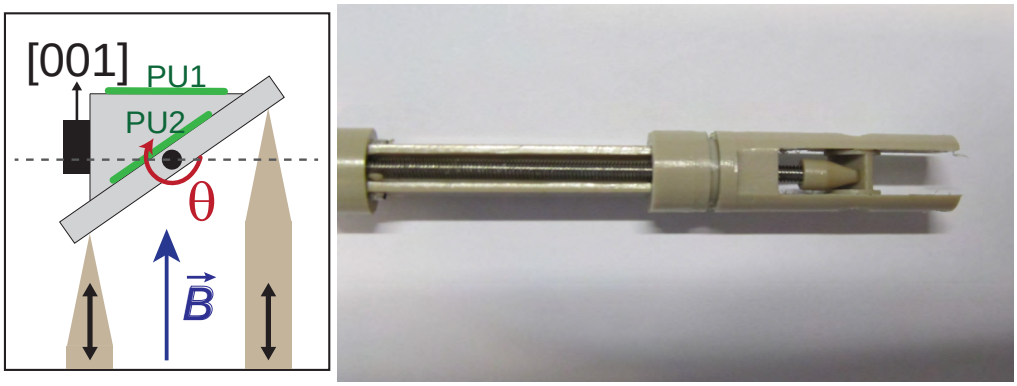

Figure 4.7: Single-axis rotating stage for pulsed field experiments. Left: principle sketch of a sample attached to the side of a triangle so that $B||[001]$. The θ-angle can be controlled via positioning the two pushing rods (see arrows). Two pickup coils, one perpendicular to the $[001]$-direction and a second one by $35°$ tilted, for a in-situ determination of the θ-orientation. Right: photo of the rotator with an outer diameter of $8\,\mathrm{mm}$.

can be tightened in-situ after the whole system has cooled down to liquid ^{4}He temperatures. For the automatized θ-rotations the same piezo-electric motor in combination with a switchable gear are used as for the insert described in the previous section.

Single-axis rotator designed for pulsed fields

The strong magnetic torque felt by the NCCO in magnetic fields has to be considered when it comes to building sensitive probes, especially in pulsed magnetic fields. A single-axis rotating insert was designed and built in collaboration with the HLD for 4-probe-magnetoresistance measurements in pulsed magnetic fields of up to $70\,\mathrm{T}$ at liquid ^{4}He temperatures fitting to a relatively narrow sample space of Ø$\approx 8\,\mathrm{mm}$. A special rigid design , sketched in Fig. 4.7, was chosen to withstand the expected strong magnetic torque of the NCCO samples. Two cone-headed pushing-rods, made from plastic, press against the rotation platform. The sample is fixed on a triangular prism so that, having the platform set to an angle of $\approx 35°$, the initial polar orientation is $\theta = 0°$. Two small pickup coils (green bars in Fig. 4.7) were used to determine the precise angle $in\ situ$.

4.4 Torque magnetometry

A sample, having a volume magnetization $\mathbf{M} = \mathbf{m}/V$, in a magnetic field $\mathbf{B}$ experiences a magnetic torque:

$$\boldsymbol{\tau} = V\mathbf{M} \times \mathbf{B} \tag{4.1}$$

For a layered anisotropic material like NCCO a magnetic torque develops for field orientations away from the principal crystal axes. The magnetization $\mu_0\mathbf{M} \approx \chi_{ij}\mathbf{B}$ (for $\mu_B/k_\mathrm{B}T << 1$) is described by the susceptibility tensor χ_{ij}, with $i, j = x, y, z$. Thus,

$$\boldsymbol{\tau} = \frac{V}{\mu_0}(\chi_{ij} \cdot \mathbf{B}) \times \mathbf{B}. \tag{4.2}$$

Assuming the base of the susceptibility tensor lies in the directions of the crys-

tal axes x, y, z, it can be written as:

$$\chi_{ij} = \begin{pmatrix} \chi_{xx} & 0 & 0 \\ 0 & \chi_{yy} & 0 \\ 0 & 0 & \chi_{zz} \end{pmatrix} \tag{4.3}$$

One can show that for a field aligned in a plane perpendicular to one of the main crystal axes there is only one torque component parallel to that direction. For example, a field $B = (0, B\sin\theta, B\cos\theta)$ aligned perpendicular to the x-axis results in a torque:

$$\boldsymbol{\tau} = \begin{pmatrix} B^2(\chi_{yy} - \chi_{zz})\sin\theta\cos\theta \\ 0 \\ 0 \end{pmatrix} \tag{4.4}$$

parallel to the x-direction changing proportionally to $\sin\theta\cos\theta = 0.5\sin(2\theta)$. Therefore, the torque is strongest for the field aligned $45°$ away from perpendicular to the conducting layers.

Taking into account the de Haas-van Alphen effect (see Sect. 2.3.2), the oscillatory component of the the magnetic torque can be expressed in terms of the magnetization parallel to the field Eq. (2.31)

$$\tilde{\tau} = VM_{\perp}B = -\frac{1}{F(\theta)}\frac{\partial F(\theta)}{\partial\theta}M_{||}BV. \tag{4.5}$$

The torque oscillation amplitude $|\tilde{\tau}|$ is zero for $\theta = 0°$ and $90°$, i.e. for field aligned parallel to a symmetry axis of the crystal. From Eq. (4.4) and Eq. (4.5) one can estimate the optimal angle for detecting de Haas-van Alphen oscillations.

Microcantilever torque detection

In pulsed magnetic fields at the LNCMI-T the magnetic torque was measured using a commercially available silicon piezoresistive microcantilever, fabricated for atomic force microscopy. A piezoresistive path, implanted on the cantilever detects the stress change on the cantilever due to the torque felt by the attached crystal. The experimental setup and principle of detection by the use of a resistive Wheatstone bridge was provided by the LNCMI-T, for details see [128]. In Fig. 4.8 a microcantilever with a lever-length of $120\,\mu m$ under the optical microscope is shown. An slightly overdoped NCCO, $x = 0.15$, sample of the size $(20 \times 70 \times 15)\,\mu m^3$ was glued to to the cantilever with UHU two component glue.

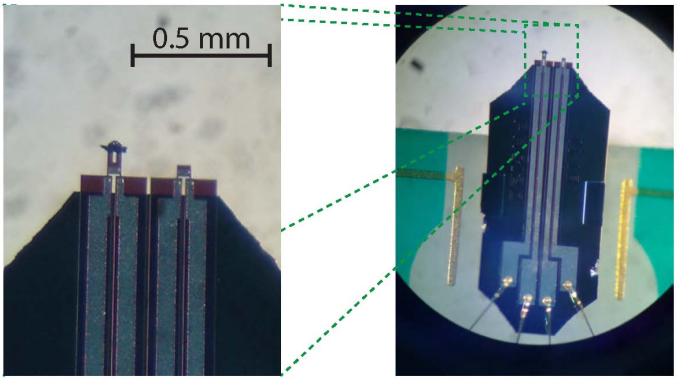

Figure 4.8: Microcantilever with a lever-length of $120\,\mu m$ under the optical microscope. A sample of the size $(l_a \times l_b \times l_c) \approx (20 \times 70 \times 15)\,\mu m^3$ was glued to it with the UHU two-component glue.

Capacitive cantilever torque detection

A capacitive torque magnetometer was built for the 2-axis-rotating insert described in Sect. 4.3. In Fig. 4.9 a principle sketch of the torque meter is shown. The capacitance between an approximately $25 - 50\,\mu m$ thick CuBe-cantilever beam and a ground plate is measured using a GR 1615A capacitance bridge. A more detailed description of the technique can be found in Refs. [129, 130].

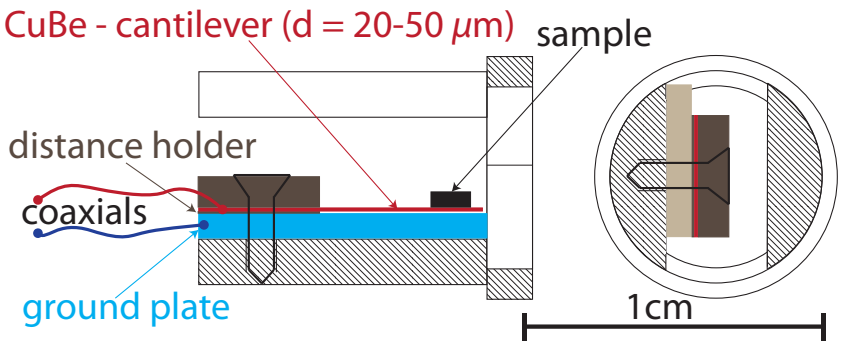

Figure 4.9: Sketch of the capacitive torque magnetometer constructed for the $45\,T$-rotating insert (Fig. 4.6). The capacitance between a metallic ground plate and the CuBe-cantilever separated by an insulating distance plate is measured.

Part III

Results and Discussions

5 Magnetic quantum oscillations in overdoped $Nd_{2-x}Ce_xCuO_4$: evidences for a well established reconstructed Fermi surface

As described in the theoretical introduction, Sect. 2.3, magnetic quantum oscillations (MQO) can provide important information about the Fermi surface properties. For example, the frequency of the oscillations is a direct measure of the Fermi surface (FS) area. In the following, results on Shubnikov-de Haas (SdH) oscillations are presented, that provide deep insights into the electronic structure of $Nd_{2-x}Ce_xCuO_4$ (NCCO).

5.1 Shubnikov-de Haas oscillations in NCCO

5.1.1 First magnetic quantum oscillations in electron-doped NCCO

The first discovery of MQO in single crystals of the n-doped cuprate superconductor NCCO during the diploma work of the author [101] demonstrated the importance of high field experiments for exploring the Fermi surface (FS) in this material and initiated the in-depth studies of its high-field properties presented in the following.

Fig. 5.1 presents the interlayer magnetoresistivity for three different doping levels recorded in pulsed magnetic fields aligned parallel to the c-axis of the crystals (see inset). After superconductivity (SC) is suppressed (sharp transitions in Fig. 5.1) the magnetoresistance (MR) increases almost quadratically towards highest fields. The anomalous negative MR observed for the $x = 0.15$ sample

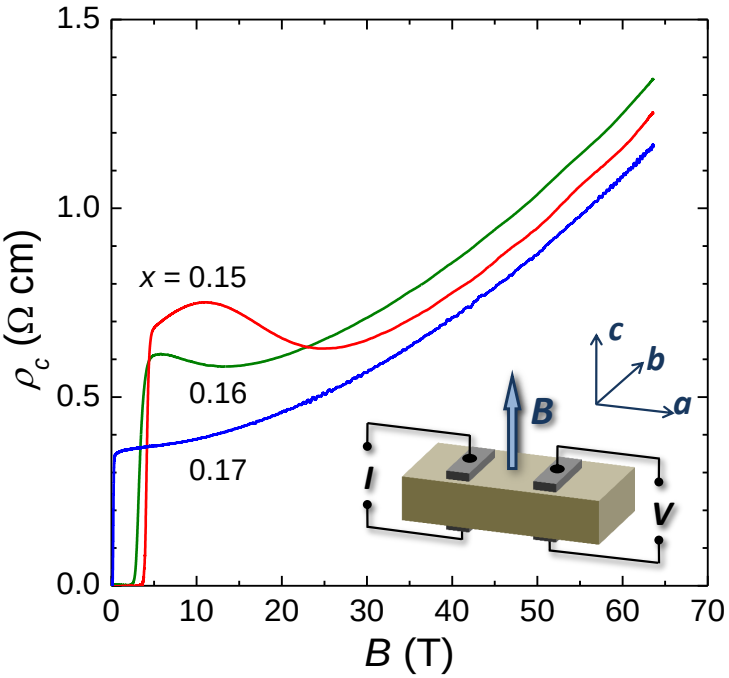

Figure 5.1: c-axis resistivity of NCCO plotted vs. magnetic field applied perpendicular to the CuO_2-layers at $T = 4\,\mathrm{K}$ for different doping levels x. The inset illustrates the geometry of the experiment [102].

right above the superconducting transition will be discussed later in Sect. 7.1. The reader can resolve slowly varying oscillations already with bare eyes on the MR curve for the $x = 0.15$ composition. These are magnetic quantum oscillations (MQO). After subtracting a low order polynomial, fitting the non-oscillating MR, the oscillations become better visible, as can be seen in Fig. 5.2. Shubnikov-de Haas (SdH) oscillations in the interlayer magnetoresistance with a high frequency of about $11\,\mathrm{kT}$ proved the existence of a well established FS for a strongly overdoped, $x = 0.17$, composition at temperatures below the superconducting critical temperature T_c. The corresponding FS area, covering approximately $42\,\%$ of the first Brillouin zone (BZ), nicely agreed with that predicted by band structure calculations for the expected carrier concentration, according to the doping x [48]. Fig. 5.3 (a) shows the large 2D FS centered around the corner of the BZ, as it is expected for an electron-doping of $17\,\%$. Surprisingly, this large FS was found to change tremendously as x was lowered by only 1%: For doping levels of $x = 0.16$ and 0.15 SdH oscillations with a rather small frequency of about $0.3\,\mathrm{kT}$ were de-

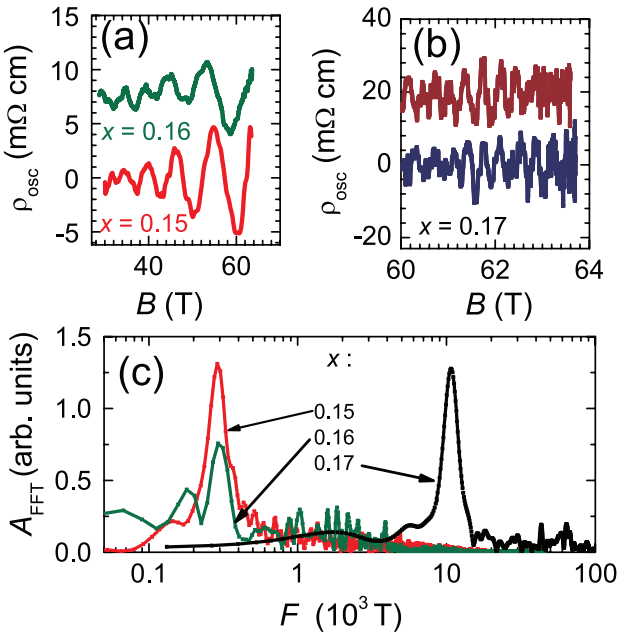

Figure 5.2: First MQO observed in the magnetoresistivity of the n-doped cuprate NCCO recorded in pulsed fields at $T = 2.5\,\mathrm{K}$ [102]. (a) Oscillatory component of the interlayer resistivity showing low-frequency oscillations with $F \approx 300\,\mathrm{T}$ for slightly overdoped compositions. (b) For the strongly overdoped, $x = 0.17$, sample a large frequency of $\approx 11\,\mathrm{kT}$ was observed in two pulses at $T = 3.5\,\mathrm{K}$. (c) Corresponding fast Fourier transform spectra of the oscillatory resistivity. For $x = 0.17$ the spectrum corresponds to an average of the two data sets shown in (b).

tected, indicating a small FS pocket, occupying about $1\,\%$ of the Brillouin zone. Obviously the FS is reconstructed due to a broken symmetry. Fig. 5.3 (b) shows a possible FS due to a suggested $(\frac{\pi}{a}, \frac{\pi}{a})$-ordering as discussed in Sect. 1.3.3.

From these results one could suggest that the FS of $Nd_{2-x}Ce_xCuO_4$ experiences a sudden reconstruction in a narrow doping interval between $x = 0.17$ and 0.16, supporting the idea of a quantum critical point, associated with a translational symmetry breaking, within the superconducting region [96]. However, as noted in [101], the observed fast SdH oscillations do not unambiguously rule out that the reconstructed FS persists even at $x = 0.17$. A possible origin for such a large FS orbit might be the effect of magnetic breakdown, in case the potential responsible for the FS reconstruction is weak enough.

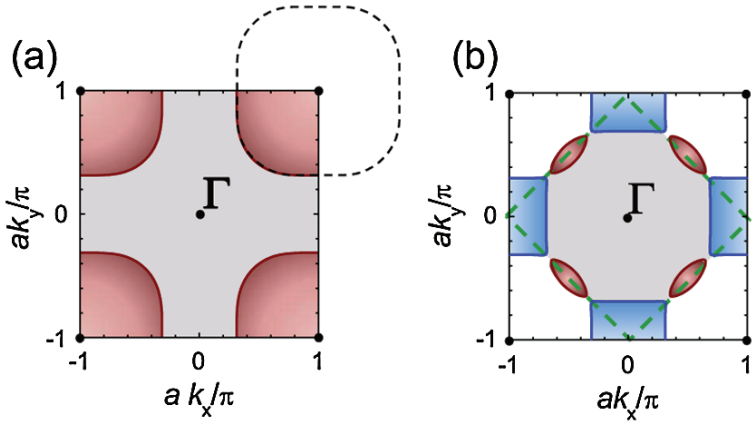

Figure 5.3: (a) Unreconstructed hole-like FS centered around $(\frac{\pi}{a}, \frac{\pi}{a})$ corresponding to Eq. 1.2 for $x = 0.17$. (b) Suggested reconstructed FS, consisting of hole- and electron-like parts, in the presence of a $(\frac{\pi}{a}, \frac{\pi}{a})$-ordering according to Eq. (1.3).

5.1.2 Shubnikov-de Haas oscillations at various doping levels

Since the discovery of the first SdH oscillations in NCCO a tremendous progress in terms of the experimental signal resolution has been achieved. In the following newest results on SdH oscillations for various doping levels will be presented that slightly change the picture obtained from the very first results [102] and provide a more robust explanation for the doping-dependent evolution of the FS in NCCO [131, 132].

In Fig. 5.4 the oscillatory component of the interlayer magnetoresistance for several doping levels of NCCO is presented. The data were recorded in pulsed magnetic fields (at the HLD in Dresden-Rossendorf) up to 70 T at liquid ^{4}He temperatures. Thanks to successful optimization of the sample preparation and measurement setups, as described in the experimental chapter II (Sect. 4), the signal-to-noise ratio has been improved by two orders of magnitude as compared to the first pulsed-field experiment and was $\leq 5 \times 10^{-}5$. A signal of two SdH oscillations can be resolved for doping levels ranging from $x = 0.15$, slight overdoping, until $x = 0.17$, close to the upper edge of the superconducting region in the phase diagram of NCCO. For optimally doped, $x = 0.145$, samples only slow oscillations, with a frequency of $F = 300$ T, are found: no appreciable signal of a fast oscillation is discernible.

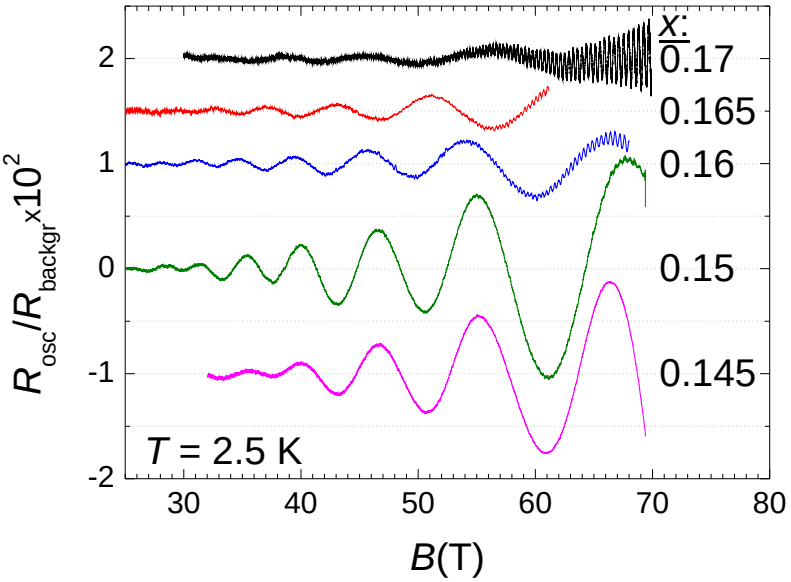

Figure 5.4: Oscillatory component of the interlayer magnetoresistance NCCO for several doping levels, in pulsed fields up to $70\,\mathrm{T}$ applied perpendicular to the conducting CuO-layers, at $T = 2.5\,\mathrm{K}$. The data are normalized by low-order polynomial fits representing the non-oscillating magnetoresistance background $R_{\mathrm{backgr.}}$. On top of the slow SdH oscillations with frequency F_α, an additional high frequency F_β can be resolved for $x \geq 0.15$ at fields above $50\,\mathrm{T}$. Note: The curves are vertically shifted for better visibility.

The slow oscillations, originating from a tiny FS area of less than 1% of the Brillouin zone, from now on will be labeled with α and the fast ones with β. The latter originate from a large cyclotron orbit covering more than 40% of the Brillouin zone. Fig. 5.5 presents the relative oscillatory component of the β-frequency after filtering out the slow α-part. As can be seen for $x = 0.145$, i.e. optimal doping, above $67\,\mathrm{T}$ there are weak oscillations in the pulse resolvable that might be related to the SdH effect. But till present this signal has not been confirmed satisfactorily. In Table 5.1 all the observed frequencies and the corresponding FS areas in units of the Brillouin zone area S_{BZ} are listed.

Obviously, the α-frequency is still observed for $x = 0.17$, indicating that the reconstructed FS is present up to the highest accessible doping. Hence the scenario of a quantum critical transition around $x = 0.165$, mentioned above, becomes rather unlikely.

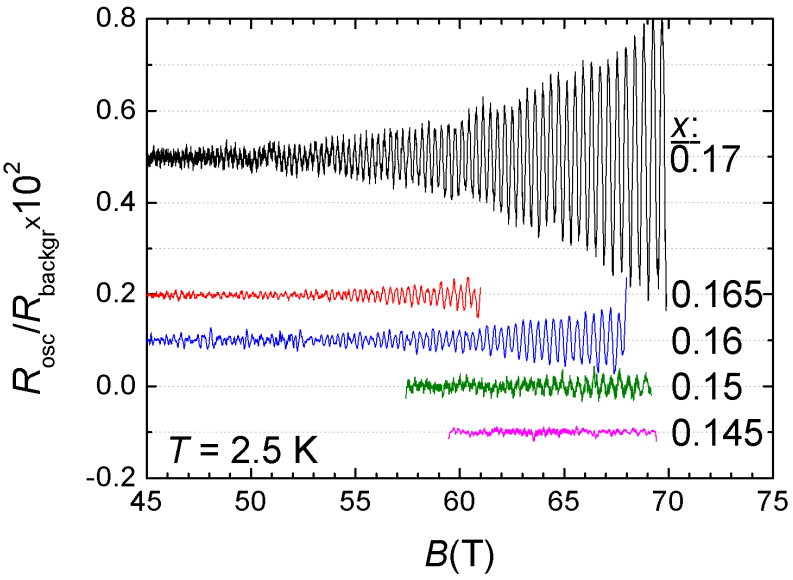

Figure 5.5: High-frequency SdH oscillations for several doping levels x after filtering out the slow α-oscillations. For $x_{\mathrm{opt}} = 0.145$ no appreciable signal at the high β-frequency has been observed so far. Note: The curves are vertically shifted for a better visibility.

x	$F_{\alpha,x}$ (T)	$S_\alpha/S_{\mathrm{BZ}}(\%)$	$F_{\beta,x}$ (T)	S_α/S_{BZ} (%)
0.145	300 ± 5	1.19 ± 0.02	-	-
0.15	292 ± 2	1.17 ± 0.01	11250 ± 100	42.4 ± 0.4
0.16	290 ± 5	1.15 ± 0.02	11170 ± 100	42.1 ± 0.4
0.165	270 ± 5	1.05 ± 0.02	11100 ± 50	41.9 ± 0.2
0.17	250 ± 5	0.99 ± 0.02	10960 ± 50	41.3 ± 0.2

Table 5.1: Measured SdH frequencies. Indexes α and β denote the slow and fast oscillations, respectively. The corresponding FS areas are obtained by applying Eq. (2.24).

5.1.3 Origin of the coexistence of two frequencies in the SdH oscillation spectrum

A possible reason for the observation of both α- and β-frequencies on one and the same sample might be a coexistence of two phases, with different carrier concentrations, corresponding, respectively, to the reconstructed and unreconstructed FSs.

It should be noted that the samples were characterized carefully including x-ray and magnetization measurements, assuring a high crystal quality and doping homogeneity within $\pm 0.25\%$. Although the doping is non-stoichiometric, there were no indications of inhomogeneities that could be responsible for two strongly different SdH oscillations. However, the strongest argument against the phase coexistence scenario is provided by the observed doping dependence of the SdH frequencies. Assuming the samples had two phases and changing the cerium concentration would only change the volume fraction of each phase, keeping the composition unaffected, one would expect the amplitude of the oscillations to be affected by x but not the frequencies. However, this contradicts the observed doping-dependence of the oscillation frequencies, presented in Fig. 5.6.

The frequencies of both α- and β-oscillations are found to increase with growing x. Moreover, within the experimental error bars, the high frequency nicely coincides with estimations of the one expected for the large unreconstructed FS (black solid line in Fig. 5.6), assuming the obedience of Luttinger's theorem: As the electron-doping increases the volume enclosed by the hole-like FS grows proportionally to it. Thus, doping x electrons into the half-filled hole-like band results in a charge-carrier concentration of $(1-x)$ holes per unit cell. For example for $x = 0.17$ one would expect 0.83 holes per unit cell, corresponding to a large FS covering 41.5% of the 2D Brillouin zone $S_{\mathrm{BZ}} = (2\pi/a)^2$. Using Eq. (2.24) and the in-plane lattice parameter $a = 3.95$Å the expected frequency is calculated to

$$F_{0.17} = (\hbar/2\pi e) \times \frac{(1-0.17)}{2} S_{\mathrm{BZ}} = 0.415 \frac{h}{ea^2} = 11.00\,\mathrm{kT}.$$

This is very close to the measured frequency, $F_{\beta,0.17} = (10.96 \pm 0.050)\,\mathrm{kT}$.

This excellent agreement, i.e. that the carrier-concentration is exactly as expected, provides proof for the homogeneous doping at the desired level. Thus, there is no doubt on the crystal quality and the two-phases-scenario as an origin for the observed two frequencies can be ruled out. Both α-and β-oscillations are

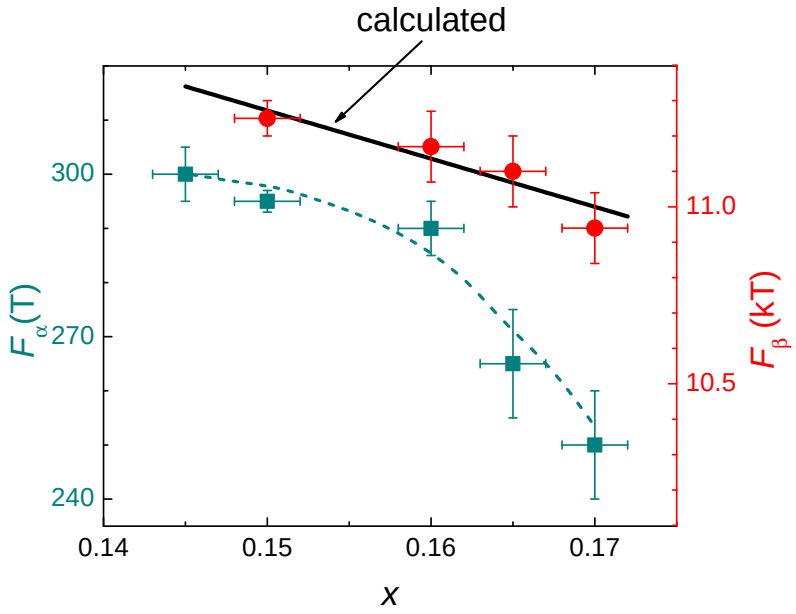

Figure 5.6: Dependence of the frequency F of the slow (squares, left-hand scale) and fast (circles, right-hand scale) SdH oscillations on the doping level x. The $F_\alpha(x)$ data points summarize results obtained on several $Nd_{2-x}Ce_xCuO_4$ single crystals of each doping level in pulsed and steady fields. The dashed line is a guide to the eye. The $F_\beta(x)$ data points have been obtained in pulse-field experiments at the Dresden and Toulouse high-field facilities. The solid black line shows the $F_\beta(x)$ dependence calculated from the nominal doping level according to the large unreconstructed Fermi surface predicted by band structure calculations [48].

intrinsic to each composition within the doping range $0.15 \leq x \leq 0.17$. Furthermore, it demonstrates the earlier stated equivalence between the concentration of electrons n and cerium x for of $Nd_{2-x}Ce_xCuO_4$ [98, 99].

A superlattice potential associated with antiferromagnetic ordering (AFM) has been proposed to be responsible for reconstructing the FS of NCCO into small hole-like and electron-like parts, as shown in Fig. 5.3 (b), giving rise to the low-frequency SdH oscillations [102]. If the gap between the FS pockets is small, it is possible, that at large enough fields the effect of magnetic breakdown occurs: Charge carriers in a magnetic field traverse the small parts of the reconstructed

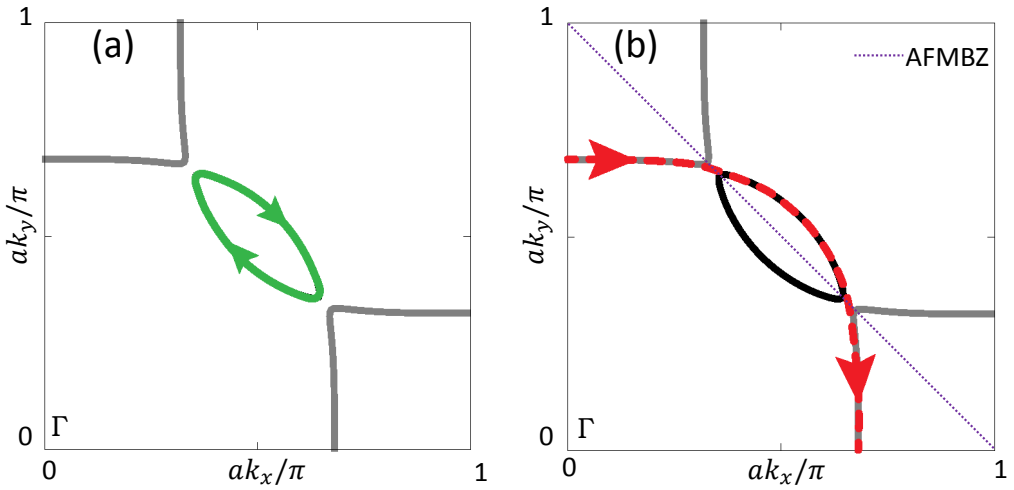

Figure 5.7: (left) No magnetic breakdown → charge carriers circulate along a small hole-like orbit. (right) Magnetic breakdown → charge carriers tunnel through the gap and traverse a large breakdown orbit.

FS, according to Fig. 5.7 (left). As the magnetic field exceeds a characteristic field they can tunnel through the gap and traverse a large cyclotron orbit, see Fig. 5.7 (right), resembling the unreconstructed hole-like FS. This can explain the emergence of the fast SdH oscillations at high fields.

Further, as the doping is increased, AFM weakens and the gap should shrink. Therefore, the amplitude of the breakdown oscillation should grow. Obviously, this is the case for the β-oscillations. The data presented here give a clear evidence for magnetic breakdown as the origin of the β-frequency, emerging even in the case of a reconstructed FS. The magnetic breakdown behavior will be analyzed in more detail in Sect. 5.1.6.

5.1.4 First estimations of the strength of the superlattice potential responsible for the FS reconstruction

Assuming a reconstructed FS due to antiferromagnetic ordering, as has been described in Sect. 1.3.3, one can get a rough idea about the magnitude of the energy gap by incorporating the experimentally determined FS areas into Eq. (1.3) as fitting parameters. In the following the α-oscillations are ascribed to the small hole-like FS pocket.

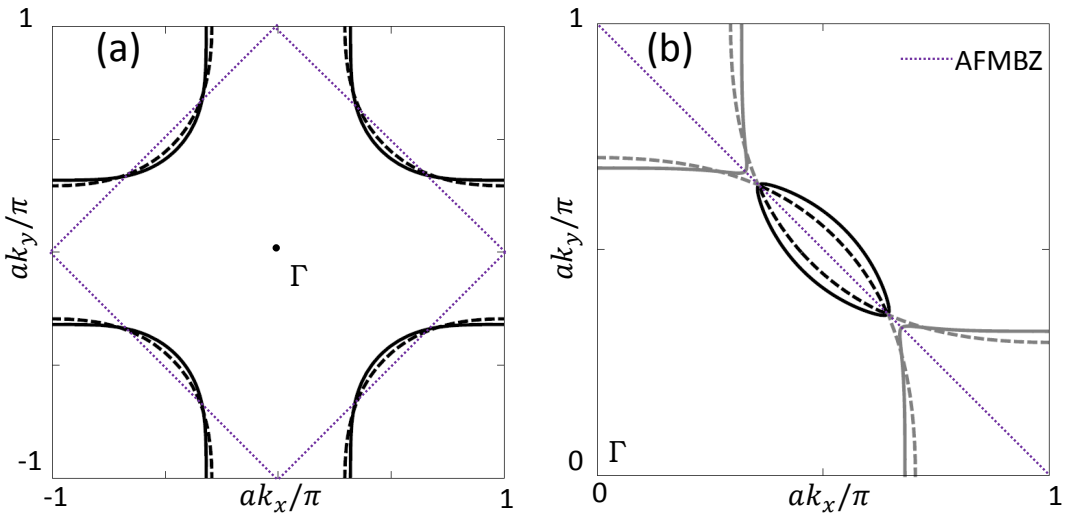

Figure 5.8: Two Fermi surfaces calculated, using Eqs. (1.2) and (1.3), with different sets of effective hopping energies: with $t = 0.38\,\text{meV}$, $t' = 0.32t$, $t'' = 0.16t$ [73] (solid lines) and $t = 0.326\,\text{meV}$, $t' = 0.25t$, $t'' = 0.1t$ [72] (dashed lines). (a) The unreconstructed FS, fitting to $41,5\,\%$ of the BZ area, according to what is expected for $x = 0.17$. (b) The reconstructed FS in the first quadrant of the BZ. Δ was chosen so that the area of the hole-pocket at $(\frac{\pi}{2a}, \frac{\pi}{2a})$ (black) is close to the one obtained from the measured frequency $F_{\alpha,0.17} = 250\,\text{T}$.

In Fig. 5.8 (a) one can see the unreconstructed FS, according to Eq. (1.2), evaluated for two sets of hoping energies (t, t', t''), which recently have been found sufficient, one for calculating the Hall effect by Lin & Millis [73] (solid line) and another one for fitting ARPES data by Kusko et al. [72] (dashed line) on $Nd_{2-x}Ce_xCuO_4$. Apparently, the latter depicts a more circular shape.

The reconstructed FS according to Eq. (1.3) for a $(\frac{\pi}{a}, \frac{\pi}{a})$-ordering is plotted in Fig. 5.8 (b). The gap was chosen so that the area of the hole-like pocket at $(\frac{\pi}{2a}, \frac{\pi}{2a})$ would be exactly equal to that obtained from the SdH data for $x = 0.17$, with $F_{\alpha,0.17} = (250\pm5)\,\text{T}$ corresponding to $(0.94\pm0.02)\%$ of the BZ area. For the data set according to Lin & Millis [73], see the solid line in Fig. 5.8, a gap value of $\Delta = (38\pm 10)\,\text{meV}$ is obtained. For the second set of hopping integrals suggested by Kusko et al. [72] it is impossible to obtain a FS pocket as large as the experimentally observed one for $x = 0.17$. Even if the gap is set to a vanishingly small value close to zero, the resulting area does not exceed 0.57% of the BZ. And hence, it

is not possible to estimate the gap, by using the second hopping-energy data-set. Apparently, the hopping parameters given in [73] are more realistic than those in [72].

As it was shown in the previous section (see Fig. 5.6) the frequency values exhibit a clear doping dependence, and thus a change in the size of the large as well as of the small FS. With the very same approach, as described in the paragraph above, for each doping, for which slow SdH oscillations were observed, the following gap values were calculated, see Table 5.2. These results only pro-

x	S_x (S_{BZ})	$F_{\alpha,x}$ (T)	Δ (meV)
0.17	41.5%	250 ± 5	38 ± 10
0.165	41.75%	275 ± 5	17 ± 10
0.16	42%	290 ± 5	17 ± 10
0.15	42.5%	292 ± 2	62 ± 10
0.145	42.75%	300 ± 5	...

Table 5.2: Gap values obtained from fits to Eq. (1.3), with $(t, t', t'') = (0.38, 0.32t, 0.5t')$ meV and α set according to the doping x, so that the area of the unreconstructed FS coincides with the one expected for the corresponding electron concentration.

vide a rough idea about the magnitude of the gap. As has been demonstrated by the comparison to the experimental data sets, already minor changes in the next-nearest hopping energies can have a relatively strong effect on the results for the small hole-like pocket. These estimations show that the gap with ≈ 20 meV is relatively small and will be discussed in terms of magnetic breakdown in Sect. 5.1.6.

Alternatively one could ascribe the observed α-oscillations to the electron-like part of the reconstructed FS centered at $(0, \frac{\pi}{a})$ and equivalent points. By assuming a much larger gap, such high that the small hole pocket would be suppressed completely, a small electron-like pocket could be obtained. The yielded value of the gap, $\Delta = 0.64$ eV, is comparable to the one measured for the undoped antiferromagnetic mother compound N_2CuO_4 [68]. Such a huge gap is rather unlikely for the overdoped regime of NCCO. Moreover, for such a scenario the corresponding carrier concentration would be ≈ 0.045 electrons per unit cell, which is inconsistent with the nominal doping range of $0.15 \leq x \leq 0.17$. Therefore, these points are in favor of the small hole pockets of the reconstructed FS being

the origin of the low frequency SdH oscillation F_α for even the strongest overdoping. In the following it will be demonstrated, how one can gain more exact information about the gap from a quantitative analysis of the SdH oscillations in terms of magnetic breakdown.

5.1.5 Effective masses

Following the standard Lifshitz-Kosevich (LK) formalism, important quantities can be extracted from the analysis of the SdH oscillation data. As presented in Sect. 2.3, the field and temperature dependence of the oscillation amplitude is expressed as:

$$A_{\mathrm{osc}} = \frac{\tilde{\sigma}}{\sigma_0} \propto R_{\mathrm{T}} R_{\mathrm{D}} R_{\mathrm{MB}},$$

where R_{T} and R_{D} are the temperature and Dingle reduction factors, respectively. R_{MB} describes the effect of damping due to magnetic breakdown. Using the LK expression for the temperature reduction factor R_{T}, see Eq. (2.36), the effective cyclotron mass $\mu = m_{\mathrm{c}}/m_e$, in units of the free electron mass m_{e}, can be estimated from the T-dependence of the oscillation amplitude, providing insights about the velocities of the charge carriers. In particular, for strongly correlated systems many-body interactions are reflected in the renormalization of the effective cyclotron masses in comparison to the theoretical band mass. Furthermore, the precise values of m_{c} for different doping levels are prerequisite for the analysis of the magnetic breakdown effect, that will be presented in Sect. 5.1.6.

One of the main difficulties of experiments in pulsed magnetic fields is the temperature stabilization during the pulses. Great care has to be taken to avoid pulse-induced overheating, as has been described in the experimental Sect. 4. Experiments in steady fields usually provide a smaller noise level and stable temperature conditions. One can see from Fig. 5.4 (a) that the field dependence of the slow α-oscillations is not very steep: they can still be resolved well at $B = 25$–$30\,\mathrm{T}$. Therefore, SdH experiments in steady fields up to $35\,\mathrm{T}$ in Grenoble (France) and $45\,\mathrm{T}$ in Tallahassee (USA) were carried out.

In Fig. 5.9 SdH oscillations for five doping levels recorded at steady fields with a rather low transport current of $I = 0.4$–$0.5\,\mathrm{mA}$ are presented. This current was proved to cause no significant overheating effect ($\Delta T|_{B=1\,\mathrm{T}} < 0.1\,\mathrm{K}$). The oscillation frequencies perfectly coincide with the pulsed field data. For $x = 0.17$, the

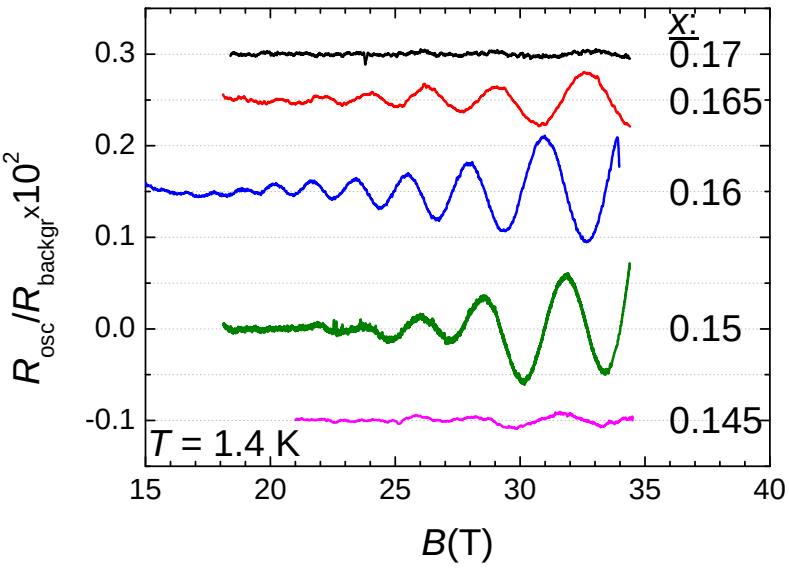

Figure 5.9: Background-normalized oscillatory component of the interlayer magnetoresistance measured in quasi-steady fields of $B \leq 35\,\mathrm{T}$ recorded at $T = 1.4\,\mathrm{K}$ for various doping levels of NCCO. The curves are vertically shifted for better visibility.

oscillation amplitude $A_{\alpha,0.17}|_{40\,\mathrm{T}} = 0.8 \times 10^{-4}$ at around $35\,\mathrm{T}$ is close to the noise level already for the lowest temperature. As the temperature is increased the amplitude decreases further, and thus a reasonable analysis of its T-dependence was not possible. However, for $x = 0.15$, 0.16, 0.165 the α-oscillations, with amplitudes large enough for a quantitative analysis, were observed down to $\sim 20\,\mathrm{T}$. Remarkably, for $x = 0.16$ maximums down to even $\sim$ 16–17 T were discernible, which is a field range accessible by the use of commercially available superconducting magnet systems.

Fig. 5.10 presents a comparison of fast SdH oscillations observed for $x = 0.17$ in (a) steady and (b) pulsed fields. It was possible to resolve the β-oscillations down to below $43\,\mathrm{T}$ in steady fields at the NHMFL in Tallahassee (USA). Curves with less than 0.5×10^{-4} relative noise, with respect to the sample signal, were recorded at different temperatures. These are to be compared with the data obtained in pulsed magnetic fields up to $64\,\mathrm{T}$ at the HLD Dresden-Rossendorf. In Fig. 5.10 (c) and (d) the Fast-Fourier-transformation amplitude divided by the temperature T is fitted to the standard LK formula, Eq. (2.34). From both sets of data the same value of $\mu_{0.17} = 2.3 \pm 0.05$ for the free cyclotron mass was obtained. This demon-

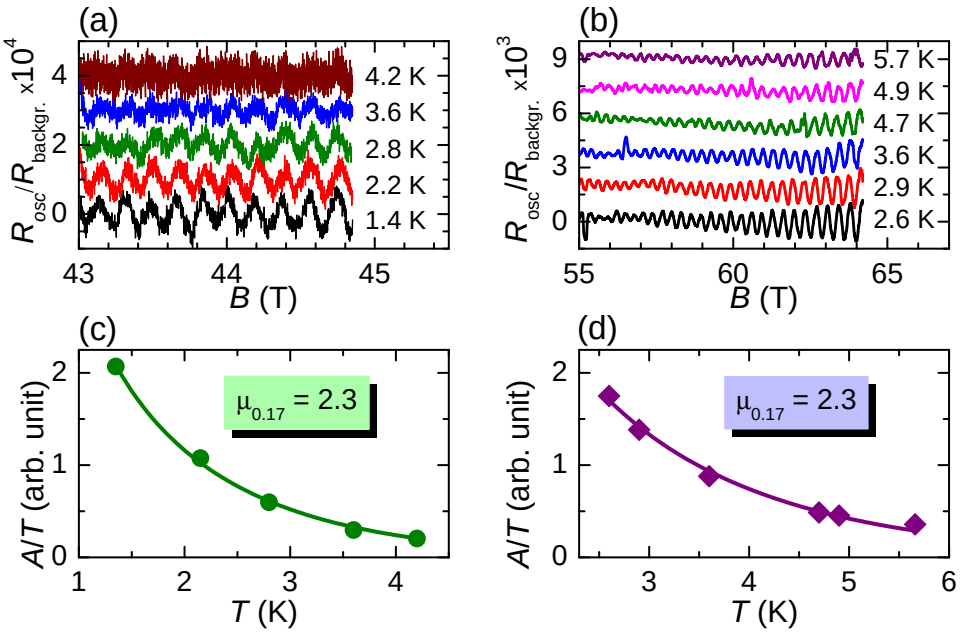

Figure 5.10: Comparison of the background-normalized fast oscillatory component of the interlayer magnetoresistance at different temperatures T for $x = 0.17$ measured in steady fields (a) in Tallahassee ($B \leq 45\,\mathrm{T}$) and in pulsed fields (b) in Dresden ($B \leq 64\,\mathrm{T}$). The curves are vertically shifted for better visibility. In the lower panels the height of the peak, A, in the Fast-Fourier-transformation amplitude spectrum is plotted vs. T for the steady (c) and pulsed (d) field data. The solid lines are fits to $A/T \propto \frac{1}{\sinh(K\mu T/B)}$ (see chapter I, Sect. 2.3) yielding $\mu = 2.3$.

strates the high precision achieved in pulsed fields, where noise and overheating effects are a much bigger issue as compared to experiments in steady fields. To resolve fast SdH oscillations in NCCO for $x < 0.17$, pulsed fields are inevitable, since they start being visible at above $50\,\mathrm{T}$, see Fig. 5.5. Furthermore, effective cyclotron masses related to the β-oscillations were obtained for $x = 0.165$, 0.16 and 0.15, presented later on in Fig. 5.12. Their values are by a factor of $1.5 - 2$ larger than the ones related to the α-oscillations.

Fig. 5.11 exhibits fits to the temperature dependence of the amplitudes of the slow SdH oscillations for slight overdoping, $x = 0.16$, obtained in steady fields of up to $35\,\mathrm{T}$ and in pulsed fields of up to $64\,\mathrm{T}$. With $\mu_{0.16} = 0.92 \pm 0.05$ it is found more than two-times smaller as compared to the β-cyclotron mass (green

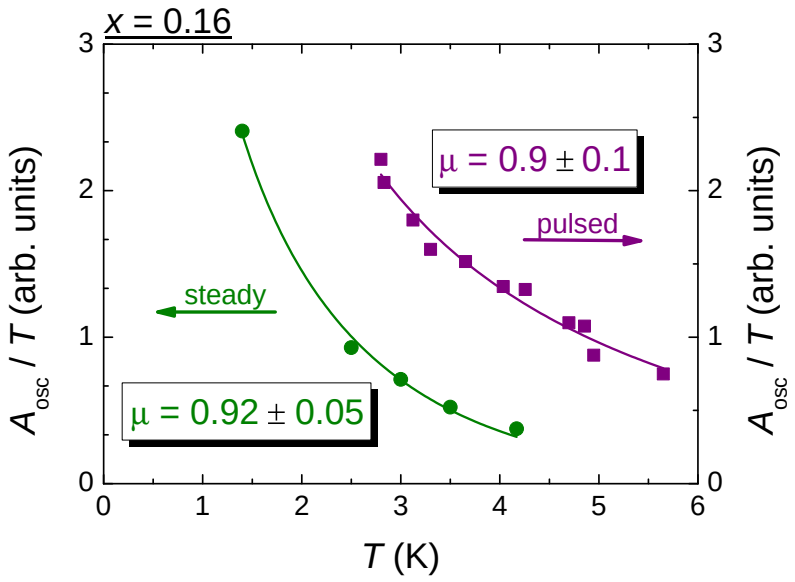

Figure 5.11: The effective cyclotron mass corresponding to the low frequency α-oscillations for $x = 0.16$ obtained from recording the temperature dependence of the amplitude in steady (green) and pulsed (purple) magnetic fields of up to $B = 35$ and $64\,\mathrm{T}$, respectively.

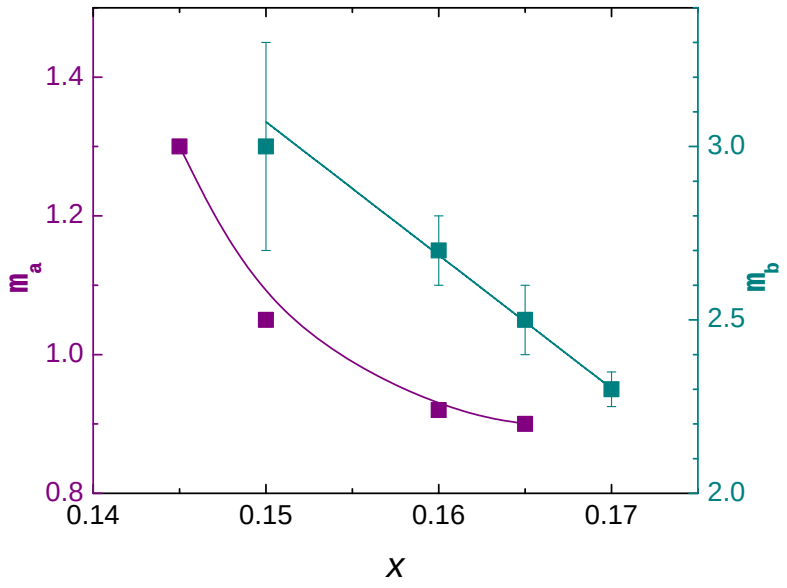

Figure 5.12: Effective cyclotron mass values obtained from the temperature dependence of the SdH oscillations recorded in pulsed and steady magnetic fields. Note: α and β denote the slow and fast SdH oscillation, respectively. Lines are guides to the eyes.

circles). This value was nicely reproduced in a pulsed field experiment, where due to pulse-induced overheating effects[1] the lowest temperature was slightly higher (purple squares). The masses obtained from combined experiments in steady and pulsed experiments are comprised in Fig. 5.12.

For $x = 0.17$ the α-oscillation amplitude was too low with respect to the noise level. In addition, it seems to show the weakest T-dependence and therefore no satisfactory estimation of $\mu_{0.17}$ have been obtained up to present. For strong overdoping $\mu(x)$ seems to flatten (see solid purple line in Fig. 5.12) and extrapolates to $\mu_{0.17} \approx 0.85$, which will be used further on in the simulations for the magnetic breakdown analysis.

5.1.6 Magnetic breakdown

Above, SdH data for various doping levels, $0.15 \leq x \leq 0.17$ were presented, showing low frequency oscillations (related to a small FS) superimposed with a high frequency (related to a large FS). The emergence of the second cyclotron orbit at higher fields can be easily explained by magnetic breakdown between the hole- and electron-like parts of the reconstructed FS. The two cyclotron orbits were sketched in Fig. 5.7.

The criterion for magnetic breakdown (MB) to occur was given by Blount [115], see Eq. (2.44). In Sect. 5.1.4, gap values of $\Delta \approx 20$–$60\,\mathrm{meV}$ were obtained from fitting the suggested model for the reconstructed FS according to the electron concentration and the measured SdH frequencies (see Table 5.2). Now, after the effective cyclotron masses are known from the previous analysis, a characteristic MB field B_{MB} can be estimated using Eq. (2.44) and $\omega_{\mathrm{c}} = eB_{\mathrm{MB}}/m_{\mathrm{c},\beta}$. $m_{\mathrm{c},\beta} = \mu_\beta m_{\mathrm{e}}$ is the cyclotron mass obtained from the T-dependence of the fast β-oscillations. Hence,

$$B_{\mathrm{MB}} = \frac{\Delta^2 m_{c,\beta}}{E_F \hbar e}. \tag{5.1}$$

The results for each doping level at which the effective cyclotron mass of the fast SdH oscillations was determined are exhibited in Table 5.3.

In Sect. 1.3.3 it was shown that the values for the energy gap strongly depends on the shape of the in-plane FS. Since SdH data only provide information about

[1] Overheating was taken into account by using the superconducting transition in the MR as a reference, see Sect. 3.3.2.

x	0.17	0.165	0.16	0.15
B_{MB} (T)	58	12	14	200

Table 5.3: Magnetic breakdown fields B_{MB} evaluated using Eq. (5.1) in combination with the effective cyclotron mass values μ_β, obtained from T-dependence of fast SdH oscillations, and the gap values given in Table 5.2.

the area of the cyclotron orbit these values are rather rough estimates and so are the obtained breakdown fields in Table 5.3, too. In the case of $x = 0.17$ MB oscillations have been observed already at fields of less than $43\,\mathrm{T}$, which is even smaller than the estimated value of $B_{\mathrm{MB}} \approx 58\,\mathrm{T}$. Nevertheless, the estimations show that MB can indeed be expected for NCCO within the experimentally available magnetic field range.

5.1.7 2D or 3D?

In the next section analyses on SdH oscillations in terms of magnetic breakdown will be shown, where the standard LK formalism, Eq. (2.34), is applied. NCCO is a highly anisotropic system . The a ratio between the inter- and intralayer resistivities is $\rho_\perp/\rho_{||} \approx 10^3$. Therefore, it is not immediately obvious why the transport is assumed to be more 3D than 2D. A criterion for the dimensionality is provided by the comparison of the Landau level (LL) spacing with the interlayer corrugation strength, i.e. the ratio $4t_\perp/\hbar\omega_{\mathrm{c}}$. Taking $2t_\perp/\epsilon_{\mathrm{F}} \approx \sqrt{\rho_\perp/\rho_{||}} \approx 1/\sqrt{1000}$, with $\epsilon_{\mathrm{F}} = 0.5\,\mathrm{eV}$ [133], the effective interlayer transfer energy can be estimated as $t_\perp \approx 17\,\mathrm{meV}$. One can evaluate the magnitude of the LL spacing for the large magnetic breakdown orbit at a typical field of $B = 50\,\mathrm{T}$:

$$\hbar\omega_{\mathrm{c}} = \frac{\hbar eB}{m_{\mathrm{c}}} = \frac{1.055e^{-34}\,\mathrm{Js}\cdot 50\,\mathrm{T}}{2.3\cdot 9.11e^{-31}\mathrm{kg}}e = 2.5\,\mathrm{meV},$$

using the effective cyclotron mass $\mu_{\beta,0.17} = 2.3$, obtained from the T-dependence of the β-oscillations (Sect. 5.1.5). For the small FS pockets the LL spacing would be bigger, simply because μ_α is smaller. Obviously is for both, the large and for the small orbits,

$$\hbar\omega_{\mathrm{c}} < 4t_\perp.$$

Thus, the application of the standard 3D-Lifshitz-Kosevich (LK) theory is appropriate for the analysis of SdH oscillations in NCCO.

By contrast to hole-underdoped $YBa_2Cu_3O_{6.5\pm\delta}$, for which several low SdH frequencies have been reported [134–137], only a single frequency is observed for NCCO. Moreover, neither slow nor fast SdH oscillations show beating [2], which could give insights in the interlayer corrugation of the FS cylinder. Fig. 5.13 shows pulsed field data for a strongly overdoped, $x = 0.17$, composition recorded in two different pulsed magnets. The fast β-oscillations are discernible over a broad field range of 50–$70\ \mathrm{T}$ and 60–$86\,\mathrm{T}$, respectively. The absence of beats, i.e. nodes in the oscillations, implies a distance between the Landau levels, $\hbar\omega_c$, larger than the interlayer dispersion (see Sect. 2.3). At first glance, this would mean, that the electronic transport had a strongly two-dimensional (2D) character. However, a quantitative analysis of the semiclassical AMRO effect (presented later on in Sect. 6) reveals a complex FS corrugation in the interlayer direction, that provides a plausible explanation for the absence of beats in the β-oscillations even in the 3D case.

The α-oscillations have a rather low frequency. Consequently, only few oscillation maximums are observable, too few to resolve any beats in the accessible field range.

5.1.8 Doping dependence of the magnetic-breakdown field from SdH data analysis

The observed SdH oscillations in the magnetic-breakdown (MB) regime can be described by the standard LK theory modified by the MB factor R_{MB} [35], see Sect. 2.4.3. The effect of MB on the amplitude of SdH oscillations is given by the field-dependent damping factor Eq. (2.45). Hence, fitting the field dependence of the oscillations can be a tool for extracting values of the characteristic MB field B_{MB}. The α-orbit on the small hole-like pocket of the $(\frac{\pi}{a}, \frac{\pi}{a})$-reconstructed FS involves no tunneling events, $n_1 = 0$, and two Bragg reflections, $n_2 = 2$. Therefore,

[2] Beats, i.e. nodes in the field dependence of the amplitude, arise from the interference of two oscillations that are close in frequency to each other [35, 36]. For example a conventional cosine shaped interlayer warping could result in two extremal, maximum and minimum FS areas that might induce beats in MQO.

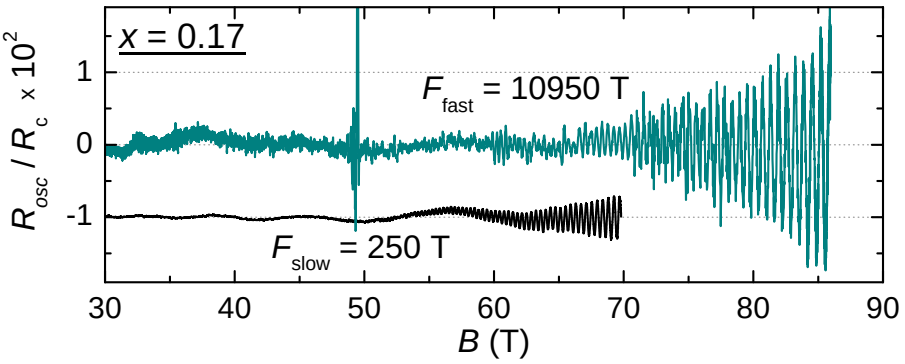

Figure 5.13: SdH oscillations obtained from pulsed field data after background normalization for $x = 0.17$ recorded during a $70\,\mathrm{T}$ (black) and $87\,\mathrm{T}$ pulses.

the corresponding MB factor is:

$$R_{\mathrm{MB},\alpha} = 1 - \exp\left(-B_{\mathrm{MB}}/B\right) \tag{5.2}$$

For β-oscillations related to the large MB orbit with $n_1 = 8$ and $n_2 = 0$

$$R_{\mathrm{MB},\beta} = \exp\left(-4B_{\mathrm{MB}}/B\right), \tag{5.3}$$

because of eight gaps along the MB trajectory, i.e. per single closed orbit, see Fig. 5.3.

The combination of the two kinds of cyclotron orbits, that is the small hole-like FS pocket and the large MB orbit, is reflected in a superposition of two SdH oscillations in the conductivity, with α representing the small hole-like FS and β the large MB orbit. In the following the oscillatory part of the conductivity described by the LK formalism including MB is denoted as

$$L_{\alpha(\beta)}(B) \equiv \frac{\tilde{\sigma}_{\alpha(\beta)}(B)}{\sigma_{\alpha(\beta),0}(B)}. \tag{5.4}$$

To analyze this superposition one has to estimate, first, the contributions from these orbits to the total interlayer conductivity σ_{zz}. These contributions depend on details of the FS warping, in other words on the effective interlayer transfer integral $t_\perp(\mathbf{k}_{||})$, which, in general, depends on the in-plane wave vector $\mathbf{k}_{||}$. $\sigma_{ii}(B)$ is determined by the i-th velocity component, see Sect. 2.2. For the α-orbit $\bar{v_z}$ saturates at high fields to a finite value which is determined by the position k_z^0

of the given orbit along k_z [120, 138]. Thus, $\sigma_{zz,\alpha}(B)$ decreases only slightly and saturates at high B, which is a usual behavior of the conductivity for field aligned parallel to the current [36]. Thus, for the following analysis one can assume

$$\sigma_{zz,\alpha}(B) \approx \sigma_{zz,\alpha}(B = 0).$$

The non-saturating strong field dependence of the experimentally observed magnetoresistivity that increases almost proportional to B^2, is a rather unusual behavior. Its origin lies in the complex φ-dependent warping characteristic of the large FS associated with MB cyclotron orbit, as shown in Fig. 2.5. As the magnetic field increases further above the MB field, the main contribution to the B-dependence of the background conductivity originates from the large MB orbit, that is $\sigma_0(B) = \sigma_\beta(B)$ at high fields. While the β-oscillations are contributed by all the charge carriers on the large FS, only the small hole-pockets contribute to the α-oscillations. This reduced contribution has to be taken into account, when it comes to the simulations of the superposition.

For weak warping one can assume

$$\rho_{zz}(B) \approx 1/\sigma_{zz}(B),$$

to a high accuracy. The measured relative oscillation amplitudes of less than 1% (compare for example with Fig. 5.5) are much smaller than the overall resistivity. In this case one can show that

$$\Delta\tilde{\sigma}/\sigma \approx -\Delta\tilde{\rho}/\rho.$$

Using the expression of Eq. (5.4), the oscillatory component of the measured conductivity, describable by the standard LK theory, is composed as follows:

$$\frac{\Delta\tilde{R}}{R_0(B)} = -\frac{\Delta\tilde{\sigma}}{\sigma_0(B)} = -L_\alpha(B) \cdot \frac{R_0(0)}{R_0(B)K_\alpha} - L_\beta(B), \tag{5.5}$$

where $K_\alpha = \sigma_\alpha(0)/\sigma_\beta(0)$ is the relative contribution of the carriers on the small hole-like pocket of the reconstructed FS to the zero-field conductivity. Above $\approx 25 - 30\,\mathrm{T}$, $R_0(B)$ can be fitted sufficiently well by an $O(2)$ polynomial, $R_0(B) = R_0(0) + R_1 B + R_2 B^2$.

In order to simulate the as-measured SdH oscillations the LK formula for the SdH effect, is applied, adjusted by a correction term $c_\alpha = \frac{\rho_{\beta,0}/K_\alpha}{R_0(B)}$ and $c_\beta = 1$ due

to different conductivity contributions of small and large orbits:

$$\frac{\Delta\tilde{R}}{R_0(B)} = B^{1/2}A \cdot \sum_{i=\alpha,\beta} m_{c,i} R_{\mathrm{T},i} R_{\mathrm{D},i} R_{\mathrm{S},i} R_{\mathrm{MB},i} \cos\left(2\pi\frac{F_i}{B} + \gamma_i\right) \cdot c_i, \tag{5.6}$$

where $m_{c,i}$ is the cyclotron mass, F_i the frequency and γ_i the phase of each oscillation; A is a constant scaling factor; $R_{\mathrm{T},i}$, $R_{\mathrm{D},i}$, $R_{\mathrm{S},i}$,$R_{\mathrm{MB},i}$ are the corresponding reduction factors, see Sect. 2.3. Having the field oriented perpendicular to the conducting layers yields $R_{S,i} \approx const.$ and is assumed to be the same for both the α- and the β-orbit. To finally simulate the observed SdH oscillations, the corresponding effective cyclotron mass values are extracted from the T-dependence (see Fig. 5.12), the Dingle temperatures from the field dependence of the slow α-oscillation (described in the next Sect. 5.1.9) and combined into the following relation:

$$\begin{aligned}\frac{\Delta\tilde{R}}{R_0(B)} = \; & B^{1/2}A\Bigg(m_{c,\alpha} R_{\mathrm{T},\alpha} R_{\mathrm{D},\alpha} R_{\mathrm{MB},\alpha} \cos\left(2\pi\tfrac{F_\alpha}{B} + \gamma_\alpha\right) \cdot \tfrac{\rho_{\beta,0}/K_\alpha}{\rho_{\beta,0}+\rho_1 B+\rho_2 B^2} + \\ & + m_{c,\beta} R_{\mathrm{T},\beta} R_{\mathrm{D},\beta} R_{\mathrm{MB},\beta} \cos\left(2\pi\tfrac{F_\beta}{B} + \gamma_\beta\right)\Bigg)\end{aligned} \tag{5.7}$$

The numerous parameters can be determined independently before using Eq. (5.7) for evaluating the MB field B_{MB}. Only the amplitude factor A and B_{MB} are left as free fitting parameters.

5.1.9 Determination of the necessary parameters for simulating the SdH oscillations in NCCO

In order to extract B_{MB} from the SdH oscillations, it is important to find precise values of the effective cyclotron masses and Dingle temperatures for each doping. As it is described in Sect. 5.1.5, the effective cyclotron masses μ_i are extracted from the temperature dependence of the SdH oscillation amplitude. Mathematically, the MB damping factor for the large β-orbit, Eq. (5.2),

$$R_{MB,\beta} \propto \exp\left(-const./B\right) \tag{5.8}$$

has the same field dependence as the Dingle damping factor, Eq. (2.38),

$$R_D \propto \exp\left(-const./B\right). \tag{5.9}$$

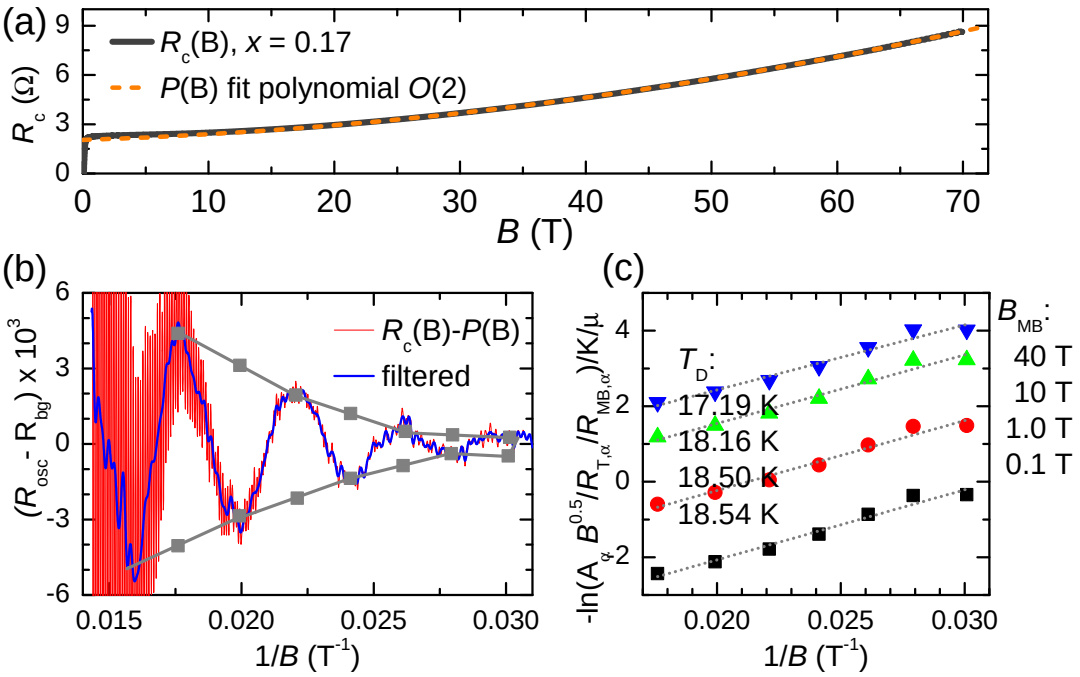

Figure 5.14: (a) Field dependence of the interlayer MR for $x = 0.17$ (grey). The red dashed line is a fit of the non-oscillating background MR to an $O(2)$ polynomial. (b) Slow SdH oscillations for $x = 0.17$ after subtracting the non-oscillating background (red) and filtering out the F_α (blue). (c) Corresponding Dingle plots [35] for different fixed breakdown fields ranging from $0.1\,\mathrm{T}$ to $40\,\mathrm{T}$.

However, the damping of the α-oscillation due to magnetic breakdown, Eq. (5.3),

$$R_{MB,\alpha} \propto 1 - \exp\left(-const./B\right) \tag{5.10}$$

is opposite to R_D. Hence, it should be possible to estimate the Dingle temperature for each doping applying usual Dingle plots [35] to the slow α-oscillation with a fixed MB field. That is, the field dependent total amplitude of the background-subtracted slow SdH oscillation A_α is fitted to

$$T_D \cong -\frac{1}{K\mu_\alpha} \ln\left(\frac{A_\alpha B^{1/2}}{R_{T,\alpha}R_{MB,\alpha}}\right) \cdot \frac{1}{B}, \tag{5.11}$$

with $K = 2\pi^2 k_\mathrm{B} m_\mathrm{e}/\hbar e \approx 14.69\,\mathrm{T/K}$. This is basically Eq. (2.34) solved for T_D.

As an example, Fig. 5.14 demonstrates the results for a strongly overdoped, $x = 0.17$, sample. The magnetic breakdown factor $R_{\mathrm{MB},\alpha}$ is included with different

fixed breakdown fields B_{MB}. First, the raw field sweep is fitted to the polynomial $R(B) = R_0 + R_1\,B + R_2\,B^2$ for $30 \leq B \leq 70\,\mathrm{T}$, see Fig. 5.14 (a). Then A_α, i.e. the grey-colored "peak-to-peak" envelope in Fig. 5.14 (b), is extracted. In step three A_α is plotted in the Dingle-plot coordinates, as shown in Fig. 5.14 (c), and T_{D} is determined from the slope of the obtained linear fits. Fig. 5.14 (c) shows several Dingle plots distinguished by different MB fields assumed.

Steady field experiments for this doping revealed fast oscillations already at fields below $43\,\mathrm{T}$. Thus the MB field is expected to be much smaller than $40\,\mathrm{T}$ which is used as an upper limit for the fits. One can see that the obtained Dingle temperature is largely insensitive to the exact value of B_{MB}. The yielded Dingle temperature is $T_{\mathrm{D},0.17} = 18 \pm 0.5\,\mathrm{K}$. For the lower doping levels $x = 0.165$, 0.16, and 0.15 values of $T_{\mathrm{D}} = 17$, 14 and $14\,\mathrm{K}$, respectively, were obtained, which varied slightly from sample to sample due to differences in the sample quality. For further use it is assumed that T_{D} is the same for both α- and β-orbits.

Another parameter in Eq. (5.7) is K_α, the relative contribution of the small hole-like pockets to the total conductivity at zero-field. The interlayer component σ_{zz} of the conductivity tensor can be evaluated using the Boltzmann transport equation in the presence of an electric field. With the generally accepted in-plane dispersion Eq. (1.2) plus a cosine-shaped interplane dispersion Eq. (2.57) and assuming the $(\frac{\pi}{a}, \frac{\pi}{a})$-reconstructed FS topology, Fig. 5.3 (b), with 4 hole-like pockets in the first Brillouin zone, the ratio of the contributions of the large and the small FSs is

$$K_\alpha = \sigma_{zz,\alpha}(0)/\sigma_{zz,\beta}(0) = 0.39.$$

The corresponding calculations can be found in Appendix A. Due to the additional $a_m \sin(m\varphi)$-terms Eq. (2.56), reflecting the specific crystal symmetry of the tetragonal crystal lattice in NCCO, K_α has to be adjusted according to the complex φ-dependent warping, which has a considerable effect on the interlayer conductivity of the large β-orbit. For the simplest case:

$$\epsilon_\perp = t_\perp \cos(k_z d) \cdot \sin(2\varphi),$$

a ratio of $K_\alpha = 0.68$ was obtained. Additional warping-terms with a_6 and a_{10} lead to a decrease of K_α towards 0.39, the value that corresponds to the φ-independent form, see Appendix A. K_α is unimportant for the determination of μ and T_{D}. It only has an effect on the SdH oscillation amplitudes, and thus the error ΔK_α is

x (%)	μ_α	F_α (T)	γ_α	μ_β	F_β (kT)	γ_β	T_D (K)	R_0 (Ω)	R_1 (Ω/T)	R_2 (Ω/T^2)
17	0.85	246	-0.6	2.3	10.94	0.1	18	2.045	0.0244	0.001
16.5	0.9	275	+0.4	2.5	11.07	0	17	2.05	0.025	0.001
16	0.92	290	-0.64	2.7	11.17	-1	14	2.78	0.0093	0.001
15	1.05	292	+0.3	3.0	11.22	1	14	158	-0.65	0.035

Table 5.4: Independently determined fixed parameters used for the simulations presented in Fig. 5.15.

x (%)	0.17	0.165	0.16	0.15
A	0.53	0.69	0.16	0.18
B_MB (T)	0.5 ± 0.3	1.5 ± 0.5	3.0 ± 0.5	12 ± 5

Table 5.5: MB field values, obtained from simulating the superposition of the α- and β-oscillations. The amplitude prefactor A was the second free parameter. The independently determined, fixed parameters used in the fits can be found in Table 5.4.

considered in the error bars of the obtained MB fields. Consequently, only the overall amplitude A and the breakdown field B_MB are left unknown and can be obtained from simple least-squares fits to Eq. (5.7).

Fig. 5.15 exhibits SdH oscillations normalized to the background magnetoresistance and the corresponding simulations (orange curves) according to Eq. (5.7). The corresponding parameters and results can be found in Tables 5.4 and 5.5.

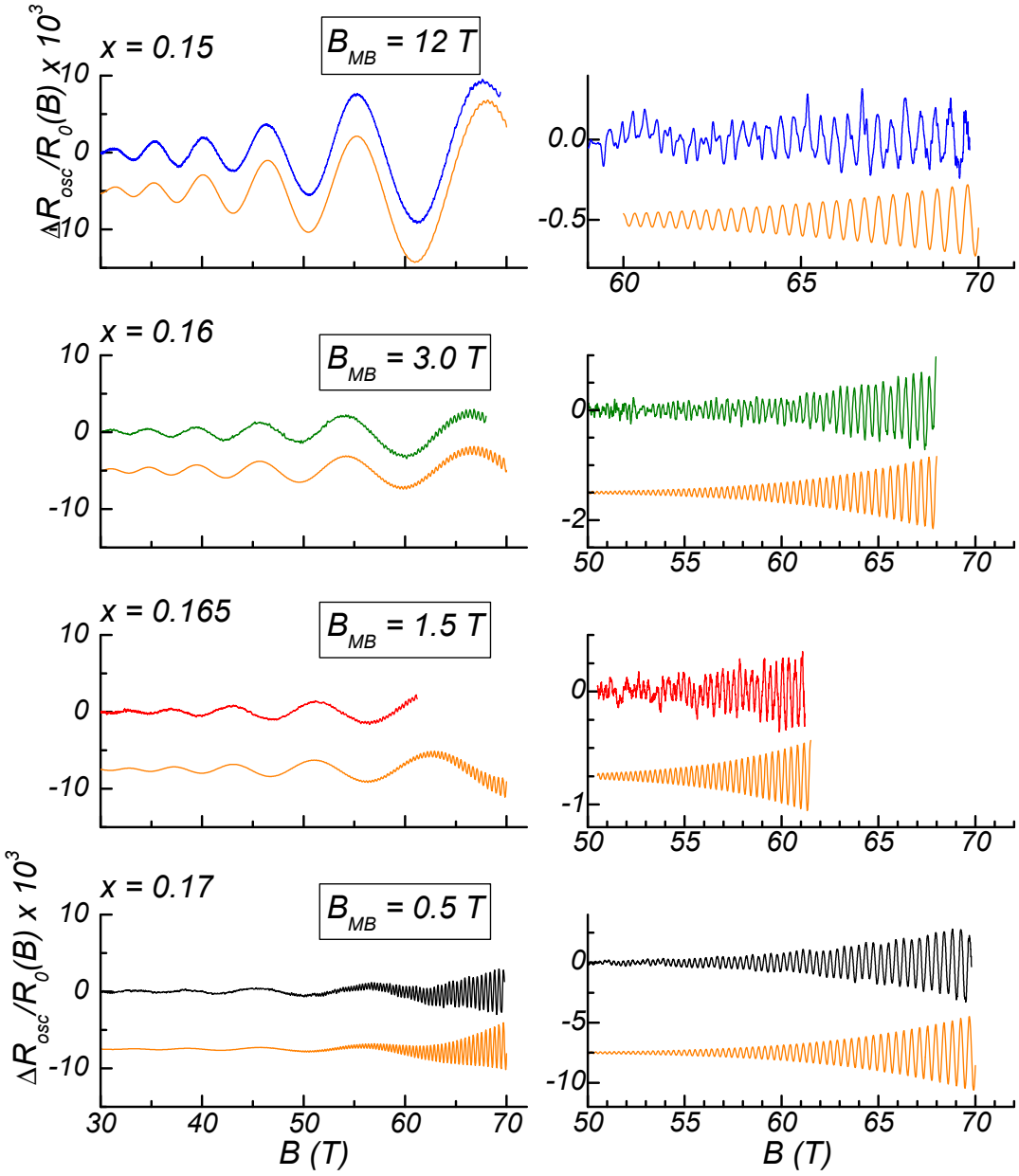

Figure 5.15: (left column) Slow α- and fast β-SdH oscillations for different x normalized to the background magnetoresistance $R_0(B)$, recorded in pulsed fields at $T = 2.5\,\mathrm{K}$ ($2.8\,\mathrm{K}$ for $x = 0.165$). The orange curves are simulations according to Eq. (5.7). The corresponding parameters can be found in Tables 5.4 and 5.5. (right column) Filtered fast β-oscillations at high fields and corresponding simulations (orange curves).

5.1.10 Conclusion: The MB gap closes right at the upper edge of the superconducting dome

The data on the slow α-SdH oscillations, presented in the previous sections, indicated that the FS stays reconstructed even in the overdoped range all the way up to the highest doping level available for bulk NCCO crystals. Magnetic breakdown (MB) was identified as the origin for the emergence of fast β-oscillations on top of the slow ones at high fields. Therefore, the presence of a quantum critical point, related to a sudden FS transformation, within the still superconducting doping range of $0.15 \leq x \leq 0.17$ can be ruled out for NCCO.

In the last paragraphs it was demonstrated how the characteristic MB fields were estimated from fitting the experimental SdH oscillation data for overdoped NCCO. Based on the obtained values the MB gap is evaluated for each doping using the Blount criterion, Eq. (5.1). Fig. 5.16 shows the doping dependence of the gap, $\Delta(x)$ in comparison to the one of the superconducting critical temperature $T_c(x)$ up to the highest available doping $x = 0.17$. The dotted grey line is a

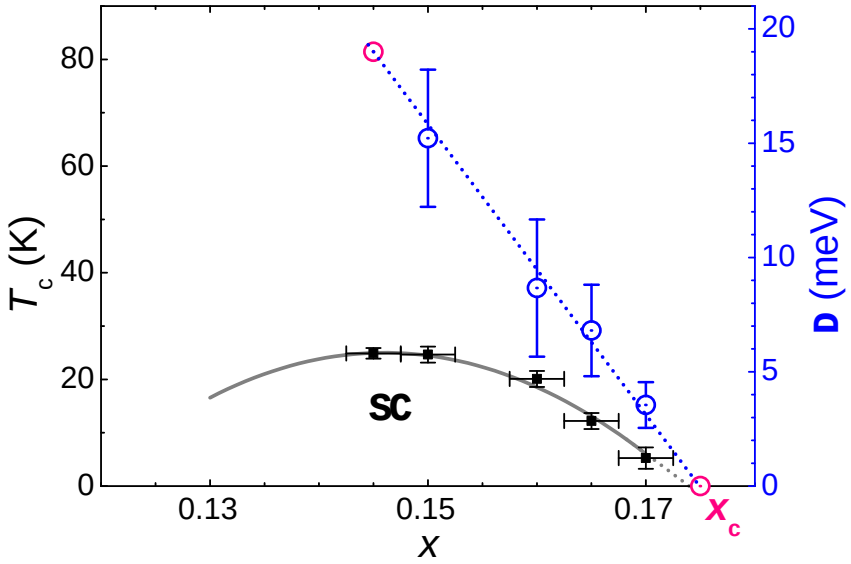

Figure 5.16: MB gap (blue circles), obtained from SdH oscillations, and superconducting critical temperature T_c (black squares) plotted versus the doping x. Zero field T_c was taken from the $\chi'(T)$ curves on the same samples, see Fig. 3.6. Note: The red circles highlight the extrapolation to lower and higher doping levels.

guide to the eye. Apparently the energy gap, which separates the electron-like from the hole-like parts of the reconstructed FS, and thus is representative of the strength of the relevant superlattice potential, weakens approximately linearly towards strong overdoping. Most interestingly, it seems to vanish right at the edge of the superconducting dome, at approximately $x_c = 0.175$. This suggests that SC only appears together with a superlattice potential, which in NCCO most likely is related to antiferromagnetism. However, neutron scattering experiments performed at zero field have not detected any signature of long-range AFM for overdoped samples with $x \geq 0.15$ [37, 75]. A fluctuating regime was suggested, where the ordering responsible for the observed FS reconstruction might well be slowly fluctuating. These fluctuations should at least be stable within the time a charge carrier needs for traversing one full cyclotron orbit to enable the detection of the SdH effect in NCCO. From the cyclotron frequency ω_c one can estimate the time for one oscillation. In the case of $x = 0.16$ where the α-oscillations are observable already around $B = 20\,\mathrm{T}$:

$$t = \frac{2\pi}{\omega_\mathrm{c}} \approx \frac{2\pi e B}{\mu_{\alpha,0.16} m_e} \approx (1.6) \times 10^{-12}\,\mathrm{s}, \tag{5.12}$$

with $\mu_{\alpha,0.16} = 0.92$. Thus, a possible fluctuating ground state should be stable at least for more than $1.6\,\mathrm{ps}$. Above's results were obtained from studies in strong magnetic fields. Hence, AFM induced by magnetic field, as was suggested from results of neutron scattering experiments performed in magnetic fields [139] is a likely scenario. Further, as was noted in the introduction, Sect. 1.1, the presence of a reconstructed FS does not rule out other possible orderings. Another proposed candidate for the $(\frac{\pi}{a}, \frac{\pi}{a})$-ordering is a d-spin-density-wave, also known as hidden order, associated with orbital AFM [81, 140]. But to date there is no profound experimental proof of its existence in cuprates. A charge modulation with the characteristic $(\frac{\pi}{a}, \frac{\pi}{a})$-wave vector would be also a candidate, but the results presented in the following provide clear evidences for the magnetic nature of the ground state in NCCO, see Sect. 5.2.

A further proof of the suggested $(\frac{\pi}{a}, \frac{\pi}{a})$ FS reconstruction would be obtained by the observation of a SdH oscillation associated to the electron-like FS parts. So far no frequency which could be attributed to the electron pockets has been resolved. Charge carriers traversing such a pocket would pass 4 Bragg-reflection points per single circulation, see e.g. Fig. 5.3 (b). Therefore, the damping due to MB, that

is the reduction factor $R_{\mathrm{MB,e^-}}$, is expected much stronger than for the hole-like α-pocket. Namely, according to Eq. (2.45) it is calculated as

$$R_{\mathrm{MB},e^-} = \left[1 - \exp\left(\frac{-B_{\mathrm{MB}}}{B}\right)\right]^2 . \tag{5.13}$$

For $x = 0.15$ with $B_{\mathrm{MB}} \approx 12\,\mathrm{T}$ the damping at a typical field of $50\,\mathrm{T}$ due to MB is 5 times stronger for contributions from the electron-like than from the hole-like cyclotron orbits. Therefore, MB can be one of the reasons for the absence of signatures of the electron-like pockets in the SdH oscillation spectra. A stronger suppression of these contributions to the SdH signal is also possible due to an enhanced effective cyclotron mass and, thus, a stronger Dingle reduction factor Eq. (2.38). Another possible origin may be a weaker corrugation of these parts of the FS along the k_z-direction, giving rise to a smaller contribution of the electron-like parts of the FS to the interlayer conductivity.

5.2 Magnetic nature of the ground state in overdoped NCCO

The Zeeman splitting in a magnetic field gives rise to an additional damping term $R_{\mathrm{S}} = \cos(\pi g \mu_0 / 2\cos\theta)$, where θ is the polar field orientation with respect to the conducting layers and μ_0 the effective cyclotron mass at $\theta = 0°$, see Eq. (2.40). It can be shown that in strongly anisotropic layered compounds all the quantities affecting the SdH oscillations described by the LK formula, Eq. (2.34), except R_{S}, scale with the perpendicular field component $B_\perp = B\cos\theta$:

$$\frac{\tilde{\sigma}}{\sigma_{\mathrm{bg}}} \propto R_{\mathrm{T}}(B_\perp) R_{\mathrm{D}}(B_\perp) R_{\mathrm{MB}}(B_\perp) \cos\left(\frac{\pi g \mu_0}{2\cos\theta}\right) \cdot \cos\left(2\pi \frac{F_0}{B_\perp} + \gamma\right) \tag{5.14}$$

The effective cyclotron mass μ_0, determined from the T-dependence of the SdH oscillation amplitude for $x = 0.15$, is used in the following.

Experiments in steady magnetic fields up to $45\,\mathrm{T}$ were performed, using a homemade 2-axis-rotator probe, described in Sect. 4.3, to investigate the angle dependence of SdH oscillations in a slightly overdoped, $x = 0.15$, NCCO crystal. Oscillations were observable for tilt-angles up to $\theta \leq 62°$ from perpendicular to the conducting layers, as can be seen in Fig. 5.17 (a). (b) shows the oscillation frequency plotted versus the in-situ determined angle θ. Evidently, it increases proportional to $1/\cos\theta$, as it is expected for a layered metal with weak interlayer tranfer [35], showing that an analysis in terms of Eq. (5.14) is applicable. As was explained in Sect. 5.2, the spin-splitting factor R_{S} changes sign upon passing a spin-zero. From Fig. 5.17 (a) one can see that no phase inversion of the oscillations is discernible when plotted versus $B_\perp$. The amplitude of the oscillations is steadily decreasing as the polar angle increases. There is no signature for a spin-zero up to the highest angle.

Fig. 5.17 (c) shows the angular dependence of the oscillation amplitude obtained from a Fast Fourier transformation (FFT) taken over a field window of $27\,\mathrm{T}$ to $40\,\mathrm{T}$. The dotted and solid lines are fits of the experimental data to Eq. (5.14):

$$\begin{aligned} |A_{\mathrm{osc}}| &= a \cdot \frac{B^{1/2}\mu}{\cos\theta} R_{\mathrm{T},\alpha} R_{\mathrm{D},\alpha} R_{\mathrm{MB},\alpha} |R_{\mathrm{S},\alpha}| \\ &= a \cdot \frac{K\mu^2 T[1 - \exp(-B_{\mathrm{MB}}/B_\perp)] \exp(-K\mu T_{\mathrm{D}}/B_\perp)}{B^{1/2}\cos^2\theta \sinh(K\mu T/B_\perp)} \cdot \left|\cos\left(\frac{\pi\mu g}{2\cos\theta}\right)\right|, \end{aligned} \tag{5.15}$$

where a is a θ-independent constant. With the independently determined values

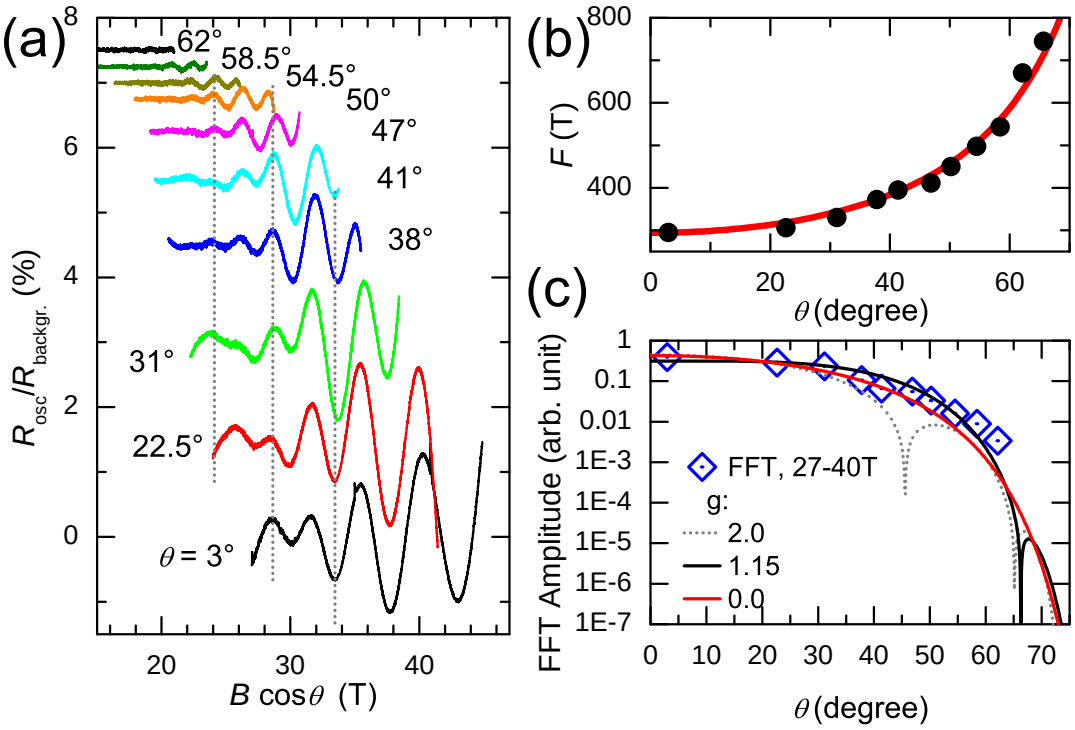

Figure 5.17: (a) SdH oscillations at different polar angles θ plotted vs. the out-of-plane field component $B\cos\theta$ for an $x = 0.15$ sample, recorded in steady fields. (b) Angle dependence of the oscillation frequency vs. in-situ determined angles. The red curve shows the theoretically expected frequency increase $F = F_0/\cos\theta$, with $F_0 = 292\,\mathrm{T}$. (c) Angle dependence of the oscillation amplitude obtained from a FFT over a window of 27 to 40 T. The dotted, grey and solid, black and red curves are fits using Eq. (5.15) with $g = 2.0$, 1.15 and 0, respectively.

of the effective cyclotron mass, $\mu_{0.15,\alpha} = 1.05$, in units of the free electron mass m_e (Sect. 5.1.5), the Dingle temperature, $T_{\mathrm{D},0.15} = 14\,\mathrm{K}$ and a MB field, $B_{\mathrm{MB},0.15} = 12\,\mathrm{T}$ (Sect. 5.1.9), the data are fitted for different g-factors. For $g = 2.0$ (grey dotted curve) a spin-zero would be expected around $\theta = 45°$. Only for $g \leq 1.2$ the first zero would lie beyond the accessed angular range. Apparently, g deviates significantly from the non-renormalized free electron value $g \approx 2.0$, which can be related to strong many-body interactions present in the system. It must be noted, however, that the above estimate is not unambiguous: Setting g equal zero gives a similarly good fit to the experimental data, see red curve in Fig. 5.17 (c). A more accurate value can only be obtained from "spin-zero" positions. Unfortu-

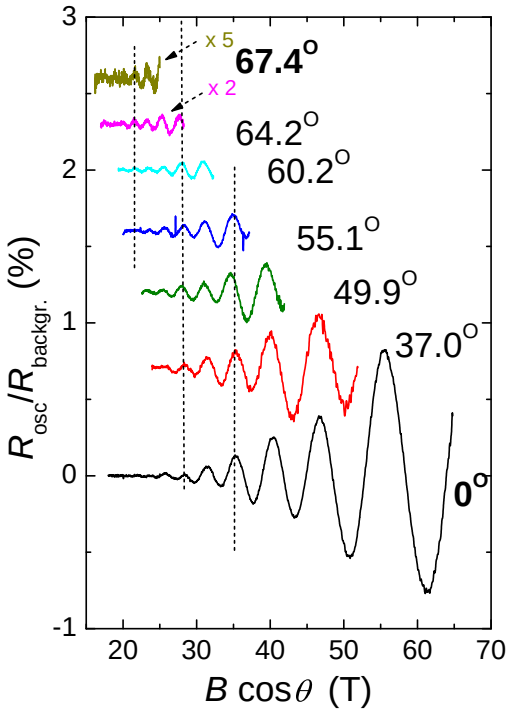

Figure 5.18: SdH oscillations in pulsed fields at different polar angles θ plotted vs. the out-of-plane field component $B_\perp = B\cos\theta$ for an $x = 0.15$ sample.

nately the oscillation amplitude at $40\,\mathrm{T}$ was too small to resolve oscillations at $\theta > 60°$ with a reasonable resolution, see Fig. 5.17. Therefore, further experiments at higher (pulsed) magnetic fields were necessary for a reliable determination of the g-factor.

A single-axis rotator was used especially designed for angle-dependent pulsed-field experiments with NCCO (for details see Sect. 4.3). Fig. 5.18 presents SdH oscillations recorded in pulsed magnetic fields up to $64\,\mathrm{T}$ at different polar angles plotted versus the out-of-plane field component $B_\perp = B\cos\theta$. The evolution of the oscillations was traced over 3 decades of their amplitude, in a broad angular range, up to $71°$. The vertical dashed lines connect maximums at constant $B_\perp$ for different angles and highlight the absence of a phase inversion up to the highest angle. Also there is no obvious deviation from a monotonic θ-dependence of the overall peak-to-peak oscillation amplitude, that might be a trace of a spin-zero.

Fig. 5.19 shows the θ-dependent oscillation amplitude obtained from a Fast-Fourier-transformation (FFT) for a fixed field window of 40 to $60\,\mathrm{T}$. Two addi-

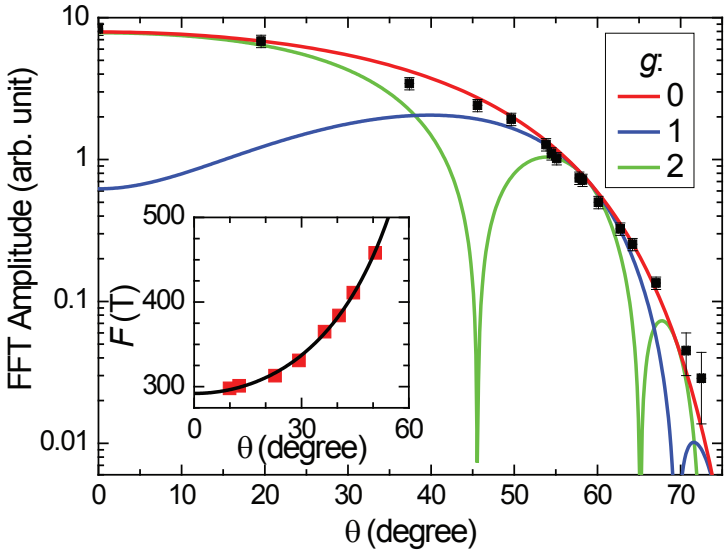

Figure 5.19: SdH oscillation amplitude obtained from FFT for a field window of $40 \leq B \leq 60\,\mathrm{T}$ for different polar angles θ: experimental data (squares) and simulation based on Eq. (5.15) with $g = 0$ (red), 1.0 (blue) and 2.0 (green). Inset: SdH oscillation frequency vs. the angle θ; the black curve is a fit to $F = F_0/\cos\theta$, with $F_0 = 292\,\mathrm{T}$.

tional points at $\approx 70°$ and $71°$ are included where the FFT still gives a reasonable signal from oscillations close to the background noise level of $0.05\,\%$ with respect to the absolute MR signal. The inset in Fig. 5.19 shows the oscillation frequency plotted versus the *in situ* determined angle θ and demonstrates that the $1/\cos\theta$ scaling for the frequency holds also at higher fields as compared to Fig. 5.18 (b). According to Eq. (5.15), the θ-dependence can be fitted using a mean field-value (averaged in the $1/B$-scale) of $48\,\mathrm{T}$. The temperature- and Dingle- damping factors are included in the fit, as well as a correction for the effect of MB. For comparison it is shown, what would be expected for $g = 2.0$ (green curve) and for $g = 1.0$, showing a *spin-zero* close to $70°$. Apparently, only if spin-splitting is excluded completely by choosing $g = 0$ (red curve), the fit reproduces the experimental results.

For the p-doped cuprate superconductor $YBa_2Cu_3O_{6+x}$ (YBCO) the first experiments on angle-dependent SdH oscillations also reported an absence of spin-zeros [136], which was confuted later by more detailed studies and improved analysis techniques [134, 141]. For YBCO several frequencies were observed that

originates from different FSs and had different spin-splitting factors, R_S. Therefore, there is an overlap of different amplitude profiles, that gives rise to a non-vanishing contribution in the quantum oscillations at angles, where a spin-zero position is reached for one FS but not for another. By contrast to YBCO, NCCO has a much simpler crystal structure, i.e. no chains or bilayers. Therefore, no signatures of additional SdH frequencies were found. In the present work, SdH oscillations of three different $x = 0.15$ samples have been investigated in the angular range of $0° \leq \theta \leq 71°$. Neither signs of a phase-inversion nor deviations of the monotonic decrease of the oscillation amplitude that might be related to spin-zeros have been resolved. Thus, the results presented above provide a strong evidence for the absence of the spin-splitting effect on MQO in overdoped NCCO.

5.2.1 The origin of the absence of the spin-splitting effect

As already pointed out, the FS of NCCO is expected to be rather simple. The presence of an additional FS pocket with its area close to that of the α-pocket but of different magnetic origin and thus responsible for a compensating superposition of spin-zero profiles as in the case of YBCO is unlikely. The observed unambiguous absence of spin-zeros, that is $g = 0$, for the α-oscillations provides a strong argument for the magnetic nature of the ground state of overdoped NCCO.

One possible candidate for explaining the origin of the $(\frac{\pi}{a}, \frac{\pi}{a})$-ordering in NCCO is long-range antiferromagnetism (AFM). The spin-splitting factor g for an antiferromagnet is described by two components: $g_{||}$ is the component parallel and $g_{\perp}$ perpendicular to the direction of the staggered magnetization in real-space [142, 143]. It was shown by Ramazashvilli [144] that, due to a strong anisotropic character of the Zeeman coupling (i.e. $g_{\perp}$ depends on the azimuthal field orientation φ), the spin-splitting effect on the amplitude of quantum oscillations is modified with φ. In Fig. 5.20 the theoretically expected dHvA-oscillation amplitude is shown as a function of the azimuthal and polar field-orientation for a layered antiferromagnet (left) and for a nonmagnetic layered metal (right) at zero-temperature (taken from Kabanov and Alexandrov [145]). For a conventional nonmagnetic metal spin-zeros are expected for θ-rotations independent of the azimuthal orientation φ. For an antiferromagnetic metal in fields up to which

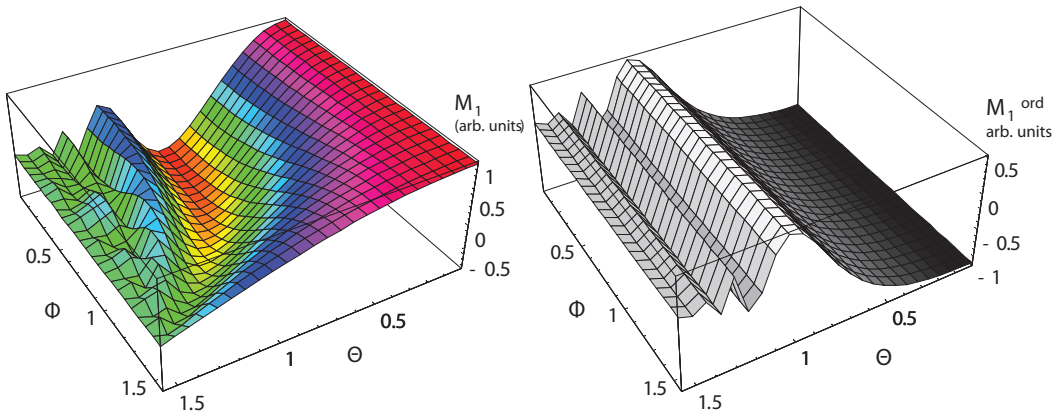

Figure 5.20: Theoretically expected dHvA-oscillation-amplitude as a function of the azimuthal (φ) and polar (θ) field-orientation in a layered antiferromagnet (left) and a nonmagnetic layered metal (right) at zero-temperature (taken from [145]).

no spin-flop[3] occurs, one would expect spin-zeros when varying polar angle θ in the plane parallel to the spin-hard axis, i.e. $\varphi = 0°$. By contrast for $\varphi = \pi/2$ the Zeeman-splitting of the Landau levels is completely suppressed. Thus, for $\varphi = \pi/2$ the reduction factor R_S, Eq. (2.40), equals unity, leading to a monotonic decrease of the oscillation amplitude without spin-zeros as θ increases [146]. For magnetic fields, exceeding the spin-flop threshold B_{SF}, the magnetization axis remains perpendicular to the field orientation, and thus spin-splitting is absent independently of φ. Since for NCCO $B_{SF} \leq 10\,\mathrm{T}$, see Sect. 1.3.2, the presented results are a strong argument in favor of an antiferromagnetic low-temperature ground state for overdoped NCCO.

[3]Spin-flop means that the direction of the staggered magnetization in an antiferromagnet aligns perpendicular to the field by a flop, i.e turns by $90°$, conserving AFM ordering.

5.3 Magnetic torque of NCCO - in search of de Haas-van Alphen oscillations

To gain further information on the Fermi surface properties it would be highly desirable to observe and analyze oscillations of thermodynamic quantities such as magnetization, i.e. de Haas-van Alphen (dHvA) oscillations, see Sect. 2.3. Compared to the SdH effect, where theory has to make certain assumptions concerning different possible scattering mechanisms, oscillations in the magnetization have the advantage to be explicitly described by an exact thermodynamic theory. For NCCO it is a very challenging task to detect the dHvA effect from itinerant electrons, since the magnetization is dominated by a huge non-saturating anisotropic contribution from localized Nd^{3+} ($J = 9/2$) spins. For detecting dHvA oscillations in small single crystals of layered metals, the magnetic torque technique proved very efficient [35].

As was shown in the previous section, the amplitude of MQO decreases as θ is increased, whereas torque does increase (see Sect. 4.4). Using the piezoelectric micro-cantilever technique, measurements of magnetic torque, searching for the dHvA effect in a slightly overdoped, $x = 0.15$, NCCO crystal were performed in pulsed magnetic fields. The main challenge when trying to measure the dHvA effect at a tilted field orientation is the very strong anisotropic contribution of Nd^{3+} moments to the magnetization. One could, however, expect the magnetization to saturate at high fields, as for example it is the case for YBCO [32]. This made it easier to find quantum oscillations on a flattened background. The sample chosen for the experiment had a very small size, $70 \times 20 \times 10\,\mu m^3$ ($m \approx 0.1\,\mu g$). [4] Nevertheless, the torque signal associated with Nd^{3+} was still extremely strong and the measurements could only be done at very small tilt angles (between the field and the crystal c-axis) $\theta \leq 2°$. At $\theta = 2.4°$ the cantilever deflection reached 60% of the critical value at which the cantilever breaks.

Fig. 5.21 shows examples of the field-dependent torque at $T = 4.2\,K$. Surprisingly, the torque shows a monotonic superlinear growth up to the highest field applied. At $\theta = 2.4°$ a kink is detected in the up-sweep, indicating that the sample holder is slightly turned in the field due to the too strong torque. At lower

[4] A photo showing the crystal attached to the micro-cantilever is exhibited in the experimental Sect. 3.2

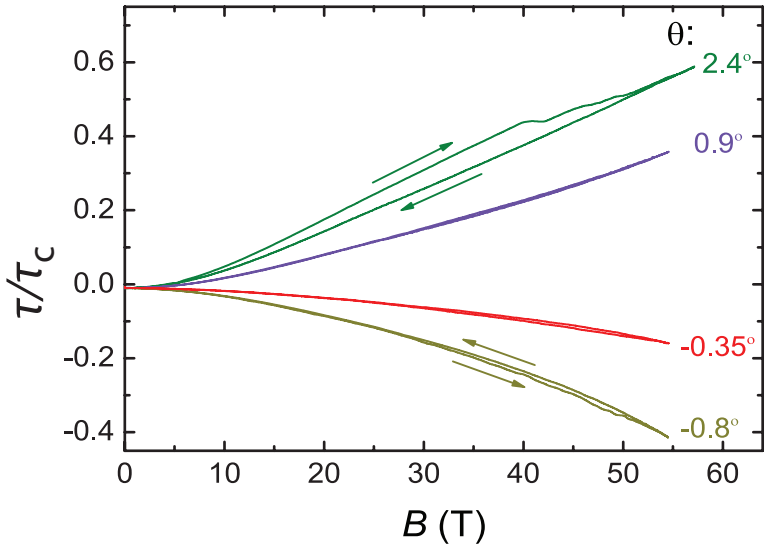

Figure 5.21: Magnetic torque τ (in units of the critical torque of the cantilever τ_c) in pulsed field. Already at very small tilt angles ($\sim 1°-2°$) a strong non-saturating torque has been observed. Note: The kink in the $\theta = 2.4°$ curve is due to a slight turn of the cantilever caused by the strong torque.

θ reversible signals were achieved. However, no dHvA oscillations were found at these small angles. Higher tilt-angles were desirable since the torque oscillation amplitude should become stronger upon increasing θ. The optimal angle can be estimated from Eq. (2.31) by substituting the angle dependence of the dHvA oscillation amplitude, analogous to that in Eq. (5.15):

$$\begin{aligned}\tilde{\tau} &= -B\frac{1}{F}\frac{\partial F}{\partial \theta}\tilde{M} \\ &\propto \tan\theta \frac{(1-\exp\left(B_{\mathrm{MB}}/B_{\perp}\right)\exp\left(-K\mu_0 T_{\mathrm{D}}/B_{\perp}\right)}{\cos\theta \sinh(K\mu_0 T/B_{\perp})},\end{aligned} \tag{5.16}$$

where $F = F_0/\cos\theta$. The optimal angular position should be the maximum of Eq. (5.16). Taking the previously determined values $\mu_{\alpha,0.15} = 1.05$; $T_{\mathrm{D}} = 14\,\mathrm{K}$; $B_{\mathrm{MB}} = 12\,\mathrm{T}$ an optimal angle θ of about $30°$ is obtained.

To overcome the difficulty of the huge background in torque and get access to higher angles, measurements were carried out on two slightly overdoped, equally shaped crystals with $x = 0.15$, placed in a "compensated" geometry as shown in the inset of Fig. 5.22. The samples were oriented at an angle of $90°$ with

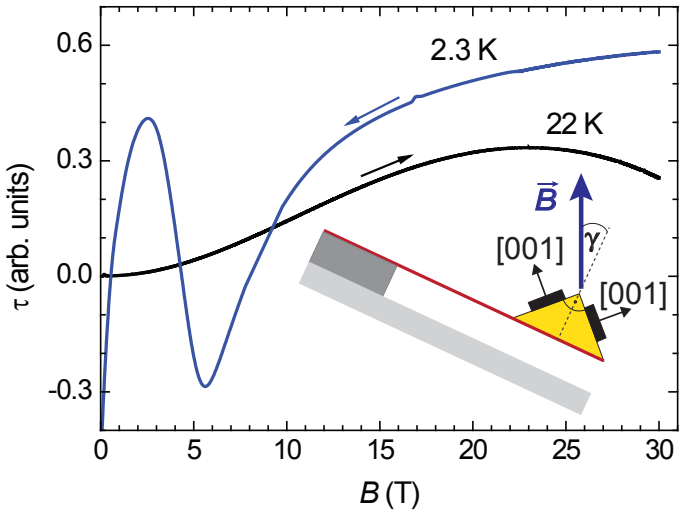

Figure 5.22: Examples of field-dependent torque in steady fields. At $2.3\,\mathrm{K}$ (blue) measurements were performed with a very slow sweep rate between $20 \leq 30\,\mathrm{T}$. The strong oscillation at $B \leq 10\,\mathrm{T}$ is due to superconductivity. Inset: the principle orientation of the two samples mounted on top of a prism glued to a capacitive torque magnetometer.

respect to each other. For such a configuration the contributions to the steady part of magnetic torque, Eq. (4.4), of each sample should cancel out and only the oscillating components will be left. In addition, setting the orientation of one sample to the optimal angle $\theta \approx 30°$, consequently, the second one will be oriented at $75°$. Hence, the contribution of the second sample to dHvA oscillations will be negligibly small, due to the strong angle dependence of the oscillation amplitude. Of course, such geometry cannot be realized on a microcantilever used in pulsed fields. Therefore, it was applied in combination with the standard capacitance cantilever beam technique (see Sect. 4.4) in steady fields up to $30\,\mathrm{T}$.

The resulting torque signal in the compensated geometry, see Fig. 5.22 was, indeed, reduced by a factor of $\sim 10^2$ in comparison to the individual torque from each sample. This allowed to perform measurements at reasonably high tilt angles, $\theta \approx 30°$, at which the oscillating signal was expected to be the strongest. Below T_c a large superconducting signal was observed. The field was swept upwards at $T = 22\,\mathrm{K}$ (black) where SC is weak enough, to overcome the strongly unstable superconducting regime. After cooling in a constant field of $20\,\mathrm{T}$ down to $2.3\,\mathrm{K}$ the field was swept very slowly ($0.5\,\mathrm{T/min}$) between 20 and $30\,\mathrm{T}$ to en-

sure lowest possible noise conditions. However, quantum oscillations were not detected to an accuracy of 10^{-4} of the torque signal in the present field range.

5.4 Conclusion: A magnetic ground state in overdoped NCCO

As concluded already in Sect. 5.1.10 the superlattice potential, responsible for the FS reconstruction is found to weaken upon increasing doping. It, however, persists up to the highest available doping, $x = 0.17$, the upper edge of the superconducting dome. The detection of SdH oscillations showed that the ordering is strong and stable enough at least for $\sim 1.6\,\mathrm{ps}$, that is approximately the time electrons need to fulfill one full cycle along the cyclotron orbit in pulsed fields of $50\,\mathrm{T}$.

The apparent absence of the Zeeman spin-splitting effect in the angle dependence of SdH oscillations for an slightly overdoped, $x = 0.15$ sample (Sect. 5.2), is a hint on the electronic ground state in this system. The observed monotonic decrease of the SdH oscillation amplitude as the field orientation was tilted away from perpendicular to the conducting layers, can only be fitted by assuming a g-factor equal zero. Such a behavior was predicted for antiferromagnetic ordering [143, 146] and provides a strong argument for AFM as the ground state in overdoped NCCO, at least in high magnetic fields.

6 Angle-dependent magnetoresistance oscillations in overdoped NCCO: studying the Fermi surface geometry in three dimensions

The data on SdH oscillations, presented in the previous section, provide information about the size of the FS and its doping dependence. Another important question is related to the exact shape of the in-plane FS and its corrugation in direction perpendicular to the conducting layers. The semiclassical effect of Angle-dependent MagnetoResistance Oscillations, so-called AMRO, see Sect. 2.5, has proven an efficient tool for mapping the in-plane FS of layered conductors [26, 36, 83, 118, 120, 138]. In this section results on Angle-Dependent Magneto Resistance (ADMR) measurements are presented and analyzed in terms of the AMRO effect.

6.1 Identifying AMRO

Figure 6.1 (a), (b) shows the interlayer resistivity ρ_c of NCCO with $x = 0.16$ and 0.17 upon rotating the samples in the plane parallel to their crystallographic c-axis for a fixed azimuthal angle of $\varphi = 45°$. The field was kept constant at $28\,\mathrm{T}$ while the polar orientation represented by θ was gradually changed (speed of $\sim 15°/\mathrm{min}$) from $\theta = -90°$ to $0°$ and further to $+90°$, corresponding to $B||[110]$, $B||[001]$ and $B||[1\bar{1}0]$, respectively [1]. At this field, superconductivity at low tem-

[1] see Fig. 4.3 for the definition of the angles θ and φ

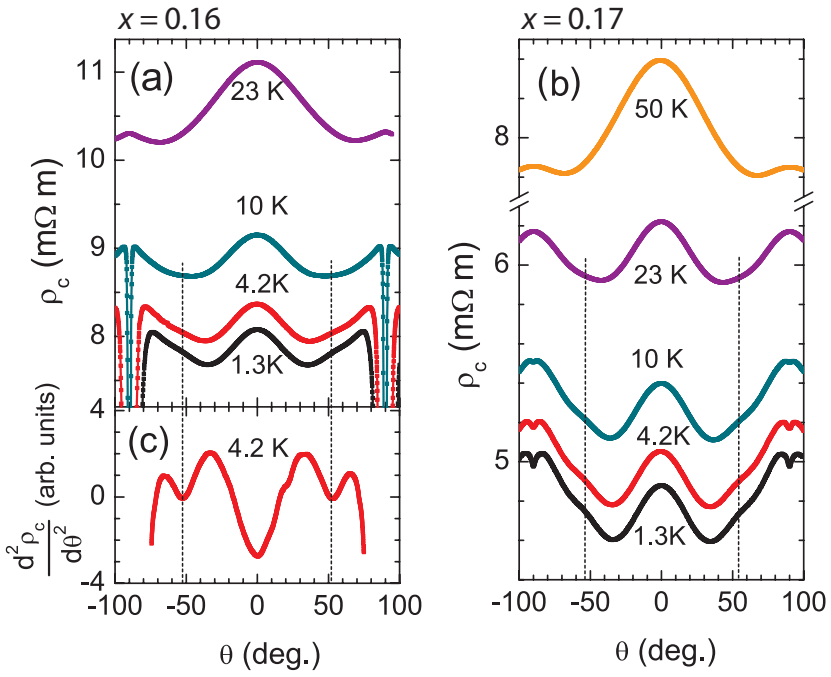

Figure 6.1: (a) Interlayer resistivity ρ_c of a slightly overdoped NCCO sample ($x = 0.16$) as a function of field-tilt-angle θ, at different temperatures, constant $\varphi = 45°$ and $B = 28\,\mathrm{T}$. The range $|\theta| < 75°$ corresponds to the normal conducting state. The rapid drop of ρ_c outside this range is due to the onset of superconductivity. The vertical dashed lines are drawn through the AMRO features centered at $|\theta| \approx 53°$, which are independent of temperature. (b) Same as (a), for a strongly overdoped sample ($x = 0.17$) [131]. (c) Second derivative of the resistivity in (a) exhibiting dips at the AMRO peak positions.

peratures is manifest by a sharp dip within a narrow angular range around $\pm 90°$. Its significance dependents on the doping x. In the normal state, a maximum at $\theta = 0°$ and, in addition, a pair of shallow humps superimposed on the monotonic background around $\theta \approx \pm 53°$ are observed. To illustrate the position of these features more clearly, Fig. 6.1 (c) shows the second derivative $d^2\rho_c/d\theta^2$ for the $x = 0.16$ sample, exhibiting dips at these angles. These features, though rather weak, were reproduced for several samples at doping levels ranging from $0.16 \leq x \leq 0.17$. To the accuracy of the experiment, the angular positions of the features are independent of temperature, see the vertical, grey dotted lines in Fig. 6.1.

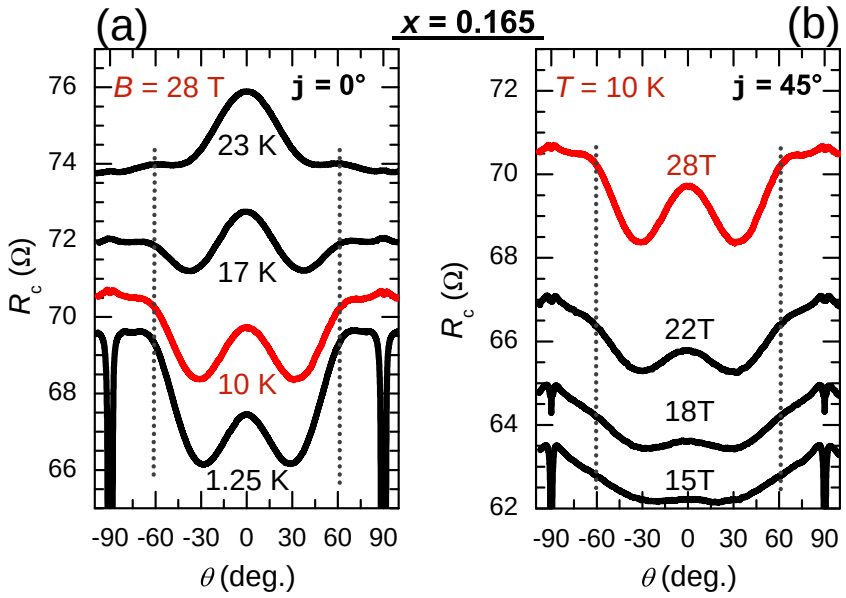

Figure 6.2: Interlayer resistance R_c of a strongly overdoped NCCO sample ($x = 0.165$) for a fixed azimuthal angle $\varphi = 0°$ as a function of tilt angle θ: (a) at different temperatures in a constant field of $B = 28\,\mathrm{T}$ and (b) in different fields at constant temperature of $T = 10\,\mathrm{K}$. The range $|\theta| < 85°$ corresponds to the normal conducting state. The rapid drop of R_c outside this range is due to the onset of SC. The vertical dashed lines are drawn through the AMRO features centered at $|\theta| \approx 61°$, which are independent of temperature and magnetic field strength.

For an $x = 0.165$ sample a more detailed study of the T-dependence of the ADMR was done for $\varphi = 0°$, as presented in Fig. 6.2. The shallow hump feature lying on the positive slope between $\theta = 30$–$70°$ does not lose intensity when T is increased to $23\,\mathrm{K}$. At the same time the overall shape of the ADMR does change: i.e. the central hump (for $T = 1.3\,\mathrm{K}$ at $-30° \leq \theta \leq +30°$) broadens considerably with T. Furthermore, it was checked, see Fig. 6.2 (b), that the features do not shift on reducing the field strength down to $18\,\mathrm{T}$. This is exactly what one expects for AMRO, whose positions are solely determined by the Fermi surface geometry and, therefore, independent of both field and temperature.

For $T \leq 10$ K, the magnetoresistance behavior shown in Fig. 6.1 and 6.2 resembles that observed earlier on hole-overdoped cuprate superconductor $Tl_2Ba_2CuO_{6+\delta}$ (Tl-2201) [26, 147], the similarities and differences will be discussed

later in Sect. 6.4. In the case of Tl-2201 it was shown that both the central hump and the side features originated from the AMRO effect on the large cylindrical Fermi surface. In particular, the resistivity peak at $\theta = 0°$ was considered as a fingerprint of a warped Fermi cylinder centered at the corner of the Brillouin zone and satisfying the symmetry requirements of a body-centered tetragonal lattice [26]. Since NCCO has the same crystal symmetry, it is tempting to also attribute the central hump in the ADMR curves to the large Fermi cylinder. However, unlike at $\theta \approx \pm 53°$, the field direction corresponding to $\theta = 0°$ coincides with the crystal symmetry axis normal to the layers, which should always lead to an extrema in the $\rho_c(\theta)$ dependence. Therefore, one should not disregard other possible mechanisms, besides AMRO, which could cause a maximum at this field direction. Indeed, the experimentally observed evolution of the central hump with temperature is opposite to that expected for AMRO. Since AMRO are an effect of the cyclotron motion of charge carriers in a strong magnetic field, they require a sufficiently large scattering time τ. As τ decreases with increasing T, the AMRO are expected to gradually vanish. This is, indeed, the case for the hump-like features around $\theta \approx \pm 53°$ in Fig. 6.1, which can hardly be resolved above $23\,\mathrm{K}$, see the $50\,\mathrm{K}$ curve (orange) in Figs. 6.1. By contrast, the central hump notably increases in magnitude, dominating the angular dependence at elevated temperatures. In fact, the overall shape of the $23\,\mathrm{K}$ curve for $x = 0.16$ and 0.165 and the $50\,\mathrm{K}$ curve for $x = 0.17$ in Fig. 6.1, exhibiting a global maximum at $\mathbf{B}$ normal to the layers and parallel to the current direction, is at odds with the usual orbital effect of a magnetic field on the coherent interlayer charge transport. While the exact mechanism responsible for this anomalous behavior has still to be established, it is clear that, at least at high T, the central hump cannot be attributed to the AMRO.

As the scattering time increases at cooling down below $20\,\mathrm{K}$, the conventional orbital effect becomes significant, which is evidenced by the development of the "wing-like" positive slope $d\rho_c/d|\theta|$ at $|\theta| \geq 30°$ and the AMRO features at $|\theta| \approx 53°$. It is also possible that the central hump is partly due to the AMRO at low temperatures.

Later on, in Sect. 8.2, it will be shown that spin-effects on the ADMR, observed for underdoped samples, still contribute, though rather weakly, to the magnetotransport in the overdoped regime.

6.2 AMRO at low temperature and highest fields

In Fig. 6.3 ADMR curves for $x = 0.17$ recorded at $T = 1.4\,\mathrm{K}$ in even higher fields of $B = 34\,\mathrm{T}$ and $45\,\mathrm{T}$ for various φs are shown. No additional peaks developed, as compared to lower fields, but the AMRO feature at $53° \leq \theta \leq 62°$ is much stronger pronounced and has evolved, for certain φs, to a real maximum, as highlighted by stars in Fig. 6.3. The main characteristics of the ADMR at low T and high B in NCCO are:

- a central hump around $-30° \leq \theta \leq 30°$
- a "wing-like" positive slope, $d\rho/d|\theta| > 0$, for higher polar angles, which varies in steepness for different azimuthal angles φ
- a φ-dependent shallow hump on top of the "wing"
- and at $B = 34\,\mathrm{T}$ a narrow cusp close to $\theta = 90°$ related to remnant superconductivity.

As expected from a tetragonal crystal symmetry, the variation of the azimuthal field orientation, that is angle φ, gives a $45°$ periodicity.

The polar θ-position of the AMRO feature plotted versus φ is presented in Fig. 6.5. This position oscillates with a period of $\Delta\varphi = 45°$ between $\theta \approx 62°$ and $53°$. Within the experimental error bars for $0.16 \leq x \leq 0.17$ the AMRO show a similar angle-dependence.

The weakness of the AMRO features for all doping levels indicates that even in a strong field of $45\,\mathrm{T}$ the high field criterion, $\omega_c\tau \gg 1$, is by far not fulfilled. A rough estimation of $\omega_c\tau$ can be obtained using the Shubnikov-de Haas results.For example, for $x = 0.17$, at $B = 45\,\mathrm{T}$, with the Dingle temperature $T_D = 18\,\mathrm{K}$ and effective cyclotron mass $\mu = 2.3$, see Sect. 5.1,

$$\omega_c\tau = \frac{eB}{m_c} \cdot \frac{\hbar}{2\pi k_B T_D} = 3.44 \times 10^{12}\,\mathrm{s}^{-1} \cdot 67.5 \times 10^{-15}\,\mathrm{s} = 0.23 < 1, \qquad (6.1)$$

with the Boltzmann constant k_B. This is a lower estimation for the transport scattering rate τ, which is usually bigger [35]. Anyway, it demonstrates that $\omega_c\tau >> 1$ is not reached. In this situation analytical expressions for the high-field MR [36, 116, 138] are not valid and a detailed numerical analysis of the

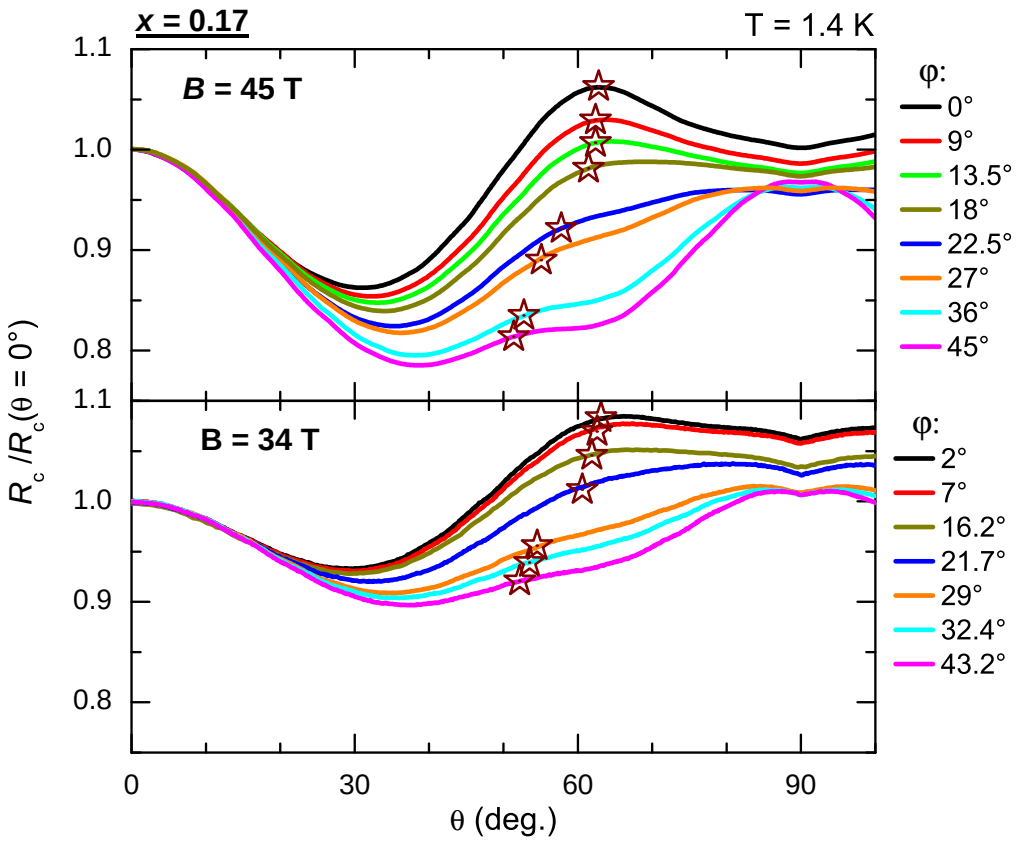

Figure 6.3: Angle-dependent interlayer magnetoresistance of strongly overdoped, $x = 0.17$, crystals, $T = 1.4$ K; $B = 45\,\mathrm{T}$ (upper panel) and $34\,\mathrm{T}$ (lower panel). Each curve is a rotation of the sample with respect to the field orientation from perpendicular to the CuO_2-layers, $\theta = 0°$, to parallel, $\theta = 90°$, at a fixed azimuthal (in-plane) angle φ.

ADMR is required for the determination of the relevant Fermi surface geometry [26, 120, 147].

In Fig. 6.4 ADMR curves recorded at $28\,\mathrm{T}$, $34\,\mathrm{T}$ and $45\,\mathrm{T}$ for $x = 0.17,\ 0.16$ and 0.15 are presented. For an easier comparison the absolute value of the magnetoresistance was normalized to its value at $B||c$-axis ($\theta = 0°$). As doping is decreased, the dip at $\theta = 90°$ becomes stronger pronounced, due to stronger SC.

A detailed quantitative analysis will be given later in Sect. 6.4. But already here a very important qualitative statement can be done from the present data. Comparing the AMRO features in Fig. 6.4 for $x = 0.16$ to 0.17 they show a remarkable similarity in shape, position and angle dependence. Moreover, as illustrated in

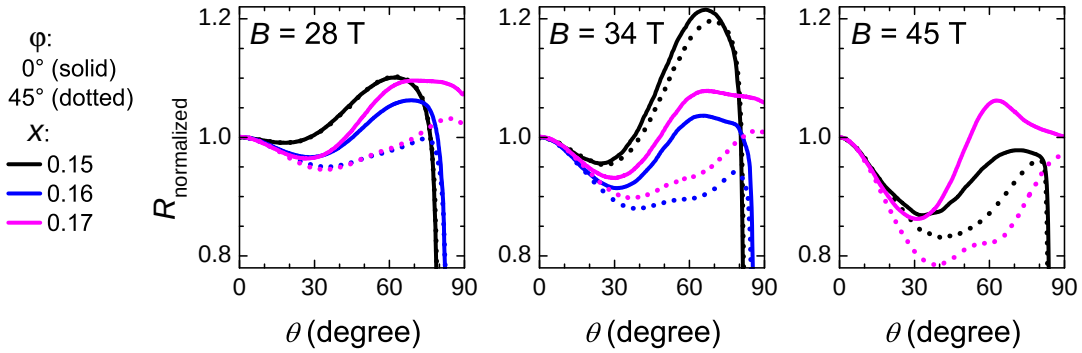

Figure 6.4: Angle-dependent magnetoresistance for different doping levels at constant magnetic fields and $\varphi = 0°$ (solid lines) and $45°$ (dotted lines), respectively, $T = 1.5\,\mathrm{K}$. The resistance is normalized by its value at $\theta = 0°$. At angles $\theta \geq 80°$ superconductivity is not suppressed completely, resulting in zero resistance at lower doping and in a weak cusp (minimum) at $90°$ at higher x.

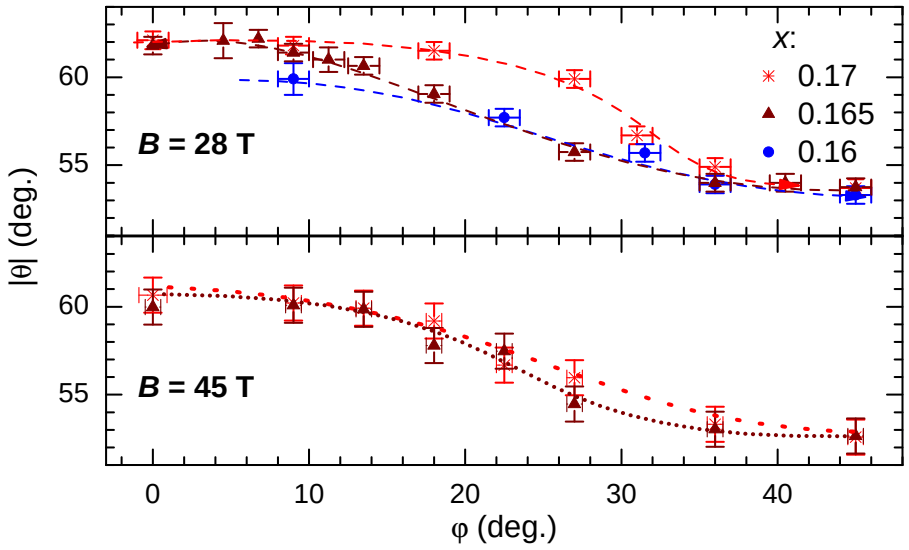

Figure 6.5: Dependence of the positions of the AMRO features in NCCO with $x = 0.16$ (blue circles), 0.165 (brown triangles) and 0.17 (red stars) on the azimuthal orientation φ of the field rotation plane at $B = 28\,\mathrm{T}$ and $45\,\mathrm{T}$. Dashed and dotted lines are guides to the eye.

Fig. 6.5 they exhibit the same dependence on the azimuthal angle φ of the field direction. This means that the cyclotron orbits responsible for the AMRO are identical for $0.16 \leq x \leq 0.17$. In fact, this important observation [131] was a strong evidence against a critical FS transformation within this doping interval, when it was indicated by the first SdH results in NCCO [101].

Fig. 6.4 also shows the ADMR curves at $\varphi = 0°$ and $45°$ for $x = 0.15$, close to optimal doping. Up to $B = 34,\mathrm{T}$ the features related to AMRO are absent, see black curves in Fig. 6.4: no φ-dependent AMRO features on top of the "wings" are discernible. Only at $45\,\mathrm{T}$ a φ-dependence shows up, similar to what is found for the overdoped compositions.

In Fig. 6.6 ADMR curves for $x = 0.15$ at different constant magnetic fields of up to $28\,\mathrm{T}$ are shown. At $10\,\mathrm{T}$ and $15\,\mathrm{T}$ (purple and dark-cyan curves) the ADMR has a weak negative slope until at $\theta > 50°$ and $\theta > 63°$, respectively, superconductivity sets in. This negative ADMR is similar to what was measured for lower doped, $x = 0.13$, samples (presented and discussed in Sect. 8.2). In the $20\,\mathrm{T}$ curve (green) there are already some deviations discernible that develop for higher fields into a maximum at angles close to the SC onset, resembling the prominent "wing-like" positive slope. Close to $B||c$-axis, i.e. $\theta = 0°$, a weak central hump emerges. Thus

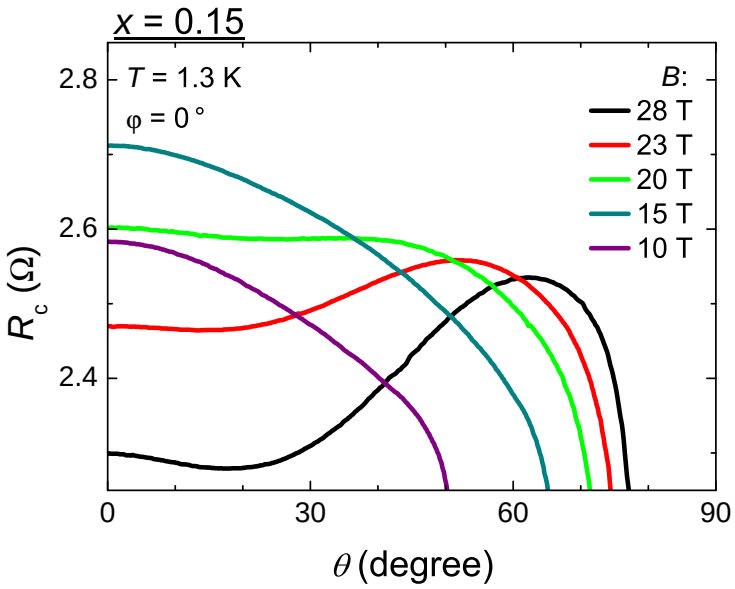

Figure 6.6: ADMR curves for $x = 0.15$ recorded at different fields for $\varphi = 0$ and $T = 1.3\,\mathrm{K}$.

the overall shape of the ADMR curve for $x = 0.15$ above $20\,\mathrm{T}$ resembles the one found for the overdoped samples, associated with conventional orbital effects. However, the θ-position of the maximum right before the SC onset strongly depends on the magnetic field value. This is a clear evidence that it has nothing to do with the AMRO effect, which is field independent.

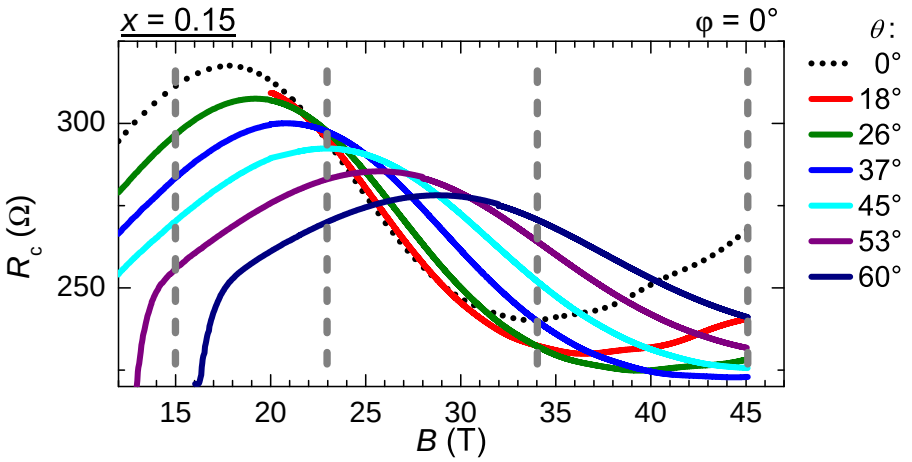

Figure 6.7: Interlayer MR as a function of B at different tilt-angles $0\,^\circ \leq \theta \leq 70\,^\circ$ with respect to the c-axis ($\theta = 0°$) for $x = 0.15$, recorded at $T = 1.4\,\mathrm{K}$. The grey dashed lines indicate the angle-dependence of the MR at fixed fields discussed in the text.

The qualitative origin of this maximum in the ADMR of $x = 0.15$ can be understood from Fig. 6.7, where several field sweeps up to $45\,\mathrm{T}$ at different θ-positions but fixed polar orientation, $\varphi = 0°$, are presented. The interlayer MR for $B||[001]$, that is $\theta = 0°$, (dotted black curve) has a maximum around $18\,\mathrm{T}$. What becomes obvious immediately is that the anomalous field range, where the magnetoresistance is negative, broadens and shifts to higher fields as the tilt angle θ is increased. As a result, the overall ADMR shape for rotations at a constant field changes (compare MR along the dashed grey lines in Fig. 6.7 with the ADMR curves in Fig. 6.6 and 6.4). While rotating at fields below $18\,\mathrm{T}$ the slope $dR_c/d\theta$ is negative all the way from $\theta = 0°$ to $66°$ (SC onset). For $B = 23\,\mathrm{T}$ the ADMR stays relatively flat for $\theta \leq 25°$ and at high tilt-angle a maximum evolves due to the broadening of the anomaly in the MR. Above $34\,\mathrm{T}$ the positive MR, similar to that of overdoped samples, is observable for $\theta \leq 30°$, giving rise to the prominent central hump. But at high tilt-angles the broad anomalous negative MR is

responsible for the wing-like maximum in the ADMR. Obviously, one could expect from this evolution that AMRO can be detected at fields around $50\,\mathrm{T}$ and larger, where the field-dependent magnetoresistance acquires the conventional positive slope even at relatively high θ. However, this field range is not accessible with presently available steady-field magnet systems, which are needed for the ADMR experiments.

For $x \geq 0.15$ the anomalous MR rapidly shifts to lower fields. For $x = 0.16$ the orbital behavior is pronounced much stronger already at lower fields and the anomalous ADMR vanishes around $10\,\mathrm{T}$, see e.g. Fig. 5.1. For even higher doping it is almost suppressed.

6.3 Origin of AMRO in overdoped NCCO

From the data presented above it is clear that the AMRO effect in NCCO is most pronounced for strong overdoping. At decreasing x the features gradually weaken and are not observable any longer for $x = 0.15$, close to optimal doping. Comparing the doping dependence of the Shubnikov-de Haas oscillation (SdH) data, presented in Sect. 5.1, one can make further qualitative assumptions to the relation between AMRO and the FS of NCCO. It was shown that the SdH amplitudes, corresponding to the α- and β-orbits, have opposite dependencies on doping. The fast β-oscillations, associated with a large magnetic breakdown (MB) orbit, are strongest at doping levels where the most prominent AMRO is observed. By contrast the amplitude of the slow α-oscillations has its maximum near optimal doping, where the AMRO effect is the weakest. This behavior can be considered in relation to the increase of the MB field towards optimal doping. From SdH oscillations for $x = 0.17$ a relatively low MB field of $B_{\mathrm{MB}} = 0.5\,\mathrm{T}$ was obtained, see Sect. 5.1.9. Thus, at fields $B \geq 20\,\mathrm{T}$, where AMRO features are observed for $x = 0.17$, MB orbits should already give the leading contribution to the ADMR. In Fig. 5.7 (Sect. 5.1.6) it was demonstrated that these orbits, are geometrically identical to those on the unreconstructed FS. The MB gap determined by the $(\frac{\pi}{a}, \frac{\pi}{a})$-superlattice potential strengthens as x is lowered from strong overdoping towards the optimum. The comparison of ADMR data for different field and temperature ranges suggests that, at least at high B and low T, the central hump is very likely related to the AMRO effect. All these findings give a good

ground for a quantitative analysis of AMRO, as it has been successfully done for the strongly hole-overdoped cuprate superconductor Tl-2201 [26, 83, 147].

6.4 Simulations of the AMRO effect in NCCO

The main information obtained from the above qualitative investigation of the doping- and field-dependent AMRO evolution is that the large MB orbit is most likely responsible for the AMRO features and has to be incorporated into a numerical approach to this effect in $Nd_{2-x}Ce_xCuO_4$. A large closed FS cylinder was also found to be the origin for AMRO in the p-doped cuprate compound $Tl_2Ba_2CuO_{6+\delta}$ (Tl-2201) by Hussey et al. [26, 83, 147]. Fig. 6.8 demonstrates how similar the experimental AMRO data for strongly overdoped Tl-2201 and NCCO ($x = 0.17$) are. Both show a central hump, a φ-dependent "wing-like" positive ADMR with a broad maximum/shoulder (arrows in Fig. 6.8) on top of it, that shifts from higher to lower polar angle θ as φ is varied from $0°$ to $45°$.

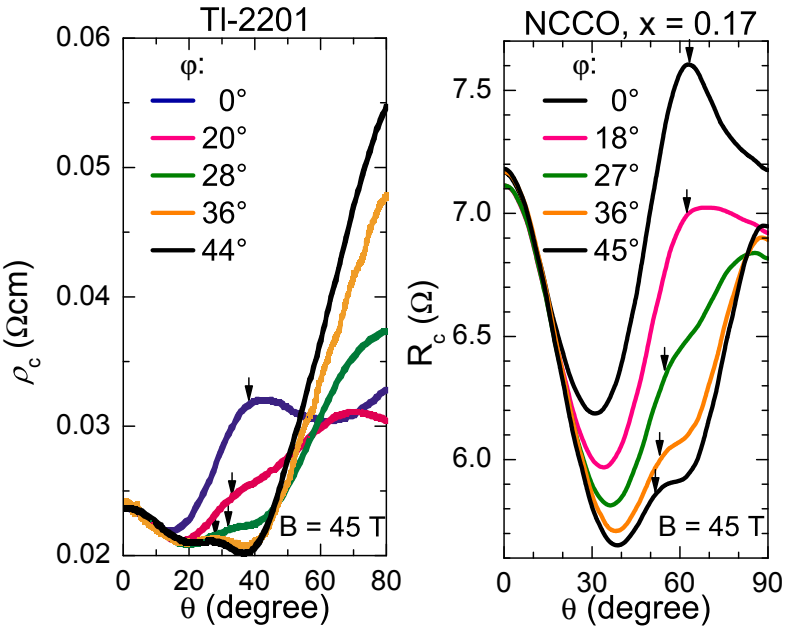

Figure 6.8: (left) Angle-dependent magnetoresistance at different fixed azimuthal angles φ for $Tl_2Ba_2CuO_{6+\delta}$ (Tl-2201) published by Hussey et al. [26]; $T = 4.2\,\mathrm{K}$ and (right) for $Nd_{2-x}Ce_xCuO_4$ (NCCO) with $x = 0.17$; $T = 1.4\,\mathrm{K}$.

But there are clear differences as well: upon changing θ, the ADMR of Tl-2201 increases by almost a factor of $1.5-2$, whereas for NCCO the ADMR does not exceed $\pm 22\,\%$ of the its value at $\theta = 0°$; the angular positions of the φ-dependent AMRO feature for Tl-2201 are clearly closer to $B||c$-axis than in the case of NCCO; the φ-dependence of the ADMR at $\theta \geq 60°$ for Tl-2201 is opposite to that for NCCO, where only at very high θ the curves for different φs come close to each other.

With a small energy gap of $3.5\,\mathrm{meV}$ obtained for $x = 0.17$, (Sect. 5.1.9), at $45\,\mathrm{T}$ the probability for MB, according to Sec. (2.4.3) is:

$$P = \exp \frac{-B_{\mathrm{MB}}}{B} = \exp \frac{-0.5\,\mathrm{T}}{45\,\mathrm{T}} = 0.9890 \tag{6.2}$$

Thus, in the following analysis the gap between different parts of the reconstructed FS is neglected and the AMRO are considered to originate solely from the large MB orbit. As has been shown in Sect. 2.6 the unreconstructed Fermi surface (FS) of NCCO can be described, according to Eq.(2.57) by a weakly warped cylinder determined by an intralayer dispersion-relation $\epsilon_{||}(k_{||}, \varphi)$ and an interlayer part $\epsilon_{\perp}(k_z, \varphi)$, representing the hopping between adjacent layers:

$$\epsilon(\mathbf{k}) = \epsilon_{||}(k_{||}, \varphi) + \epsilon_{\perp}(k_z, \varphi) \tag{6.3}$$

The area of the large unreconstructed in-plane FS, predicted by local-density-approximation calculations [48], nicely fits to the MB orbit revealed by SdH oscillations (as was shown in Fig. 5.6 Sect. 5.1.3). For the following numerical calculations the in-plane dispersion $\epsilon_{||}$ will be used according to Eq. (1.2) in Sect. 1.3.3, with the generally accepted in-plane hopping-integrals t; t'; t'' published by Lin & Millis [73].

In the Sect. 5.1 the absolute size of the large MB orbit was directly determined. For example, for $x = 0.17$, $F_{\beta,0.17} = 10940\,\mathrm{T}$ corresponds to $41.5\,\%$ of the Brillouin zone area. This value nicely coincides with what is expected for 17% of electron doping. It will be used as a fixed parameter in Eq. (1.2) to set the band filling for $\epsilon(k) = 0$, i.e. at the Fermi level, so that the $\epsilon(k)$ encloses exactly 41.5% of the first Brillouin zone of NCCO, yielding $\alpha_{0.17} = -21.23\,\mathrm{meV}$.

As it is described in Sect. 2.6, due to the symmetry of the BZ of NCCO, a complex warping with φ-dependent harmonics of higher-order in the interlayer-hopping is expected, see Fig. 2.5. Due to this, an analysis of the AMRO observed

in NCCO in terms of Yamaji's conditions, Eq. (2.49), is not applicable. The simple geometrical argument, as it was described by Yamaji does not hold for such a warping. This can be easily seen from the integral Eq. (2.48) already for the lowest order φ-harmonic with $a_2 \cos(2\varphi)$ included into the interlayer warping Eq. (2.56). The integral

$$\int_0^{\pi} t_\perp \cos\left(k_z^0 d - k_\mathrm{F} \tan\theta \cos\varphi\right) \cdot a_2 \sin(2\varphi)\, \mathrm{d}\varphi \tag{6.4}$$

equals zero, independent of the orientation θ.

Following Yagi et al. [117] one can calculate the conductivity numerically using the linearized Boltzmann theory with a constant scattering time τ, see Sect. 2.5. For only closed cyclotron orbits the interlayer component σ_{zz} of the conductivity tensor (see Eq. (2.8) in Sect. 2.2) can be calculated by the Shockley-Chambers tube integral [148–150]:

$$\sigma_{zz} = \frac{e^2}{4\pi^3\hbar^2} \int \mathrm{d}k_{B_\parallel} \int_0^{2\pi} \mathrm{d}\varphi\, v_z(\varphi, k_{B_\parallel}) \int_0^{+\infty} \mathrm{d}\varphi'\, v_z(\varphi - \varphi', k_{B_\parallel}) \frac{m_\mathrm{c}}{\omega_\mathrm{c}} e^{(-\varphi'/\omega_\mathrm{c}\tau)}, \tag{6.5}$$

where ω_c is the cyclotron frequency and $k_{B_\parallel}$ the wave vector parallel to the magnetic field. v_z is the interlayer component of the electron group velocity on the FS, Eq. (2.2), and m_c is the cyclotron mass, Eq. (2.4). The phase variable φ' is defined as

$$\varphi' = \frac{\hbar}{m_\mathrm{c}} \int_{k_{||}(0)}^{k_{||}(t)} \frac{\mathrm{d}k_{||}}{v_\perp}, \tag{6.6}$$

i.e. it represents the time-dependent angular position of the electron at $k_{||}$ on the cross-sectional orbit normal to the magnetic field (see Fig. 2.2 in Sect. 2.5) defined by

$$k_{B_\parallel} = k_z^0 \cos\theta, \tag{6.7}$$

with $\mathbf{k}_z = \mathbf{k}_z^0 + \mathbf{k}_{||}$. According to Yamaji [116] and Yagi et al. [117], the vector $\mathbf{k}_z^0$ is introduced as the point of the intersection between the k_z-axis and the orbital plane running from $-\pi/d$ to $+\pi/d$ for NCCO.

In Fig. 2.2 one can see that the position k_z of an electron on an orbit can be described using k_z^0 and k_F, the projection of $k_{||}$ on the azimuthal $k_x k_y$-plane as

$$k_z = k_z^0 - k_F(\varphi - \varphi_\mathrm{set}) \tan\theta \cos\varphi, \tag{6.8}$$

where $\mathbf{k}_F(\varphi - \varphi_{set})$ is the azimuthal Fermi vector and $k_F(\varphi - \varphi_{set}) \tan\theta \cos\varphi$ its projection on the θ-rotation plane defined by φ_{set}. For $\varphi_{set} = 0°$ this would be

the $k_z k_x$-plane. At large enough fields and for angle θ not too close to $90°$ the trajectories are closed and electrons can traverse several cycles until they are scattered. Taking into account the periodicity of the cyclotron motion, $v_z(\varphi, k_B)$ is periodic with $v_z(\varphi + 2\pi, k_{B_\parallel}) = v_z(\varphi, k_{B_\parallel})$ the upper limit for the integration over φ' can be reduced to 2π taking the progressive contribution from several cycles into account by the prefactor $\sum_{n=0}^{\infty} e^{-2\pi n/\omega_c\tau} = (1 - e^{2\pi/\omega_c\tau})^{-1}$ [117]. Hence, the expression for the conductivity, Eq. (6.5) can be written as

$$\sigma_{zz} = \frac{e^2}{4\pi^3\hbar^2} \int_{\frac{-\pi}{d}}^{\frac{\pi}{d}} \mathrm{d}k_z^0 \frac{\cos\theta}{1 - e^{-2\pi/\omega_c\tau}} \int_0^{2\pi} \mathrm{d}\varphi\, v_z(\varphi, k_{B_\parallel}) \int_0^{2\pi} \mathrm{d}\varphi'\, v_z(\varphi - \varphi', k_{B_\parallel}) \frac{m_c}{\omega_c} e^{(-\varphi'/\omega_c\tau)}. \tag{6.9}$$

The simulations [2] are accomplished by evaluating Eq. (6.9) for a given set of parameters, $\{\omega_c\tau,\ \varphi_{\mathrm{set}},\ \theta\}$. Using Eqs. (2.2) and (2.56), the interlayer component of the electron velocity is evaluated as a function of φ for each cyclotron orbit with given index k_z^0. The φ-dependence of k_z given by Eq. (6.8) is substituted into v_z.

The program for evaluating ADMR from Eq. (6.9) does the following: The energy dispersion Eq. (2.57) in combination with the in-plane dispersion Eq. (1.2) is evaluated for literature parameters t, t', t'' [73] and the band-filling parameter α corresponding to $x = 0.17$. First it evaluates for a number of different k_z^0 in the interval $0 : 2\pi/d$ the FS cross-sections perpendicular to the magnetic field direction given by θ. It was found that $N = 30$ to 50 cross-sections per half unit cell are sufficient for the calculations. The integral over φ in Eq. (6.9) is evaluated for approximately $5N$ points for each k_z^0. Since a weak warping with $2t_\perp \approx 1/30\epsilon_F$ is assumed it is neglected by the program for calculating the cyclotron orbits. In addition it disregards effects, such as closed orbits at high tilt-angles.

First, the program code (see Appendix B) for evaluating Eq. (6.9) has been tested by simulating the AMRO observed on Tl-2201 by Hussey at al. [26]. Thus, the code was initialized with their published parameters[3], namely $k_{00} = 7.45$; $k_{40} = -0.19$; $k_{21} = 0.31$; $k_{61} = 0.21$; $k_{101} = -0.085$, using the parametrized cylindrical FS according Eq. (2.55); $\omega_c\tau = 0.45$ as an isotropic scattering parameter; and of course the corresponding lattice parameters $a = 3.866\,\text{Å}$; $c = 11.6\,\text{Å}$. Fig. 6.9 (a) shows two simulated angular sweeps of $0° \leq \theta \leq 80°$ for $\varphi_{set} = 0°$ and

[2] The computing program for evaluating σ_{zz} from Eq. (6.9) was written in collaboration with P. D. Grigoriev (L. D. Landau Institute for Theoretical Physics, Chernogolovka, Russia).

[3] Note: In the original publication [26] there was a misprint in the best fitting values for k_{61} and k_{101}. The published values were 10 times smaller than actually used in the calculations [83]

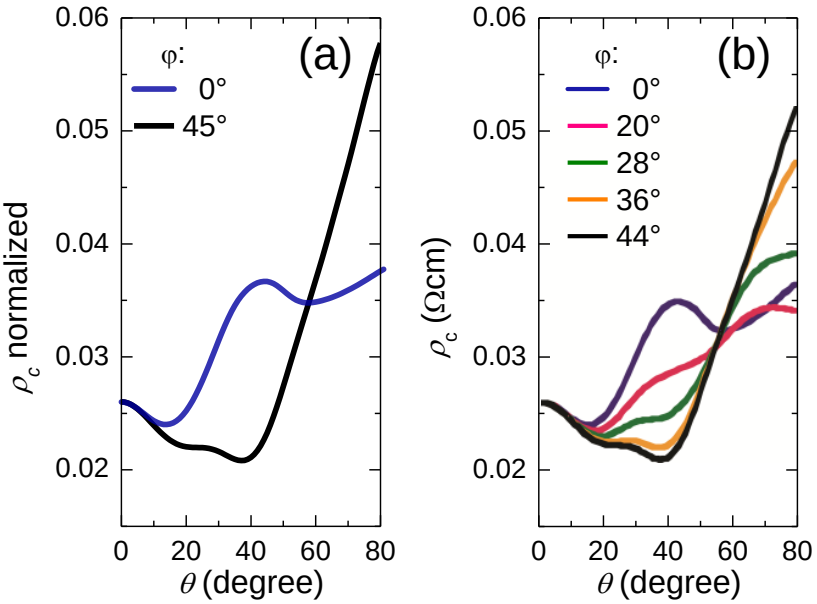

Figure 6.9: (a) Results from the program used later on for AMRO simulations for NCCO initialized with parameters according to [26]. (b) Simulations for Tl-2201 taken from [26].

$45°$, respectively. The plotted resistivity is normalized to show the same value at $\theta = 0°$ as for the Tl-2201 data in Fig. 6.9 (b). The comparison nicely demonstrates the functioning of the used program.

In the following, the results of the simulations of AMRO in NCCO are presented. The experimental AMRO data were fitted progressively by including step by step harmonic terms, $a_m \sin(m\varphi)$, in the φ-dependence of the interlayer energy dispersion Eq. (2.57). The first results are presented in Fig. 6.10 (a) where the ADMR was calculated for $\varphi = 0°$ and $45°$ using $t = 0.38\,\text{eV}$; $t' = 0.32t$; $t'' = 0.5$ and $\alpha = -0.02321\,\text{eV}$ and only a simple interlayer warping term Eq. (2.56) of

$$\epsilon_\perp = -2t_\perp \cos\kappa_z \cdot a_2 \sin(2\varphi). \tag{6.10}$$

The results for different $\omega_c\tau$, ranging from 0.3 to 1.0, are compared with the experimental data for $x = 0.17$ recorded at $B = 45\,\text{T}$, $T = 1.4\,\text{K}$ (grey solid and dashed-dotted curves for $\varphi = 0°$ and $45°$, respectively, highlighted by the light-green filling in between the curves).

Keeping $\omega_c\tau$ fixed at 0.5, the interlayer dispersion is then extended by the next, higher order term $a_6 \cdot \sin(6\varphi)$. The results for varying a_6 from 0.1 to 0.7 are shown

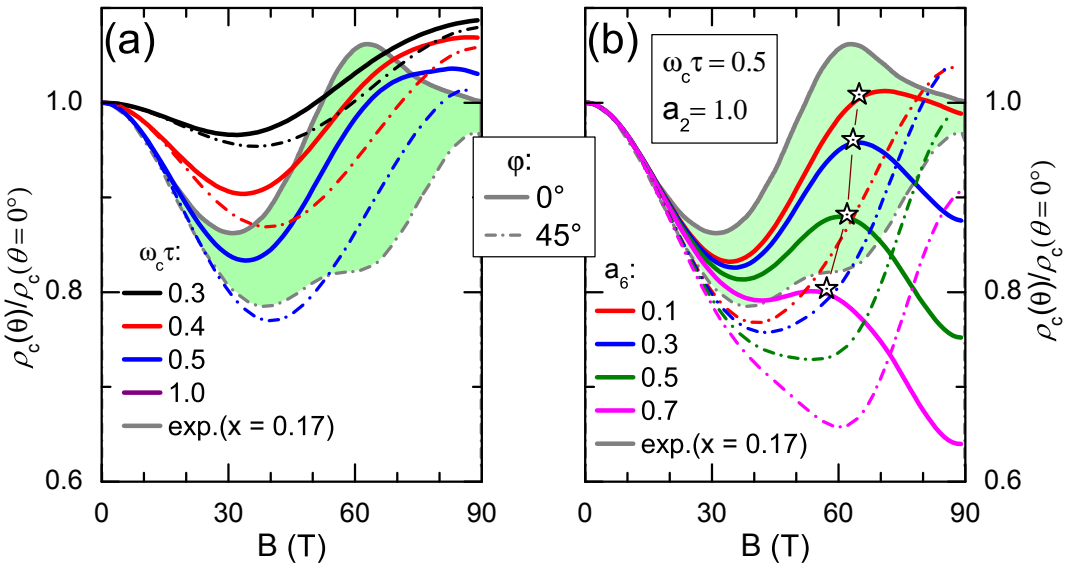

Figure 6.10: AMRO simulations using the in-plane FS according to Eq. (1.2) with band structure parameters $\{t = 0.38$ meV; $t' = 0.32t$; $t'' = 0.5t'\}$ taken from [73] and a simple interlayer warping term of $\cos\kappa_z[a_2\sin(2\varphi) + a_6\sin(6\varphi)]$. (a) $a_6 = 0$, various $\omega_c\tau$. (b) $\omega_c\tau = 0.5$, various a_6. The solid and dashed lines correspond to $\varphi = 0°$ and $45°$, respectively. The stars illustrate how the maximum for $\varphi = 0°$ depends on a_6.

in Fig. 6.10 (b). As soon as the a_6-term is introduced, a maximum evolves for the $\varphi = 0°$ curve at high tilt angles (indicated by stars in Fig. 6.10 (b)). Its θ-position roughly coincides with the maximum position of the as-measured data, for $a_6 \approx a_2/3$. However, the overall shape is quite different and does not really coincide with the experimental data. For $\varphi = 45°$ the AMRO feature is much weaker, as compared to the experiment.

Fig. 6.11 (b) presents a set of calculated ADMR curves normalized to the initial value, at $\theta = 0°$, for various φ. $\omega_c\tau = 0.7$ is set rather high, because for lower $\omega_c\tau$ the maximum for φ-orientations close to $45°$ is much too weak. These results are to be compared with the normalized as-measured data shown in Fig. 6.11 (a). The positions of the maximum between $\theta = 53°$ and $62°$ are plotted in Fig. 6.11 (c). They were extracted from the minimum in the second derivative $\frac{d\rho^2}{d^2\theta}$, as already described in Sect. 6.1. One can see that for this set of parameters the positions nicely coincide with the experimental results. Furthermore, the magnitude of the AMRO feature is similar to that observed in the experiment. Moreover, at high

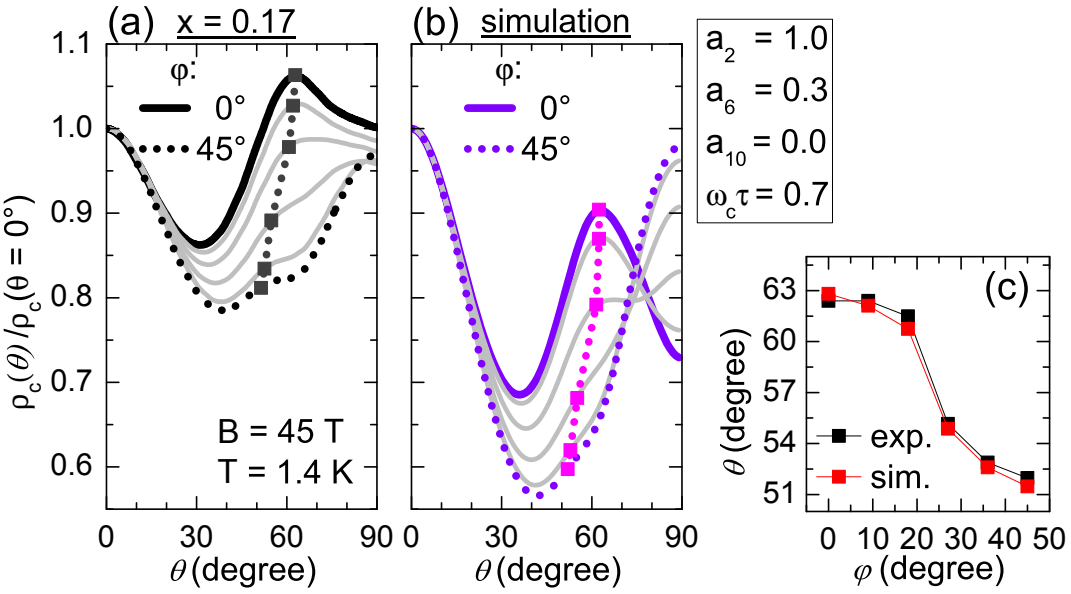

Figure 6.11: (a) Set of experimental θ-sweeps, normalized to $\rho_c(\theta = 0°)$, at different azimuthal angles $\varphi = 0, 9, 18, 27, 36, 45°$ for $x = 0.17$. (b) AMRO simulation with parameter set $\{a_2 = 1; a_6 = 0.3; a_{10} = 0; \omega_c\tau = 0.7\}$. (c) θ-positions of the φ_{set}-dependent maximum marked with black and magenta squares in (a) and (b), respectively.

tilt angles the φ-dependence of the resistivity behaves opposite to what is actually measured. This result is rather unsatisfying, since only similar positions and magnitudes of AMRO are reproduced but the overall ADMR is very different from what is found in the experiment. Obviously there is still a need in improvements of the fitting procedure.

In Fig. 6.12 the 2D projections of the FS and its interlayer corrugation (exaggerated) for two different sets of parameters is shown. Fig. 6.12 (a) shows the projection for the parameter set used up to this point:

$$\{t; t'; t''; \alpha\} = \{0.38; 0.32t; 0.5t'; -0.02321\}\,\text{eV}, \tag{6.11}$$

yielding a relatively quadratic shape of the in-plane FS cross-section. The parameters $a_2 = 1$ and $a_6 = 0.3$ give *zero*-warping, i.e. nodes, along the $(0, \pm\frac{\pi}{a})$- and $(\pm\frac{\pi}{a}, 0)$- directions. The simulations showed no significant changes when the next φ-harmonic a_{10} was introduced. Up to this point the shape of the in-plane Fermi surface has been kept untouched, i.e. t, t', t'' were fixed and only the interlayer dispersion term was varied. As will be shown in the following, it turned out that

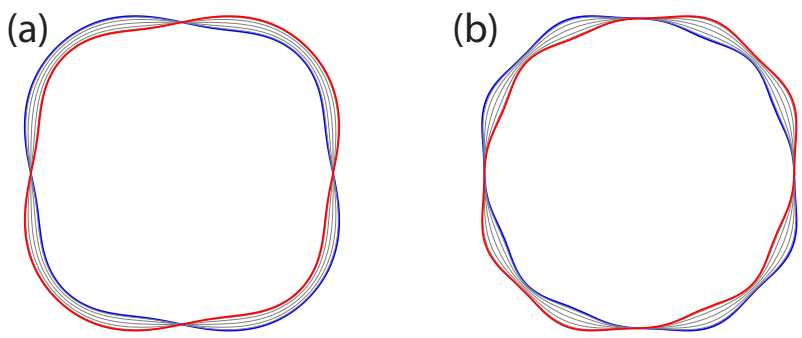

Figure 6.12: Two-dimensional projection of the interlayer FS and its corrugation of the FS for two different sets of parameters (a) $\{t; t'; t''; \alpha\} = \{0.38; 0.32t; 0.5t'; -0.02321\}\,\mathrm{eV}$ [73], and (b) $\{0.38; 0.08t; 2.0t'; -0.13016\}\,\mathrm{eV}$ used in the calculations with the results depicted in Fig. 6.11 (b) and 6.13 (b), respectively.

tuning the in-plane hopping parameters can help to improve the fits significantly. After several attempts the following parameters gave the best results:

$$\{t; t'; t''; \alpha\} = \{0.38; 0.08t; 2.0t'; -0.13016\}\,\mathrm{eV}. \tag{6.12}$$

The new parameter set, Eq. (6.12), yields a more circular cross-section of the FS cylinder with nodes of the warping along the $(0, \pm\frac{\pi}{a})$- and $(0, \pm\frac{\pi}{a})$-directions and a very weak, but non-zero, warping along $(\pm\frac{\pi}{a}, \pm\frac{\pi}{a})$, as can be seen in Fig. 6.12 (b). The corresponding simulations are presented in Fig. 6.13 (b), the central plot. One can see that, compared to previous simulations (Figs. 6.10 and 6.11) not only the positions but also the strength of the AMRO features, observed in the experiment, are satisfactorily reproduced at a much smaller and more reasonable value of $\omega_c\tau = 0.47$, see Fig. 6.13. One can also note that the numerical results fit the experimental data for $x = 0.165$ even better than for $x = 0.17$.

For the in-plane parameters of Eq. (6.12) a much stronger sensitivity of the ADMR to the a_{10} harmonic is observed. For negative a_{10}, especially at high tilt-angles above the main AMRO feature, the curves for different φs are separated from each other and show correct φ-dependence. The more negative a_{10} is set, the weaker they are separated. The value of $a_{10} = -0.3$ was found as the optimum where the high field ADMR and φ-dependence fits the experimental data the best. This set of a_m is more similar to what was found in the AMRO fits for Tl-2201 [26]. In the latter case 8 nodes were found in the interlayer hopping

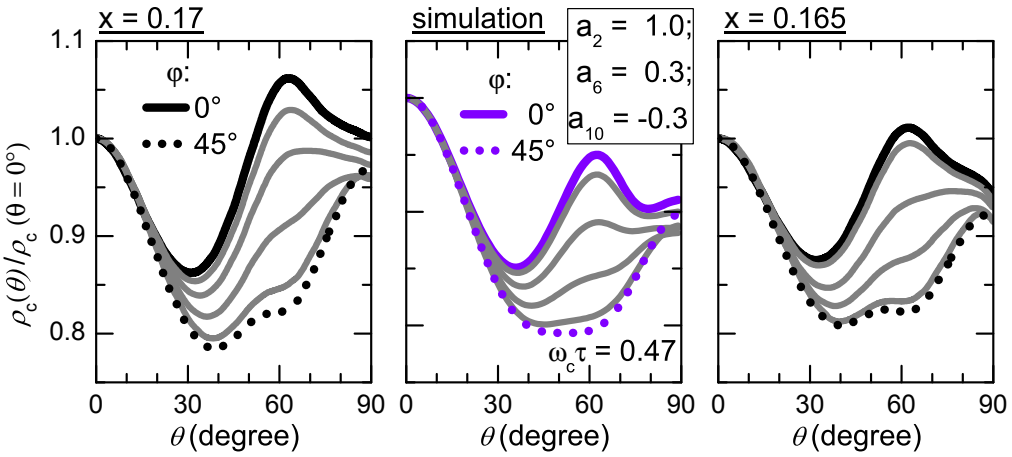

Figure 6.13: (central plot) Numerically calculated AMRO for $\varphi = 0$ to $45°$ in $9°$ steps, with the parameter set for the in-plane dispersion given in Eq. (6.12) and a φ-dependent warping with $a_2 = 1.0$; $a_6 = 0.3$; $a_{10} = -0.3$, in comparison to the experimental AMRO data on $x = 0.17$ (left) and 0.165 (right).

term around the FS, i.e. *zero* warping along the $(0, \frac{\pi}{a})$- and $(\frac{\pi}{a}, \frac{\pi}{a})-$ and equivalent positions in k-space.

6.5 Conclusion: Magnetic breakdown as the origin of AMRO in NCCO

Semiclassical oscillations in the angle-dependence of the interlayer magnetoresistance in overdoped NCCO, so-called AMRO, were identified by their field- and temperature-dependence. The data provide clear evidences that the AMRO originate from magnetic breakdown cyclotron orbits, which are geometrically identical to orbits on the unreconstructed large Fermi cylinder. However, an analysis in terms of a conventional geometrical effect [36] cannot be applied. The observed features are too weak due to a rather low $\omega_c\tau$ of less than 0.5 even at $B = 45\,\mathrm{T}$. Therefore, the interlayer conductivity has to be calculated numerically by applying semiclassical Boltzmann transport equations in the constant τ approximation. Furthermore, due to certain symmetry constraints the interlayer corrugation is relatively complex, giving rise to strong implications on the MR and ADMR of NCCO. Following the approach applied for the AMRO analysis for a strongly overdoped p-doped cuprate Tl-2201 [26], the experimental data on NCCO were reproduced with a satisfying coincidence. The numerical simulations of AMRO yield quantitative information on the 3D FS. In particular, details on the in-plane dispersion relation and the interlayer corrugation were obtains.

From the study of the doping dependence it was found that, as the doping is lowered, not only MB weakens but also the angle-dependence of the MR acquires a shape, resembling that observed on underdoped compositions, where spin-effects are strongly involved in the electronic transport.

7 Passing through optimal doping towards the lower edge of the superconducting dome

7.1 Anomalies observed in the magnetoresistance

One peculiar feature of magnetotransport in NCCO is an anomalous negative slope of the field-dependent magnetoresistance (MR) observed for various doping levels and most pronounced near optimal doping. In the following the behavior of this anomalous MR will be examined and confronted with what was observed for angle-dependent MR (ADMR) and Shubnikov-de Haas (SdH) oscillations. Interestingly, orbital effects such as SdH oscillations and AMRO are found to emerge in fields only above this anomalous regime.

In Fig. 7.1 the interlayer magnetoresistance for different electron concentrations x is plotted versus the magnetic field applied parallel to the c-axis. As the magnetic field is increased, superconductivity is suppressed at a critical field, that varies with doping. Even for optimal doping, where SC is strongest, the normal state is reached above $\sim 10\,\mathrm{T}$. An anomaly, that is a maximum followed by a negative slope, is spotted. For example, for $x = 0.15$, $R_\mathrm{c}(B)$ shows an almost linear increase right above the superconducting transition. At around $18\,\mathrm{T}$ the slope changes to negative and turns back to positive above $28\,\mathrm{T}$. The field B^*, where $R_\mathrm{c}(B)$ starts to deviate from its monotonic increase (marked with grey arrows in Fig. 7.1), is the field at which the first derivative dR_c/dB has a maximum. The turning point B', indicated by black arrows, is determined by the point where the quadratic fit to the high-field MR starts deviating from the experimental data (see the grey dotted lines in Fig. 7.1). For higher doping levels B^* and B' move towards lower fields, see Table 7.1. For example, for $x = 0.16$, $B' \approx 17\,\mathrm{T}$ and for

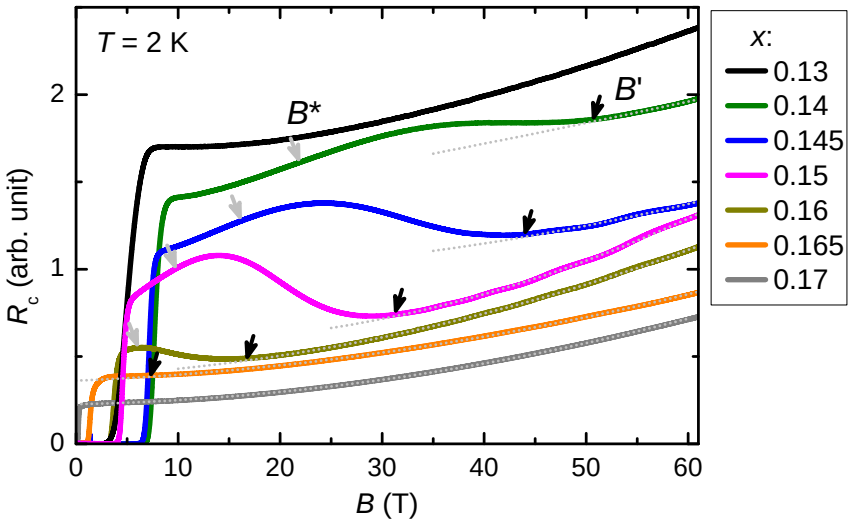

Figure 7.1: Interlayer magnetoresistance R_c recorded in pulsed magnetic fields for different doping levels x, having B perpendicular to the CuO_2-layers. Note: The curves were normalized so that they do not overlap, for a better visibility. The arrows point to the characteristic fields B^* and B', discussed in the text. The grey dotted lines are quadratic fits.

$x = 0.17$ the negative MR is absent and $\frac{\Delta\rho}{\rho} \propto B^{1.8}$ all the way up in the normal state. On the other side, below $x = 0.15$, B' shifts to even higher fields. Finally, for strong underdoping, $x = 0.13$, the magnetoresistance is found to monotonically, almost quadratically increase up to $60\,\mathrm{T}$.

Table 7.1 gives an overview of the characteristic fields, B^* and B' for different doping levels. In the third row it shows the magnetic breakdown (MB) field values, R_{MB}, obtained from SdH data (Sect. 5.1). Apparently, the anomalous MR

x	0.14	0.145	0.15	0.16	0.165	0.17
B' (T)	≥ 51	44	31	17	~ 7	
B^* (T)	25.5	16	10	~ 6	< 5	< 1
B_{MB} (T)			12	3.5	1.5	0.5

Table 7.1: Characteristic fields of the anomalous MR behavior and MB fields with respect to the Ce concentration x. B^* is the field, at which $R_c(B)$ starts to deviate from its initial monotonic increase and B' is the point, above which the high-field MR increases quadratically.

behavior develops in the field range in which the MB effect becomes significant.

For $x = 0.13$, right above the superconducting transition at a critical field and visibly different from the broad anomaly, seen for higher doping levels, there is a weak peak structure in the MR in Fig. 7.1. This second feature is observed for several x in a certain temperature range. Its difference from the broad anomaly becomes even more obvious, when investigating the MR at higher temperatures. For example, in Fig. 7.2 (a), for $x = 0.15$ at $8\,\mathrm{K}$ there are two features discernible: A negative MR is found right above the superconducting transition down to a lower minimum field, B_{LM}, (circles) after which the slope turns positive until a second negative contribution sets in at around B^* (stars), giving rise to the broad anomaly described in the previous paragraph. The negative MR close to the superconducting transition starts being observable near the zero-field superconducting critical temperature, $T_{\mathrm{c}} = 25\,\mathrm{K}$. As T is decreased, it shifts towards higher fields, indicated by the yellow circles. Below $10\,\mathrm{K}$ the second anomalous negative MR at higher fields evolves characterized by B^* (blue stars). Fig. 7.2 (b) shows the MR depending on the temperature while the magnetic field is kept constant. Down to $10\,\mathrm{K}$ the MR decreases as the field increases and the $R(T)$-curves for lower fields cross the ones recorded in higher B due to a small upturn right

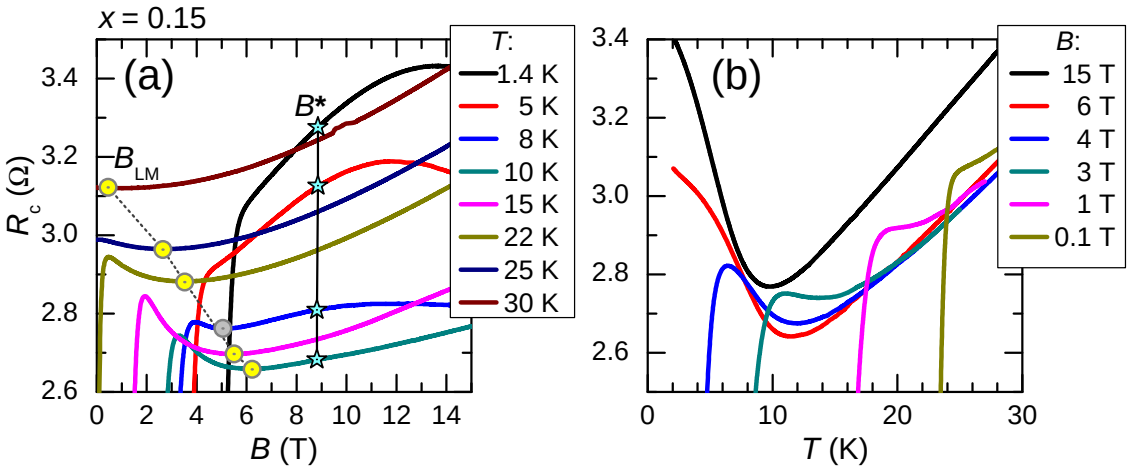

Figure 7.2: Interlayer magnetoresistance R_{c} of an $x = 0.15$ sample recorded in a superconducting $15\,\mathrm{T}$ magnet for (a) field sweeps at different temperatures, $T \leq 30\,\mathrm{K}$ and (b) temperature sweeps in different fields. In addition to B^* (stars), the same as in Fig. 7.1, a new characteristic field related to a low field negative MR is indicated (circles).

above the superconducting transition, although the overall resistance decreases.

A peak in the MR right above the superconducting transition has been also observed in granular [151] and layered organic superconductors [152, 153]. In those cases the peak was attributed to density-of-states fluctuations near the superconducting transition that are responsible for a suppression of the interlayer conductivity [154, 155]. This effect seems to be closely related to vortex dynamics in a quasi 2D superconductor [104, 156]. Nernst effect measurements in n-doped compounds have shown that vortices of the mixed superconducting phase do not play any further role for fields above $10\,\mathrm{T}$ [104, 157]. Thus, while the upturn right above the superconducting transition might be related to SC, the broad maximum in $R(B)$ has a different origin.

Below $10\,\mathrm{K}$ the MR shows a strong increase in field and the $R(T)$-curves do not cross any longer. Obviously below that temperature also the normal-state resistance starts to increase as T goes down. Fig. 7.2 demonstrates that these two anomalies behave differently with respect to their B- and T-dependence, indicating their different origins. Comparing (a) and (b) it becomes clear that the second broad anomaly at higher fields is related to the strong upturn in the normal-state $R(T)$.

The negative MR slope at low T, as well as an upturn in the T-dependence of the resistivity as T decreases, observed in both the hole- and electron-doped cuprates [58, 97, 158–161], is discussed controversially in literature. For example, in p-doped cuprates like $Bi_2Sr_2CaCu_2O_{8+y}$ a doping-dependent minimum in the resistivity is interpreted as the temperature of closing/opening of the pseudogap in this system [58, 60, 162]. For electron-doped $Pr_{2-x}Ce_xCuO_4$ (PCCO) an upturn in $R(T)$ below a minimum temperature has been discussed in terms of weak localization due to disorder [161]. Another suggestion was, that it might be related to Kondo-scattering-processes on impurities, induced by remnant apical oxygen [160].

For thin films of n-doped PCCO at low temperatures Dagan et al. [97] distinguished between an orbital MR, that is present over the whole accessible doping range and a nearly isotropic spin-related MR, that sets in below a critical doping of $x = 0.16$. From magnetotransport measurements in strongly underdoped NCCO samples with $x \leq 0.13$, see the next Chapter 8, negative slopes in $R_c(B)$ were observed. It is known that magnetic interactions are dominating

at low temperatures and can affect the transport in NCCO. Kang et al. [139] investigated the magnetic ordering in NCCO, $x = 0.15$, single crystals by neutron-scattering experiments while changing the external field and temperature. They interpreted their results in terms of antiferromagnetic ordering induced by magnetic field as a consequence of the suppression of SC above the critical magnetic field. These facts suggest that even for slightly overdoped, $x = 0.15$, NCCO the MR is strongly influenced by spin-dependent transport, which is reflected in the anomalous transport. It seems that even for $x = 0.16$ there is such an anomalous MR behavior at considerably lower field of $B \leq 10\,\mathrm{T}$, see Fig. 7.1.

In addition, an interesting fact is that, independently of doping, no magnetic quantum oscillations (MQO) have been observed at fields below the broad maximum in $R(B)$!

This is illustrated in Fig. 7.3, in which the oscillatory component for dopings in the vicinity of the optimum, $x_{\mathrm{opt}} = 0.145$, is exhibited. Of course one might argue that the oscillations simply cannot be resolved any longer at lower fields due to their damping profile. However, both the Dingle damping factor, R_{D}, Eq. (2.38), and the MB reduction factor, R_{MB}, Eq. (2.45), are larger in the case of $x = 0.15$ as compared to those for $x = 0.16$, see Sect. 5.1.6. Indeed, the oscillation amplitude at high fields was found much larger for $x = 0.15$. However, SdH oscillations were resolved for $x = 0.16$ in a much broader field range, down to below $18\,\mathrm{T}$, see, for example, Fig. 5.9. By contrast for $x = 0.15$, no MQO were discernible below $20\,\mathrm{T}$, i.e. below the maximum in the $R(B)$ curve. Moreover, the study of the ADMR in this fields also showed that orbital effects are strongly suppressed in the anomalous regime, see Sect. 6.2.

The fact that MQO are suppressed near the maximum (as indicated by the arrows in Fig. 7.3) is not very surprising, since the anomalous MR in this region is most likely governed mainly by spin-dependent transport. From the present results the exact origin of the broad anomalous maximum in the MR cannot be identified unambiguously. Maybe techniques like muon-spin-resonance or nuclear magnetic resonance performed in high magnetic fields for the doping levels of interest that are sensitive to local magnetism might give further insight into the origin of the anomalies.

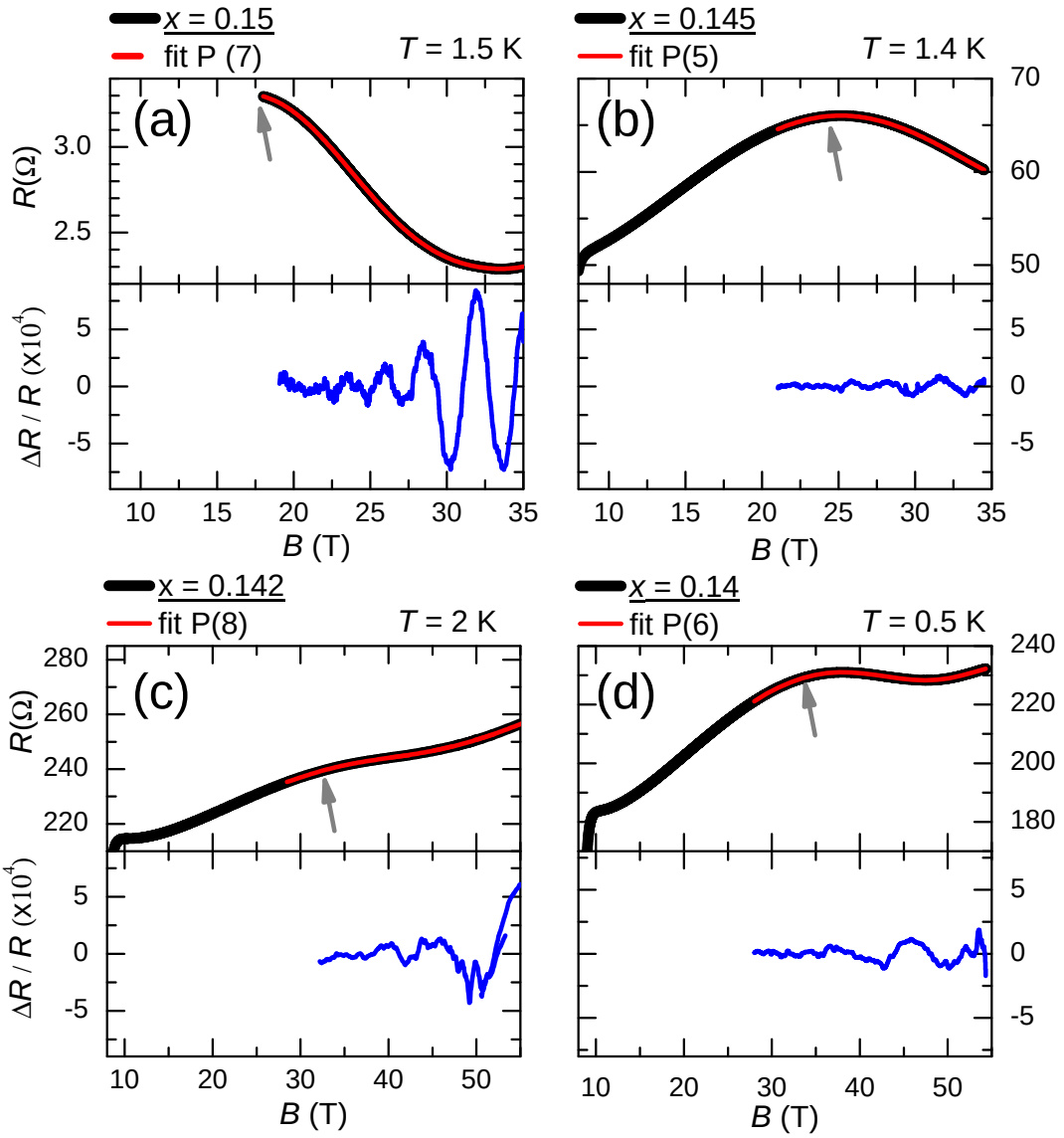

Figure 7.3: Interlayer magnetoresistance (MR) recorded in steady fields up to $35\,\mathrm{T}$ for (a), $x = 0.15$ and (b), 0.145 and recorded in pulsed fields up to $65\,\mathrm{T}$ for (c), $x = 0.142$ and (d), 0.14, with $B||c$-axis. Below each MR curve the oscillatory component (blue), obtained by normalizing the data to a polynomial fit (red), is shown in the vicinity of the broad MR anomaly.

7.2 Abrupt changes right below optimal doping

The slow SdH oscillations, associated with the small α-pocket of the reconstructed FS, presented in Fig. 7.3 for doping levels slightly below the optimal doping, $x_{\mathrm{opt}} = 0.145$, are too weak to be analyzed quantitatively in terms of their B- and T-dependence. By a minor decrease of only $\sim 0.3\%$ in doping the amplitude is suppressed by more than an oder of magnitude. No SdH oscillations were resolved for $x < 0.14$. In Fig. 7.4 (lower panel, blue circles) the peak-to-peak amplitude of the background-normalized α-oscillations at $B = 55\,\mathrm{T}$ and $T = 2\,\mathrm{K}$ is plotted versus x. Near optimal doping the amplitude is strongest

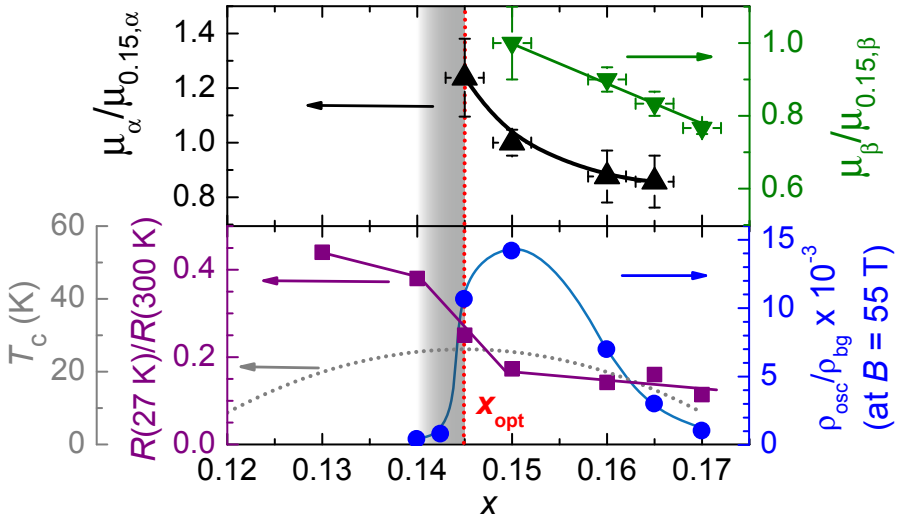

Figure 7.4: Upper panel: Effective masses determined from the α- (black) and β- (green) SdH oscillations (normalized to the value at $x = 0.15$), same as in Fig. 5.12. Lower panel: The relative peak-to-peak α oscillation amplitude at $B = 55\,\mathrm{T}$, $T = 2\,\mathrm{K}$ (blue circles) and the resistance ratio $R(T = 27\,\mathrm{K})/R(T = 300\,\mathrm{K})$ (purple squares) plotted versus the doping x. The grey dotted line indicates T_{c}.

and as x is increased further it weakens monotonically. Due to MB, oscillations from the α-pocket are damped stronger the larger the MB probability, Eq. (5.1), grows. For example, for $x = 0.17$, where $B_{\mathrm{MB}} = 0.5\,\mathrm{T}$, at $55\,\mathrm{T}$ the reduction due to MB for the α-oscillations, Eq. (5.2), is twenty times stronger than for $x = 0.15$, where $B_{\mathrm{MB}} \geq 12\,\mathrm{T}$. This explains the decrease of the α- and the growth of the β-oscillation amplitudes as the doping increases, see e.g. Fig. 5.15. In addition, the

Dingle temperature was found to be larger at strong overdoping, which would contribute to an overall damping of the SdH oscillations at increasing x.

Therefore, for $x < x_{\mathrm{opt}}$ the SdH oscillations would be expected to become even better pronounced which clearly contradicts the experiment. Obviously, their sudden strong damping observed right below x_{opt} (illustrated by plotting $\tilde{\rho}/\rho_{\mathrm{backgr.}}$ at $B = 55\,\mathrm{T}$ in the lower panel of Fig. 7.4) is related to some other severe changes in the electronic properties of NCCO.

In the upper panel of Fig. 7.4 the doping-dependence of the effective cyclotron masses, μ_α and μ_β (already presented in Sect. 5.1.5) normalized to the value at $x = 0.15$, $\mu_{0.15,\alpha} = 1.05$ and $\mu_{0.15,\beta} = 3.0$, are plotted versus x. μ_α grows by almost $50\,\%$ as x is tuned from 0.17 down to optimal doping, see the black triangles in Fig. 7.4. Since the oscillation frequency of $F_{\alpha,0.14} \approx 300\,\mathrm{T}$ did not change very much compared to that at x_{opt}, this enhancement of the effective cyclotron mass cannot easily be explained by changes in the size of the α-pocket. On the other hand, μ could be increased due to strong many-body interactions [35]. For example, it is found to strongly diverge in the vicinity of quantum critical points [163, 164]. While it is too early to speak about a diverging effective cyclotron mass in NCCO, its enhancement towards x_{opt} obviously reflects the increasing role of many-body interactions.

Since the mass contributes to the temperature and Dingle reduction factors R_{T} and R_{D}, a considerable increase of μ could be responsible for the strong suppression of the oscillation amplitude. A strong change for the main charge carriers should also have an impact on the zero-field interlayer resistance. Indeed, the ratio between the resistance at low temperatures above the superconducting transition and at room temperature, $R(27\,\mathrm{K})/R(300\,\mathrm{K})$, shows a rapid growth below x_{opt}, see Fig. 7.4 (purple squares).

Summarizing, in a narrow interval of x, right below optimal doping highlighted by the grey colored region in Fig. 7.4 the SdH signal is strongly suppressed and the effective cyclotron mass seems to be strongly enhanced. Furthermore, there is a jump in the zero-field resistance. These observations suggest a considerable change in the electronic system occurring in this doping interval. An access to information about the FS by MQO is not possible in this range. Thus, other experimental techniques, i.e., Hall effect and thermoelectric measurements are needed to gain further insights to the FS evolution in the underdoped region.

7.3 Hall effect in NCCO

7.3.1 Experimental results

To gain further insights in the electronic structure of NCCO, in particular below optimal doping, a series of measurements of the low-temperature Hall effect were accomplished for superconducting crystals with doping ranging from $x = 0.165$, strong overdoping, to 0.13, strong underdoping. The results recorded in steady and pulsed magnetic fields up to $15\,\mathrm{T}$ and $60\,\mathrm{T}$, at temperatures of $T = 4.5\,\mathrm{K}$ and $1.8\,\mathrm{K}$, respectively, are presented in Fig. 7.5 (a) and (b). The data below $15\,\mathrm{T}$ is consistent with that reported earlier [98]. At fields below $15\,\mathrm{T}$ for all doping levels except for $x = 0.165$ an almost linear, negative Hall signal is found right above

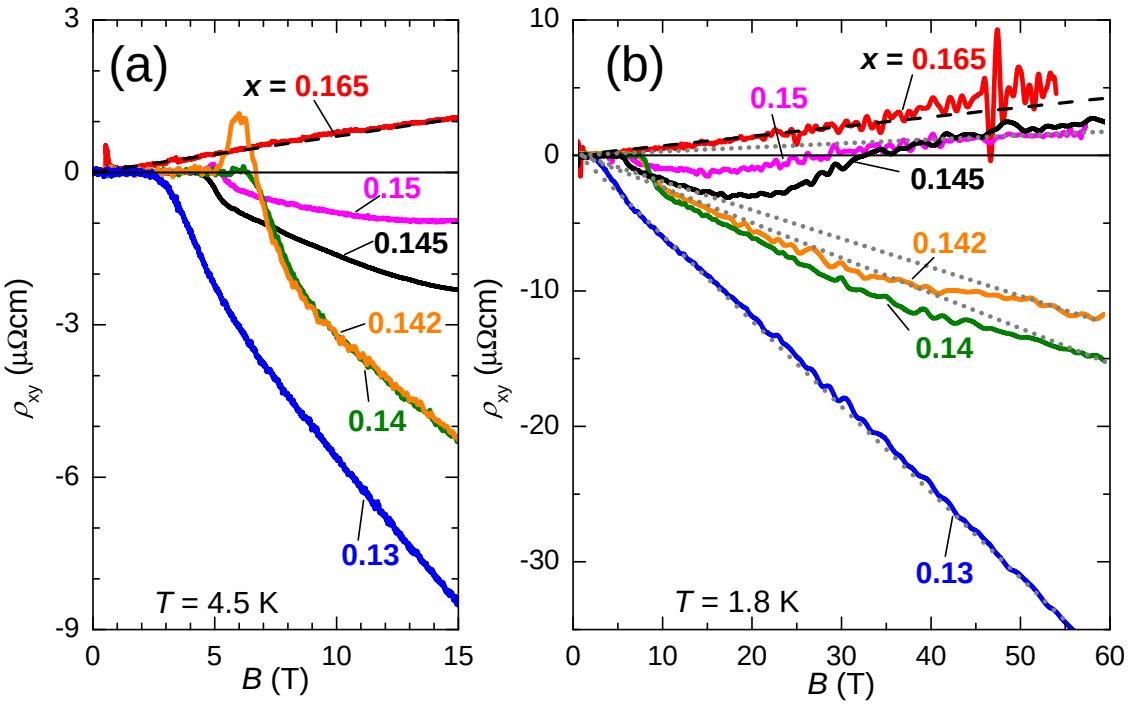

Figure 7.5: (left) Hall resistivity for NCCO crystals with $0.13 \leq x \leq 0.165$ recorded in steady (sweep rate $0.5\,\mathrm{T/min}$) magnetic field up to $15\,\mathrm{T}$ at $T = 4.5\,\mathrm{K}$. (right) The same samples measured in pulsed fields up to $60\,\mathrm{T}$ at $T = 1.8\,\mathrm{K}$. (dashed line) theoretically expected linear dependence for $x = 0.165$ with $R_\mathrm{H} = 0.071\,\mu\Omega\mathrm{cm/T}$ due to a solely hole-like unreconstructed FS. (dotted lines) linear fits of the high field parts.

the superconducting transition. The black dashed line is a calculated curve of the field dependent Hall resistivity $\rho_{xy} = R_{\mathrm{H}}B$ for $x = 0.165$ according to Eq. (2.14) from Sect. 2.2. The slope corresponds to the Hall coefficient expected for a solely hole-like FS covering $(1 - x) \cdot 100\,\% / 2 = 41.75\,\%$ of the first Brillouin zone of NCCO. It nicely coincides with the as-measured curve for the $x = 0.165$ sample. ρ_{xy} of the $x = 0.165$ sample recorded in pulsed fields increases further, following the linear theoretical curve up to the highest field, see Fig. 7.5 (b). For $x = 0.13$ ρ_{xy} keeps its initial negative slope up to $55\,\mathrm{T}$. For the intermediate doping levels the observed high-field curves show deviations from their low-field dependence, see Fig. 7.5 (b). In the case of optimal doping (black curve) the signal starts turning towards a positive slope, finally crosses zero as the field increases above $\sim 30\,\mathrm{T}$ and continues linearly with a slope, similar to that of the overdoped samples with $x = 0.15$ and 0.165. By only a minor change in doping of $\sim 0.3\,\%$ below x_{opt} the strong positive contribution suddenly vanishes and the signal displays a monotonic B dependence with a rather steep negative slope. For $x = 0.142$ and 0.14, there is an interval at which the negative signal deviates only weakly from its initial linear dependence. However, at fields above 45−-$50\,\mathrm{T}$ it turns back to a non-saturating linear dependence extrapolating to zero at $B = 0\,\mathrm{T}$, see the grey dotted lines in Fig. 7.5.

Fig. 7.6 exhibits the pulsed field data recorded at various temperatures for the same samples described above. For $x = 0.165$ the high-field Hall signal approaches zero as the temperature is increased to approximately $100\,\mathrm{K}$. For optimal doping, $x = 0.145$, the anomalous minimum, at $B = 18\,\mathrm{T}$ and $T = 1.4$–$4.2\,\mathrm{K}$ broadens and shifts to higher fields as the temperature is increased. At $T \geq 10\,\mathrm{K}$ $\rho_{xy,0.145}(B)$ is negative up the highest field. The temperature dependence for the slightly overdoped $x = 0.15$ sample is similar to that of the latter. However, the fields at which $\rho_{xy}(B)$ changes to positive are smaller and the temperature at which the high-field signal turns negative is higher as compared to $x_{\mathrm{opt}} = 0.145$. For dopings below the optimum the overall Hall signal stays negative at elevated temperatures, at least in the accessed T-range of $1.4\,\mathrm{K}$ to $90\,\mathrm{K}$. Moreover, the relative change of ρ_{xy} with temperature becomes significantly weaker, as the doping level is decreased below x_{opt}. Apparently both $\rho_{xy}(B)$ and $\rho_{xy}(T)$ change dramatically right below x_{opt}.

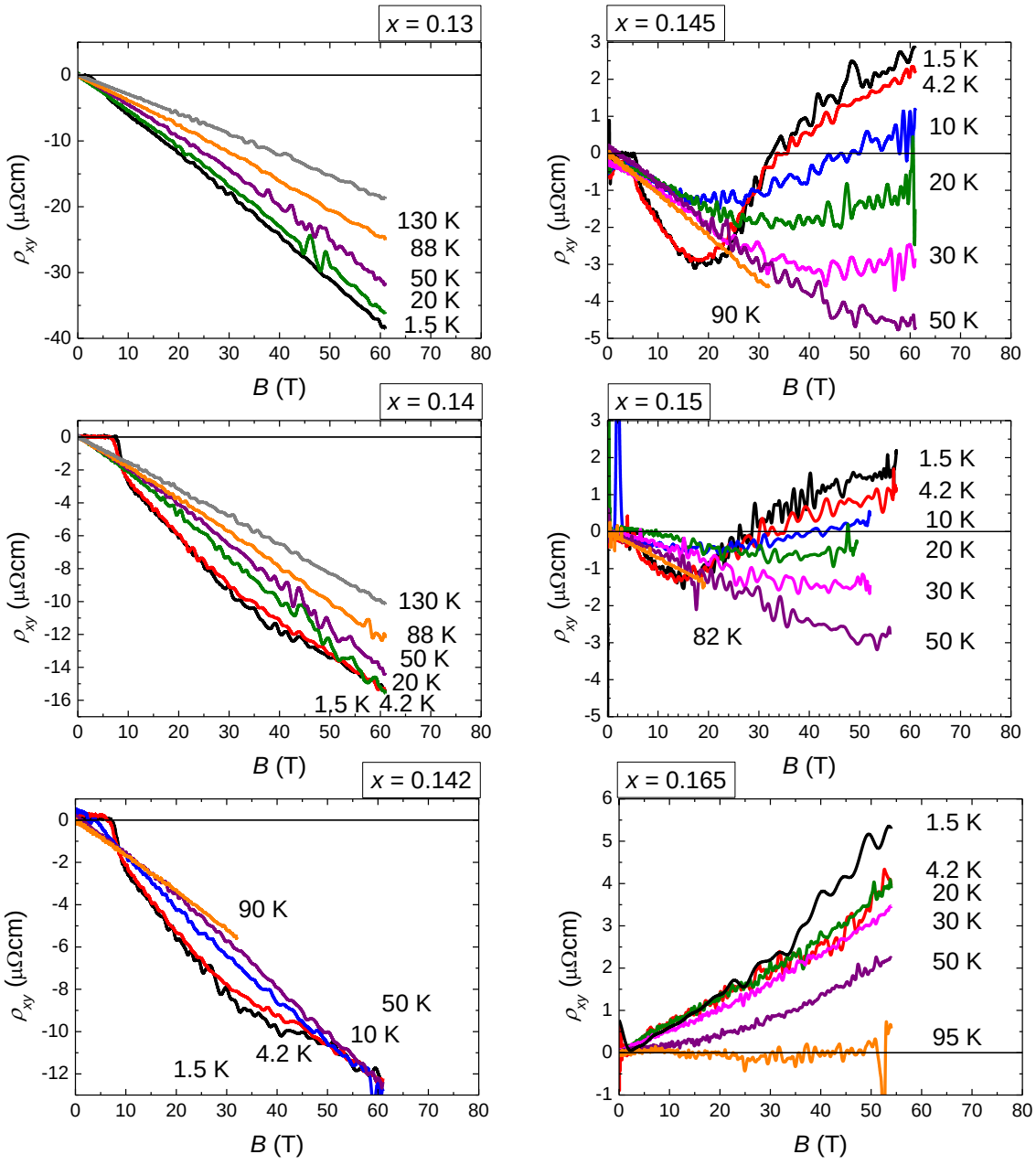

Figure 7.6: Hall resistivity, ρ_{xy}, versus the applied magnetic field $B = \mu_0 H_{\mathrm{ext}}$ for various doping levels x recorded in pulsed magnetic fields up to $60\,\mathrm{T}$ at different temperatures.

7.3.2 Discussion

At low temperatures, between $1.4\,\mathrm{K}$ and $4.2\,\mathrm{K}$ no considerable T-dependence is discernible. Thus, a real low-T regime is reached, where inelastic scattering effects can be neglected. At low fields, due to competing contributions of electron- and hole-like charge carriers on the reconstructed FS, a small negative Hall signal is induced. The sign change of the Hall signal for $x = 0.145$ and 0.15 can be perfectly understood in terms of magnetic breakdown (MB). According to the suggested reconstructed FS the electron-like pockets are much larger than the hole pockets, see Sect. 1.3.3. And hence a negative Hall coefficient is qualitatively consistent with the expectations. The analysis of SdH data for $x = 0.15$ yielded a MB field of $B_{\mathrm{MB}} = 12\,\mathrm{T}$ (see Sect. 5.15), which is close to the point where the low-T Hall signal (Fig. 7.5) starts to deviate from its linear negative field dependence. The higher the field grows, the stronger the large hole-like MB orbit contributes, giving rise to the observed overall positive high-field Hall signal for $x \geq 0.145$. Also consistent with what was found from SdH analysis in Sect. 5.1.9, is that the MB field shifts towards lower values as the doping increases. For the $x = 0.15$ sample, the sign-change in the Hall signal is at a smaller field as compared to $x_{\mathrm{opt}} = 0.145$. For strong overdoping only a positive signal is left and no negative contribution is resolvable, obviously due to the very low MB field, $B_{\mathrm{MB},0.6} = 1.5\,\mathrm{T}$. Therefore, these findings are consistent with a two-band model suggested by previous Hall experiments on n-doped cuprate compounds [73, 96, 98, 165].

One of the most interesting observations here is the dramatic changes in $\rho_{xy}(B)$ and $\rho_{xy}(T)$ right below $x_{\mathrm{opt}} = 0.145$ by only a minor step in doping (of $\sim 0.3\,\%$). The sudden change becomes even better visible when plotting the low-T Hall coefficient, $R_{\mathrm{H}} = \rho_{xy}/B$, at a fixed magnetic field versus the doping, as depicted in Fig. 7.7. In addition, the coefficients are plotted which one would expect from the large MB orbit corresponding to the unreconstructed FS with $(1 - x)$ holes per unit cell, i.e. per Cu-site, (magenta curve) and from a FS consisting solely of electron-like pockets with x electrons per Cu-site (dark cyan curve), that is

$$R_{\mathrm{H}} = \frac{1}{ne} = \frac{V_{\mathrm{cell}}}{Ne}, \tag{7.1}$$

with $V_{\mathrm{cell}} = a^2 d = 3.95^2 \cdot 6.04\,\text{Å}^3$ and $N = 1 - x$, for hole-like and $N = -x$, for electron-like charge carriers. As one can see in Fig. 7.7, the positive high-field Hall

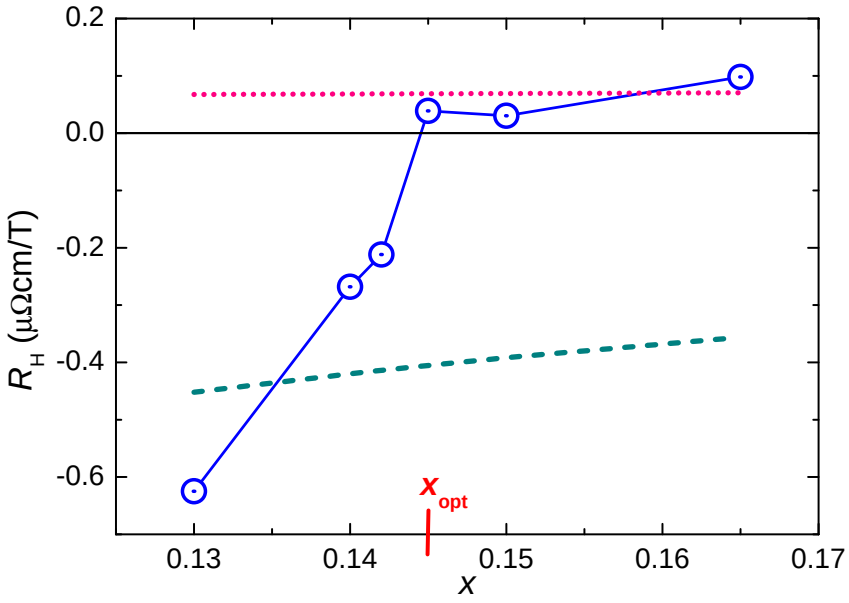

Figure 7.7: (blue circles) Hall coefficient R_{H} at $B = 50\,\mathrm{T}$ and $T = 1.8\,\mathrm{K}$; (dotted curve) theoretically expected R_{H} for the unreconstructed hole-like FS according to the doping x and for a reconstructed FS consisting solely of electron-like pockets (dashed curve).

coefficient for $x = 0.145, 0.15$ and 0.165 is close to that expected for the MB orbit (magenta curve). For $x = 0.142$ and 0.14 it is significantly below the absolute value expected for solely electron-like contributions and in the case of 0.13 its absolute value is found even larger by $\approx 20\,\%$.

A feasible explanation for the step in R_{H} is that the MB field simply grows as the doping decreases, and thus for $x < x_{\mathrm{opt}}$ a field of $60\,\mathrm{T}$ is not high enough any longer. While for $x \geq x_{\mathrm{opt}}$ the field, at which the Hall signal turns up, changes by less than $20\,\%$ for $\Delta x = 0.5\,\%$, below x_{opt} for only $\Delta x = -0.3\,\%$ there is suddenly no upturn foreseeable up to at least three times larger fields. This suggests that the MB gap enhances strongly. For $x \geq x_{\mathrm{opt}}$ a small energy gap of the order of $\sim 10\,\mathrm{meV}$ was found for which the MB regime is fully accessible by relatively low fields, as discussed in Sect. 5.1. Evidently, optimal doping $x = 0.145$ is a critical point in the normal state phase diagram of NCCO.

The strong enhancement of the energy gap, representing the superlattice potential responsible for the FS reconstruction, might be related to the onset of long-range AFM in NCCO. As was sketched in the introduction (Sect. 1.4) the doping

at which long-range AFM sets in is controversially discussed in literature. Although inelastic neutron scattering experiments [75] suggested no overlap of the SC and AFM, their data on the spin-correlation length $\xi(T)$ is consistent with long-range AFM setting in below $x_{\mathrm{opt}} = 0.145$, see Fig. 1.6 in Sect. 1.4.

Very weak slow SdH oscillations were observed below x_{opt} for $x = 0.142$ and 0.14, see Fig. 7.3, with a frequency of $F \approx 300\,\mathrm{T}$, similar to that for x_{opt}. It cannot be excluded that there is a minor inhomogeneous doping distribution of x_{opt}. For $x < x_{\mathrm{opt}}$ the SdH signals are too weak for quantitative analysis. But, a weak contribution of the small hole-like α-pockets could also be responsible for the slightly smaller absolute Hall coefficient at $x = 0.142$ and 0.14 as compared to what it is expected, according to the nominal doping x, for solely electron-like contributions, see Fig. 7.7.

Similar Hall effect experiments, as presented in this work, on thin films of n-doped $Pr_{2-x}Ce_xCuO_4$ were performed in pulsed fields by Li et al.[165]. The observed low-T Hall signal for an $x = 0.15$ PCCO film is negative, showing a strong curvature in the normal state, but does not turn to positive even at highest field of $60\,\mathrm{T}$. For higher doping, $x \geq 0.16$ Li et al. observe an overall positive low-T Hall signal and attribute this change with a FS transformation from reconstructed to unreconstructed at a critical doping, as it was suggested by previous Hall effect and thermopower results on PCCO films [96, 166] at slightly higher doping. Qualitatively, the overall positive Hall signals for overdoped PCCO, are similar to that observed for overdoped, $x = 0.165$, NCCO. However, the SdH oscillation analysis in Sect. 5.1 provide clear evidences for the presence of the reconstructed FS till the upper edge of the superconducting region. A reason, why there are no pronounced features observed for PCCO that can be related to MB, might be because of a lower quality of thin films, as compared to bulk single crystals and a broader Ce distribution in the samples. In addition, for bulk crystals of PCCO it is known that they have a slightly by $\sim 1\,\%$ shifted phase diagram [98] as compared to NCCO. It is likely that the results on PCCO indicate the same critical point near x_{opt} in the phase diagram as for NCCO, associated with the point where long-range-AFM sets in.

So far, when it came to quantitative analysis of Hall effect data in n-doped cuprates the considerable contribution of magnetic breakdown has been neglected completely [73, 167]. It is likely that some results, such as the ones on

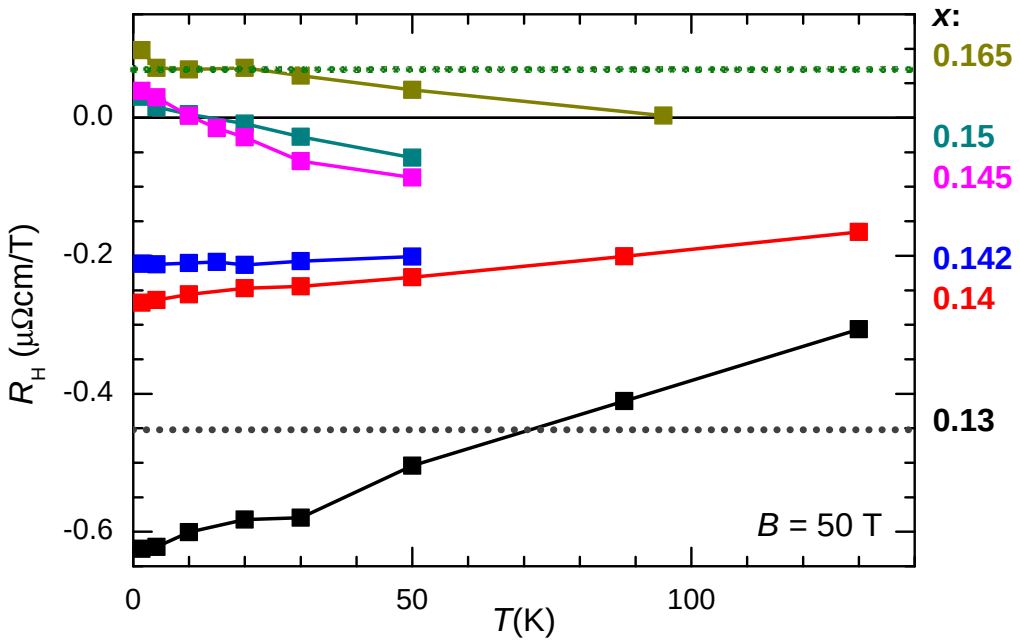

Figure 7.8: Temperature dependence of the high-field Hall coefficient R_{H} at $B = 50\,\mathrm{T}$ extracted from Fig. 7.6. Dashed lines show the expected R_{H} for $x = 0.165$ and 0.13, respectively.

PCCO [165] have to be revisited, taking into account MB. The small MB field values ($\sim 1\,\mathrm{T}$) for overdoped samples of NCCO, obtained from SdH oscillations (Sect. 5.1), show that MB can give rise to positive contributions to the Hall signal already at relatively low fields.

The fact that $|R_{\mathrm{H}}|$ for $x = 0.13$ is larger than expected could be due to several reasons. One is that due to a non-homogeneous current distribution the actual thickness of the investigated sample was smaller than estimated from its apparent geometry. However, $20\,\%$ seems too much. Similarly stronger negative Hall signals have been reported for underdoped thin films of n-doped $Pr_{2-x}Ce_xCuO_4$. Charpentier at al. [100] showed that in their case the annealing process had a strong impact on the Hall coefficient. Due to an improved heat treatment, they were able to reduce precipitations, with dimensions comparable to the film thickness, that have a strong effect on transport in thin films. However, for bulk single crystals, where the current is distributed over the bulk, the effect should be much weaker. In the present study two samples of strongly underdoped, $x = 0.13$, compositions were measured, showing both a too large negative Hall coefficient.

Another possibility to explain the anomalous enhancement of R_{H} for $x = 0.13$ is to imagine that the area of the electron-like FS pockets is much smaller than expected, meaning a reduced electron concentration at the Fermi level, and thus a violation of Fermi liquid model. The strongly enhanced gap in the underdoped regime might have an effect on the size of the electron-like FS parts, too. Further investigations are needed to clarify this point in more detail. The large absolute value of the Hall coefficient for both n- and p-doped cuprates is actually one of the anomalous transport properties which has not been understood completely to date.

For quantitative analysis of the temperature-dependent Hall coefficient further detailed measurements are still to be done. A qualitative idea can be obtained from Fig. 7.8, where the T-dependence of the Hall coefficient extracted from the pulsed field data at $B = 50\,\mathrm{T}$ for temperatures of up to $T = 150\,\mathrm{K}$ is presented.

The growth of $|R_{\mathrm{H}}|$ upon decreasing temperature for underdoped cuprates has been associated with an emerging pseudogap [167]. This has raised doubts that cuprates can be described in terms of conventional Fermi-liquids [65, 167]. Kontani at al. [167] developed a theory capable to explain the anomalous enhancement of R_{H} and its temperature dependence within the Fermi-liquid model. They apply the Landau-Fermi liquid theory, taking into account so-called current vertex corrections due to strong magnetic fluctuations in an almost antiferromagnetic metal. A detailed explanation goes beyond the scope of this thesis. The basic idea is that during the scattering process at the "hot-spot" regions, i.e. the crossing points of the FS with the antiferromagnetic Brillouin zone, the quasiparticles exchange a low-energy antiferromagnetic magnon fluctuation responsible for changes in the scattering time and the sign of the Fermi-velocity. Due to this sign change a negative current contribution emerges that leads to enhancing corrections in the Hall coefficient. This theory may be able to explain the dependence of R_{H} at high temperatures of $T \geq 100\,\mathrm{K}$. But, since the effect of current vertex corrections is expected to weaken as the temperature approaches the regime, where the damping rate due to antiferromagnetic fluctuations becomes smaller than the elastic scattering rate, a further increase of the negative Hall coefficient (as it is found for the underdoped samples) cannot be explained any more.

7.4 Conclusion: A second critical point in the phase diagram

The interlayer MR of NCCO shows an anomalous, doping-dependent peak structure that depends on magnetic field and temperature. While a negative MR right above the superconducting transition seems to be closely related to SC, the broad anomalous maximum at higher fields is mainly related to a spin-dependent transport. This anomalous regime is found to persist up to increasingly higher fields as the doping is decreased. Apparently, effects like AMRO and MQO are only observable above the latter anomaly, for fields where the MR shows a more conventional behavior.

A severe change in the electronic system near optimal doping, $x_{\mathrm{opt}} = 0.145$, is indicated by a strong enhancement of the effective cyclotron mass μ_α and a significant step in the zero-field resistance, as the doping is decreased towards the underdoped side. This is indicative for an enhancement of many-body interactions in the system.

The detailed investigation of the low-temperature Hall effect for various dopings revealed a sudden and strong growth of the energy gap that represents the superlattice potential responsible for the FS reconstruction in the overdoped region, right below $x_{\mathrm{opt}} = 0.145$. Obviously x_{opt} is the point in the phase diagram, below which long-range AFM sets in.

8 The strongly underdoped regime - playing with spins

Understanding how the electrons in the antiferromagnetic underdoped regime of NCCO are coupled to the spin system is a very important issue. An anomalous background is found, for example, in the angle dependence of the magnetoresistance (MR) for $x = 0.15$, see Sect. 6.2, which clearly has an origin different from conventional orbital. As was shown in Sect. 7.1, anomalies in the T- and B-dependence of the resistivity associated with a spin-dependent transport are observed and become stronger pronounced as the doping is decreased. From the absence of the spin-splitting effect in the angle dependence of SdH oscillations in slightly overdoped samples (Sect. 5.2) an antiferromagnetic ground state is suggested that may be very weak or fluctuating but at least stable enough to reconstruct the FS of NCCO. In Sect. 7.3 the study of Hall effect at various doping levels revealed a strong enhancement of the superlattice potential right below optimal doping, $x_{\mathrm{opt}} = 0.145$, suggesting that long-range AFM sets in at this point. In strongly underdoped NCCO far away from the superconducting region AFM is fully established and plays a dominant role in the electronic properties of the system. For the undoped mother compound Nd_2CuO_4 it is known that the coupling between Nd^{3+} and Cu^{2+} becomes stronger upon decreasing T due to the increasing magnetic moment of the neodymium ($\sim 1.3\mu_{\mathrm{B}}$ at $0.4\,\mathrm{K}$) [43]. For low T also the Nd^{3+} sublattice orders antiferromagnetically, similar to the Cu spins, see Sect. 1.3.2. In the following selected data on angle-dependent MR (ADMR) with a field varied either in a plane perpendicular or parallel to the CuO_2-layers will be presented. The observations demonstrate the influence of competing magnetic interactions at low T on the interlayer transport in high magnetic fields.

8.1 Varying the field orientation parallel to the conducting layers for strongly underdoped non-superconducting samples

Figures 8.1 (a) and (b) present data on MR of strongly underdoped, $x = 0.10$ and 0.05, NCCO samples in magnetic field oriented parallel to the CuO_2-layers. The field was swept up to $14\,\mathrm{T}$ and oriented either parallel to the crystallographic a-axis, that is the $[100]$ direction along the Cu-O-Cu chains (black curves), or at $45°$ from the a-axis, that is the $[110]$ direction along the Cu-Cu chains (red curves). For comparison, analogous data on even lower doped NCCO, $x = 0.033$ and 0.025, published recently by Wu et al. [47], are shown in Fig. 8.1 (c) and (d). For all four doping levels there is a step-like feature at $B \approx 1.1\,\mathrm{T}$ and $3.5\,\mathrm{T}$ for $B||[110]$ and

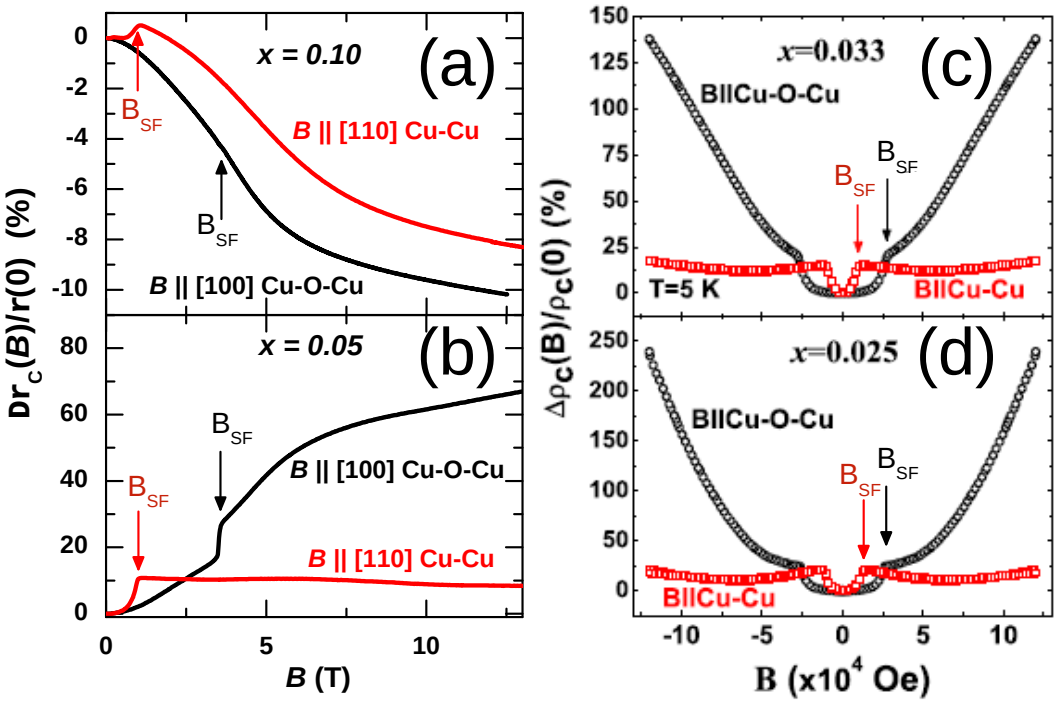

Figure 8.1: Interlayer magnetoresistance (MR) for the field oriented parallel to the conducting layers, (red) $B||[110]$ and (black) $B||[100]$, for $x = 0.10$ (a) and 0.05 (b) at $1.4\,\mathrm{K}$. Similar data for $x = 0.033$ (c) and 0.025 (d) at $5\,\mathrm{K}$ reported by Wu et al. [47].

$B||[100]$, respectively. For $x = 0.10$ the step in the curve recorded for $B||[100]$ is hardly discernible, but the position is not different from the lower doping levels. A large anisotropy was observed for the strongly underdoped samples [47]. For example, for $x = 0.025$ the MR, $\Delta\rho_c(B)/\rho(0)$, increases for $B||[100]$ by more than $230\,\%$ and for $B||[110]$ by only $20\,\%$. This difference weakens as the doping increases. For $x = 0.033$ it is already by a factor of two smaller. By contrast to the strong slope of the MR curve at $B||[100]$ in Fig. 8.1 (c) and (d), in the case of $x = 0.05$ [Fig. 8.1 (b)] there is a bending around $5 - 8\,\mathrm{T}$ above which the MR increases further almost linearly but with a weaker slope. For $x = 0.10$ [Fig. 8.1 (a)] the MR changes sign and the anisotropy is opposite. With a difference between the two extremal orientations of $\approx 2\,\%$, it is rather small. Again at around $5 - 8\,\mathrm{T}$ the MR changes its slope but increases further almost linearly.

As the azimuthal field orientation is varied within the ab-plane, the MR oscillates with a fourfold symmetry, see Figs. 8.2 and 8.3. For $x = 0.05$ the curve

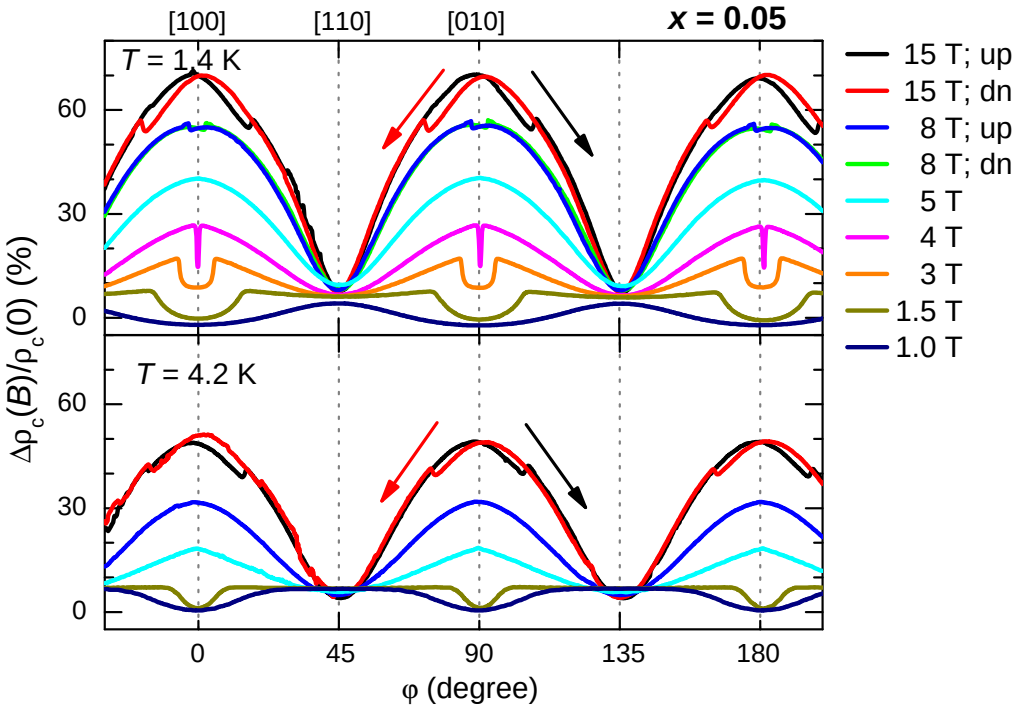

Figure 8.2: Angle-dependent interlayer MR of an $x = 0.05$ sample for field rotations in the plane parallel to the conducting layers at $T = 1.4\,\mathrm{K}$ (top) and $4.2\,\mathrm{K}$ (bottom).

recorded for $B = 1.0\,\mathrm{T}$ shows a maximum at the $[110]$-direction and a minimum at $B||[100]$. At larger fields a step occurs as the orientation approaches the $[110]$-direction. Around $B \leq 5\,\mathrm{T}$ the step-like feature is gone and the anisotropy is opposite to that at $1\,\mathrm{T}$. For $B \geq 8\mathrm{T}$ a new step-like feature becomes visible that, in addition, depends on the rotation direction (indicated by the arrows).

As one can see in Fig. 8.2 rotations at a higher temperature of $T = 4.2\,\mathrm{K}$ are qualitatively similar. However, already in the $1\,\mathrm{T}$ curve a step-like feature can be traced, and thus it seems to occur already for lower fields at this temperature. The hysteretic feature observed in the $15\,\mathrm{T}$ curves cannot be resolved for $B = 8\,\mathrm{T}$ any more. Apparently this feature needs higher fields as T increases.

The rotation data for $x = 0.10$ in Fig. 8.3, recorded at $T = 1.4\,\mathrm{K}$, shows a similar φ-dependence as observed for the lower doping levels at fields below $2\,\mathrm{T}$. The main difference at larger fields comes from the overall negative MR, as was shown in Fig. 8.1. At $B = 1\,\mathrm{T}$ the MR is positive. But as the field grows it becomes negative and, thus, the anisotropy in the MR changes its sign. Again there are step-like features in the vicinity of the $[100]$-direction at low and high fields. The hysteretic one at higher fields is already discernible starting from $B = 5\,\mathrm{T}$, which is even lower than for $x = 0.05$ but due to the reduced φ-anisotropy it appears much stronger pronounced.

At the critical field B_{SF} the Cu^{2+} spin-lattice undergoes a spin-flop transition from the noncollinear to collinear antiferromagnetic ordering, see Sect. 1.3.2,

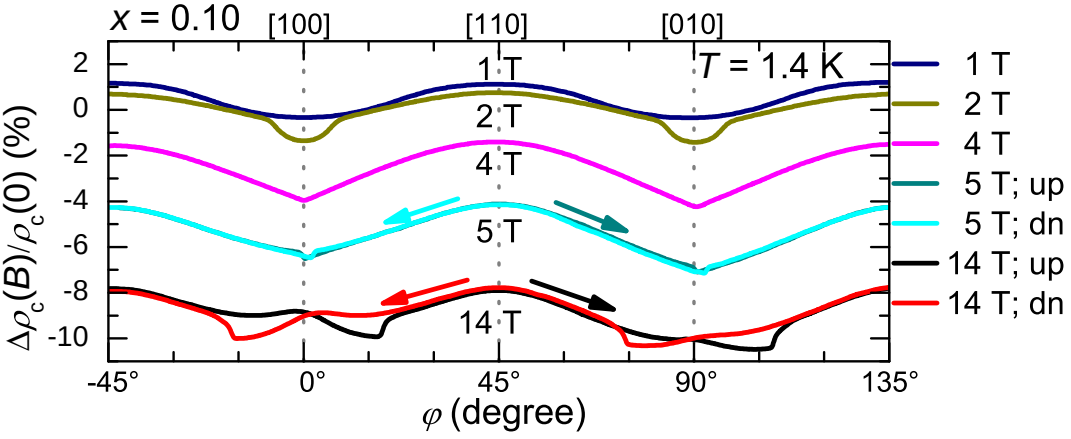

Figure 8.3: Angle-dependent interlayer MR for $x = 0.10$ for fields oriented parallel to the conducting layers.

giving rise to the step-like feature in the MR. This phase transition has been studied by magnetotransport and neutron scattering for several n-doped systems [39, 47, 168, 169]. B_{SF} is considerably smaller for $B||[110]$ than for $B||[100]$. In the non-collinear low-field phase the hard spin axes correspond to the diagonal Cu-Cu directions, whereas in the collinear ordered phase the hard and easy axes switch by $45°$ depending on the field direction. According to what was found for the undoped mother compounds [170], a magnetic field perfectly aligned along the $[100]$ direction causes a first-order phase transition. For intermediate orientations, it first induces a collinear ordered spin structure with the staggered moment ordered along $[110]$, which, as the field grows further, gradually rotates to a configuration perpendicular to the field. This consistently explains the lower B_{SF} for the [110]-direction, where the step in the field-dependent MR indicates the spin-flop. For rotations at $5\,\mathrm{T}$ no jump around $\varphi = 0°$ is found any longer. Thus the collinear phase is stable, independent of the azimuthal field-orientation. At even higher fields the φ-anisotropy grows further and a new step-like feature, which depends on the rotational direction, is observed near the $[100]$-direction. In Fig. 8.2 (lower panel) similar data on the same $x = 0.05$ sample can be found, which were recorded at a slightly higher temperature of $T = 4.2\,\mathrm{K}$. The anisotropy decreased clearly and the second feature at higher fields is weaker pronounced. As was shown by Wu et al. [47], the magnetization also follows a fourfold symmetry upon rotation with the field aligned parallel to the conducting layers. This periodicity and a jump-like feature in the vicinity of $B||[100]$, i.e. the Cu-O-Cu direction, were ascribed to a reorientation of the magnetic Nd^{3+}-sublattice. The Nd^{3+}-Nd^{3+} interaction was found to enhance as temperature decreases [43, 45, 46]. It interferes with the Nd^{3+}-Cu^{2+} interactions. Due to this competition, different magnetic structures are suggested at low or high magnetic fields, respectively, see Sect. 1.3.2. Thus, the main anisotropic contributions at fields above $\sim 4 - 5\,\mathrm{T}$ are closely related to the magnetic moments of Nd^{3+}. According to Richard et al. [171] this magnetic ordering can transform from antiferromagnetic into paramagnetic at a critical magnetic field. Since the conducting CuO_2-layers are sandwiched between insulating Nd_2O_2 layers, which can be regarded as barriers in the case of interlayer transport, such magneto-structural changes depending on the field orientation can be understood in terms of a "spin valve" effect [47]. Depending on the orientation of the neodymium spins the ef-

fect of this barrier on the interlayer transport can be varied.

8.2 Varying the polar field orientation

In Fig. 8.4 (a) the ADMR of a strongly underdoped, $x = 0.05$, sample recorded for θ-rotations at a constant field aligned in the plane parallel to the c- and a-axes and $T = 1.4\,\mathrm{K}$ is shown. For fields above $4\,\mathrm{T}$ a step-like feature is observed, shifting towards smaller θ at increasing field, as indicated by the yellow stars. The inset shows the feature near $B||c$-axis in the $15\,\mathrm{T}$ curve.

It is tempting to associate the step-like feature with the spin-flop transition observed at $B_{SF} = 3.5\,\mathrm{T}$ in the field sweeps for $B||[100]$, see Fig. 8.1 (a). Indeed, the positions of the step in the $R(\theta)$ curves at $4\,\mathrm{T}$ and $5\,\mathrm{T}$, in Fig. 8.4 (a), corresponds to the in-plane field component $B_{||} = 3.5 - 4\,\mathrm{T}$. However, at $B \geq 8\,\mathrm{T}$ the observed step does not scale with the in-plane field component $B_{||} = B\sin\theta^*$. This becomes even more obvious when plotting the scaled in-plane component at the angular position of the step-like feature, θ^*, versus the set field, see Fig 8.4 (b). For

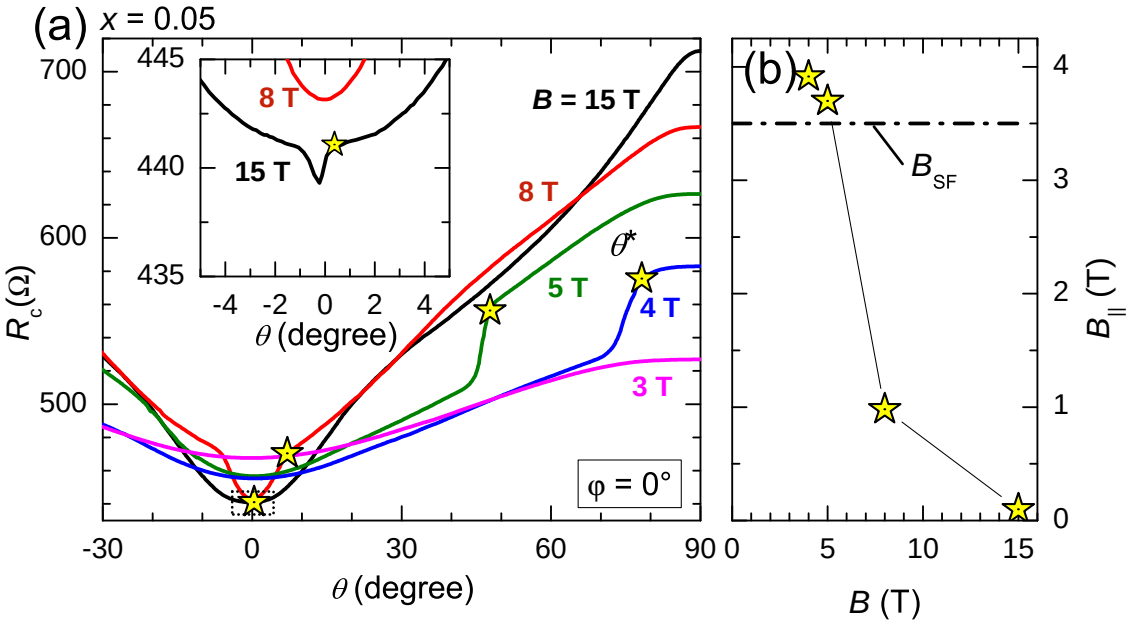

Figure 8.4: (a) ADMR curves at different fields for an $x = 0.05$ sample at $\varphi = 0°$ and $T = 1.4\,\mathrm{K}$. Inset: zoom near $\theta = 0°$. (b) In-plane component $B_{||} = B\sin\theta^*$ at the step-like features marked by stars.

the $4\,\mathrm{T}$ and $5\,\mathrm{T}$ curves the step is near B_{SF} (indicated by the dashed-dotted line), whereas for higher fields the in-plane field component is much lower. There is a weak shoulder discernible on both the $8\,\mathrm{T}$ and $15\,\mathrm{T}$ curves in Fig. 8.1 (a) at an angle of approximately $35°$. They actually scale with B_{SF} and could be the spin-flop feature but less pronounced. Obviously, the feature near $\theta = 0°$ is of a different origin.

A similar step-like feature in the ADMR is observed for θ-rotations in the plane at $\varphi = 45°$. It also shifts towards the $B||c$-direction upon increasing field.

Fig. 8.5 presents the ADMR of the same underdoped, $x = 0.05$, sample as above, recorded for θ-rotations at a constant field of $B = 15\,\mathrm{T}$ aligned in the plane parallel to the crystallographic c-axis at two different azimuthal orientations, $\varphi = 0°$ (parallel to $[100]$) and $45°$ (parallel to $[110]$) in the upper and lower panel, respectively. For orientations close to perpendicular, $\theta = 0°$, the tiny step-

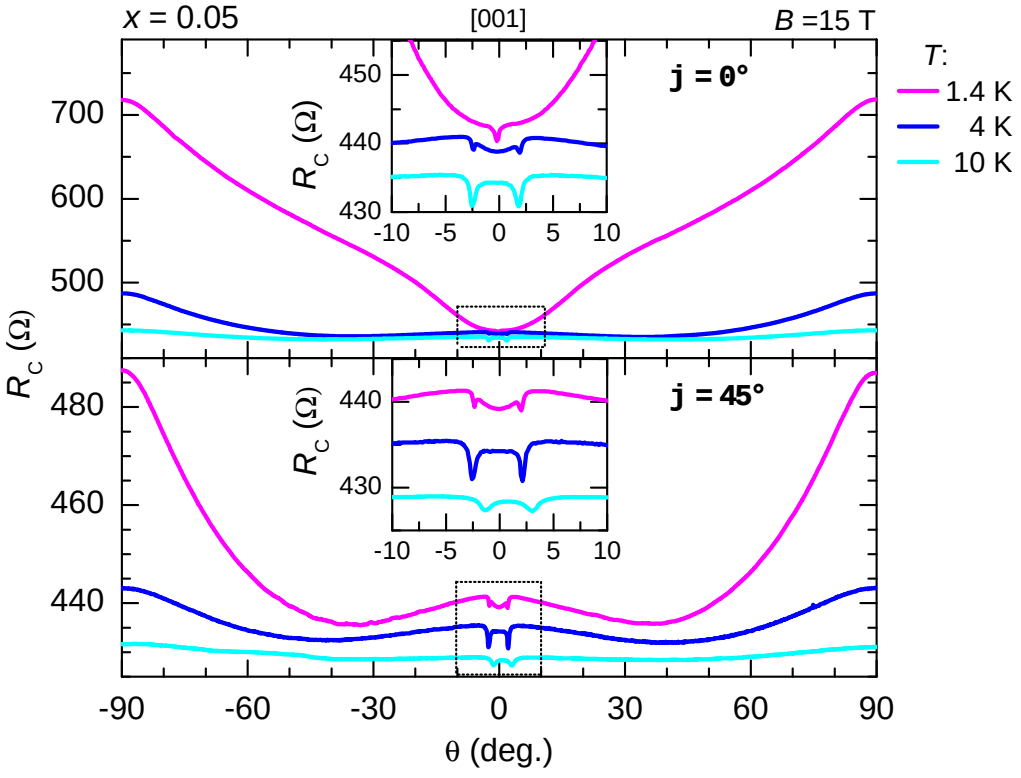

Figure 8.5: ADMR for a strongly underdoped, $x = 0.15$, NCCO sample at different temperatures. (top) $\varphi = 0°$ and (bottom) $\varphi = 45°$. Insets: zoom into the region near $\theta = 0°$ marked by the dotted square.

like feature is observed. Again, the angle is very small, and thus the in-plane component is much smaller than B_{SF}. As the temperature increases, this feature stays at the same angular position. For $\varphi = 0°$ the main difference is that for $1.4\,\mathrm{K}$ there is only one kink right at $\theta = 0°$, whereas there are two for higher T. For $\varphi = 45°$ there are always two kinks over the full T range. The overall $R(\theta)$ curves look similar for both φ orientations. A central hump evolves for $-30° \leq \theta \leq 30°$ upon decreasing T. However, this hump is absent at the lowest T for $\varphi = 0°$, see the inset in the upper panel of Fig. 8.5.

In Fig. 8.4 it was shown that for strongly underdoped $x = 0.05$ samples at lower fields there is a step in the ADMR curves, which seems to be related to the critical spin-flop field B_{SF}, associated with the transition of the Cu^{2+} spin lattice back to the noncollinear configuration as the in-plane field-component weakens. At a field orientation almost perpendicular to the layers, i.e. close to $B||c$-xis, the effective in-plane field component is not strong enough any longer to stabilize the collinear phase within the CuO_2-layers. However, another step-like feature is observed that does not scale with B_{SF}. At the lowest temperature there seems to be a difference in the position of this step between $\varphi = 0°$ and $45°$. As one can see in the insets of Fig. 8.4. The ADMR curve at $1.4\,\mathrm{K}$ for $\varphi = 0°$ shows only a single cusp around $\theta = 0°$, whereas there are still two for $\varphi = 45°$, as seen at higher temperatures.

As already discussed, at low T the influence of the Nd^{3+}-moment can lead to a competition between the different ordering processes of the spin-sublattices. Therefore it is difficult to ascribe the exact origin of the jumps in the ADMR curves. For a detailed analysis further studies are needed.

Interestingly, a prominent central hump is observed in the ADMR curves for $\varphi = 45°$ (similar to what is observed in ADMR experiments on the overdoped samples, see Sect. 6.2) that grows upon decreasing temperatures for θ-rotation in the plane parallel to the diagonal $[110]$-direction. For $x = 0.15$ this anomalous negative slope in $\frac{\mathrm{d}R}{\mathrm{d}|\theta|}$ was found to be closely connected to the anomaly in the MR, as was discussed in Sects. 6.2 and 7.1. Examples of the low-T field and angular dependence of the MR at different x are presented in Fig. 8.6. In the left panels $R(B)$ curves recorded at $B||[001]$ ($\theta = 90°$) are shown. The right panels show ADMR curves recorded at the same temperature in a constant field of $B = 34\,\mathrm{T}$. The polar angle θ is changed from $0°$ ($B||[001]$) to $90°$ ($B||[100]$ or $||[011]$, at fixed

azimuthal angles $\varphi = 0°$ or $45°$, respectively). For the optimally doped composition, $x = 0.145$, the behavior is similar to that found earlier for $x = 0.15$: as B increases, an anomalous low-field MR, mainly determined by the out-of-plane field component $B_\perp$, comes to a maximum and is then gradually changed by a conventional, orbital MR. At decreasing x the maximum shifts to higher fields and exceeds the maximum field of $35\,\mathrm{T}$ already for $x = 0.14$. Starting from this doping level the angular dependence of MR (right panel of Fig. 8.6) mimics the dependence on $B_\perp$ (left panel of Fig. 8.6). It is most likely related to the influence of the field on a spin-dependent transport in presence of magnetic ordering. For the non-superconducting composition, $x = 0.10$, the hysteresis observed in the

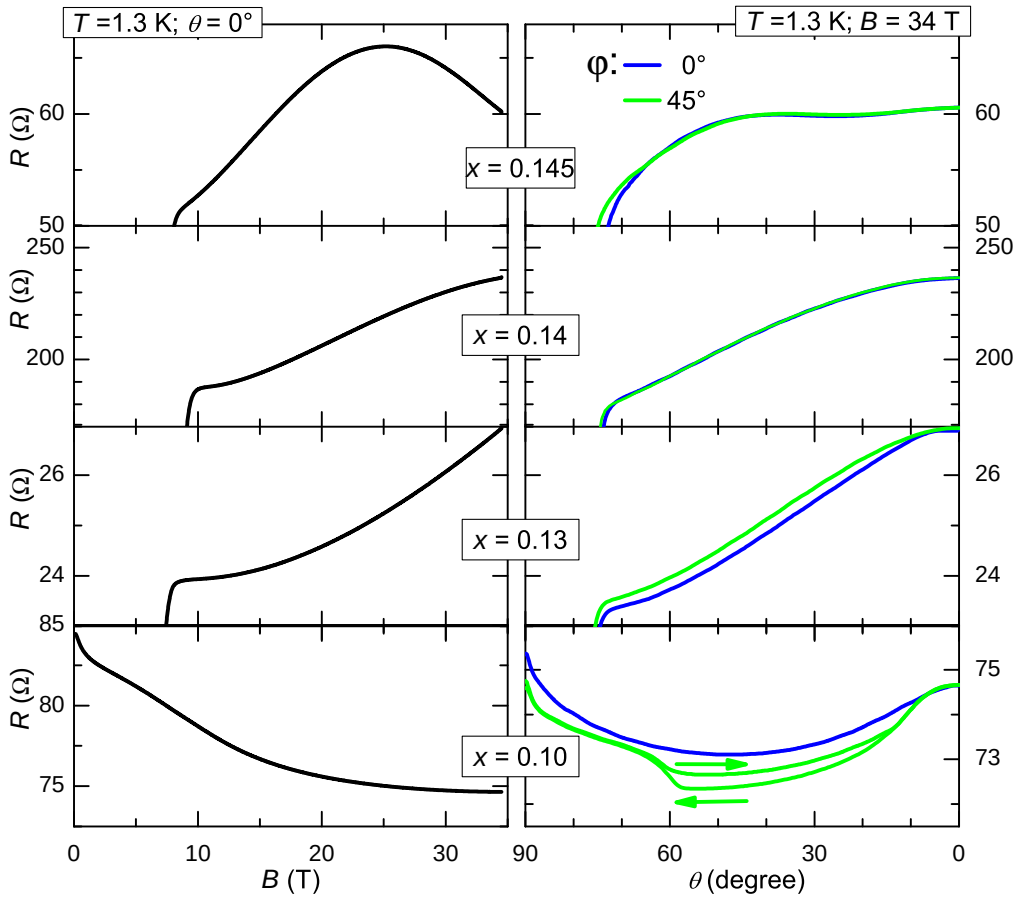

Figure 8.6: (left) B-dependent interlayer magnetoresistance (MR) for different x at $T = 1.3\,\mathrm{K}$ and $B||[001]$. (right) Polar-angle(θ)-dependent MR at $B = 34\,\mathrm{T}$ and $T = 1.3\,\mathrm{K}$ for azimuthal angles $\varphi = 0°, 45°$. Arrows indicate the sweep direction.

angular sweeps for $\varphi = 45°$ clearly manifests field-induced rearrangements of antiferromagnetically ordered spins.

8.3 Conclusion

Traces of the spin-flop transition in the Cu^{2+} spin-structure, well known for the undoped NCO, and additional features related to the Nd^{3+} spin-sublattice were observed for doping levels up to $x = 0.10$. The comparison of the field- and angle-dependent MR of samples with different x shows that the interlayer transport is strongly affected by spin-dependent scattering even at doping levels where SC already emerges. Due to the complex interference of the magnetic substructures it is difficult to ascribe the exact origins of the observed features. At this point, further detailed high-field studies on the azimuthal and polar ADMR are required to derive a comprehensive description for the spin-related effects.

Summary and Outlook

9 Summary

The electronic phase diagram of the electron-doped cuprate compound $Nd_{2-x}Ce_xCuO_4$ was probed by the help of the world's strongest nondestructive magnetic fields, as illustrated in Fig. 9.1. High-quality single crystals were available for a broad doping range, covering almost the full electron-doped side. The interlayer magnetoresistance (MR) was measured depending on the field strength and orientation at various temperatures for doping levels ranging from strongly underdoped non-superconducting, $x = 0.05$, till strongly overdoped superconducting, $x = 0.17$, samples.

The discovery of magnetic quantum oscillations in the normal-state MR for $x \geq 0.14$ has proven the existence of a well established Fermi surface (FS) in an electron-doped cuprate. Two oscillation frequencies were observed, revealing a reconstructed FS that persists in the overdoped regime of NCCO, at least in high magnetic fields, $B > 17\,\mathrm{T}$. The slow α-frequency ($\sim 300\,\mathrm{T}$) is associated with a small, hole-like FS pocket and the fast β-frequency ($\sim 11\,\mathrm{kT}$) was identified to originate from magnetic breakdown (MB) in strong magnetic fields. The doping dependence of these two frequencies proved the equivalence between the nominal cerium concentration and the electron-doping for NCCO.

The presented data on Shubnikov-de Haas (SdH) oscillations provides unambiguous evidences for the existence of a reconstructed FS for doping levels until the upper edge of the superconducting region. This suggests that the $(\frac{\pi}{a}, \frac{\pi}{a})$-superlattice potential responsible for the FS reconstruction is stable, at least, for the time electrons need to traverse a full cyclotron orbit until they scatter. The corresponding energy gap of $\sim 10\,\mathrm{meV}$ separates the electron- and hole-like parts of the FS. From the simulations of the SdH data of overdoped NCCO samples the doping dependent evolution of the gap was extracted, showing a linear decrease upon increasing x. Apparently, it closes at the doping, $x_\mathrm{c} = 0.175$. Remarkably, this is exactly the carrier concentration for which superconductivity (SC) in

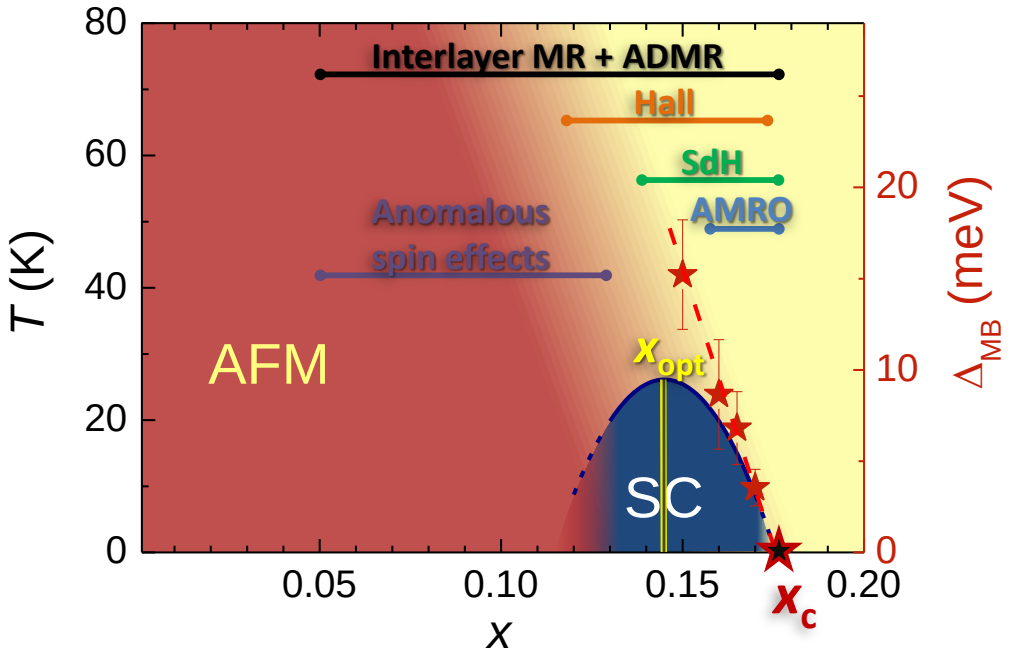

Figure 9.1: Phase diagram of $Nd_{2-x}Ce_xCuO_4$ containing two critical points, x_c and x_{opt}. The horizontal bars mark investigated areas of the observed main effects. The evolution of the gap Δ_{MB} that represents the superlattice potential responsible for the FS reconstruction is included (red stars, scale on the right).

NCCO is expected to vanish.

The magnetic nature of the ground state for overdoped NCCO has been revealed by the unambiguous absence of the spin-splitting effect on the angle-dependent SdH oscillation amplitude. Whether this ground state is associated with slow antiferromagnetic fluctuations or field induced steady antiferromagnetism or a hidden magnetic order such as a d-symmetry spin-density-wave, is to be clarified in future studies.

SdH oscillations were only resolvable down to slightly below optimal doping $x_{opt} = 0.145$. Right below x_{opt} they become suddenly suppressed and therefore, no further information on the FS in the underdoped regime was obtainable from this kind of experiments.

Semiclassical angle-dependent magnetoresistance oscillations (AMRO), originating from the large MB orbit, were observed for overdoped samples, $x \geq 0.16$,

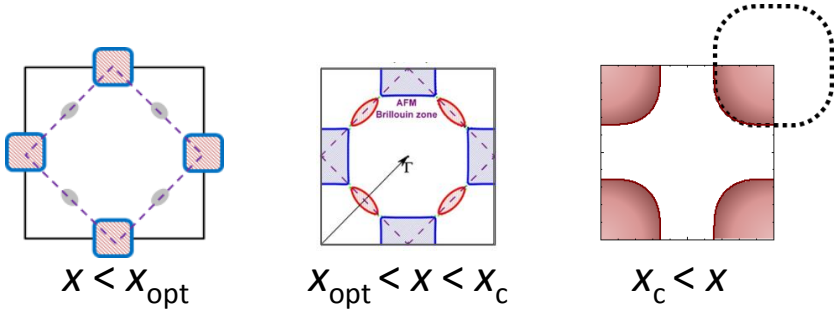

Figure 9.2: Evolution of the FS in NCCO depending on the electron concentration, see text.

that provided insights in the φ-dependent 3D shape of the FS in NCCO. Numerical calculations of the angle-dependent MR (ADMR) were accomplished. They demonstrated that a conventional approach, based on the Boltzmann transport theory in the relaxation time approximation, is capable of deriving the high-field ADMR in overdoped NCCO.

For slightly overdoped, $x = 0.15$, samples no AMRO have been resolved in the available fields. However, from the study of the field and temperature dependence of the MR and ADMR it has been found that above a characteristic anomalous field range the MR is approaching conventional behavior. Two different anomalies in the MR have been identified: A weak peak structure close to the superconducting transition and a broad maximum in the MR at higher fields. The former is most likely associated with superconducting fluctuations in the highly anisotropic, quasi-two-dimensional superconducting system. The high-field anomaly emerges below a characteristic temperature of approximately $10\,\mathrm{K}$, where the normal state resistivity is found to increase significantly. It seems to be closely related to the anomalous spin-dependent transport observed for underdoped samples.

Below optimal doping, $x_{\mathrm{opt}} = 0.145$, the MR loses its conventional character. The sudden suppression of SdH oscillations accompanied by an enhancement of the effective cyclotron mass and a step in the zero-field resistivity indicate strong changes in the electronic system right below x_{opt}.

A series of intralayer transport measurements, were accomplished for NCCO samples ranging from strongly overdoped, $x = 0.165$, to still superconducting, strongly underdoped, $x = 0.13$, compositions. In particular, the Hall effect was

measured, disclosing a dramatic enhancement of the energy gap, representing the $(\frac{\pi}{a}, \frac{\pi}{a})$-superlattice potential, right below x_{opt}: By only a minor change in doping the signature of MB gets lost completely while cyclotron orbits on the small hole-like FS pockets become strongly suppressed (indicated in Fig. 9.2 by the grey pockets in the left drawing). Apparently, this is the point where the longe-range AFM is fully established.

For strongly underdoped samples, effects originating from both the Cu^{2+}- and Nd^{3+}-spin-sublattices that order antiferromagnetically at low temperatures emerge.

As the central result of this thesis, two critical points in the normal-state phase diagram of the electron-doped cuprate superconductor NCCO that pin the superconducting region are established, see Fig. 9.1. The upper edge of the superconducting dome, i.e. the electron concentration, $x = 0.175$, at which SC vanishes, coincides with the point at which the $(\frac{\pi}{a}, \frac{\pi}{a})$-superlattice potential extrapolates to zero. For higher doping the FS is expected to reestablish its conventional shape, as predicted by band theory (right drawing in Fig. 9.2). As the doping decreases, this ordering potential strengthens and, in parallel, SC becomes more pronounced. Optimal doping, $x_{\mathrm{opt}} = 0.145$, i.e. the x corresponding to the highest superconducting critical temperature T_{c}, is located at the point below which a strong enhancement of the ordering potential, associated with the onset of long-range AFM, is observed. The presented observations provide strong arguments for an intimate relation between the ordering in the normal state and SC. A fundamental explanation of the mechanism of this ordering and its exact effect on SC stays beyond the scope of this thesis. While HTSC in cuprates stays enigmatic and demands further experimental and theoretical efforts to be understood completely, the present findings establish important constraints on the possible model.

Open questions

The commonly accepted FS reconstruction by the $(\frac{\pi}{a}, \frac{\pi}{a})$ potential comprises hole- and electron-like pockets. Unlike the hole pockets, the electron ones have not been detected in the magnetic quantum oscillation experiments. One of the reasons for the weak contribution of the electron pockets to the SdH oscillations in the interlayer MR, discussed in Sect. 5.1.10, may be a relatively weak warping in the k_z-direction. Therefore, one can expect a larger contribution of these parts of the FS in the MQO of in-plane magnetotransport. However, the main challenge for in-plane transport in single-crystalline NCCO is the small sample thickness needed for reasonably large signals due to the large anisotropic transport properties of this system. Preliminary results from thermoelectric measurements, where magnetic quantum oscillations have been observed in the thermopower of an slightly overdoped NCCO sample, are promising. A first analysis revealed an enhanced oscillation amplitude as compared to the SdH oscillations measured in the same field and temperature ranges [172]. Thus, if the electron-like parts of the FS contributed stronger to the in-plane transport, thermopower might give further answers.

The exact origin of the FS reconstruction in the overdoped superconducting region of the phase diagram stays unidentified. Although the magnetic nature of the ground state has been revealed by the observations presented, a possible field-induced character or even completely different nature, like a hidden order, cannot be excluded unambiguously. Other techniques, such as nuclear magnetic resonance or muon spin resonance performed in magnetic fields could be useful to distinguish field induced from field independent effects in NCCO.

And, of course, fundamental differences between the numerous cuprate compounds, for both hole- and electron-like compositions, have to be identified and further sorted out for understanding the correlations between the competing phases in the generic phase diagram.

Appendix

A Relative contribution of the hole pockets of the reconstructed FS to the inter-layer conductivity

One can evaluate the contribution of a volume element dV in k-space to the current density as:

$$dj_z = 2|e|v_\perp \frac{dV}{(2\pi)^3}, \tag{A.1}$$

with the carrier concentration in k-space, $n = 2dV/(2\pi)^3$ and the interlayer velocity component $v_\perp$. Due to the application of an electrical field in the k_z-direction the FS experiences a shift by $\Delta k_z = eE_z\tau/\hbar$. For a cylindrical FS with the interlayer dispersion $\epsilon(k_z) = -t_\perp(\varphi)\cos(k_z a_z)$, with the interlayer periodicity a_z. The volume fraction in cylindrical coordinates is $dV = k_{||} \cdot dk_{||} d\varphi dk_z$, with the $k_\parallel$ the in-plane momentum. Taking the integral gives

$$j_z = 2\frac{t_\perp^0 a_z e}{\pi^3\hbar}\int_0^{2\pi} d\varphi \int_{\pi/a_z}^{\pi/a_z} dk_z \int_{k_\parallel(k_z)}^{k_\parallel(k_z+\Delta k_z)} k_z \sin(k_z a_z)\; k'_{||} \cdot w(\varphi) dk'_{||}, \tag{A.2}$$

$t_\perp(\varphi) = t_\perp^0 w(\varphi)$ describes the dependence of the interlayer hopping on the direction of the in-plane momentum according to the symmetry of the Brillouin zone (see Sect. 2.6). The factor 2 has to be added taking both, positive and negative k_z parts into account. Eq. A.2 was numerically evaluated using Mathematica, the dispersion relation for the unreconstructed FS, Eq. (1.2), and for the reconstructed hole-like pocket, Eq. (1.3), with $a = 3.95$Å, $a_z = 6.04$Å, $\alpha = -0.021$ eV (for $x = 0.17$), $t = 0.38eV$, $t' = 0.32t$, $t'' = 0.5t'$, $t_\perp = E_\mathrm{F}/60$, and $\Delta k_z = 0.02$.

The ratio between the conductivity contributions of the four small hole-like FS pockets and the large MB orbit is equivalent to $K_\alpha = 4\sigma_{zz,\alpha}/\sigma_{zz,\beta}$. For different higher harmonics in the warping term the results are presented in Table A.1. It ranges from 0.39 for a conventional φ-independent warping to 0.68, with the ad-

$w(\varphi)$	K_α
1	0.39
$\sin(2\varphi)$	0.68
$\sin(2\varphi) + 0.3\sin(6\varphi)$	0.43
$\sin(2\varphi) + 0.3\sin(6\varphi) - 0.3\sin(10\varphi)$	0.42

Table A.1: Overview on the evaluated conductivity contribution ratio between the four small FS pockets and the large MB orbit at $x = 0.17$ using the FS dispersion Eq. (1.2) and Eq. (1.3) for different φ-dependencies of the interlayer corrugation represented by $w(\varphi)$.

ditional $\sin(2\varphi)$-term. The more complex the warping gets, the more the ratio approaches the conventional value.

B Source code of the program applied for simulating AMRO

Reproducing AMRO simulations for Tl-2201

```
%interlayer␣hopping;␣lattice␣constants%
tz1␣=␣1/60.0;␣a␣=␣3.866;␣c␣=␣11.6;
%number␣of␣orbits;␣number␣of␣chargecarriers␣per␣orbit%
n1␣=␣30.0;␣n3␣=␣5*n1;
%azimuthal␣angles␣(\varphi)%
f01␣=␣0.0/18.0*Pi;␣f02␣=␣4.5/18.0*Pi;
%in-plane␣Fermi␣surface␣according␣to␣Hussey␣et␣al.[25]%
k00␣=␣0.745;␣k04␣=␣-0.019;
␣%␣interlayer␣warping␣parameters␣according␣to␣Hussey␣et␣al.[25]%
be0␣=␣0.031;␣be␣=␣0.021;␣bee␣=␣-0.0085;
%starting␣polar␣(\theta)␣orientation%
tt0␣=␣0.0/18.0*Pi;
%\omega_c␣\tau%
ot[f_]␣:=␣ot1;
%interlayer␣velocity␣component%
vz[kz_,␣f_]␣:=␣tz1*Cos[kz*c]*g[f];
%warping␣terms%
g[f_]␣:=␣(be0*Sin[2*f]␣+␣be*Sin[6*f]␣+␣bee*Sin[10*f]);
%in-plane␣dispersion%
e2a[k_,␣f_]␣:=␣(k00␣+␣k04*Cos[4*f])^2;
%in-plane␣Fermi␣velocity%
v1[k_,␣f_]␣:=␣2*(k00␣+␣k04*Cos[4*f]);
%in-plane␣Fermi␣vector%
k1[y_]␣:=␣k00␣+␣k04*Cos[4*y];
%position␣on␣an␣orbit%
kz7[t_,␣kz0_,␣fi_,␣fi1_]␣:=␣kz0␣-␣k1[fi␣+␣fi1]*Cos[fi1]*Tan[t];
```

```
%eff. mass%
n2 = 400;
mH = 1.0*Sum[
     Abs[k1[Pi*(i - 0.5)/n2]/
       v1[k1[Pi*(i - 0.5)/n2], Pi*(i - 0.5)/n2] ], {i, n2}]/n2;
%timedependent angular position on the orbit%
dpsim[fi_, fi1_] := Abs[k1[fi + fi1]/v1[k1[fi + fi1], fi + fi1]]/mH;
psim1[fi_, f_] := (ni = Floor[f*20 + 1];
   p = Sum[dpsim[fi, -f*(i - 0.5)/ni], {i, ni}]*f/ni; Return[p]; );
%calculation of the conductivity%
s2[t_, fi_] := (If[ot[fi]*Cos[t] > 1.0, alp = 1.0,
    alp = ot[fi]*Cos[t]]; w1 = 0.0;
   For[l = 0, l < n3, l++, kz0i = 1.0*\[Pi]*l/n3/c;
    (* Begin the circle for calculation of w2: *)
    w2 = 0.0; fdj1 = 2.0*Pi/n1/dpsim[fi, 0]; fdj2 = fdj1; fdj = fdj1;
    For[fj2 = 0, fj2 < 2*\[Pi] - fdj1/1.9, dp3 = 1.0*dpsim[fi, fj2];
     dp2j = dp3;
     If[fj2 + fdj1 + fdj < 2*Pi, fdj = 2*Pi/n1/dp2j,
      fdj = 2*Pi - fdj/2 - fdj1/2.0 - fj2];
     fj2 = fj2 + fdj/2 + fdj2/2, fdj2 = fdj;
     kz2j = 1.0*kz7[t, kz0i, fi, fj2]; kz3 = kz2j;
     (* Calculation of w3: *)
     w3 = 0.0; ep3 = 1.0; fdi1 = 2.0*Pi*alp/n1/dp3; fdi = fdi1;
     fdi2 = fdi;
     For[fiv = 0, fiv < 2 \[Pi]*alp - fdi1/1.9,
      If[fiv + fdi1 + fdi < 2*Pi*alp, fdi = 2.0*Pi*alp/n1/dp3,
       fdi = 2.0*Pi*alp - fdi1/2 - fdi/2 - fiv];
      fiv = fiv + fdi/2 + fdi2/2, fdi2 = fdi; f1 = fj2 - fiv;
      f2 = fj2 - fiv - fdi/2; f3 = fj2 - fiv - fdi;
      dp1 = dp3; dp2 = N[1.0*dpsim[fi, f2]];
      dp3 = N[1.0*dpsim[fi, f3]];
      ep1 = ep3;
      ep2 = ep1*Exp[-fdi*(dp1 + dp2)/4/ot[fiv]/Abs[Cos[t]]];
      ep3 = ep2*Exp[-fdi*(dp2 + dp3)/4/ot[fiv]/Abs[Cos[t]]];
      kz1 = kz3; kz2 = kz7[t, kz0i, fi, f2];
      kz3 = kz7[t, kz0i, fi, f3];
      w3 =
```

```
␣␣␣␣␣␣␣w3␣+␣(dp2*ep2*
␣␣␣␣␣␣␣␣␣␣␣␣vz[kz2,
␣␣␣␣␣␣␣␣␣␣␣␣␣fi␣+␣f2]␣+␣(dp1*ep1*vz[kz1,␣fi␣+␣f1]␣+
␣␣␣␣␣␣␣␣␣␣␣␣␣dp3*ep3*vz[kz3,␣fi␣+␣f3]␣-␣2*dp2*ep2*vz[kz2,␣fi␣+␣f2])/
␣␣␣␣␣␣␣␣␣␣␣6.0)*fdi;];
␣␣␣␣␣(*␣Calculation␣of␣w2:␣*)
␣␣␣␣␣w2␣=␣w2␣+␣w3*vz[kz2j,␣fi␣+␣fj2]*2*Pi/n1;];
␣␣␣␣w1␣=␣w1␣+
␣␣␣␣␣␣w2*1.0/ot[fi␣+␣fj2]/mH/(1.0␣-␣Exp[-2*Pi/ot[fi␣+␣fj2]/Cos[t]]);];
␣␣␣Return[N[w1*(1.0/Cos[t])*2.0*\[Pi]/n3]];);
Clear[tt];␣Clear[tr];␣i1␣=␣0;
For[tt1␣=␣tt0,␣tt1␣<␣9.0/18.0*Pi,␣tt1␣=␣tt1␣+␣1.0/180.0*Pi,
␣␣u1␣=␣1.0/s2[tt1,␣f01];␣u2␣=␣1.0/s2[tt1,␣f02];
␣␣Print["\[Tau]\[Omega]=",␣N[ot1],␣"␣␣\[Theta]\[Degree]=",␣tt1*180/Pi,
␣␣␣␣"␣␣tan\[Theta]=",␣N[Tan[tt1]],␣"␣␣R(\[CurlyPhi]0)=",␣u1,
␣␣␣"␣␣R(\[CurlyPhi]2)=",␣u2(*,"␣␣R(\[CurlyPhi]3)=",u3,
␣␣␣"␣␣R(\[CurlyPhi]4)=",u4,"␣␣R(\[CurlyPhi]5)=",u5,
␣␣␣"␣␣R(\[CurlyPhi]6)=",u6,"␣␣R(\[CurlyPhi]7)=",u7,"R(\[CurlyPhi]8)=",
␣␣␣u8,"␣␣R(\[CurlyPhi]9)=",u9,"␣␣R(\[CurlyPhi]10)=",u10,
␣␣␣"␣␣R(\[CurlyPhi]11)=",u11*)];
␣␣tr[i1,␣1]␣=␣tt1*180/Pi;␣tr[i1,␣2]␣=␣u1;␣tr[i1,␣3]␣=␣u2;
␣␣i1␣=␣i1␣+␣1;
␣␣];
tt␣=␣Table[tr[it,␣jt],␣{it,␣0,␣i1␣-␣1},␣{jt,␣1,␣3}];
MatrixForm[tt];
ListPlot;
```

Bibliography

[1] H. Kamerlingh Onnes, Comm. Phys. Lab. Univ. Leiden **120b** (1911).

[2] J. Bardeen, L. N. Cooper, and J. R. Schrieffer, Physical Review **106**, 162 (1957).

[3] J. Bardeen, L. N. Cooper, and J. R. Schrieffer, Physical Review **108**, 1175 (1957).

[4] J. G. Bednorz and K. A. Müller, Z. Phys. B **64**, 189 (1986).

[5] M. K. Wu, J. R. Ashburn, C. J. Torng, P. H. Hor, R. L. Meng, L. Gao, Z. J. Huang, Y. Q. Wang, and C. W. Chu, Physical Review Letters **58**, 908 (1987).

[6] A. Ramirez, Fortune Magnazine (1988).

[7] U. Onbasli, Y. T. Wang, A. Naziripour, R. Tello, W. Kiehl, and A. M. Hermann, physica status solidi (b) **194**, 371 (1996).

[8] Z. Hiroi, J. Phys. Soc. Jpn. (2013).

[9] Y. Kamihara, H. Hiramatsu, M. Hirano, R. Kawamura, H. Yanagi, T. Kamiya, and H. Hosono, Journal of the American Chemical Society **128**, 10012 (2006).

[10] N. F. Mott, Proceedings of the Physical Society. Section A **62**, 416 (1949).

[11] M. Dixon, Physica C: Superconductivity **174**, 117 (1991).

[12] D. J. Scalapino, arXiv e-print (2006), "Handbook of High Temperature Superconductivity", J. R. Schrieffer, editor, Springer, 2006.

[13] P. A. Lee, N. Nagaosa, and X.-G. Wen, Reviews of Modern Physics **78**, 17 (2006).

[14] D. Scalapino, Physics Reports **250**, 329 (1995).

[15] J. Orenstein and A. J. Millis, Science **288**, 468 (2000).

[16] A. Damascelli, Z. Hussain, and Z. X. Shen, Reviews of Modern Physics **75**, 473 (2003).

[17] y. Fischer, M. Kugler, I. Maggio-Aprile, C. Berthod, and C. Renner, Reviews of Modern Physics **79**, 353 (2007).

[18] P. A. Lee, Reports on Progress in Physics **71**, 012501 (2008).

[19] H. Alloul, J. Bobroff, M. Gabay, and P. J. Hirschfeld, Reviews of Modern Physics **81**, 45 (2009).

[20] A. Mann, Nature News **475**, 280 (2011).

[21] P. W. Anderson, Science **235**, 1196 (1987).

[22] P. Monthoux, A. V. Balatsky, and D. Pines, Physical Review Letters **67**, 3448 (1991).

[23] H. Takagi, S. Uchida, and Y. Tokura, Physical Review Letters **62**, 1197 (1989).

[24] Y. Tokura, A. Fujimori, H. Matsubara, H. Watabe, H. Takagi, S. Uchida, M. Sakai, H. Ikeda, S. Okuda, and S. Tanaka, Physical Review B **39**, 9704 (1989).

[25] N. P. Armitage, P. Fournier, and R. L. Greene, Reviews of Modern Physics **82**, 2421 (2010).

[26] N. E. Hussey, M. Abdel-Jawad, A. Carrington, A. P. Mackenzie, and L. Balicas, Nature **425**, 814 (2003).

[27] M. Abdel-Jawad, M. P. Kennett, L. Balicas, A. Carrington, A. P. Mackenzie, R. H. McKenzie, and N. E. Hussey, Nature Physics **2**, 821 (2006).

[28] N. Doiron-Leyraud, C. Proust, D. LeBoeuf, J. Levallois, J.-B. Bonnemaison, R. Liang, D. A. Bonn, W. N. Hardy, and L. Taillefer, Nature **447**, 565 (2007).

[29] E. A. Yelland, J. Singleton, C. H. Mielke, N. Harrison, F. F. Balakirev, B. Dabrowski, and J. R. Cooper, Physical Review Letters **100**, 047003 (2008).

[30] A. F. Bangura, J. D. Fletcher, A. Carrington, J. Levallois, M. Nardone, B. Vignolle, P. J. Heard, N. Doiron-Leyraud, D. LeBoeuf, L. Taillefer, S. Adachi, C. Proust, and N. E. Hussey, Physical Review Letters **100**, 047004 (2008).

[31] B. Vignolle, A. Carrington, R. A. Cooper, M. M. J. French, A. P. Mackenzie, C. Jaudet, D. Vignolles, C. Proust, and N. E. Hussey, Nature **455**, 952 (2008).

[32] C. Jaudet, D. Vignolles, A. Audouard, J. Levallois, D. LeBoeuf, N. Doiron-Leyraud, B. Vignolle, M. Nardone, A. Zitouni, R. Liang, D. Bonn, W. Hardy, L. Taillefer, and C. Proust, Physical Review Letters **100** (2008).

[33] S. E. Sebastian, N. Harrison, E. Palm, T. P. Murphy, C. H. Mielke, R. Liang, D. A. Bonn, W. N. Hardy, and G. G. Lonzarich, Nature **454**, 200 (2008).

[34] A. P. Cracknell and W. A. C., *The Fermi surface* (Oxford University Press, London, 1973).

[35] D. Shoenberg, *Magnetic Oscillations in Metals*, Cambridge Monographs on Physics Series (Cambridge University Press, 1984).

[36] M. V. Kartsovnik, Chemical Reviews **104**, 5737 (2004).

[37] P. K. Mang, O. P. Vajk, A. Arvanitaki, J. W. Lynn, and M. Greven, Physical Review Letters **93**, 027002 (2004).

[38] J. W. Lynn and S. Skanthakumar, *Neutron Scattering Studies of Lanthanide Magnetic Ordering*, edited by K. A. Gschneidner, L. Eyring, Jr., and M. B. Maple, Handbook on the Physics and Chemistry of Rare Earths, Vol. 31 (North Holland, Amsterdam, 2001) Chap. 199.

[39] A. Lavrov, H. Kang, Y. Kurita, T. Suzuki, S. Komiya, J. Lynn, S.-H. Lee, P. Dai, and Y. Ando, Physical Review Letters **92** (2004).

[40] S. Skanthakumar, J. W. Lynn, J. L. Peng, and Z. Y. Li, Physical Review B **47**, 6173 (1993).

[41] S. Skanthakumar, J. W. Lynn, and I. W. Sumarlin, Physical Review Letters **74**, 2842 (1995).

[42] T. R. Thurston, M. Matsuda, K. Kakurai, K. Yamada, Y. Endoh, R. J. Birgeneau, P. M. Gehring, Y. Hidaka, M. A. Kastner, T. Murakami, and G. Shirane, Physical Review Letters **65**, 263 (1990).

[43] M. Matsuda, K. Yamada, K. Kakurai, H. Kadowaki, T. R. Thurston, Y. Endoh, Y. Hidaka, R. J. Birgeneau, M. A. Kastner, P. M. Gehring, A. H. Moudden, and G. Shirane, Physical Review B **42**, 10098 (1990).

[44] A. S. Cherny, E. N. Khatsko, G. Chouteau, J. M. Louis, A. A. Stepanov, P. Wyder, S. N. Barilo, and D. I. Zhigunov, Physical Review B **45**, 12600 (1992).

[45] J. W. Lynn, I. W. Sumarlin, S. Skanthakumar, W.-H. Li, R. N. Shelton, J. L. Peng, Z. Fisk, and S.-W. Cheong, Physical Review B **41**, 2569 (1990).

[46] P. Richard, M. Poirier, and S. Jandl, Physical Review B **71** (2005), 10.1103/PhysRevB.71.144425.

[47] T. Wu, C. H. Wang, G. Wu, D. F. Fang, J. L. Luo, G. T. Liu, and X. H. Chen, Journal of Physics: Condensed Matter **20**, 275226 (2008).

[48] O. K. Andersen, A. I. Liechtenstein, O. Jepsen, and F. Paulsen, Journal of Physics and Chemistry of Solids **56**, 1573 (1995).

[49] C. Bergemann, A. P. Mackenzie, S. R. Julian, D. Forsythe, and E. Ohmichi, Advances in Physics **52**, 639 (2003).

[50] N. Armitage, D. Lu, D. Feng, C. Kim, A. Damascelli, K. Shen, F. Ronning, Z.-X. Shen, Y. Onose, Y. Taguchi, and Y. Tokura, Physical Review Letters **86**, 1126 (2001).

[51] H. Matsui, K. Terashima, T. Sato, T. Takahashi, M. Fujita, and K. Yamada, Physical Review Letters **95**, 017003 (2005).

[52] S. R. Park, Y. S. Roh, Y. K. Yoon, C. S. Leem, J. H. Kim, B. J. Kim, H. Koh, H. Eisaki, N. P. Armitage, and C. Kim, Physical Review B **75**, 060501 (2007).

[53] R. W. Hill, C. Proust, L. Taillefer, P. Fournier, and R. L. Greene, Nature **414**, 711 (2001).

[54] G.-q. Zheng, T. Sato, Y. Kitaoka, M. Fujita, and K. Yamada, Physical Review Letters **90**, 197005 (2003).

[55] C. Proust, K. Behnia, R. Bel, D. Maude, and S. I. Vedeneev, Physical Review B **72**, 214511 (2005).

[56] C. Proust, E. Boaknin, R. W. Hill, L. Taillefer, and A. P. Mackenzie, Physical Review Letters **89**, 147003 (2002).

[57] S. Nakamae, K. Behnia, N. Mangkorntong, M. Nohara, H. Takagi, S. J. C. Yates, and N. E. Hussey, Physical Review B **68**, 100502 (2003).

[58] T. Shibauchi, L. Krusin-Elbaum, M. Li, M. P. Maley, and P. H. Kes, Physical Review Letters **86**, 5763 (2001).

[59] Y. Onose, Y. Taguchi, K. Ishizaka, and Y. Tokura, Physical Review B **69**, 024504 (2004).

[60] T. Valla, A. V. Fedorov, J. Lee, J. C. Davis, and G. D. Gu, Science **314**, 1914 (2006).

[61] L. P. Gorkov, Physical Review Letters **97** (2006).

[62] J. Kang, S.-L. Yu, T. Xiang, and J.-X. Li, Physical Review B **84**, 064520 (2011).

[63] P. W. Anderson, Science **256**, 1526 (1992), PMID: 17836318.

[64] T. Timusk and B. Statt, Reports on Progress in Physics **62**, 61 (1999).

[65] H. Kontani, K. Kanki, and K. Ueda, Physical Review B **59**, 14723 (1999).

[66] H. Matsui, K. Terashima, T. Sato, T. Takahashi, S.-C. Wang, H.-B. Yang, H. Ding, T. Uefuji, and K. Yamada, Physical Review Letters **94** (2005).

[67] N. Armitage, D. Lu, C. Kim, A. Damascelli, K. Shen, F. Ronning, D. Feng, P. Bogdanov, Z.-X. Shen, Y. Onose, Y. Taguchi, Y. Tokura, P. Mang, N. Kaneko, and M. Greven, Physical Review Letters **87** (2001).

[68] N. P. Armitage, F. Ronning, D. H. Lu, C. Kim, A. Damascelli, K. M. Shen, D. L. Feng, H. Eisaki, Z.-X. Shen, Y. Onose, Y. Taguchi, and Y. Tokura, Physical Review Letters **88** (2002), 10.1103/PhysRevLett.88.257001.

[69] N. P. Armitage, D. H. Lu, C. Kim, A. Damascelli, K. M. Shen, F. Ronning, D. L. Feng, P. Bogdanov, X. J. Zhou, W. L. Yang, Z. Hussain, P. K. Mang, N. Kaneko, M. Greven, Y. Onose, Y. Taguchi, Y. Tokura, and Z.-X. Shen, Physical Review B **68**, 064517 (2003).

[70] T. Sato, Science **291**, 1517 (2001).

[71] H. Matsui, T. Takahashi, T. Sato, K. Terashima, H. Ding, T. Uefuji, and K. Yamada, Physical Review B **75** (2007).

[72] C. Kusko, R. S. Markiewicz, M. Lindroos, and A. Bansil, Physical Review B **66** (2002).

[73] J. Lin and A. Millis, Physical Review B **72** (2005), 10.1103/PhysRevB.72.214506.

[74] T. Das, R. S. Markiewicz, and A. Bansil, Journal of Physics and Chemistry of Solids **69**, 2963 (2008).

[75] E. M. Motoyama, G. Yu, I. M. Vishik, O. P. Vajk, P. K. Mang, and M. Greven, Nature **445**, 186 (2007).

[76] M. Matsuda, Y. Endoh, K. Yamada, H. Kojima, I. Tanaka, R. J. Birgeneau, M. A. Kastner, and G. Shirane, Physical Review B **45**, 12548 (1992).

[77] T. Uefuji, K. Kurahashi, M. Fujita, M. Matsuda, and K. Yamada, Physica C: Superconductivity **378**, 273 (2002).

[78] K. Yamada, K. Kurahashi, T. Uefuji, M. Fujita, S. Park, S.-H. Lee, and Y. Endoh, Physical Review Letters **90**, 137004 (2003).

[79] B. Kyung, V. Hankevych, A.-M. DarÃ©, and A.-M. S. Tremblay, Physical Review Letters **93**, 147004 (2004).

[80] R. S. Markiewicz, Physical Review B **70**, 174518 (2004).

[81] S. Chakravarty, R. B. Laughlin, D. K. Morr, and C. Nayak, Physical Review B **63**, 094503 (2001).

[82] M. Abdel-Jawad, J. G. Analytis, L. Balicas, A. Carrington, J. P. H. Charmant, M. M. J. French, and N. E. Hussey, Physical Review Letters **99**, 107002 (2007).

[83] J. Analytis, M. Abdel-Jawad, L. Balicas, M. French, and N. Hussey, Physical Review B **76**, 1098 (2007).

[84] D. J. Singh and W. Pickett, Physica C **203**, 193 (1992).

[85] E. Pavarini, I. Dasgupta, T. Saha-Dasgupta, O. Jepsen, and O. K. Andersen, Phys. Rev. Lett. **87**, 047003 (2001).

[86] A. Millis and M. Norman, Physical Review B **76** (2007).

[87] D. LeBoeuf, N. Doiron-Leyraud, J. Levallois, R. Daou, J.-B. Bonnemaison, N. E. Hussey, L. Balicas, B. J. Ramshaw, R. Liang, D. A. Bonn, W. N. Hardy, S. Adachi, C. Proust, and L. Taillefer, Nature **450**, 533 (2007).

[88] R. K. Kaul, Y. B. Kim, S. Sachdev, and T. Senthil, Nature Physics **4**, 28 (2007).

[89] I. Dimov, P. Goswami, X. Jia, and S. Chakravarty, Physical Review B **78** (2008).

[90] A. S. Alexandrov, Journal of Physics: Condensed Matter **20**, 192202 (2008).

[91] X. Jia, P. Goswami, and S. Chakravarty, Physical Review B **80**, 134503 (2009).

[92] C. M. Varma, Physical Review B **79**, 085110 (2009).

[93] M. A. Hossain, J. D. F. Mottershead, D. Fournier, A. Bostwick, J. L. McChesney, E. Rotenberg, R. Liang, W. N. Hardy, G. A. Sawatzky, I. S. Elfimov, D. A. Bonn, and A. Damascelli, Nature Physics **4**, 527 (2008).

[94] P. Seng, J. Diehl, S. Klimm, S. Horn, R. Tidecks, K. Samwer, H. Hänsel, and R. Gross, Physical Review B **52**, 3071 (1995).

[95] Y. Onose, Y. Taguchi, K. Ishizaka, and Y. Tokura, Physical Review Letters **87**, 217001 (2001).

[96] Y. Dagan, M. M. Qazilbash, C. P. Hill, V. N. Kulkarni, and R. L. Greene, Phys. Rev. Lett. **92**, 167001 (2004).

[97] Y. Dagan, M. Barr, W. Fisher, R. Beck, T. Dhakal, A. Biswas, and R. Greene, Physical Review Letters **94** (2005).

[98] M. Lambacher, *Crystal Growth and Normal State Transport of Electron Doped High Temperature Superconductors*, Ph.D. thesis, Technical University of Munich (2008).

[99] M. Lambacher, T. Helm, M. Kartsovnik, and A. Erb, The European Physical Journal Special Topics **188**, 12 (2010).

[100] S. Charpentier, G. Roberge, S. Godin-Proulx, X. Béchamp-Laganière, K. D. Truong, P. Fournier, and P. Rauwel, Phys. Rev. B **81**, 104509 (2010).

[101] T. Helm, *Transport Measurements in 214-High-Temperature Superconductors*, Diploma thesis, Technical University of Munich (2009).

[102] T. Helm, M. V. Kartsovnik, M. Bartkowiak, N. Bittner, M. Lambacher, A. Erb, J. Wosnitza, and R. Gross, Physical Review Letters **103** (2009).

[103] Y. Ando, G. S. Boebinger, A. Passner, L. F. Schneemeyer, T. Kimura, M. Okuya, S. Watauchi, J. Shimoyama, K. Kishio, K. Tamasaku, N. Ichikawa, and S. Uchida, Phys. Rev. B **60**, 12475 (1999).

[104] Y. Wang, L. Li, and N. P. Ong, Phys. Rev. B **73**, 024510 (2006).

[105] A. A. Abrikosov, *Fundamentals of the theory of metals* (Physical Sciences and Engineering Devision, 1988).

[106] S. E. Sebastian, N. Harrison, G. G. Lonzarich, S. E. Sebastian, N. Harrison, and G. G. Lonzarich, Philosophical Transactions of the Royal Society A: Mathematical, Physical and Engineering Sciences **369**, 1687 (2011).

[107] L. Landau, Zeitschrift für Physik **64**, 629 (1930).

[108] W. J. de Haas and P. M. van Alphen, Proc. Amsterdam Acad. Sci. **33**, 1106 (1930).

[109] L. M. Lifshitz and A. M. Kosevich, Zh. Eksp. Teor. Fiz. **29**, 730 (1956).

[110] E. N. Adams and T. D. Holstein, J. Phys. Chem. Solids **10**, 254 (1959).

[111] A. B. Pippard, *Magnetoresistance in Metals* (Cambridge University Press, 1989).

[112] R. B. Dingle, Proc. R. Soc. A **211**, 517 (1952).

[113] E. H. Sondheimer and A. H. Wilson, Proceedings of the Royal Society of London. Series A. Mathematical and Physical Sciences **210**, 173 (1951).

[114] M. H. Cohen and L. M. Falicov, Phys. Rev. Lett. **7**, 231 (1961).

[115] E. I. Blount, Physical Review **126**, 1636 (1962).

[116] K. Yamaji, Journal of the Physical Society of Japan **58**, 1520 (1989).

[117] R. Yagi, Y. Iye, T. Osada, and S. Kagoshima, Journal of the Physical Society of Japan **59**, 3069 (1990).

[118] M. V. Kartsovnik, V. N. Laukhin, S. I. Pesotskii, I. F. Shchegolev, and V. M. Yakovenko, J. Phys. I France **2**, 89 (1991).

[119] M. S. Nam, S. J. Blundell, A. Ardavan, J. A. Symington, and J. Singleton, J. Phys.: Condens. Matter **13**, 2271 (2001).

[120] P. D. Grigoriev, Physical Review B **81**, 205122 (2010).

[121] K.-T. Wilke, *Kristallzuechtung*, Oxford Classic Texts in the Physical Sciences (Verlag Harri Deutsch, Thun, 1988).

[122] A. Erb, E. Walker, and R. Flükiger, Physica C: Superconductivity **258**, 9 (1996).

[123] A. Maljuk, A. Jokhov, I. Naumenko, I. Bdikin, S. Zver'kov, and G. Emel'chenko, Physica C: Superconductivity **329**, 51 (2000).

[124] M. Matsuda, Y. Endoh, and Y. Hidaka, Physica C: Superconductivity **179**, 347 (1991).

[125] A. Erb, B. Greb, and G. Müller-Vogt, Physica C **259**, 83 (1996).

[126] M. Klaeser, J. Kaiser, F. Stock, G. Mueller-Vogt, and A. Erb, Physica C **306**, 188 (1998).

[127] D. Andres, *Effects of high magnetic fields and hydrostatic pressure on the low temperature density wave state of the organic metal alpha-(BEDT-TTF)$_2$KHg(SCN)$_4$*, Ph.D. thesis, Technical University of Munich (2005).

[128] E. Ohmichi and T. Osada, Review of Scientific Instruments **73**, 3022 (2002).

[129] P. Christ, W. Biberacher, H. Müller, and K. Andres, Solid State Communications **91**, 451 (1994).

[130] P. Christ, *Untersuchungen des magnetischen Grundzustands in alpha-(BEDT-TTF)2KHg(SCN)4 mit Drehmomentmagnetometrie*, Ph.D. thesis, Technical University of Munich (1997).

[131] T. Helm, M. V. Kartsovnik, I. Sheikin, M. Bartkowiak, F. Wolff-Fabris, N. Bittner, W. Biberacher, M. Lambacher, A. Erb, J. Wosnitza, and R. Gross, Physical Review Letters **105**, 247002 (2010).

[132] M. V. Kartsovnik, T. Helm, C. Putzke, F. Wolff-Fabris, I. Sheikin, S. Lepault, C. Proust, D. Vignolles, N. Bittner, W. Biberacher, A. Erb, J. Wosnitza, and R. Gross, New Journal of Physics **13**, 015001 (2011).

[133] R. S. Markiewicz, S. Sahrakorpi, M. Lindroos, H. Lin, and A. Bansil, Physical Review B **72**, 054519 (2005).

[134] B. J. Ramshaw, B. Vignolle, J. Day, R. Liang, W. N. Hardy, C. Proust, and D. A. Bonn, Nat Phys **7**, 234 (2011).

[135] A. Audouard, C. Jaudet, D. Vignolles, R. Liang, D. Bonn, W. Hardy, L. Taillefer, and C. Proust, Physical Review Letters **103** (2009).

[136] S. E. Sebastian, N. Harrison, C. H. Mielke, R. Liang, D. A. Bonn, W. N. Hardy, and G. G. Lonzarich, Physical Review Letters **103**, 256405 (2009).

[137] S. E. Sebastian, N. Harrison, R. Liang, D. A. Bonn, W. N. Hardy, C. H. Mielke, and G. G. Lonzarich, Physical Review Letters **108**, 196403 (2012).

[138] M. V. Kartsovnik, V. N. Laukhin, S. I. Pesotskii, I. F. Schegolev, and V. M. Yakovenko, Journal de Physique I **2**, 89 (1992).

[139] H. J. Kang, P. Dai, J. W. Lynn, M. Matsuura, J. R. Thompson, S.-C. Zhang, D. N. Argyriou, Y. Onose, and Y. Tokura, Nature **423**, 522 (2003).

[140] H. J. Schulz, Physical Review B **39**, 2940 (1989).

[141] S. E. Sebastian, N. Harrison, M. M. Altarawneh, F. F. Balakirev, C. H. Mielke, R. Liang, D. A. Bonn, W. N. Hardy, and G. G. Lonzarich, preprint arxiv:1103.4178 (2011).

[142] S. A. Brazovskii and I. A. Luk'yanchuk, Journal of Experimental and Theoretical Physics **69**, 1180 (1989).

[143] R. Ramazashvili, Physical Review Letters **105**, 216404 (2010).

[144] R. R. Ramazashvili, Journal of Experimental and Theoretical Physics Letters **73**, 505 (1991).

[145] V. V. Kabanov and A. S. Alexandrov, Physical Review B **77**, 132403 (2008).

[146] V. V. Kabanov and A. S. Alexandrov, Physical Review B **81**, 099907 (2010).

[147] N. E. Hussey, Journal of Physics and Chemistry of Solids **67**, 227 (2006).

[148] W. Shockley, Physical Review **79**, 191 (1950).

[149] R. G. Chambers, Proceedings of the Physical Society. Section A **65**, 458 (1952).

[150] J. Ziman, *Electrons and Phonons: The Theory of Transport Phenomena in Solids*, Oxford Classic Texts in the Physical Sciences (OUP Oxford, 1960).

[151] M. Steiner and A. Kapitulnik, Physica C: Superconductivity **422**, 16 (2005).

[152] M. Kartsovnik, G. Logvenov, K. Maki, and N. Kushch, Synthetic Metals **103**, 1827 (1999).

[153] F. Zuo, J. A. Schlueter, and J. M. Williams, Physical Review B **60**, 574 (1999).

[154] A. A. Varlamov, G. Balestrino, E. Milani, and D. V. Livanov, Advances in Physics **48**, 655 (1999).

[155] A. Glatz, A. A. Varlamov, and V. M. Vinokur, Physical Review B **84**, 104510 (2011).

[156] G. Briceno, M. Crommie, and A. Zettl, Physica C: Superconductivity **204**, 389 (1993).

[157] P. Li and R. L. Greene, Physical Review B **76**, 174512 (2007).

[158] W. Yu, B. Liang, and R. L. Greene, Physical Review B **74**, 212504 (2006).

[159] T. Kawakami, T. Shibauchi, Y. Terao, and M. Suzuki, Physical Review B **74**, 144520 (2006).

[160] T. Sekitani, M. Naito, and N. Miura, Physical Review B **67** (2003).

[161] P. Fournier, J. Higgins, H. Balci, E. Maiser, C. J. Lobb, and R. L. Greene, Physical Review B **62**, R11993 (2000).

[162] T. Jacobs, S. O. Katterwe, H. Motzkau, A. Rydh, A. Maljuk, T. Helm, C. Putzke, E. Kampert, M. V. Kartsovnik, and V. M. Krasnov, Physical Review B **86**, 214506 (2012).

[163] H. v. Löhneysen, A. Rosch, M. Vojta, and P. Wölfle, Reviews of Modern Physics **79**, 1015 (2007).

[164] P. Walmsley, C. Putzke, L. Malone, I. Guillamon, D. Vignolles, C. Proust, S. Badoux, A. I. Coldea, M. D. Watson, S. Kasahara, Y. Mizukami, T. Shibauchi, Y. Matsuda, and A. Carrington, Physical Review Letters **110**, 257002 (2013).

[165] P. Li, F. F. Balakirev, and R. L. Greene, Phys. Rev. Lett. **99**, 047003 (2007).

[166] P. Li, K. Behnia, and R. Greene, Physical Review B **75** (2007).

[167] H. Kontani, Reports on Progress in Physics **71**, 026501 (2008).

[168] S. Li, S. Wilson, D. Mandrus, B. Zhao, Y. Onose, Y. Tokura, and P. Dai, Physical Review B **71** (2005).

[169] X. Chen, C. Wang, G. Wang, X. Luo, J. Luo, G. Liu, and N. Wang, Physical Review B **72** (2005).

[170] V. P. Plakhty, S. V. Maleyev, S. V. Gavrilov, F. Bourdarot, S. Pouget, and S. N. Barilo, Europhysics Letters **61**, 534 (2003).

[171] P. Richard, S. Jandl, M. Poirier, P. Fournier, V. Nekvasil, and M. Sadowski, Physical Review B **72** (2005).

[172] S. Arsenijevic, V. Tzanos, T. Helm, and M. V. Kartsovnik, "Results on therompower experiments in steady fields," (2013), unpublished.

List of publications

Jacobs, T., Katterwe, S. O., Motzkau, H., Rydh, A., Maljuk, A., Helm, T., Putzke, C., Kampert, E., Kartsovnik, M. V., Krasnov, V. M. "Electron-tunneling measurements of low-T_c single-layer $Bi_{2+x}Sr_{2-y}CuO_{6+\delta}$: Evidence for a scaling disparity between superconducting and pseudogap states." *Physical Review B* **86**, 214506 (2012).

Kartsovnik, M.V., Helm, T., Putzke, C., Wolff-Fabris, F., Sheikin, I., Lepault, S., Proust, C., Vignolles, D., Bittner, N., Biberacher, W., Erb, A., Wosnitza, J., Gross, R. "Fermi surface of the electron-doped cuprate superconductor $Nd_{2-x}Ce_xCuO_4$ probed by high-field magnetotransport." *New Journal of Physics* **13**, 015001 (2011).

Helm, T., Kartsovnik, M.V., Sheikin, I., Bartkowiak, M., Wolff-Fabris, F., Bittner, N., Biberacher, W., Lambacher, M., Erb, A., Wosnitza, J., Gross, R. "Magnetic breakdown in the electron-doped cuprate superconductor $Nd_{2-x}Ce_xCuO_4$: The reconstructed Fermi surface survives in the strongly overdoped regime." *Physical Review Letters* 105, 247002 (2010).

Lambacher, M., Helm, T., Kartsovnik, M., Erb, A. "Advances in single crystal growth and annealing treatment of electron-doped HTSC." *The European Physical Journal Special Topics* 188, 12 (2010).

Helm, T., Kartsovnik, M.V., Bartkowiak, M., Bittner, N., Lambacher, M., Erb, A., Wosnitza, J., Gross, R. "Evolution of the Fermi surface of the electron-doped high-temperature superconductor $Nd_{2-x}Ce_xCuO_4$ revealed by Shubnikov-de Haas oscillations." *Physical Review Letters* **103** (2009).

unpublished manuscripts

T. Helm, M. Kartsovnik et al. "Correlation between Fermi surface instabilities and superconductivity in the electron-doped cuprate superconductor $Nd_{2-x}Ce_xCuO_4$" (2013)

T. Helm, M. Kartsovnik et al. "Magnetic nature of the ground state of the electron-doped cuprate $Nd_{2-x}Ce_xCuO_4$ in the overdoped regime. (2013)"

Acknowledgments

During the last years I have been fortunate to have met a great variety of people who have contributed to this work. At the end of this thesis I would like to express my gratitude, in particular, to:

- Walther-Meißner-Institute and the Technical University of Munich:

  Prof. Dr. Rudolph Gross for giving me the opportunity to work at the WMI in this project. Thank you for taking your time to listen and sharing your knowledge, even though the whole world wants to cut a piece from your timetable.
  Dr. Mark V. Kartsovnik for being a great mentor, colleague and friend to me. You taught me to work hard, to question what I am doing, to be exact and many other things. Thank you for sharing your experiences and knowledge with me. We have spent many days and nights together, fighting with moody setups, tough specialists, curious operators, special technicians, fatigue and french cheese. I enjoyed to brainstorm while breathing in "fresh air" and to reload my batteries with some "darker than black" black tea.
  Prof. Dr. Andreas Erb for sharing his experience in the world of cuprates, the crystal growth and their preparation with me, for letting me move and work freely in his labs at any time of the day and for having always some wise words and a good advice when I asked for it.
  Dr. Werner Biberacher for sharing his experience and knowledge with me, for his support and helpful advices and for being always so positive. He seems to never lose his good mood.
  Dr. Michael Lambacher for teaching me how to work hard and for introducing me to magnetotransport and to Mark.
  Dr. Matthias Opel and Dr. Stephan Geprägs for their help and advices in terms of the "black box" down in the cellar. I do not know how often I tried to spontaneously get some of their precious SQUID time.
  Dr. Franz Czeschka for his help when ever the famous Vista or Illustrator made me almost cry and the nice atmosphere in the office.
  Nikolaj Bittner for fighting uncountable hours with contacts and the tiniest samples I could find for him. I hope I was not the only reason why you chose to join the "other side", i.e. to become a theoretician.

Michael Kunz for always finding words to tell, for helping me whenever needed and for fighting for the tea, day after day.
Tobias Lamm for helping us in building a beautiful quasi-automatized setup.
Stefan Niekamp for helping me in the lab. I am so glad that in the end the aceton and hexan were not guilty.
Vasilis Tzanos for the greek support. Hellas!
The teatimers, everyone who has joined and shared nice stories and experiences.
Kati Danielewicz, Susanne Mayr, Karen Helm-Knapp, Astrid Habel and Michael Stanger for the hundreds of crystals I needed to be oriented, cut, polished and hugged.
Robert Müller, Georg Nitschke, Christian Reichlmeier, Julius Klaus, Helmut Thies for building the impossible. Whenever we had great ideas for complicated setups, sample holders, etc. they helped us to make it simple, efficient and work.
Sepp Höss for his support in planning and building new setups.
Ulrich Guggenberger and Sigi Wanninger for their help in terms of the electronics and electrics, the guys for some "Caramba" in our life.
Dr. Frank Deppe, Dr. Georg Wild, Ling Zongh, Dr. Mathias Weiler, Dr. Bernhard Muschler, Dr. Elisabeth Hoffman, Johannes Büttner, Max Häberlein, Hans-Martin Eiter, Matthias Danner, Christoph Zollitsch for their help and positive vibrations, that made me enjoy the atmosphere in the institute.
Dr. Matthias Althammer aka "Mace the Oldhammer" and **Dr. Christoph Barkhausen** aka "Dr. Wuff the Vegan" for sharing my deepest thoughts and my best denglish. Thank you for the usely gospeaks during our Middledayeatings!
Prof. Dr. B. S. Chandrasekhar for the nice discussions during our brown bag lunches. I enjoyed every word of yours.
Nitin Chelvani for sharing each others ups and downs during the past two years.
All colleagues at the WMI for their help and positive interference. You made my time at the WMI complete!

- European Magnet Field Laboratory (EMFL):

  Prof. Dr. Jochen Wosnitza for the great collaboration with him and his laboratory.
  Carsten Putzke for his incredible efforts in improving the pulsed field setups, for his outstanding eagerness and will to get things running. It was always a pleasure working with you, the man for no scores!
  Dr. Erik Kampert, the flying dutch, for all the help, the nice collaboration, the many extra hours and the great time in the lab.
  Dr. Frederik Wolff-Fabris for a great user support and many late night hours. I think the triple shifts with three coils together with Carsten, Erik and Nikolaj will secure us the all time lab record.
  Dr. Marek Bartkowiak for the support in the beginnings of my pulsed field experiences.
  Dr. Ilija Sheikin for the great collaboration and the nice hosting during our experiments in Grenoble
  Dr. Stevan Arsenijevic for his help and efforts in preparing and accomplishing the first TEP measurements.
  Dr. Steffen Krämer and **Prof. Dr. Gabriel Seyfarth** for the nice collaboration, the help and hosting in Grenoble.
  Laurent Lozano et Régis Milanole for spending the nights with us in Grenoble and the many nice conversations that kept us awake and aware.
  Dr. Cyril Proust for the great collaboration with him and his group, for sharing his experience with us, for the fruitful discussions and the nice hosting in Toulouse.
  Those who helped us during our experiments in Toulouse. **Prof. Dr. David Vignolles, Dr. Stephane Lepault, Dr. David Leboeuf, Dr. Baptiste Vignolle, Sven Baddoux** and **Dr. Mark Nardonne** for helping us with all of their resources and for the nice hosting in Toulouse.

- National High Magnetic Field Laboratory Tallahassee:

  Prof. Dr. James S. Brooks, Dr. Eun-Sang Choi, Andika Kiswandhi for a nice experiment, all their help and the nice hosting

- Collaborators and friends:

  Dr. Pavel D. Grigoriev for his support in theory and sharing his broad knowledge with us.
  Dr. Reimar Greager for the discussions on politics and "nukular" power. It is partially your fault that I am where I am right now.
  Dr. Steffen Rulands for introducing me to matlab and sharing great times.
  Dr. Frederik Beaujeaun, Dr. Christian Blume, Dr. Ulrich Stuetzl, Martin Kühn and **Michael Nijs** for sharing your expertize with me. Cheers!
  Matthias Kräußlein for the support in Dresden.
  Axel Fink for all the long but fruitful discussions during my stays in Dresden and for sharing each others ups and downs of the past years.

- My Family:

  Marika Helm, my adorable wife, who completes me. You bring structure into my chaos. You share my ups and downs. You are my driving force that pushes me if I am stuck and slows me down if I am too fast. Where ever you are is home to me.
  Sevina Helm, my little star. You are the sunshine in our life!
  My beloved parents, **Ute and Wolfgang**. Danke, dass es euch gibt und ich mir immer eurer Unterstützung sicher sein kann. Ich hab euch lieb.
  My mother in law, **Martina**. Ein dickes Dankeschön an meine Lieblingsschwiegermama.
  My grand parents:
  Werner Helm, Danke für deine Unterstützung;
  Irene Leuschel, Erna und Friedrich Günther. Danke für die Zeit mit euch. Ihr bleibt für immer in meinem Herzen.